
Electronic Thesis and Dissertation Repository

3-2-2011 12:00 AM

Bulk density of small meteoroids

Jean-Baptiste Kikwaya Eluo
The University of Western Ontario

Supervisor

Peter Brown

The University of Western Ontario Joint Supervisor

Margaret Campbell-Brown

The University of Western Ontario

Graduate Program in Astronomy

A thesis submitted in partial fulfillment of the requirements for the degree in Doctor of
Philosophy

© Jean-Baptiste Kikwaya Eluo 2011

Follow this and additional works at: <https://ir.lib.uwo.ca/etd>



Part of the [The Sun and the Solar System Commons](#)

Recommended Citation

Kikwaya Eluo, Jean-Baptiste, "Bulk density of small meteoroids" (2011). *Electronic Thesis and
Dissertation Repository*. 96.

<https://ir.lib.uwo.ca/etd/96>

This Dissertation/Thesis is brought to you for free and open access by Scholarship@Western. It has been accepted for inclusion in Electronic Thesis and Dissertation Repository by an authorized administrator of Scholarship@Western. For more information, please contact wlsadmin@uwo.ca.

Bulk density of small meteoroids

(Thesis format: Integrated-Article)

by

Jean-Baptiste KIKWAYA ELUO

Graduate Program

in

Astronomy

A thesis submitted in partial fulfillment
of the requirements for the degree of
Doctor of Philosophy

The School of Graduate and Postdoctoral Studies
The University of Western Ontario
London, Ontario, Canada

© Jean-Baptiste KIKWAYA ELUO 2011

Certificate of Examination

THE UNIVERSITY OF WESTERN ONTARIO
School Of Graduate And Postdoctoral Studies

CERTIFICATE OF EXAMINATION

Supervisors

Dr. Peter Brown

Dr. Margaret Campbell-Brown

Supervisory Committee

Dr. Aaron Sigut

Dr. Blaine Chronik

Examiners

Dr. Pauline Bamby

Dr. Jan Cami

Dr. Desmond Moser

Dr. Jiri Borovicka

The thesis by

JEAN-BAPTISTE KIKWAYA ELUO

entitled:

Bulk density of small meteoroids

is accepted in partial fulfillment of the
requirements for the degree of
Doctor of Philosophy

Date

Chair of the Thesis Examination Board

Abstract

The purpose of this work is to determine the bulk density of meteoroids. Unlike previous works which focused either on the dynamical properties of the meteoroids (deceleration), ignoring fragmentation; or on fitting solely the lightcurves, neglecting the dynamics of the meteoroids, we use both the photometry and astrometry to constrain our model.

Our model, based on the dustball model, considers the meteoroid to be a collection of grains held together by a lower boiling point 'glue'. It uses conservation of energy and momentum to model the change in velocity and the light production as a function of time. The free parameters in the model (mass, density, heat of ablation, temperature of fragmentation, boiling temperature, specific heat, molar mass, and thermal conductivity) are varied from values consistent with fragile cometary material, through asteroidal chondritic material, to solid iron, and the entire parameter space is explored, giving all possible solutions which are consistent with the data.

An initial study used cameras with small fields of view to achieve high spatial resolution. A total of 42 meteors were detected, but only six meteors were entirely captured in the common observing volume of the cameras, and were therefore suitable for modelling. The modelling revealed that taking fragmentation into account does not necessarily produce high bulk density values, nevertheless the fraction of high density (nearly iron composition) meteoroids observed was higher than expected, and may be underestimated by other models.

In order to analyse more data, a model of saturation was developed to correct for

meteors which were saturated on the 8-bit camera systems. The model was tested on data collected in a special campaign, and found to reproduce the unsaturated lightcurves correctly. This saturation correction was found to be very important in correctly modelling the brighter meteors in the dataset for the final study.

Finally, 92 meteors were recorded on wider field systems using higher resolution detectors to measure deceleration precisely. Density for each meteoroid was calculated, and the meteoroids were grouped by their orbital characteristics for analysis. As expected, meteoroids with asteroidal origins had high densities of 4200 kg m^{-3} in average, and those with Halley-type cometary orbits had low densities ranging from 380 kg m^{-3} to 1510 kg m^{-3} . The asteroidal densities are higher than chondritic, suggesting that some have significant iron content. Meteoroids from the Perseid meteoroid stream had densities of $620 \pm 200 \text{ kg m}^{-3}$, consistent with the sporadic Halley-type meteoroids. The most surprising result was the high density of Jupiter-family comets ($3100 \pm 300 \text{ kg m}^{-3}$ for Jupiter-family sporadics, and 3200 kg m^{-3} in average for the North Iota Aquariids, which are linked to Comet 2P/Encke). This suggests that refractory material may be a major component of Jupiter family comets in agreement with the surprising results of the Stardust mission on comet 81P/Wild 2.

Acknowledgements

Academic support:

My Thanks go to:

Peter Brown (supervisor) and Margaret Campbell-Brown (co-supervisor).

Paul Wiegert, Philip McCausland.

Robert Weryk.

Zbigniew S Krzeminski, Reto Musci, Wayne Edwards ,
Edward Stokan, Elizabeth Silber, Amanda Papadimos,
Jason Gill.

Guy Consolmagno, R. Hawkes and J. Borovicka.

All other supports: financial, spiritual, human:

My Thanks go to:

The Roman Catholic church and the Pope Benedict XVI.

The diocese of London, Bishop Ronald Fabbro, Bishop John Michael Sherlock, and Bishop William T. McGrattan.

St Peter Seminary, the Rector of Saint Peter Seminary Stevan A. Wlusek and all my brothers in priesthood, faculty and staff of Saint Peter Seminary.

The Society of Jesus, the Province of Central Africa, the province of Upper Canada.

The Vatican Observatory, the former director George Coyne and the current director Jose Funes and all members of the Vatican observatory faculty.

Father Joseph Schner, Father Robert Foliot and all my Jesuit brothers of Regis College Community.

Father Marcel Matungulu Otene, Father Donatien Bafuindinsoni, Father Augustin Ntima Nkanza.

Nadya Gorlova, Sister Lubana Nathalie, Sabina Theobalds, Gisele Ibanga, Beda Kaji-ngulu, Evelyne Mvula, Eugene Matungulu, Annie Mbula, Toussaint Imeyi Mpembele, Chantal Wana Kaba-Kaba.

Contents

Certificate of Examination	ii
Abstract	iii
Acknowledgements	v
Table of Contents	vii
List of Figures	xi
List of Tables	xix
1 Introduction	1
1.1 Background	1
1.1.1 Meteor phenomenon	2
1.1.2 Meteor trajectories	4
1.1.3 Origin of meteoroids	4
1.1.4 Meteor orbits	8
1.2 Motivation	9
1.3 Single body theory	14
1.4 Fragmentation	18
1.5 Model of Ablation	21
1.6 Thesis goals	24

2	Instrumentation and Methodology	29
2.1	Introduction	29
2.2	Instrumentation	31
2.2.1	Observations	33
2.2.2	Image intensifiers	33
2.2.3	Second generation image intensified systems: Gen II	36
2.2.4	Third generation image intensified systems: Gen III	39
2.2.5	Gated intensified system	39
2.2.6	Cooke cameras	40
2.3	Methodology	42
2.3.1	Astrometry	42
2.3.2	Photometry	47
2.4	Ablation Model	56
2.5	Method of analysis	57
2.5.1	Broad search	59
3	Physical characteristics of very small meteoroids	73
3.1	Introduction	74
3.2	Observations and Equipment	77
3.3	Data and Analysis	79
3.4	Ablation Model	86
3.5	Results	86
3.5.1	Free parameters	88
3.5.2	Evaluation of Density	89
3.6	Discussion	111
3.7	Conclusion	114
4	A model for saturation correction in meteor photometry	121
4.1	Introduction	122

4.2	Observations and Equipment	124
4.3	Data and Reduction	126
4.4	Saturation Correction Model	129
4.4.1	Synthetic lightcurve	131
4.4.2	Numerical saturation model	134
4.4.3	Effect of input parameters on saturation correction	137
4.5	Results	141
4.5.1	Group I meteors	142
4.5.2	Group II meteors	146
4.6	Discussion and Conclusion	148
5	Bulk density of small meteoroids	153
5.1	Introduction	154
5.2	Observations and equipment	157
5.3	Data and reduction	161
5.3.1	Astrometry	162
5.3.2	Photometry	164
5.4	Ablation Model	166
5.5	Analysis	168
5.5.1	Broad search	170
5.5.2	Refined search	174
5.6	Results and discussion	177
5.6.1	Origin of our meteoroids	177
5.6.2	Meteoroid strength and density	189
5.6.3	Comparison using the K_B parameter	192
5.6.4	Comparison of bulk density and meteoroid spectra	195
5.6.5	Interpretation of meteoroid physical properties	198
5.6.6	Meteor showers	201
5.7	Conclusion	202

6	Conclusions and Future Work	211
6.1	Conclusion	211
6.2	Future work	216
A	Properties of meteoroids of our sample	218
B	Decelerations and lightcurves of meteoroids of our sample	245
C	Copyright Waivers & Permissions for Published Thesis Chapters	276
D	Curriculum Vitae	290

List of Figures

1.1	Classification of comets (from Levison, 1996)	6
1.2	Comparison of the individual meteoroid bulk densities resulting from the QCF model and the single body theory applied to the same data.	19
2.1	Schematic diagram of a photomultiplier tube (PMT).	35
2.2	The energy of the incident photons is used to release electrons from the photocathode.	36
2.3	A block diagram of a lens-coupled microchannel plate image intensified CCD meteor observation system (from Hawkes, 2002).	37
2.4	The deep Gen II system.	38
2.5	The Gen III system.	40
2.6	The QImaging Intensified Retiga (model 1394) electronically gated image intensified camera.	41
2.7	External box which controls the rate of the CCD exposure and the gating system frequency.	41
2.8	Meteor 20090825-065903 recorded with the gated camera on August 25, 2009 at 06:59:03 UTC at Brussels, Ontario, Canada.	42
2.9	Trajectory solution of the meteor 20060503-091349, computed with the code Milig (Borovicka, 1990).	45
2.10	Plot showing the deceleration of the meteor 20060503-091349.	46
2.11	Velocity profile of the meteor 20060503-091349. We have inserted error bars at each point along the trajectory.	46

2.12	Systematic shift found by comparing positions of the same meteor measured by 9 persons.	48
2.13	Photometric stellar calibration for Gen III camera on April 20, 2007 at 08:23:56 UTC at Elginfield.	49
2.14	Spectral responses of Gen II, Gen III and Gated camera (extended blue).	50
2.15	Photometric stellar calibration for Gen III camera on April 20, 2007 at 08:23:56 UTC at Tavistock.	51
2.16	Photometric stellar calibration for Gen III camera on April 20, 2007 at 08:23:56 UTC at Tavistock.	52
2.17	Lightcurve of the meteoroid 20060430-084301, determined using both catalog V magnitude and catalog R magnitude.	53
2.18	The absolute lightcurves of the meteor 20060503-091349 obtained after applying the different photometric techniques.	54
2.19	Luminous efficiency versus velocity. The three groups according to the meteoroid velocity are shown.	55
2.20	All solutions with $\chi^2 < 1$ after the broad search.	65
2.21	The best lightcurve fit for the meteor 20060503-091349.	66
2.22	The best deceleration fit for the meteor 20060503-091349.	66
2.23	The density distribution of meteor 20060503-091349. The best solution is 970^{+400}_{-200} kg m ⁻³	68
2.24	The density distribution of meteor 20060503-091349 when no saturation correction is applied to the light curve.	68
3.1	Meteor captured in Kiruna (Sweden) on October 11 2007 at 02:55:32 UTC.	82
3.2	Meteor captured in Kiruna (Sweden) on October 09 2007 at 01:37:25 UTC.	82

3.3	Meteor captured in Kiruna (Sweden) on October 06 2007 at 01:54:42 UTC crossing the entire field of view	83
3.4	An example showing the velocity of a meteor before and after the filtering (smoothing) technique.	84
3.5	The velocity of meteor ELSL11 as measured from both sites along its trajectory.	84
3.6	Velocity of meteor ELSL11 from both sites along its trajectory.	85
3.7	Lightcurve of the best single grain mass solution around 1000 kg m^3 for ELSL11.	92
3.8	Lightcurve of the best single grain mass solution around 8000 kg m^3 for ELSL11.	92
3.9	Deceleration of the best single grain mass solution around 1000 kg m^3 for ELSL11.	93
3.10	Deceleration of the best single grain mass solution around 8000 kg m^3 for ELSL11.	93
3.11	Lightcurve for ELSL11 with the model fit for a density of 8000 kg m^{-3} using parameters from table 3.3.	95
3.12	Deceleration for ELSL11 for a density of 8000 kg m^{-3} using parameters from table 3.3.	95
3.13	Modified solution for 1000 kg m^{-3} using three grain masses. The sudden jump in the predicted light output from the model indicates a sudden fragmentation event.	97
3.14	Modified solution for 1000 kg m^{-3} , with three grain sizes and modified temperatures of fragmentation, boiling and fusion.	97
3.15	Plot of the best density solutions for ELSL11. The best solution falls at 5500 kg m^{-3} . The left bound is 5000 kg m^{-3} and the right bound is 8000 kg m^{-3}	101
3.16	The best model of meteor ELSL11, with a density of 5500 kg m^{-3} . . .	101

3.17	Plot of accepted solutions for ELSL01. The best solution falls at 7000 kg m ⁻³ . The left bound is 5500 kg m ⁻³ and the right bound is 8500 kg m ⁻³	103
3.18	Lightcurve and deceleration of ELSL01, with best model.	104
3.19	Plot of best solutions for ELSL09. The best solution falls at 900 kg m ⁻³ . The left bound is 750 kg m ⁻³ and the right bound is 1150 kg m ⁻³	105
3.20	Lightcurve and deceleration of ELSL09 together with the best model fit.	105
3.21	Plot of good solutions for ELSL12. The best solution falls at 4500 kg m ⁻³ . The left bound is 2000 kg m ⁻³ and the right bound is 6500 kg m ⁻³	106
3.22	Lightcurve and deceleration of ELSL12, shown together with the best fitting model.	107
3.23	Plot of good solutions for PEKI08. The best solution falls at 600 kg m ⁻³ . The left bound is 400 kg m ⁻³ and the right bound is 800 kg m ⁻³	107
3.24	Lightcurve and deceleration of PEKI08, with the best fitting model. .	108
3.25	Plot of good solutions for PEKI09. The best solution falls at 500 kg m ⁻³ . The left bound is 200 kg m ⁻³ and the right bound is 800 kg m ⁻³	109
3.26	Lightcurve and deceleration of PEKI09, with the best fitting model. .	109
4.1	Meteor recorded on October 31, 2008 at 09:38:50 UTC, which saturated camera T	127
4.2	Same meteor captured on October 31 2008 at 09:38:50 UTC on camera Q, which was not saturated.	127
4.3	Meteor recorded on November 06, 2008 at 03:34:58 UTC, which saturated camera T	128
4.4	Same meteor captured on November 06 2008 at 03:34:58 UTC; it also saturated camera Q	128

4.5	Observed light curve of meteor 20081031-093850; saturated, from camera T, and unsaturated, from camera Q	129
4.6	Observed light curve of meteor 20081106-081528; saturated, from camera T, and unsaturated, from camera Q	129
4.7	Top: Lightcurve of meteor 20081031-093438. Bottom: function ($M = 7.0 + 10.0 \sin(\frac{2.0 * \pi * t}{5.0})$) reproduces the general shape of the meteor lightcurve.	133
4.8	Diagram detailing the procedure used to create the artificial light curve.	135
4.9	Synthetic meteor created with an angular speed of 300 pixels/second, background of 50 ADUs and σ of 1 pixel.	136
4.10	Residuals between true magnitude and corrected magnitude of the synthetic lightcurve created with an angular speed of 300 pixels/second, background of 50 ADUs and σ of 1 pixel. The points at the beginning and end, where the correction was close to zero, are not plotted. Our model of saturation correction shows a residual average (rms) of 0.10 magnitudes	136
4.11	Simulated starting saturation point when the background level is varied from 10 ADUs to 70 ADUs.	138
4.12	Saturation correction for saturated light curve as the background level is varied from 10 ADUs to 70 ADUs.	138
4.13	Simulated saturation point with varying angular meteor speed from 50 pixels/second to 400 pixels/second.	139
4.14	Saturation correction for saturated meteor points with varying angular meteor speed from 50 pixels/second to 400 pixels/second.	139
4.15	Simulated saturation point with varying meteor Gaussian width from 0.7 pixels to 1.3 pixels.	140
4.16	Saturation correction for saturated light curve with varying meteor gaussian width from 0.7 pixels to 1.3 pixels.	140

4.17	Modelled and observed light curve of meteor 20081031-093850	143
4.18	Saturation correction relationship for meteor 20081031-093850	143
4.19	Saturated light curve observed by Cam T, observed unsaturated light curve by Cam Q and model-corrected saturated light curve from Cam T of meteor 20081031-093850	144
4.20	Residuals between observed unsaturated light curve measured by Cam Q and model-corrected saturated light curve from Cam T data for meteor 20081031-093850	144
4.21	Modelled and observed light curves of meteor 20081106-081528	144
4.22	Saturation correction relationship for meteor 20081106-081528	144
4.23	Saturated light curve, observed unsaturated light curve and modeled unsaturated light curve of meteor 20081031-093850.	145
4.24	Residuals between observed unsaturated light curve from Cam Q and modelled unsaturated light curve for meteor 20081031-093850 based on correction of the observed saturated light curve from Cam T . . .	145
4.25	Saturation correction applied on both observed saturated light curves from camera T and camera Q for meteor 20081106-063244	147
4.26	Residuals between the model-corrected saturated curves for T and Q.	147
5.1	Meteor 20090825-065903 recorded with the gated camera on August 25, 2009 at 06:59:03 UTC at Brussels, Ontario, Canada.	161
5.2	Plot showing the deceleration of the meteor 20060503-091349.	163
5.3	Velocity profile of the meteor 20060503-091349.	163
5.4	The absolute lightcurves of the meteor 20060503-091349 obtained af- ter applying the different photometric techniques (the correction for range has been applied).	166
5.5	All model solutions with $\chi_c^2 \cdot 1$ after the initial broad search for meteor 20060503-091349.	174

5.6	The best lightcurve fit for the meteor 20060503-091349. The corresponding density is 970 kg m^{-3} .	175
5.7	The best trajectory fit for the meteor 20060503-091349 (see Fig.??).	175
5.8	The distribution of density solutions with $\chi_c^2 \cdot 1$ for meteor 20060503-091349.	176
5.9	Histogram showing the distribution of the best fit value for our meteoroid densities from our model fit to data (92 meteoroids total).	177
5.10	Plot of known geometric albedos vs. Tisserand invariant for $T_j < 3$ NEAs and UAs (green squares) and $T_j > 3$ NEAs and UAs (purple diamonds).	181
5.11	Tisserand parameter versus density for our sample of meteoroids.	181
5.12	The perihelion distance versus bulk density for our observed sample.	184
5.13	Aphelion versus density for our meteoroid sample.	186
5.14	The orbital inclination versus bulk density for our meteoroid sample.	186
5.15	Inclination versus aphelion for meteoroid orbits with Tisserand parameter $2 < T_j < 3$ nominally in the JFC (Jupiter family comets) class.	189
5.16	Beginning height versus density of meteoroids of our sample.	192
5.17	Velocity versus density of meteoroids of our sample.	192
5.18	Histogram of K_B values of our sample.	194
5.19	Meteor beginning height as a function of initial velocity for our sample with Borovicka et al.(2005) classes.	197
5.20	Meteor beginning height as a function of initial velocity with Ceplecha (1988) groups.	198
5.21	Plot of aei of our sample for meteoroids with semi-major axis $a \cdot 4.2$ AU, and inclination $i \cdot 80^\circ$.	200
5.22	Plot of thermal conductivity versus bulk density of our sample.	201
6.1	Bulk densities of meteoroids from our sample.	214

6.2	Estimated relative exoatmospheric density distribution (from Love et al. 1994).	214
6.3	Tisserand parameter versus density of meteoroids from our sample. .	215

List of Tables

1.1	The most active annual meteor showers (table from Borovicka, 2001). ZHR and χ are described above. α_R and δ_R are the apparent shower radiant at the time of maximum.	10
2.1	Table summarizing instruments used in our study and their details. . .	32
2.2	Table summarizing all campaigns and their details.	34
2.3	Positions of meteor 20060504-093103 measured by one person.	48
2.4	Positions of the same meteor (20060504-093103) measured by another person.	48
2.5	Table of synthetic photometric magnitudes using observed video meteor spectra.	52
2.6	Average of luminous efficiency according to the meteoroid velocity . .	55
2.7	Grain mass distribution for meteor 20060503-091349 at broad search .	64
2.8	Values of free parameters for the best fit to the lightcurve and the deceleration for meteor 20060503-091349 found in the broad search . .	65
2.9	Grain mass distribution for meteor 20060503-091349 after manual adjustment in the refined search stage. This is taken as the final mass distribution	66
2.10	Values of free parameters from the best solution for meteor 20060503-091349 after manual adjustment in the refined search stage.	67
2.11	Properties of meteoroid 20060503-091349, according to our ablation model.	69

3.1	Initial grain mass distributions used for meteor ELSL11 in the first stage of analysis.	90
3.2	Values for the parameters (other than grain mass) used in the modelling (Meteor ELSL11).	91
3.3	Table summarizing parameters involved in the final stage of the high density solution model for ELSL11	94
3.4	Distribution of grains for the solution around 1000 kg m^{-3} using three grain masses.	96
3.5	Distribution of grains for the solution around 1000 kg m^{-3} , with three grain sizes and modified temperatures of fragmentation, boiling and fusion.	98
3.6	Variation of parameters used modeling lightcurves and decelerations for ELSL11 in the second stage search	100
3.7	Values of parameters producing the best model solution among 234 solutions found to describe meteor ELSL11.	102
3.8	Summary table for the six meteors modelled in detail in this study . .	110
3.9	Summary table of the six meteors and their statistical densities as given by the method	111
3.10	Summary table for the first observing campaign near London Ontario (Canada)	118
3.11	Summary table of the second observing campaign from Kiruna (Sweden) and Peera (Finland)	119
3.12	Table summarizing orbital elements of all 42 meteors	120
4.1	Saturation correction for all 30 group I meteors	130
4.2	Saturation correction for all 7 meteors of group II.	149
5.1	Table summarizing all campaigns and their details.	159
5.2	The instruments used in the data collection.	160

5.3	Free parameters of the model and the range of values used.	172
5.4	Grain distribution found from modelling for meteor 20060503-091349 for the broad search and as determined through forward modelling for the refined search.	175
5.5	The best fit values of the free parameters from the broad search and for the final best solution for meteor 20060503-091349 from the refined search	176
5.6	All nine meteoroids of the Sun-approaching orbit class and values of their different parameters.	183
5.7	All 24 meteoroids with Asteroidal-chondritic orbits (AC) (including 5 which overlap with the SA class and 4 with the ES class) and values of their different parameters.	185
5.8	All thirteen meteoroids with Jupiter Family orbits (JF) (including 4 which overlap with the SA class) and values of their different param- eters.	188
5.9	All 4 meteoroids of the Ecliptic shower orbits class (ES) and values of their different parameters.	190
5.10	Average density in Ceplecha's four meteor classes from different studies	196

Chapter 1

Introduction

1.1 Background

Meteors, generally, are an atmospheric phenomenon caused by the entrance of particles from space (meteoroids or space debris) into the Earth's atmosphere. This atmospheric phenomenon occurs as particles heat up due to collisions with air molecules, and when they reach a high enough temperature, lose atoms and molecules by evaporation and spallation, a process called ablation. Subsequent collisions between meteoroid atoms and air molecules produce excited meteoroid atoms and ionization. As excited atoms lose energy, they emit light, and the meteoroid produces a long column of ionization. We can therefore observe meteor phenomena by detecting the luminosity from these light emitting meteoric atoms or by scattering radio waves from the ionization.

The size limit of bodies that will ablate, producing a meteor, is influenced by both their composition and their speed. The lower limit for very fast meteoroids is in the neighbourhood of 10 microns (the corresponding mass would be less than 10^{-12} kg assuming a meteoroid density of 3000 kg m^{-3}) (Jones and Kaiser, 1966). This limit is called the micrometeoroid limit. Meteoroids smaller than this will radiate energy away faster than they absorb it from collisions, and will be slowed without

losing significant mass.

1.1.1 Meteor phenomenon

The penetration of a meteoroid into the Earth's atmosphere at hypersonic velocity can give rise to 4 different phenomena, depending mostly on mass and partly on velocity (Ceplecha et al. 1998). In all four types of interaction, ions and free electrons are produced during the atmospheric flight.

“Typical meteors”

“Typical” meteors are caused by meteoroids larger than 0.01 mm. Meteor magnitude is a measure of brightness expressed in absolute magnitudes (100 km distance), as determined through comparison with stars (Allen, 1973). A zero magnitude meteor is produced by a 2-cm meteoroid at a velocity of 15 km s^{-1} , by a 1-cm object at 30 km s^{-1} , and by a body of 0.5-cm size at 60 km s^{-1} . If the size of the meteoroid is between 0.05 mm and 0.5 mm, the meteoroid is heated all the way through, but for the meteoroid larger than $\gg 0.5 \text{ mm}$, only a surface layer down to a few tenths of a millimeter will be heated, depending on the thermal conductivity. When the surface temperature reaches about 2000 K - this usually occurs somewhere between heights of 100 and 110 km - the meteoroid material starts to sublime from the surface, eventually surrounding the body with hot plasma. Excited states of atoms in this plasma are gradually de-excited by radiation. Meteor light consists mostly of the radiation of single discrete emission spectral lines, belonging for the most part to metals, and in many cases mainly to iron (see Whipple, 1949, Opik, 1958, McKinley, 1961, Ceplecha et al. 1998, Borovicka, 2001 for more discussion).

The meteors analyzed in the course of this thesis project are all within the “typical meteor” size regime.

Fireballs, Bolides, Meteorite Falls

The atmospheric phenomena known as Fireballs, Bolides, Meteorite Falls occur when bodies larger than about 20 cm (for 15 km s^{-1}) enter the Earth's atmosphere. In such cases, the entire meteoroid mass does not have enough time to ablate totally, before it slows down to a critical limit of about 3 km s^{-1} . At this relatively low velocity, there is not enough energy transported to the surface of the meteoroid to keep the surface temperature above the ablation point. As the meteoroid surface starts to cool, a thin melted layer on the meteoroid surface solidifies forming a crust typical of meteorites (meteoric bodies recovered on the Earth's surface). When ablation stops, the visible portion of the trail disappears. The remnant mass (10 g or more) falls to the Earth's surface in dark-flight, and its velocity gradually approaches the free fall velocity in a resisting medium (see Spurny, 1995, Ceplecha et al. 1998, Borovicka, 2005 for more discussion).

Explosive Impacts

The probability that any meteoric body will survive the encounter with the Earth's atmosphere, giving rise to an explosive impact, is actually very low. If the meteoroid is larger than several meters and sufficiently robust, deceleration will be limited. In such cases meteoroid bodies will hit the Earth's surface at hypersonic velocity (Brown et al., 2008). When objects of such large mass strike the Earth's surface with a velocity of a few kilometers per second or more, the meteoroid plasma emits light right to the point of contact with the Earth's surface. Collisions of this type will result in the formation of explosive craters (Roddy and Shoemaker, 1995, Ceplecha et al. 1998).

Meteoric Dust Particles

The fourth type of interaction between a meteoroid and the Earth's atmosphere is not observed as a luminous phenomenon. Meteoric Dust Particles are produced by

meteoroids of a size below several hundredths of a millimeter. The speed of these smaller meteoroids slows to less than a few kilometers per second while they are still high in the atmosphere. For these small particles, the evaporation regime is never reached, and no hot vapors are present, i.e., there is no meteor phenomenon. Such a meteoroid dust particle sediments slowly and mostly unchanged through the atmosphere to reach the Earth's surface (see Whipple, 1949, Love et al., 1994, Ceplecha et al. 1998, Flynn et al., 2009).

1.1.2 Meteor trajectories

For typical meteors, the trajectory in the atmosphere can be considered a straight line for the few seconds of the ablation phase during which time most of the mass of the object is lost. Only for long-duration fireballs on nearly horizontal trajectories does the curvature due to gravity become significant. The complete trajectory of a meteoroid is given by the meteor radiant, or point in the sky from which the meteor appears to originate (right ascension and declination, in equatorial coordinates) and the speed. In general, the measured speed of the meteoroid will be slightly less than the pre-atmospheric speed (v_∞) due to atmospheric deceleration, which can be found by extrapolation. The minimum possible pre-atmospheric speed is 11.2 km s^{-1} , that is the Earth's escape velocity. The maximum possible speed for a meteoroid which is gravitationally bound to the sun is 73.5 km s^{-1} . This calculation assumes that the meteoroid has the maximum solar system bound speed of 42.4 km s^{-1} at 1 AU, and that it encounters the Earth ($v = 30.2 \text{ km s}^{-1}$) head on (see Ceplecha, 1987, Ceplecha et al. 2000, Borovicka, 2001).

1.1.3 Origin of meteoroids

Meteoroids have two main origins: comets and asteroids. Comets produce meteoroids through the processes of sublimation (Whipple, 1949, Ceplecha et al., 1998, Borovicka, 2001). Comets are mostly made of ice with embedded dust. As a comet

approaches the Sun, the sunlight warms and sublimates huge amounts of ice. The released gases drag dust from the surface and form a hazy “cloud” or temporary atmosphere called the “coma” around the comet. The weak gravity of a comet cannot hold onto this temporary atmosphere and the coma is swept away from the comet forming a tail. Disruptions of comets, in addition to normal cometary activity, also produce meteoroids. Levison (1996) suggested a classification of comets based on their Tisserand parameter with respect to Jupiter defined as:

$$T_j = \frac{a_j}{a} + 2\sqrt{(1 - e^2)\frac{a}{a_j}} \cos(i) \quad (1.1)$$

where a_j is the orbital Jupiter’s semi-major axis, a , e and i are respectively the comet semi-major axis, its eccentricity and its inclination. The classification of comets is given in Figure 1.1.

Comets with $T > 2$ are designated ecliptic comets because they have small inclinations. Comets with $T < 2$ originate from the Oort cloud and have a uniform inclination distribution. These, Levison calls nearly isotropic comets. Ecliptic comets likely originate from the Kuiper Belt and scattered disk. This class of comets is subdivided further into three groups (Levison, 1996):

1. comets with $2 < T < 3$ are on Jupiter-crossing orbits and are dynamically dominated by Jupiter. They are called Jupiter-family comets (JFC).
2. comets with $T > 3$ (not Jupiter-crossing) but $a > a_j$ (orbit is exterior to Jupiter) are Centaurs and are named after the prototype Centaur (Chiron).
3. a comet that has $T > 3$ and semi-major axis (a) such that $a < a_j$ is designated an Encke-type (the first comet to be found totally interior to Jupiter’s orbit, meaning that the aphelion distance is less than a_j).

Levison (1996) divides the nearly-isotropic comets originating from the Oort cloud into two additional groups:

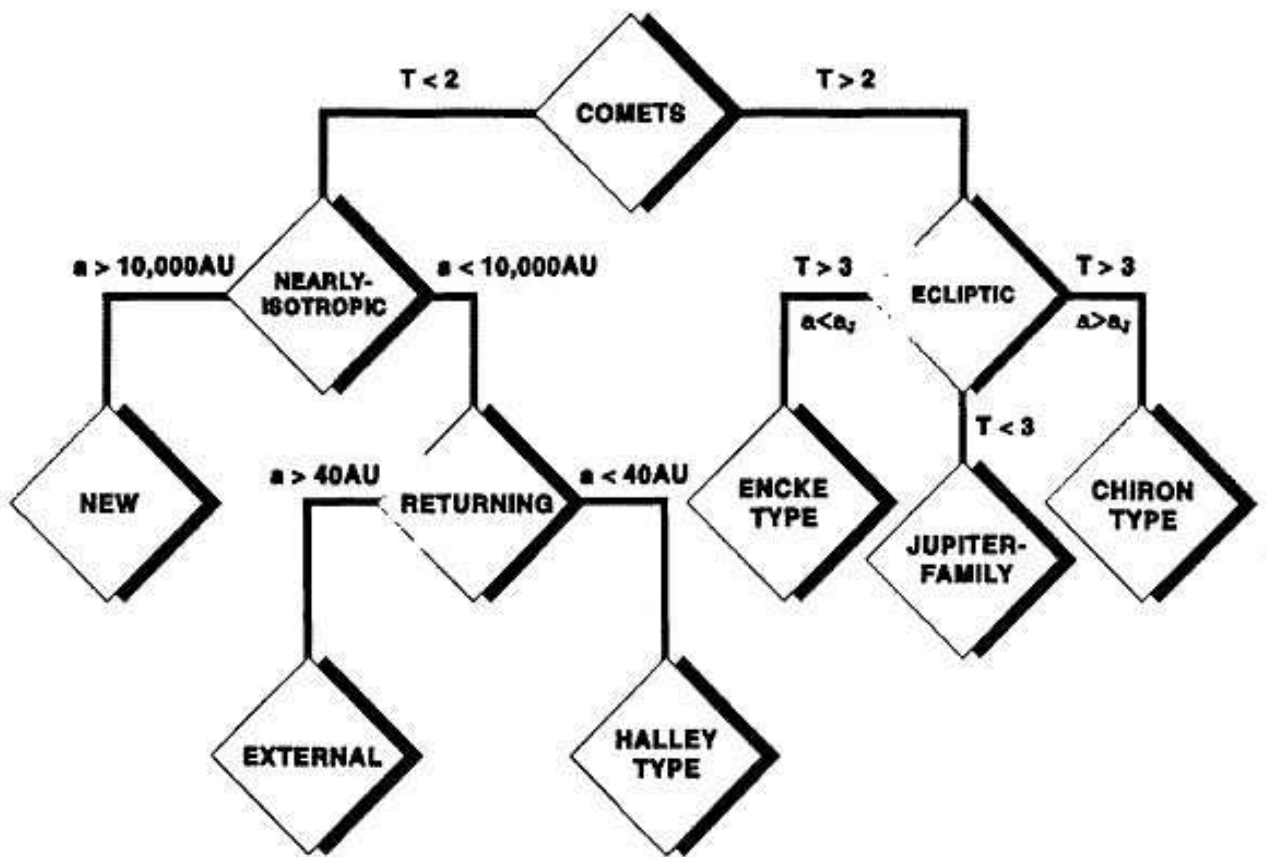


Figure 1.1: Classification of comets (from Levison, 1996)

1. new comets: these have a semi-major axis more than 10000 AU. Due to distant gravitational perturbations from the giant planets, it is unlikely that these comets will keep the same semi-major axis during successive passes through the solar system. For each recording of this class of comets, they are considered dynamically new.
2. returning comets: these have a semi-major axis less than 10000 AU. They are most likely objects that have been through the planetary system before. They are divided into two groups based on their dynamics: comets with a small enough semi-major axis ($a < 40$ AU) to be able to be trapped in a mean motion resonance with a giant planet are designated as Halley-type and those that have semi-major axes larger than that ($a > 40$ AU) as external comets.

Meteoroids released from comets tend to have a large eccentricity (e) and sometimes high inclination (i). In contrast to meteoroids derived from comets, asteroids, the second major source of meteoroids, produce meteoroids with small eccentricity and low inclination. These meteoroids are freed by asteroids through collisions (Ceplecha, 1998). Asteroids are thought to be remnants of planetesimals (material from the young Sun's solar nebula) that have not grown large enough to form planets. The majority of known asteroids orbit in the main asteroid belt between the orbits of Mars and Jupiter. However, many different asteroid groups exist with significant populations such as the Jupiter Trojans [objects that share the orbit of the planet Jupiter around the Sun; each Trojan librates around one of the two points that respectively lie 60° ahead of and behind Jupiter (these two points are called Jupiter's Lagrangian points of stability, L_4 and L_5)]. Another group is the near-Earth asteroids (NEAs). These are objects whose orbits bring them into close proximity with the Earth will have a q value (perihelion) < 1.4 AU.

Apart from this dynamical classification, individual asteroids are categorized by their characteristic spectra, with the majority falling into three main groups (de Pater and Lissauer, 2001):

1. C-type identified with carbon-rich composition. They are identical with carbonaceous chondrite meteorites.
2. S-type being mostly stony (identified with ordinary chondrite meteorites).
3. M-type possibly of metallic compositions (identified with iron meteorites).

In our work we measure meteoroid density and will try to link small meteoroids to their parent bodies based on dynamics and physical density values expected for different small body populations. We will also try to understand and explain the dynamical evolution of meteoroids after release from their parent bodies.

1.1.4 Meteor orbits

The orbit of a meteoroid can be calculated from the observed radiant and speed of its associated meteor. Both are corrected for the rotation of the Earth (diurnal aberration) and the gravitational attraction of the Earth (zenithal attraction), to obtain the heliocentric position and velocity of the meteoroid prior to its encountering the Earth (Ceplecha, 1987).

Most meteoroids, derived from asteroids or comets, begin their independent existence on an orbit very similar to their parent body. After leaving the parent body, the orbit of the meteoroid is altered by close approaches to planets (particularly Jupiter) and radiation forces, including the Poynting-Robertson effect (Burns et al., 1979). Stream meteoroids are usually recently separated from their parent (decades to a few thousand years), while sporadic meteoroids are tens of thousands to millions of years separated from their parents. The orbits of sporadic meteoroids are usually significantly altered from the parent orbit.

For several meteor streams, the individual parent comet is well known. For instance, Eta-Aquariid meteor shower is produced by comet 1P/Halley, the Perseids by the comet 109P/Swift-Tuttle. The parent body of the Taurid meteor shower is 2P/Encke, a Encke-type comet. The Geminids are associated with asteroid 3200

Phaeton. Table (1.1) gives the list of the most pronounced annual showers. ZHR in table (1.1) is the traditional measure of meteor shower activity (Zenithal Hourly Rate). It is defined as the number of meteors observable by a single visual observer with the radiant in the zenith under standard conditions with a stellar limiting magnitude of +6.5 (Borovicka, 2001). If the radiant lies at an elevation h above the horizon, the ZHR is given by the formula:

$$ZHR = HR / \sin^\gamma h \quad (1.2)$$

where γ is an empirical value estimated to be 1.4 and HR the observed hourly rate of meteors from the shower in question. If the limiting magnitude for stars is not 6.5, a correction is applied, which depends on the shower magnitude distribution index χ defined as:

$$\chi = n(m+1)/n(m) \quad (1.3)$$

where $n(m)$ is the number of meteors of magnitude m . The ZHR is given by:

$$ZHR = HR \chi^{6.5-L} \quad (1.4)$$

where L is the actual limiting magnitude.

1.2 Motivation

Density is an important physical property of meteoroids. The study of a meteoroid's density can help determine the physical structure, and potentially the chemical composition, of its parent body. However, this study remains difficult for two main reasons:

1. the meteoroid is not a solid with a spherical shape ablating uniformly in the atmosphere and remaining a single solid spherical body during its entire flight;

Table 1.1: The most active annual meteor showers (table from Borovicka, 2001). ZHR and χ are described above. α_R and δ_R are the apparent shower radiant at the time of maximum.

Name	Maximum date	Duration (days)	ZHR (maximum)	χ	Parent body	α_R	δ_R	velocity (km s ⁻¹)
Quadrantids	4 January	4	130	2.5	P/Machholz?	232	+45	43
Lyrids	22 April	6	15	2.7	P/Thatcher	272	+33	49
η -Aquarids	6 May	25	40	2.7	1P/Halley	338	-1	66
Arietids	8 June	20	50	2.7	P/Machholz?	45	+23	38
δ -Aquarids S	29 July	15	10	3.3	P/Machholz?	339	-17	43
Perseids	13 August	30	80	2.5	109P/Swift-Tuttle	44	+58	61
Orionids	22 October	15	25	3.1	1P/Halley	95	+16	67
Taurids	3 November	30	10	2.3	2P/Encke	48	+18	30
Leonids	17 November	6	20	3.4	55P/Tempel-Tuttle	153	+22	71
Geminids	14 December	10	90	2.6	(3200) Phaeton	112	+32	36

it fragments.

2. the meteoroid has unknown shapes, structures, and chemical composition.

A meteoroid ablates and generates electromagnetic radiation (including visible light) when it comes into contact with the Earth's atmosphere. Many factors influence the height at which a meteoroid starts to ablate: the entry angle, the speed of the meteoroid, its mass, the energy required to ablate the material of which it is composed, its boiling point, its structure, and its bulk density (Campbell-Brown and Koschny, 2004). All these different factors have to be taken into account when modeling the meteoroid ablation.

The ablation behaviour itself differs considerably among meteoroids. There are large variations in beginning heights, and lightcurve shapes among smaller meteoroids, and, in end height among larger meteoroids (see Ceplecha et al. 1998 for a complete discussion). These differences have to do with the physical characteristics of each meteoroid: composition, structure, bulk density and size. Koten et al. (2004) for example studied the lightcurves and heights of video meteors and find significant differences among meteors from major showers. They argue that this suggests the parent bodies have different chemical compositions or physical structure.

Reproducing all these physical differences in a particular meteoroid ablation model is already by itself difficult. Furthermore, the interpretation of these differences is substantially complicated by the process of fragmentation. Whether or not small meteoroids undergo fragmentation remains an open question, and many other questions need also to be addressed: (a) Does fragmentation occur before the onset of, or during rapid vaporization? (b) Does it happen at a critical temperature or a critical pressure?

Campbell et al. (2000) argued that fragmentation occurs before the process of ablation starts: the grains are released, and then they undergo intensive ablation. This procedure is consistent with the dustball meteoroid model (Hawkes and Jones, 1975; Jones and Hawkes, 1975). For the dustball model, meteoric bodies are as-

sumed to be composed of grains held together by a lower boiling point ‘glue’: when the binding melts, the grains are released. The dustball model predicts the weak dependence of the beginning height, maximum height and trail length of the visible meteor on the mass of the meteoroid (Campbell et al. (2000), Koten et al. (2004), Hapgood et al. (1982), Beech, 1986) and the production of wake [grains of different masses ejected from the meteoroid will decelerate at different rates, producing physical wake from the spread in the grains (Fisher et al., 2000)].

Fragmentation for meteoroids is a very complex mechanism. Contemporary meteoroid ablation modelling concentrates on attempting to formalize the process:

- ² For Campbell-Brown and Koschny (2004), the fragmentation occurs when the temperature of the surface is high enough to disrupt the binding matrix of the meteoroid; the top layer of the meteoroid (to a depth determined by the assumed thermal conductivity) is released all at once.
- ² Borovicka et al. (2007) suggested that grain separation started after the surface of the meteoroid received a certain energy flux, calculated to be 10^6 J m^{-2} (equivalent to requiring the surface to reach a particular temperature). The meteoroid then gradually fragments into grains over the first half of its trajectory, a process Borovicka et al. (2007) call thermal erosion. Meteoroids resistant to this process may still disrupt mechanically at low dynamic pressures.

Quantitative measurements of the bulk density of meteoroids are difficult to make, due to the variety of ways fragmentation may be handled in modelling. Ceplecha (1967) calculated the density of small meteoroids and classified them into four categories (A,B,C,D) based on a parameter, K_B , which depends on: (a) the atmospheric density at the beginning of the luminous trajectory, (b) the initial velocity, and (c) the elevation of the radiant. Densities ranged from 2700 to 180 kg m^{-3} corresponding to categories A through D (carbonaceous material to fragile

cometary). Asteroidal meteoroids were found to be rare among television meteors and designated by 'ast' (Ceplecha, 1998). Ceplecha did not measure the density of individual meteors, but rather estimated the average density per class from assumed theoretical parameters.

Babadzhanov (2002) examined 413 photographic Super-Schmidt meteors and applied a model which assumed quasi-continuous fragmentation (QCF). His meteoroid densities ranged from 400 kg m^{-3} to 7800 kg m^{-3} . Bellot Rubio et al. (2002) questioned the validity of the high densities for small meteoroids. For him, two questionable assumptions led Babadzhanov (2002) to these results:

- ² the fact that QCF is based essentially on fitting a model to the lightcurve, without taking into consideration the dynamical properties of the meteoroids, particularly the deceleration.
- ² the specific energy of fragmentation used by Babadzhanov (2002) was underestimated by at least a factor of 10 compared to values adopted by most other authors (e.g. Hawkes and Jones, 1975; Hawkes et al., 1978). Bellot Rubio et al. (2002) point out that, with such a small heat of fragmentation, the meteoroid will always fragment before reaching the “real” heat of ablation.

Analyzing the same meteors using the single body theory (assuming none of the meteoroids fragment), Bellot Rubio et al. (2002) found densities ranging from 400 kg m^{-3} to 4800 kg m^{-3} . Since the characteristics of fragmentation are often observed in the lightcurves of small meteoroids as transient increases in brightness (including in the sample analysed by Bellot Rubio et al., 2002), Borovicka (2005) pointed out that this is a shortcoming of Bellot Rubio's work. Clearly, the lightcurves of meteoroids should be fit with a model that takes into account the dynamical and photometric properties of the meteors simultaneously.

1.3 Single body theory

For many decades theoretical models of the motion and ablation of a meteoroid in a planetary atmosphere were based on the so called single body theory (Ceplecha et al., 1998). The mathematical form of the differential equations of meteoroid motion in the atmosphere is given by Whipple (1938) who used Hoppe's solution (1937) with constant coefficients. Levin (1961) and Bronshten (1983) presented a more elaborate solution to differential equations of meteoroid motion and ablation in the Earth's atmosphere. Single body theory is concerned with deceleration, mass loss, luminosity and ionization that accompany the motion of a single nonfragmenting body in the atmosphere, on the assumption that the coefficient of drag, heat transfer, luminosity and ionization, which figure in the fundamental equations, are constant (Bronshten, 1983). Some researchers have attempted an approach with changing coefficients (e.g. Bronshten, 1983 and Revelle, 1979).

The first fundamental equation expresses the deceleration of the meteoroid during its flight in the Earth's atmosphere. It is based on the assumption that the momentum (mdv) lost by a meteoroid is proportional to the momentum of the oncoming air flow (Bronshten, 1983). The mass impinging upon a cross-sectional area S at velocity v in time dt is given by $S\rho v dt$ where ρ is the air density. We can then write:

$$m \frac{dv}{dt} = -\Gamma S \rho v^2 \quad (1.5)$$

where Γ is the drag coefficient, expressing the fraction of the momentum of the oncoming flow that is transferred to the body (Bronshten, 1983). The drag coefficient can vary between 0 (no transfer of momentum) and 2 (perfect reflection of air molecules). We introduce another coefficient called the shape factor, A , defined so that the surface area is $S = Am^{2/3} \rho_d^{-2/3}$, where ρ_d is the bulk density of the meteoroid. Substituting this in equation (1.5) gives:

$$\frac{dv}{dt} = -\Gamma A \rho_d^{-2/3} \rho m^{-1/3} v^2 \quad (1.6)$$

The second fundamental equation, called the mass-loss equation, is based on the assumption that a certain fraction, Λ , of the kinetic energy of the oncoming air molecules is expended on ablation (vaporization or fusion and spraying) of mass of the meteoroid (Bronshten, 1983). If Q is the heat of ablation (energy that must be delivered to a mass dm in order to melt and/or vaporise it), then the mass-loss equation can be written as:

$$\frac{dm}{dt} = -\frac{\Lambda A}{2Q} \rho_d^{-2/3} \rho m^{2/3} v^3 \quad (1.7)$$

where Λ , the heat-transfer coefficient, is equal to or less than unity, since the energy expended on ablation cannot exceed the total kinetic energy of the oncoming stream molecules (Bronshten, 1983). Some of the air molecules' kinetic energy will also be used to heat the meteoroid to the point of ablation, some will be re-radiated by the meteoroid, and some will be used to excite or ionize meteoroid and air molecules (Bronshten, 1983). If fragmentation occurs, part of the energy is also used to break the mechanical bonds between meteor grains. The combined effects of all these forms of energy consumption is represented by the coefficient Λ (Bronhsten, 1983).

We can introduce two independent parameters which can be useful in describing the ablation behaviour and solving the differential equations above: the ablation coefficient σ and the shape-density coefficient K defined by (Ceplecha et al., 1998):

$$\sigma = \frac{\Lambda}{2Q\Gamma} \quad (1.8)$$

$$K = \Gamma A \rho_d^{-2/3} \quad (1.9)$$

Using (1.8) and (1.9), equations (1.6)(deceleration) and (1.7) (mass loss) can be

rewritten in the form of:

$$\frac{dv}{dt} = -i Km^{-1/3} \rho v^2 \quad (1.10)$$

$$\frac{dm}{dt} = -i K \sigma m^{2/3} \rho v^3 \quad (1.11)$$

These two equations (1.10) and (1.11) are useful because by providing the position (height), mass, and velocity of the meteoroid at a given time, the geometry of the trajectory (slope), the ablation coefficient, and the shape-density coefficient, one can compute the subsequent meteoroid deceleration and mass loss (Ceplecha et al., 1998, Borovicka et al., 2007).

The third fundamental equation, called the luminosity equation, gives the energy released by the meteoroid as luminosity, usually at visible wavelengths. Most of the radiation from the meteor comes from line emission of evaporated meteor atoms (Bronhsten, 1983). This means that the composition of the meteoroid is important in the production of light, since different elements have different line strengths in the visible. This equation assumes that the radiation intensity I (luminosity) of the meteoroid is proportional to some fraction, τ , of kinetic energy lost by the meteoroid (Ceplecha, 1998):

$$I = \tau \frac{dE_k}{dt} \quad (1.12)$$

In general, then, the equation will be:

$$I = -i \tau \left(\frac{v^2}{2} \frac{dm}{dt} + mv \frac{dv}{dt} \right) \quad (1.13)$$

where the negative sign indicates that both dm/dt and dv/dt are negative. Besides the contribution to luminosity from mass loss, there may be a contribution from the meteoroid deceleration. We can rearrange equation 1.13:

$$I = \eta \tau \left(1 + \frac{2}{v} m \frac{dv}{dm} \right) \frac{v^2}{2} \frac{dm}{dt} \quad (1.14)$$

Dividing the deceleration equation (equation 1.6) by the mass loss equation (equation 1.7) gives an expression for $\frac{dv}{dm}$:

$$\frac{dv}{dm} = \frac{1}{\sigma v m} \quad (1.15)$$

and the luminosity equation becomes:

$$I = \eta \tau \left(1 + \frac{2}{\sigma v^2} \right) \frac{v^2}{2} \frac{dm}{dt} \quad (1.16)$$

The term $2/(\sigma v^2)$ in equation 1.16 will contribute significantly to the radiation only for slow meteors with a small ablation coefficient (Ceplecha et al., 1998). If one is considering only small meteoroids where the deceleration is small, we can simplify to the case where most of the light comes from the mass loss, as opposed to deceleration:

$$I = \tau \left(\eta \frac{dm}{dt} \right) \frac{v^2}{2} \quad (1.17)$$

The luminous efficiency, τ , is not a constant parameter. It depends on the spectral region of the observations, on the chemical composition of the meteoroid and the atmosphere, on the meteoroid velocity and probably on the mass (Ceplecha et al., 1998).

Some of the variables in the fundamental equations are determined from observations, some depend on the properties of the meteoroid, and others are estimated theoretically. The air density ρ is usually determined by a model of the atmosphere for all heights reached by the meteoroid (Bronshten, 1983). The velocity as a function of time and luminosity are determined from observations. The heat of ablation depends on whether the meteoroid is vaporizing or spraying a molten layer, and

depends slightly on the meteoroid composition. The drag, heat transfer and luminosity coefficients must be determined either from theoretical considerations, from experiments, or sometimes by appeal to observational data (Bronshten, 1983). The mass of the meteoroid is obtained either from equation 1.6 (dynamical mass) or from equation 1.17 (photometric mass). The shape factor is not known, but the meteoroid is usually assumed to be spherical, in which case $A=1.21$.

1.4 Fragmentation

Figure (1.2) shows two different methods of determining the meteoroid density, which we will try to reconcile in our work: single body theory (Bellot Rubio et al., 2002) and fragmentation (Babadzanov, 2002). The form of fragmentation considered by Babadzhanov in his ablation model is that of quasi-continuous fragmentation, third of the four forms defined by Levin (1963) which are:

1. The decay of a meteoroid into comparable large non-fragmenting debris.
2. The progressive disintegration of the original meteoroid into fragments, which continue to crumble into smaller debris.
3. Quasi-continuous fragmentation (QCF): a gradual release of the smallest fragments from the the surface of a parent meteoroid and their subsequent evaporation.
4. The simultaneous ejection of a large number of very fine particles giving rise to meteor flares.

Bellot Rubio et al. (2002) found densities which ranged from 100 kg m^{-3} to 4500 kg m^{-3} . The mean density was 2400 kg m^{-3} for A-group meteoroids, 1400 kg m^{-3} for B group and 400 kg m^{-3} for C group. Borovicka (2005) suggested that the meteoroid bulk densities of Bellot et al. (2002), particularly for the C

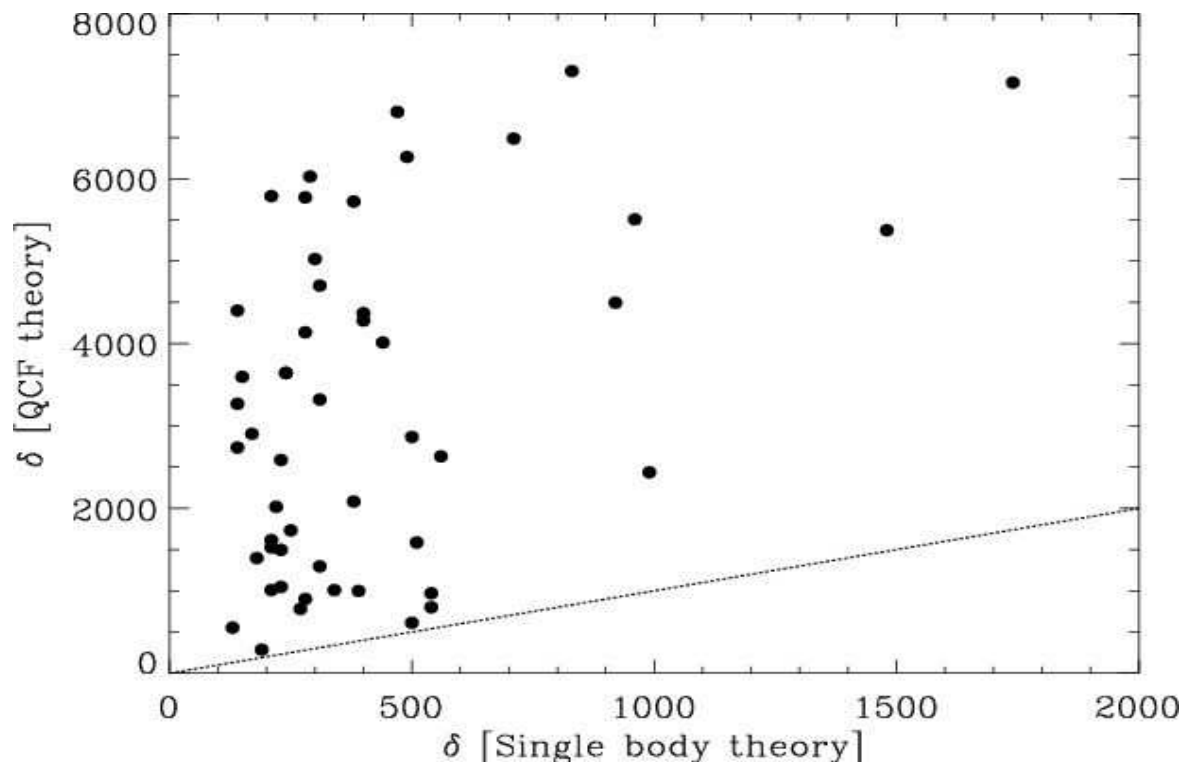


Figure 1.2: Comparison of the individual meteoroid bulk densities resulting from the QCF model and the single body theory applied to the same data. All values are in kgm^{-3} . The dashed line indicates a one-to-one correspondance (from Bellot et al., 2002)

group, were underestimated. Borovicka (2005) suggests that the main reason for this underestimation is the fact that they neglected to take into account fragmentation.

Babazhanov (2002) tried to determine the bulk density of the meteoroids through the QCF model by fitting the observed light curve. He used 111 bright photographic meteors belonging to different streams and found the mean density to vary in the range from 400 kg m^{-3} (Leonids) to 2900 kg m^{-3} (Geminids). The mean bulk density of sporadic meteoroids was equal to 2200 kg m^{-3} . In general, the bulk densities of meteoroids turned out to be one order of magnitude larger with the fragmentation than without it. Borovicka (2005) also criticized this work on another point: that it did not take into account the dynamic properties of the meteoroids. As Bellot et al. (2002) used the single body theory based solely on the dynamic properties of the meteoroids, arguing that some meteoroids, particularly most of C group meteoroids, don't undergo fragmentation and ended up with very low densities, Borovicka (2005) noted that this was contrary to a large body of other observational data which show fragmentation to be important; the fact that the fragmentation was neglected was a serious shortcoming.

In our approach to determining the bulk density of the meteoroids, we want to reconcile the two previous attempts by fitting both the light curve and the deceleration simultaneously. In fact, we need a model able to predict both the dynamical properties and lightcurves of the meteoroids. We will use the model of Campbell-Brown and Koschny (2004) based on the Hawkes and Jones (1975) dustball model.

This model is applied to high resolution measurements of lightcurves and astrometry for a suite of faint meteors observed from two stations. In particular, our measurement precision is high enough to allow routine observation of deceleration for faint meteoroids ranging from +7 magnitude to +3 magnitude. This particular model uses eight free parameters to produce a theoretical lightcurve, and allows the velocity to vary with height along the meteoroid trajectory. Our methodology is to explore the solution space of all possible parameters and compute for each meteor

hundreds of thousands of solutions whose lightcurves and decelerations are then compared to those observed. We find density limits for each meteor within which a solution can be found; from the number of solutions at each modeled density, we get a statistical measure of the density for each meteoroid and a measure of its error.

1.5 Model of Ablation

The dustball meteoroid model assumes meteoric bodies are composed of grains (usually assumed to be metallic or stony) held together by a lower boiling point 'glue' (Hawkes and Jones, 1975; Jones and Hawkes, 1975; Popova et al. 2000). When the boiling point of the 'glue' is reached, grains become separated. Simonenko (1968a, 1968b) estimated from studies of meteor flares that the grains have a fundamental size of approximately 140 micrometers. The dustball model of Hawkes and Jones assumes that grain ablation begins at the onset of the visible meteor, with no light production before the release of all of the grains. Hawkes and Jones calculated that the energy required for the disintegration of meteoroids smaller than 10^{-5} kg was around 2×10^6 J kg⁻¹.

Beech (1986) applied the dustball method of Hawkes and Jones to Super-Schmidt Draconid meteors observed by Jacchia et al (1955). he found that Draconids have a mass up to 10^{-2} kg, with an average meteor beginning height of 97.6 km. To disintegrate these meteoroids, they estimated the energy to be about 10^5 J kg⁻¹.

Beech and Murray (2003) used also the meteoroid dustball to generate synthetic Leonid meteor light curves. They considered meteoroids with total mass 10^{-6} kg disrupted into grains with masses ranging from 10^{-10} kg to 10% of the total mass. They applied the model to observed Leonid light curves of different shapes (early peaked, symmetrical, distinctly late peaked) assuming a power-law mass distribution of the grains with the mass distribution index, α , between 1.0 and 2.0. They found an interesting variation in the fundamental grain sizes of Leonid meteors between

1998 and 2001. They suggested that the 1999 Leonid meteoroids were relatively rich in larger-mass fundamental grains, suggesting that some dustball meteoroids are much richer in large-mass grains than predicted by a simple power-law model.

Campbell-Brown and Koschny (2004) modelled the ablation of dustball meteoroids in the atmosphere. While the traditional dustball model assumes that light production begins once the small grains are all released, Campbell-Brown and Koschny use the Clausius-Clapeyron equation to consider ablation before the boiling temperature of each grain is reached. They used the model to fit Leonid light curves using either a power law or a Gaussian distribution of grain masses, or a combination of the two.

The model considers three sources and sinks of energy:

- ² energy imparted to the meteoroid by collisions with atmospheric atoms,
- ² the energy lost from the meteoroid by radiation,
- ² and the energy lost through evaporation of the meteoroid material.

The change in energy (dE) in an interval of time gives the change in temperature dT : $dT_m = dE/cm_{th}$ where c is the specific heat of the meteoroid material and m_{th} the mass of the meteoroid affected by the heat (in this case m_{th} is actually the outer shell, with a thickness determined by the thermal conductivity).

Taking into account all energy terms, the temperature equation is:

$$\frac{dT_m}{dt} = \frac{1}{cm} \left(\frac{\Lambda \rho v^3}{2} A \left(\frac{m}{\rho_d} \right)^{2/3} - \right. \quad (1.18)$$

$$\left. 4\sigma_{sb}\epsilon (T_m^4 - T_a^4) A \left(\frac{m}{\rho_m} \right)^{2/3} - Q \frac{dm}{dt} \right)$$

where T_m is the meteoroid surface temperature, and Λ is the dimensionless heat transfer coefficient which describes the fraction of the kinetic energy used to heat the meteoroid (which can vary between 0 and 1). ρ is the atmospheric density, ρ_d is

the density of the meteoroid and A is the shape factor of the meteoroid, as defined in the section above (single body). T_a is the atmospheric temperature, σ_{sb} is the Stefan-Boltzmann constant and ϵ is the emissivity of the meteoroid, assumed to be 0.9. Q is the heat of ablation.

The momentum of the air molecules colliding with the meteoroid in time dt is $\rho v^2 A (m/\rho_d)^{2/3} dt$. The dimensionless drag coefficient (Γ) can vary between 0 and 2 and is used to describe the fraction of momentum actually transferred to the meteoroid: twice the momentum may be transferred if the collisions are perfectly elastic and air molecules rebound directly back along their path. The ablation model uses the momentum equation to keep track of the change in the meteoroid velocity, and any deceleration. The momentum equation is the equation (1.6).

The classical model of meteor ablation assumes the mass loss is proportional to the kinetic energy imparted to the meteoroid. The ablation begins as soon as the surface of the meteoroid reaches the boiling temperature (e.g. Bronshten 1983). The classical equation of the mass loss is then the equation (1.7).

In the Campbell-Brown and Koschny model, mass loss is calculated right from the beginning of the trajectory. The mass loss is calculated using the Knudsen-Langmuir formula, combined with Clausius-Clapeyron equation; a term proportional to kinetic energy is added to simulate spallation of liquid material when the meteoroid is very hot. The mass loss equation is:

$$\frac{dm}{dt} = A \left(\frac{m}{\rho_d} \right)^{2/3} \psi \frac{P_a \exp\left(\frac{Q\mu}{k_B T_M}\right) \exp\left(-\frac{Q\mu}{k_B T_B}\right) - p_v}{\sqrt{\frac{2\pi k_B T}{\mu}}} \quad (1.19)$$

where p_v is the vapor pressure of the meteoroid substance and ψ is the condensation coefficient, which gives the probability that an ablated meteor atom colliding with the surface will recondense. For metals, ψ is 1: following Bronshten (1983), ψ of stone is approximately 0.5. T_B is the boiling temperature of the meteoroid substance at sea level pressure (P_a), Q is the heat of ablation, μ the average mass of a meteoric atom and k_B the Boltzmann constant. For more details of this ablation model, see

Campbell-Brown and Koshcny (2004).

1.6 Thesis goals

This work uses a new approach to determining meteoroid density, based on fitting not only the light curve (as in Babazhanov 2002) or only the deceleration (as in Bellot et al., 2002), but both measurements simultaneously. This requires observing instruments able to precisely measure the deceleration of meteoroids. We will describe in chapter 2 the instruments we use to optimize the chance of measuring the deceleration.

As the lightcurve is a critical constraint to the model, an accurate photometric reduction technique is crucial. We will describe in chapter 2 a new photometric method which, unlike the traditional approach, takes into account the quantum efficiency of the observing instrument. In chapter 2, we will also describe in detail the methodology used to compute the meteoroid density by fitting the dynamic properties of the meteoroid and its lightcurve by searching the entire free parameter space.

Chapter 3 describes the analysis of faint meteoroids captured by a system using a long focal length lens attached to a Generation image intensifier the deep Gen II instrument, where the scale of the video images (0.01° per pixel) provides a resolution close to photographic (10 m per pixel).

Chapter 4 will present a new technique for photometric saturation correction, to be used with the Gen III meteors (approximately 9% of our sample) which saturated the instrument. This step is necessary before brighter meteors can be modelled.

Chapter 5 will calculate densities for meteoroids captured by a suite of Gen III cameras, which have sufficient resolution to detect deceleration with a wide field of view, unlike the Deep Gen II system. The wide field of view ensures many meteors begin and end in the field of view of one of the cameras, giving much higher

numbers, and allowing an analysis of meteoroid bulk density as a function of orbital parameters, among other things. The meteoroid bulk density combined with orbital parameters will help us to understand the dynamical evolution of meteoroids.

Chapter 6 presents our conclusions, summary and suggestions for future work.

Bibliography

- [1] Allen, C. W. 1973, *Astrophysical quantities*, 3d ed. London: Athlone Press, Spring-Verlag, 310p
- [2] Babadzhanov, P. B. 2002, *A&A*, 384, 317
- [3] Beech, M. 1986, *AJ*, 91, 159
- [4] Beech, M., Murray, I. S. 2003, *MNRAS*, 345, 696
- [5] Bellot Rubio, L. R., Martinez Gonzalez, M. J., Ruiz Herrera, L., et al. 2002, *A&A*, 389, 680
- [6] Borovicka, J. 2001, *Encyclopedia of Astronomy and Astrophysics*. Murdin, P., (ed). Institute of Physics Publishing and Nature Publishing Group, 1720
- [7] Borovicka, J. 2005, *Asteroids, Comets, and Meteors*. (eds. D.Lazzaro, S. Ferraz-Mello, J.A. Fernandez), Cambridge Univ. Press. *Proceedings IAU Symposium No.* 229, 249
- [8] Borovicka, J., Spurny, P., & Koten, P. 2007, *A&A*, 473, 661
- [9] Bronshten, V. A. 1983, *The Physics of Meteoritic Phenomena*, Reidel, Dordrecht.
- [10] Brown, P. B., Revelle, D. O., Silber, E. A., et al. 2008, *JGRE*, 113, 1
- [11] Burns, J. A., Lamy, P. L., & Soter, S. 1979, *Icarus*, 40, 1
- [12] Campbell, M. D., Brown, P. G., Leblanc, A., et al. 2000, *M&PS*, 35, 1259

- [13] Campbell-Brown, M. D., & Koschny, D. 2004, A&A, 418, 751
- [14] Ceplecha, Z. 1967, SCoA, 11, 35
- [15] Ceplecha, Z. 1987, BAICz, 38, 222
- [16] Ceplecha, Z., Borovicka, J., Elford, W. G., et al. 1998, Space Science Rev., 84, 327
- [17] Ceplecha, Z., Borovicka, J., & Spurny, P. 2000, A&A, 357, 1115
- [18] de Pater, I., & Lissauer, J. J. 2001, *Planetary sciences*, cambridge, UK, Cambridge University Press, 544p
- [19] Fisher, A. A., Hawkes, R. L., Murray, I. S., et al. 2000, Planetary and Space Science, 48, 911
- [20] Flynn, G. J., Durda, D. D., Sandel, L. E., et al. 2009, Planetary and Space Science, 57, 119
- [21] Hapgood, M., Rothwell, P., & Royrvik, O. 1982, MNRAS, 201, 569
- [22] Hawkes, R. L., & Jones, J. 1975, MNRAS, 173, 339
- [23] Hawkes, R. L., & Jones, J. 1978, MNRAS, 185, 727
- [24] Hoppe, J. 1937, AN, 264, 261
- [25] Jacchia, L. 1955, AJ, 121, 521
- [26] Jones, J., & Kaiser, T. R. 1966, MNRAS, 133, 411
- [27] Jones, J., & Hawkes, R. L. 1975, MNRAS, 171, 159
- [28] Koschny, D., Trautner, R., Zender, J., et al. 2002, Proceedings of Asteroids, Comets, Meteors - ACM 2001. ed. Barbara Warmbein, 185
- [29] Koschny, D., & Diaz, V. 2002, WGN, 30, 87

- [30] Kotev, P., & Borovicka, J. 2001, Proceedings of the Meteoroids 2001 Conference, 259
- [31] Kotev, P., Borovicka, J., Spurny, P., et al. 2004, A&A, 428, 683
- [32] Levin, B. J. 1961, *The Physical Theory of Meteors and Meteor Matter in the Solar System*, N. Richter (ed). 130p
- [33] Levin, B. J. (1963), SvA 7, 233
- [34] Levison, H. F. 1996, ASPC, 107, 173
- [35] Love, S. G., David, J., & Brownlee, D. E. 1994, Icarus, 111, 227
- [36] McKinley, D. W. R. 1961, *Meteor science and engineering*, New York, McGraw-Hill.
- [37] Murray, I., Hawkes, R., & Jenniskens, P. 1999, M&PS, 34, 949
- [38] Murray, I., Beech, M., Taylor, M., et al. 2000, EM&P, 82/83, 351
- [39] Öpik, E. J. 1958, *Physics of Meteor Flight in the Atmosphere*, Interscience Publishers Inc.
- [40] Popova, O. P., Sidneva, S. N., Shuvalov, V. V., et al. 2000, EM&P, 82/83, 109
- [41] Revelle, D. O. 1979, Journal of Atmospheric and Terrestrial Physics (JATP), 41, 453
- [42] Roddy, D. J., & Schoemaker, E. M. 1995, Meteoritics, 30, 569
- [43] Simonenko, A. N. 1968a, SvA, 12, 341
- [44] Simonenko, A.N. 1968b, IAUS, 33, 207
- [45] Whipple, F. L. 1938, Proc. Amer. Phil. Soc., 79, 499
- [46] Whipple, F. L. 1949, AJ, 54, 179

Chapter 2

Instrumentation and Methodology

2.1 Introduction

Successive improvements in radio and optical instruments (radar, photographic Super-Schmidt, and intensified video systems, for example) have contributed in improving considerably our knowledge of meteoroids and their physical properties (composition, structure, etc.). These physical properties depend mostly on observation of meteoroid deceleration and mass ablated as a function of time. Precise observations of position and brightness or ionization at many points along the meteor trail are then required in the study of meteoroids.

There are mainly two ways of directly observing meteoroids: radio and optical observations. The advantage of radio is that meteors can be observed in daytime and through clouds. However, there is a drawback: transverse backscatter systems provide ionization information for only one point (or, with special systems, a handful of points), not sufficient for meteoroid compositional studies. Radial scatter (High Power Large Aperture, or HPLA) systems can measure ionization at many points (Campbell-Brown & Close, 2007), and can be used to generate ionization curves, but the observing biases and calibration from scattered power to mass are still poorly understood.

Valuable knowledge of the complex physical structure of meteoroids comes from the analysis of meteors recorded using optical instruments and particularly Super-Schmidt photographic cameras (Jacchia & Whipple, 1961). In fact, Jacchia, Verniani & Briggs (1967a,b) provided precise information on meteors down to a magnitude of about +3: orbits, trajectories, decelerations and lightcurves of over four hundred meteors were for the first time available. From these analyses, and earlier work by Jacchia (1957), the general perception of a meteoroid as a conglomerate of tiny grains began to emerge. Differential deceleration (inferred from the presence of wake), irregularities in light curves and shorter trail lengths enhanced the idea that meteoroids are conglomerates of tiny grains.

Restricted to meteors brighter than magnitude +3, Super-Schmidt cameras could not reveal the totality of meteoroid physical properties. This project became possible by extending optical techniques to fainter meteors with the introduction of low-light-level electro-optical techniques in the 1960s, modern versions of which, coupled with image intensifier, have limiting stellar magnitudes from +6 to +9 (see Hawkes and Jones, 1986).

The sensitivity of image intensified video is much greater than photographic film, but it has drawbacks. TV systems typically have much lower spatial resolution than photographic film making it difficult to compute with high accuracy meteoroid trajectories and orbits. Even for photometry, there is a difficulty: video is typically digitised as 8-bit grayscale images, meaning each pixel can have a value from 0 to 255. A pixel saturates when too many photoelectrons are collected on one pixel, exceeding its full well capacity (Howell, 2000). When a pixel is saturated, blooming occurs while the image of a bright object spills onto neighbouring pixels; however, the maximum pixel value is truncated at 255 resulting in underestimating the brightness of the object and consequently its photometric mass.

2.2 Instrumentation

We used four different camera systems in our work: a deep Gen II system (described in Chapter 3), a Gen III system (Chapter 4 and Chapter 5), a Gated camera (Chapter 5) and the Cooke camera system (Chapter 5). We used this variety of instruments to examine meteoroid density over a range of masses and with different precisions.

The six meteors captured by the Gen II systems and for which density (see Chapter 3) has been estimated were not affected by saturation. At the same time, the field of view of the system was small (about 6°), meaning that the spatial resolution of the images is high. The deep Gen II system provided images with a scale of about 6 m/pixel, allowing meteoroid decelerations to be measured very precisely. The drawback of the deep Gen II system is the small number of meteors captured, and the prevalence of partial trail observations.

The Gen III systems also produce images digitised at 8-bit grayscale resolution, meaning they are likely to experience saturation effects. About 10% of our Gen III data set were saturated (see Chapter 4 for details of the correction).

The spatial resolution of the Gen III systems is relatively poor, but their wide fields allow us to capture the entire trail of most meteors. The Gated camera, with a resolution of about 50 m/pixel, is used simultaneously with the Gen III systems to help constrain the deceleration of meteoroids. We don't use the Gated camera for photometry, because each frame contains many closely-spaced images of the meteor, which contaminate one another, making photometry unreliable. The Cooke camera system is excellent for both astrometry and photometry. The images captured by this system have 14 bit optical depth, meaning that for meteors in our size range, no saturation occurs. The disadvantage of the Cooke system is the slower frame rate, making the trail of the meteor in each frame so long that it can be difficult to detect possible fragmentation events occurring in one frame.

Table 2.1 gives a summary of the instruments used in this work. The next sections describe each setup in detail.

Table 2.1: Table summarizing instruments used in our study and their details.

Name	Intens.	CCD frame rate	lens	(FOV)	Im. size (pxl)	Pxl size (microns)	pixel scale of images	Image (bit)	resol (100 km)	stellar magn. limit	avg mass(kg)	study chap.
Deep Gen II	Litton G2	30fps (cohu)	155 mm f/0.75	$5.4^\circ \times 4.1^\circ$	640×480	8.4×9.8	0.008°	8	13 m	+11.0	$\sim 10^{-7}$	chap 3
Gen III	ITT Nitecam 380i	30 fps (cohu)	25 mm f/0.85	$34.4^\circ \times 24.9^\circ$	640×480	8.4×9.8	0.05°	8	94m	+8.5+9.5	$\sim 10^{-6}$	chap 4,5
Gated	ITT extended blue	5 fps	50 mm f/0.75	$15.2^\circ \times 11.5^\circ$	1360×1036	6.45×6.45	0.01°	14	20m	+8.0	$\sim 10^{-6}$	chap 5
Cooke	ITT Nitecam model 380i	20 fps (pco 1600)	50 mm f/0.95	$20.7^\circ \times 20.7^\circ$	1024×1024	8.4×9.8	0.02°	14	35m	+8.0	$\sim 10^{-6}$	chap 5

2.2.1 Observations

Our entire work was based on 151 meteors gathered from 2004 to 2009 (see table (2.2) for more details).

2.2.2 Image intensifiers

Typical limiting stellar sensitivity for a commercial video rate CCD is about +2 astronomical magnitude, and one would require hours of recording for a single meteor, except during a strong shower (Hawkes, 2002). To improve the sensitivity for meteors, the approach which has been used in meteor research is to interface the CCD to an image intensifier.

Image intensifiers are essentially light multiplication imaging devices. They have an input window and an output phosphor, with the image on the output phosphor being much brighter than that which is incident on the input window (Hawkes, 2002). They employ a microchannel plate (MCP), which works similarly to a multi-stage photomultiplier tube (PMT). A PMT consists of an evacuated glass tube, on one end of which is photocathode (a film of material such as Indium antimonide). This photocathode has the property that if it is struck by a photon, an electron is often liberated from the material. Each electron liberated from the cathode is directed away from the cathode by an electric field, and is amplified into a pulse of electrons by a series of metal plates (called dynodes) and an accelerating electric field in the tube (Romanishin, 2001). We have thus the situation where a single photon hitting the cathode results in an easily counted pulse of many electrons (figure 2.1). The drawback of a PMT is that it is essentially a single channel device, meaning that there is no positional information in the signal.

In a MCP, like in a PMT, electrons are released at a photoelectrode and are accelerated towards a high positive potential (Hawkes, 2002). The optically released electrons are guided down many tiny microchannel plates, and a cascade effect is created when a high energy electron strikes the MCP wall and generates several

Table 2.2: Table summarizing all campaigns and their details.

Campaign	Duration	#usable nights	stations	location			baseline	instruments	nb events
				site 1	site 2	site 3			
London Ontario	20040517-20040527	3	2	Elginfield 43°11'58N 81°18'90W	Silo 43°12'23N 81°22'62W		5.50 km	Gen II camera Gen II Camera	13
Arizona	20060430-20060506	5	2	Kitt Peak 31°57'70N 111°36'01W	Whipple obs 31°40'51N 110°57'17W		77.04 km	Gen III camera Gated system Gen III camera	09
London Ontario	20070420-20070422	2	2	Elginfield 43°11'58N 81°18'90W	Tavistock 43°15'84N 80°46'32W		44.61 km	Gen III camera Gated system Gen III camera	05
London Ontario	20070519-20070520	1	2	Elginfield 43°11'58N 81°18'90W	Tavistock 43°15'84N 80°46'32W		44.61 km	Gen III camera Gated system Gen III camera	05
London Ontario	20070812-20070813	2	2	Elginfield 43°11'58N 81°18'90W	Tavistock 43°15'84N 80°46'32W		44.61 km	Gen III camera Gated system Gen III camera	17
Peera Finland	20071006-20071013	7	2	Peera (Finland) 68°53'39N 21°3'34E	Kiruna (Sweden) 67°53'39N 20°25'98E		117.00 km	Gen II camera Gen II Camera	29
London Ontario	20080910-20080911	2	2	Elginfield 43°11'58N 81°18'90W	Tavistock 43°15'84N 80°46'32W		44.61 km	Gen III camera Gated system Gen III camera	27
London Ontario	20090625-20090911	8	2	Elginfield 43°11'58N 81°18'90W	Tavistock 43°15'84N 80°46'32W		44.61 km	Cooke camera Gated system Cooke camera	31
London Ontario	20090624-20090825	3	3	Elginfield 43°11'58N 81°18'90W	Tavistock 43°15'84N 80°46'32W	Brussels 48°44'88N 81°12'42W	61.36 km 44.61 km 64.14 km	Cooke camera Gated system Cooke camera	15

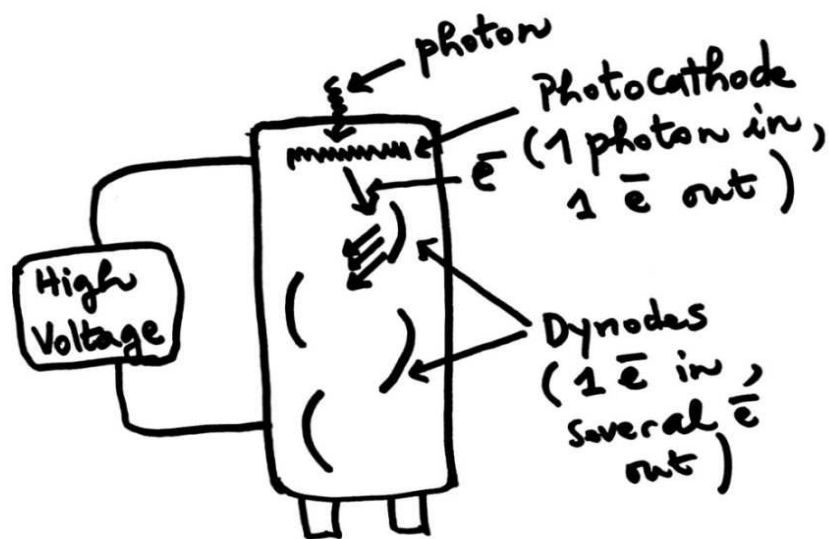


Figure 2.1: Schematic diagram of a photomultiplier tube (PMT). The high voltage supply creates an electric field that accelerates electrons along the tube. At each dynode, an impinging electron releases several electrons, which are then accelerated towards the next dynode, where each of them knock loose several more electrons. Through this cascade, a single photon hitting the photocathode releases an easily counted pulse of many electrons (after Romanishin, 2001).

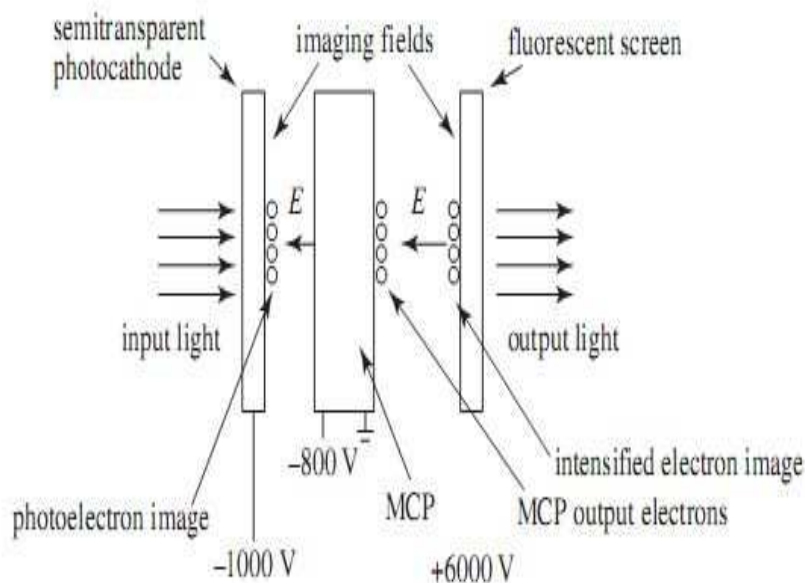


Figure 2.2: The energy of the incident photons is used to release electrons from the photocathode. They are accelerated in a strong electrical field in the microchannel plate, with electron multiplication taking place. The electrons strike a phosphor, recreating a light image which is many thousands of times brighter than the original image (from Hawkes, 2002).

secondary electrons. The principle of operation of a microchannel plate image intensifier is shown in figure (2.2).

MCP is the technology behind second (Gen II) and third (Gen III) generation image intensifiers. A typical gain of 35,000 can be achieved in a single stage. In the CCD meteor observation system, the MCP is placed between the objective lens and the CCD. In our systems either a Gen II or a Gen III, intensifier is mounted to a Cohu 4910 CCD. Figure (2.3) shows a complete video-based MCP image intensified CCD meteor observation system (Hawkes, 2002).

2.2.3 Second generation image intensified systems: Gen II

In our observations, second generation (Gen II) (Fig. 2.4) refers to a 25mm diameter Litton microchannel plate image intensifier with S-20 spectral response. Gen II intensifiers have a spectral response from 340 - 870 nm, and have less sensitivity

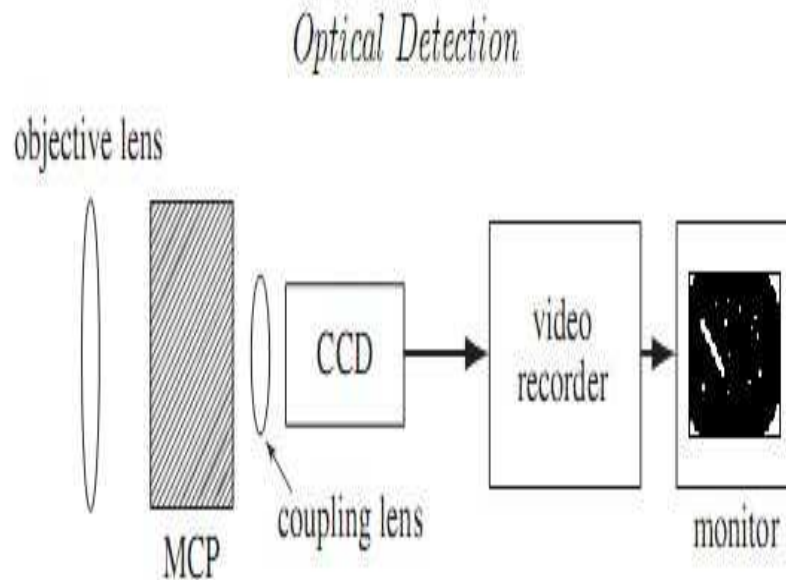


Figure 2.3: A block diagram of a lens-coupled microchannel plate image intensified CCD meteor observation system (from Hawkes, 2002).

in the red, and shorter tube lifetimes, than Gen III intensifiers, but are otherwise comparable. They are significantly more sensitive than Gen I intensifiers whose luminous gain is typically 75 against 35000 for Gen II. Gen II intensifiers are also less susceptible to blooming when imaging bright point objects.

Gen II intensifiers were used in these systems because they were simpler to integrate with the large lenses required to capture images with good spatial resolution, which are able to detect deceleration of the meteoroid during its flight in the Earth's atmosphere. We used a catadioptric objective lens with 155 mm focal length with $f/0.75$. The intensifiers were lens coupled to Cohu 4910 series video CCD cameras, which are high performance, relatively sensitive, monochrome CCD cameras with analog output (Hawkes et al., 2001).

The field of view of the system was $5.4^\circ \times 4.1^\circ$, producing a resolution of 0.008° per pixel ($0.48'$ per pixel). For a meteor occurring at a range of 100 km, one pixel represents 13 m, close to photographic resolution which is around 10 m. The limiting stellar magnitude was around +11.

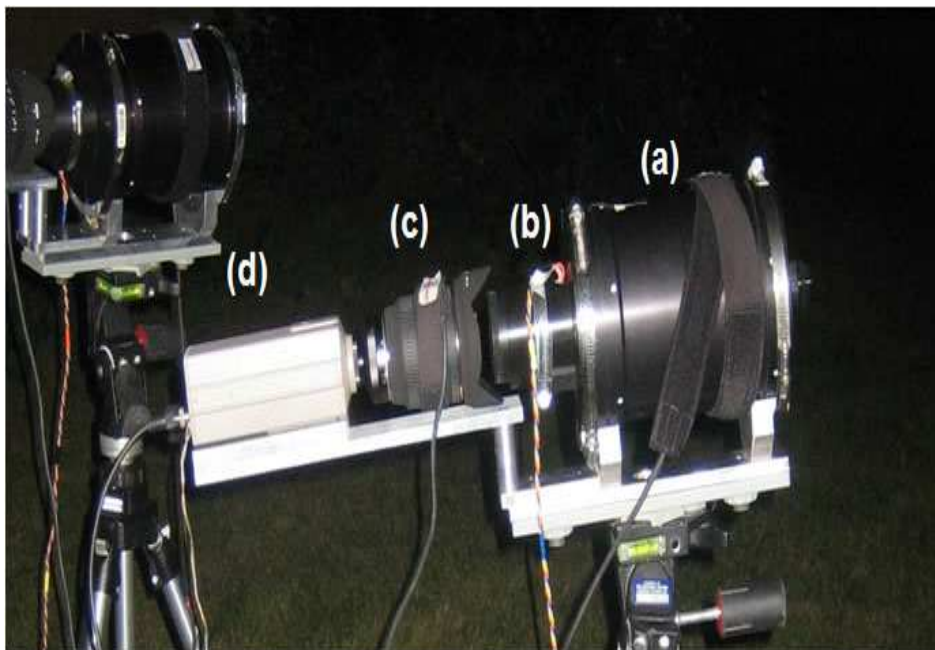


Figure 2.4: The deep Gen II system. Component (a) is a 155mm f/0.75 Catadioptric lens, (b) is a Litton 25 mm diameter Generation 2 image intensifier, (c) is a relay lens which focuses the light from the output phosphor at the back of the Gen 2 to the CCD camera, shown as element (d). The CCD used is a COHU model 4910 which records 30 NTSC frames per second at 640x480 resolution. This output is then streamed to a digitizer and computer and stored to disk.

2.2.4 Third generation image intensified systems: Gen III

The third generation (Gen III) systems (Fig. 2.5) are based on an ITT NiteCam (model 380i) microchannel plate image intensifier with 18 mm GaAs detectors (Hawkes et al., 2001). These intensifiers were lens coupled to the same Cohu CCDs as the Gen II systems. On each of the two systems, a 25mm Fujinon f/0.85 lens was used as the objective.

Gen III intensifiers are similar to Gen II, in that they are less susceptible to blooming than first generation intensifiers when imaging bright point objects. The main improvements over previous generations are tube lifetime, sensitivity at longer wavelengths and the elimination of persistence from one video frame to another, making it possible to accurately measure the light from the meteor in each frame. The 8-bit, 640x480 pixel images were streamed directly to computer at the standard NTSC rate of 30 interlaced frames per second and digitized onto disk. No compression routines were involved in the storage of the image data. Individual deinterlaced fields (60 per second) were used in this work (see also Hawkes et al., 2001).

The field of view of each system was $34.4^\circ \times 24.9^\circ$, producing a resolution of 0.05° per pixel ($3.1'$ per pixel). For a meteor occurring at a range of 100 km, one pixel represents 94 m. The limiting stellar magnitude of each video camera system was +8.5 to +9.5.

2.2.5 Gated intensified system

The Gated camera is a QImaging Intensified Retiga CCD camera (model 1394) with an integrated Gen III image intensifier (figure 2.6) using a ITT NiteCam microchannel plate image intensifier with 18 mm photocathode. It produces 14-bit, 1360 \times 1036 pixel images. The intensifier can be electronically gated, allowing multiple short exposures to be taken in each CCD frame. An internal electronic device is responsible for setting both the length of the CCD exposure, and the rate of gating. The rate of the CCD exposure time and the gating system frequency are controlled



Figure 2.5: Component (a) 25 mm f/0.85 Fujinon objective, (b) Gen III Nitemate (380i), (c) Cohu 4910 CCD, (d) Analog CCD output to be digitized at the computer.

through an external box (figure 2.7).

During all the campaigns where the gated system was used, the CCD exposure time was set to 5 frames per second (200 ms) and we used two frequencies for the gating system. From 2006 to 2007, we used 200 Hz, and from 2008 to 2009, to ensure that dotlike meteor images were well separated (eg figure 2.8), we used 100 Hz. The intensifier duty cycle was set to 1:5, meaning that the intensifier was on for 1 ms in each gating interval from 2006 to 2007, and 2 ms from 2008 to 2009. The gated system was used with a 50-mm Fujinon f/0.75 lens, giving a field of view of $15.2^\circ \times 11.5^\circ$ and pixel scale of 0.01° .

2.2.6 Cooke cameras

From 2009 onward, the Gen III systems were replaced by high resolution systems, hereafter called Cooke systems, after the name of the camera manufacturer (Cooke Corporation). They operate automatically and collect data whenever the appropriate conditions of weather and darkness are met. They consist of a Cooke pco.1600



Figure 2.6: The QImaging Intensified Retiga (model 1394) electronically gated image intensified camera.



Figure 2.7: External box which controls the rate of the CCD exposure and the gating system frequency.

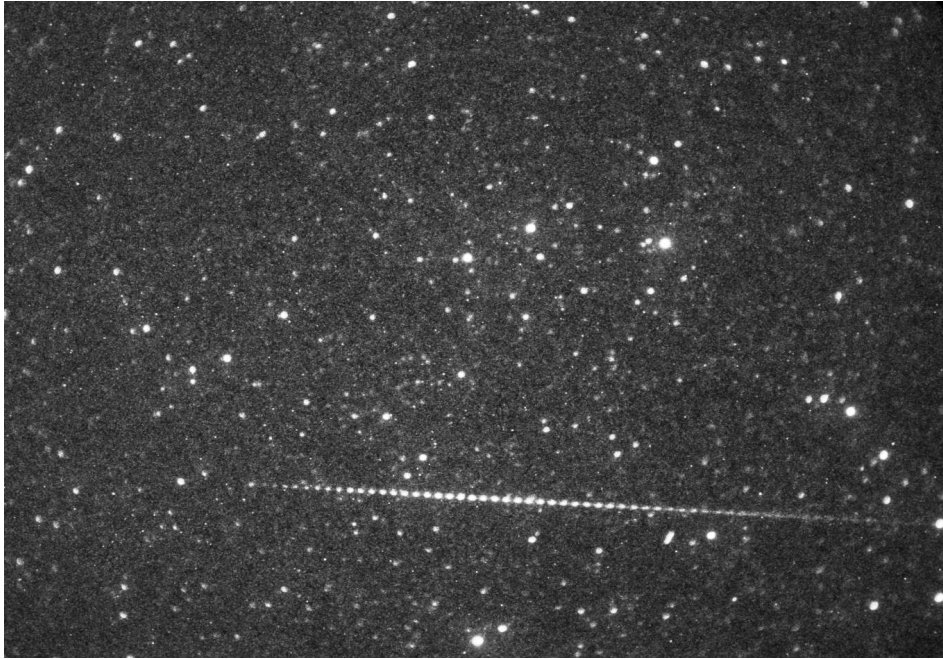


Figure 2.8: Meteor 20090825-065903 recorded with the gated camera on August 25, 2009 at 06:59:03 UTC at Brussels, Ontario, Canada. The frequency of the CCD was set to 5 Hz and the frequency of the gating system was 100 Hz.

camera lens coupled to a Gen III intensifier. The system, when used with a 25-mm Fujinon f/0.85 objective lens, has a field of view of $20.67^\circ \times 20.67^\circ$ with images of 1024×1024 pixels, giving a scale of 0.02° per pixel ($1.21'$ per pixel). For a meteor occurring at an altitude of 100 km, 1 pixel represents 35 m. The camera was operated at a rate of 20 progressive scan frames per second.

2.3 Methodology

2.3.1 Astrometry

We used standard astrometric techniques (Ceplecha et al. 1998, Ceplecha et al. 2000, Hawkes, 2000, Koten et al. 2004, 2006, 2007, Borovicka et al. 2007, Kikwaya et al. 2009) to extract the astrometric positions of meteors. These positions are calibrated using field stars. These are the different steps for the astrometric procedure.

1. We find the pixel locations of the stars using a centre-of-mass algorithm (How-

ell, 2000), and we compared the pixel locations against the SKY2000v4 catalogue (Myers et al. 2001).

2. We convert the star right ascension and declination into local zenith and azimuth angles using standard routines (see Explanatory Supplement to the Astronomical Almanac, Seidelmann and Urban, 2010). We use a third order polynomial least squares fit across the field to convert pixel value (x,y) to azimuth and altitude (Hawkes, 2002); in order to fit a frame close to or including the zenith, we use rotation to re-reference each point so that no singularities occur.
3. We reference all star coordinates about the centre of the frame. After this, they are projected onto a plane, and then fitted against the pixel locations. We use the third order fit instead of a second order fit which may be adequate simply for better lens distortion corrections.
4. The errors in the fit are calculated based on the angular separation between the catalogue and fitted coordinates to allow a single error for each star. This is more meaningful than quoting separate errors for azimuth and zenith angles, knowing that azimuth error is dependent on the zenith angle. On the Gen III systems for example, typical errors of 0.016° are found for the fits, which represents ≈ 0.32 pixels for these systems (meaning the stars are located to better than a pixel with the centroiding). On the gated system, the calibration errors were around 0.007° (corresponding to 0.6 pixels), and on the Cooke system errors were around 0.012° (0.3 pixels).
5. We measure manually the meteor positions by selecting a point on the leading edge of the meteor. This technique results in errors (due to lack of sub-pixel precision) of order 1-2 pixels and constitutes the dominant source of error in our measurements. We don't use centroiding for meteor positions because the meteor images are elongated.

6. After the astrometric positions of the meteor (astronomical azimuth and zenithal angle of each point of the meteor from each station) have been calculated for a given field (or frame), we use software developed by Borovicka (1990), called Milig, to compute the in-atmosphere trajectory of all simultaneous meteors. This software calculates the physical position of the meteor in the atmosphere, including the height, range to each station, and distance along the trail as a function of time by performing a non-linear least squares fit of all sight lines from all stations.
7. When we find the trajectory line, we can compute the velocity from each station for each pair of points on the trajectory. The pick error is large point to point since small errors introduced in the determined position of the meteor (of order 1 pixel) in each frame produce large random errors in the velocity at each point.
8. To produce a smoother measurement of velocity versus time (or height), we use a filtering technique (see Kikwaya et al. 2009). This technique consists of calculating the speed using measurements from widely separated images instead of neighbouring images (the number of points skipped varies between 5 and 15 for the Gen III systems, between 15 and 25 for the Gated camera, and between 5 to 10 for Cooke system). This smoothing acts as a low pass filter for our data, discarding the high frequency velocity jitter. This smoothing technique allows the deceleration to be seen clearly.

Figure (2.9) shows the raw velocity profile for the Gen III and Gated system for meteor 20060503-091349 recorded on May 3, 2006 at 09:13:49 UTC in Tucson, Arizona. The deceleration in these data is clear even without smoothing. We can make the presence of deceleration clearer by plotting the difference in position between a meteoroid travelling at constant speed and the observed one (Fig 2.10). The computed distance along the trail for the hypothetical non-decelerating meteoroid

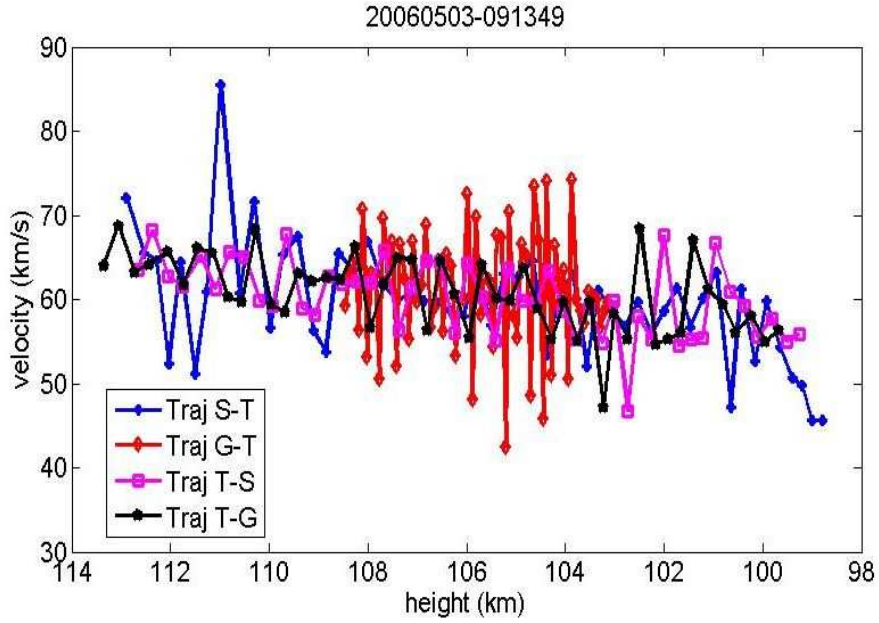


Figure 2.9: Trajectory solution of the meteor 20060503-091349, computed with the code Milig (Borovicka, 1990). Three cameras (two Gen III systems (S and T) at Kitt Peak and one (T) at Whipple Observatory in Arizona, USA) give four trajectories: S-T (trajectory at Kitt Peak from S and T), T-S (trajectory at Whipple Observatory from S and T), G-T where G is the gated camera (trajectory at Kitt Peak from G and T) and T-G (trajectory at Whipple Observatory from G and T). The velocity shown is for each trajectory pair in turn using the first camera in the pairing. No smoothing has been applied (see table (2.2) for a summary of the observing locations).

is $l_{ic} = \frac{v_{\infty}}{t_i}$ where v_{∞} is the pre-atmospheric velocity of the meteor, t_i the time since the start of the trajectory, and i the frame number.

To determine the pre-atmospheric velocity (v_{∞}) for each meteor, we took a series of points at the beginning of the trajectory, the number of which was equal to the number of points used to smooth the curve. We plotted the distance along the trail of the meteor on each of these frames versus time, and applied a first order linear least squares fit. The slope of this line is taken to be the pre-atmospheric velocity of the meteor. The error on the pre-atmospheric velocity was calculated as the standard deviation of the initial velocities of the same meteor using different cameras. The pre-atmospheric velocity of the meteor 20060503-091349, for example, was $61.30 \pm 0.99 \text{ km s}^{-1}$.

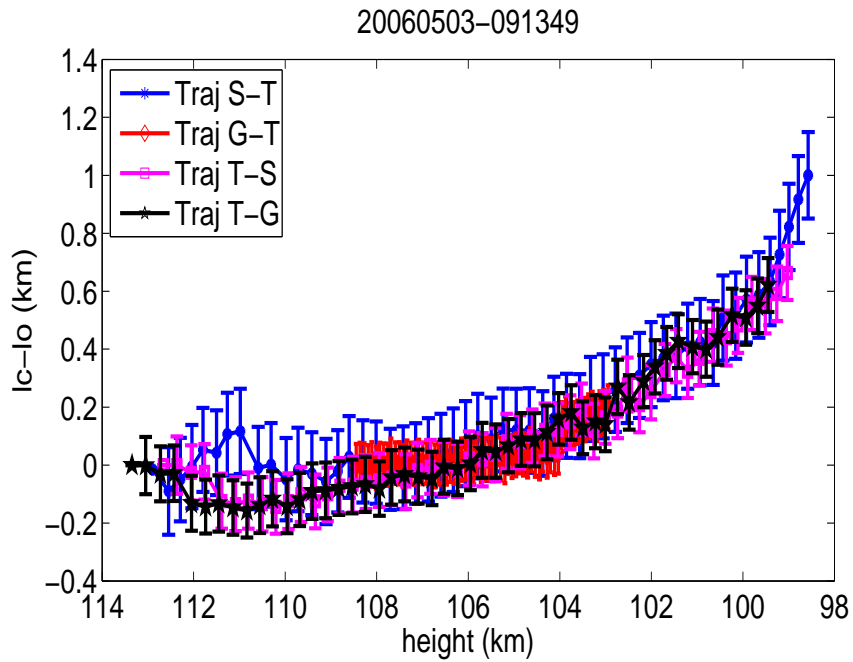


Figure 2.10: Plot showing the deceleration of the meteor 20060503-091349. l_c is the computed length along the trail assuming a constant velocity of 61.3 km s^{-1} in this example. l_o is the observed length along the trail as function of height. Each camera pair produces a separate, quasi-independent measure of velocity, with the first camera in each pairing plotted.

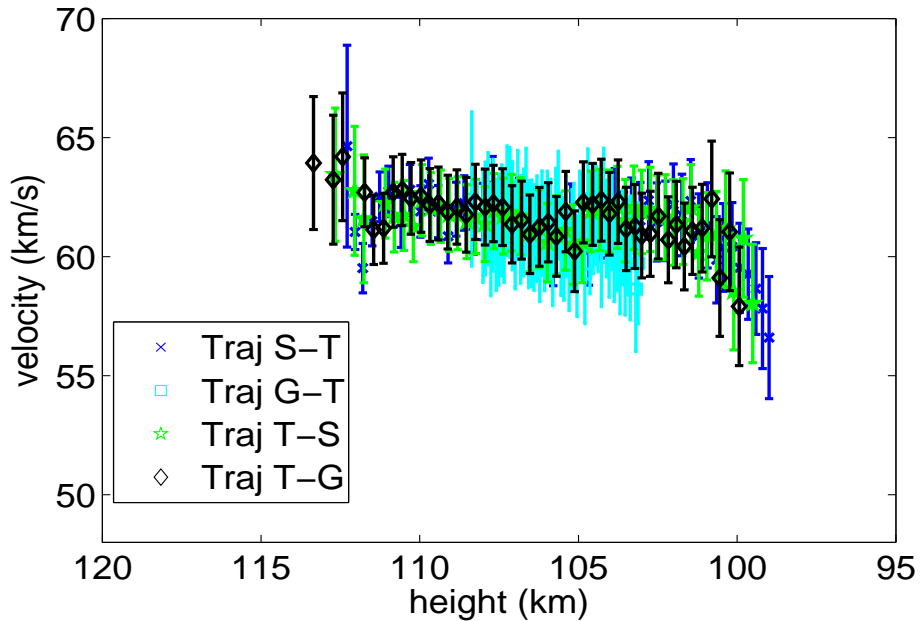


Figure 2.11: Velocity profile of the meteor 20060503-091349. We have inserted error bars at each point along the trajectory.

Errors in velocity at each point on the trail are the result of a combination of systematic error and random error when picking the position of the meteor on each frame along its trajectory. To estimate the systematic error, we compared the measured positions of the same meteor as found by 9 persons (see for example tables (2.3) and (2.4) showing positions of the meteor 20060504-093103 measured by two different persons). This process was repeated for 8 meteors resulting in a series of 14040 error estimates. Overall, we found that the systematic shift from one person to another was about 0.6 pixels, which we then took to be the systematic error (Fig. 2.12). The random error is evaluated using the trail fit residuals, since the meteor is a straight line to high precision. Knowing the angular velocity of the meteor and the scale of the image, we were able to find the random point-to-point error from this average residual fit. For the Gen III systems, the random error ranged from 0.2 to 0.3 pixels; for the gated camera, it was between 0.4 and 0.6 pixels; and for the Cooke cameras, the random error was about 0.5 pixels. We added these two types of error to all measured points of a particular meteor in a Monte Carlo simulation, where Milig was run 2500 to 5000 times per event, with the trajectory calculated for each clone. We were then able to determine physical errors in position, height, range and velocity for each measured point of the meteor.

2.3.2 Photometry

We used standard routines for meteor photometry. Briefly, our procedure was to flat field each frame, and then to compute the photometric magnitude of the meteor by calibrating the log-sum-pixel of the meteor with those of surrounding stars (Hawkes et al., 2001; Hawkes, 2002, Kikwaya et al., 2009, Kikwaya et al., 2010). Figure (2.13) shows an example of this photometric calibration. A total of about 100 stars are used. The log sum pixel of each star is calculated by taking a disc covering the whole star and a surrounding ring representing the background. The median value of pixels in the background ring is subtracted from the disc (taking into account pixel

Table 2.3: Positions of meteor 20060504-093103 measured by one person. Zero degree of the azimuth angle is located at East, North is -90 degrees and South is +90 degrees.

# of frames	x pixels	y pixels	zen angle (°)	azimuth (°)
34	378	263	17.990	-88.125
35	378	259	17.778	-88.131
36	378	254	17.513	-88.137
37	378	249	17.248	-88.145
38	378	244	16.983	-88.152
39	378	240	16.771	-88.159
40	378	235	16.506	-88.167
41	378	231	16.294	-88.174
42	378	226	16.029	-88.183
43	378	222	15.817	-88.191
44	378	218	15.605	-88.199
45	378	213	15.340	-88.209
46	378	208	15.075	-88.220
47	378	204	14.863	-88.229
48	378	200	14.651	-88.239
49	378	195	14.385	-88.251
50	378	190	14.120	-88.264
51	378	186	13.907	-88.275
52	378	181	13.642	-88.289
53	378	176	13.376	-88.304
54	378	172	13.164	-88.317
55	378	168	12.951	-88.330
56	378	163	12.685	-88.347
57	379	159	12.472	-88.585
58	379	154	12.206	-88.608
59	379	149	11.940	-88.633
60	379	145	11.726	-88.654
61	379	140	11.460	-88.681
62	379	135	11.193	-88.710
63	379	131	10.979	-88.734

Table 2.4: Positions of the same meteor (20060504-093103) measured by another person. Zero degree of the azimuth angle is located at East, North is -90 degrees and South is +90 degrees.

# of frames	x pixels	y pixels	zen angle (°)	azimuth (°)
34	378	263	17.990	-88.125
35	378	259	17.778	-88.131
36	378	253	17.460	-88.139
37	378	249	17.248	-88.145
38	378	245	17.036	-88.151
39	378	240	16.771	-88.159
40	378	237	16.612	-88.164
41	378	232	16.347	-88.172
42	378	227	16.082	-88.181
43	378	223	15.870	-88.189
44	378	219	15.658	-88.197
45	379	214	15.394	-88.389
46	379	209	15.128	-88.403
47	379	205	14.916	-88.414
48	379	200	14.651	-88.429
49	379	195	14.386	-88.445
50	379	191	14.173	-88.458
51	379	186	13.908	-88.476
52	379	181	13.642	-88.494
53	380	176	13.377	-88.721
54	379	172	13.164	-88.529
55	380	165	12.793	-88.776
56	380	162	12.633	-88.792
57	379	157	12.366	-88.594
58	380	153	12.154	-88.842
59	380	148	11.887	-88.873
60	380	143	11.621	-88.904
61	380	140	11.460	-88.924
62	380	134	11.140	-88.966
63	380	128	10.819	-89.010

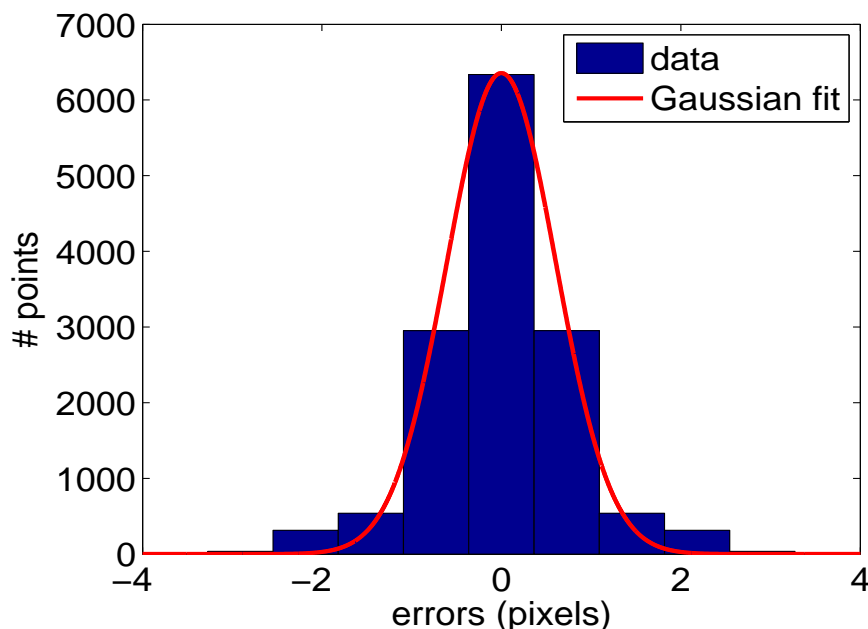


Figure 2.12: Systematic shift found by comparing positions of the same meteor measured by 9 persons. The standard deviation of the Gaussian fit was 0.6 pixels, which we took to be the systematic error.

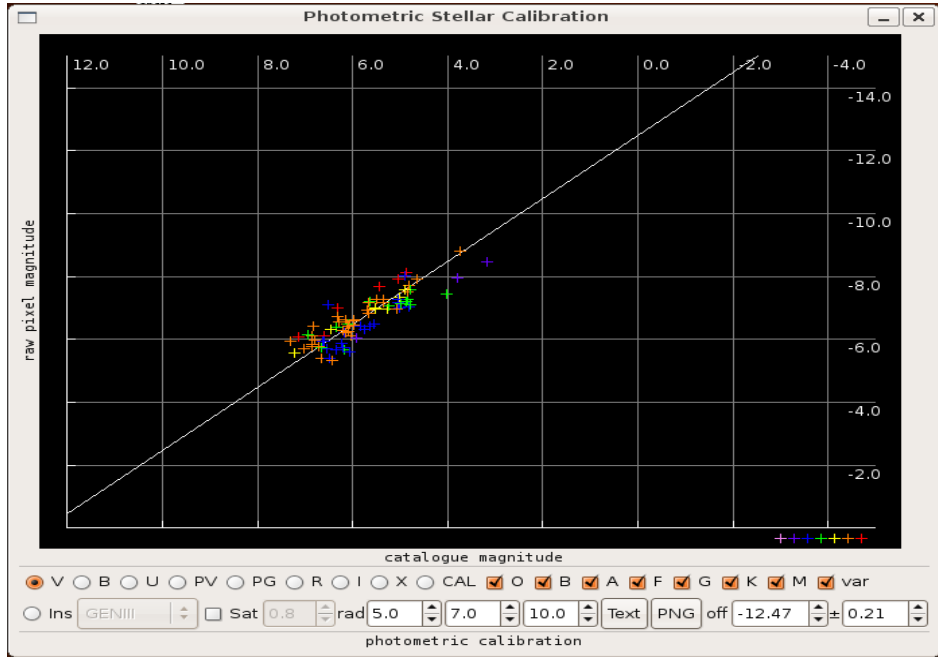


Figure 2.13: Photometric stellar calibration for Gen III camera on April 20, 2007 at 08:23:56 UTC at Elginfield (see table (2.2) for a summary of the observing locations).

areas), and the instrumental magnitude of the star is computed as the logarithm of the sum of the pixel intensities in the disc: these are compared to catalog V (visual) magnitudes (from SKY2000v4, Myers et al., 2001) with a linear fit to obtain the calibration. The meteor log-sum-pixel is found by manually selecting the brightness region of the meteor in each frame. This photometric mask extended as far back as the leading edge of the meteor as measured on the previous frame, but no further, to avoid contamination from persistence.

R magnitude calibration versus V magnitude calibration

The Gen III and Cooke system are more sensitive in the R (red) band than Visible. The spectral response of the Gen III cameras, for example, covers a range from the Blue band to the Infrared band, with a peak around 40% quantum efficiency in the Red region. A bandpass is the overall sensitivity of an instrument as function of wavelength: it includes the effects of filters, plus characteristics of the detector. The spectral response of the gated camera, compared to the Gen III, is visibly extended

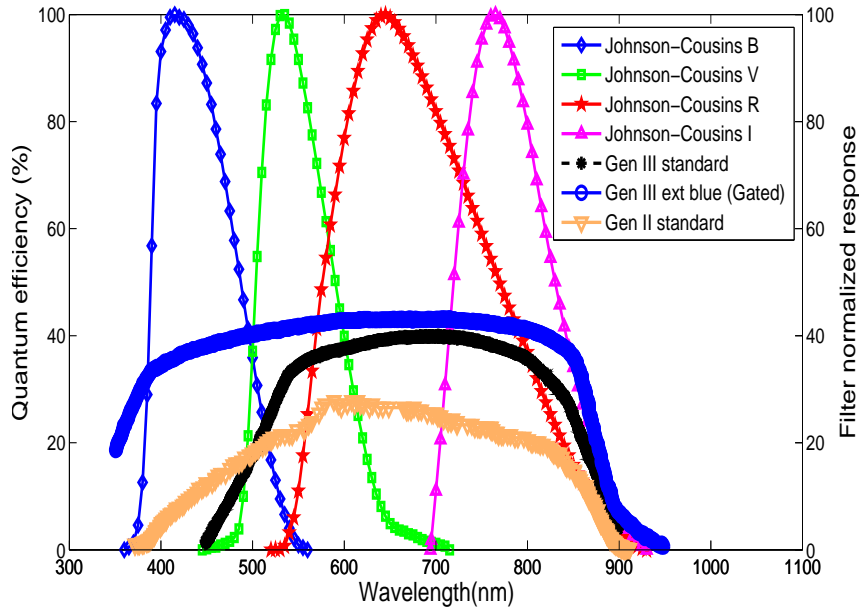


Figure 2.14: Spectral responses of Gen II, Gen III and Gated camera (extended blue).

in the blue region. The Gen II system has the lowest spectral response and peaks around 25% in the visible region (see Fig. 2.14).

Because the Gen III systems are more sensitive in the R band than the V band, the R band gives less scatter when plotting instrumental magnitude versus catalogue R magnitude (see for example the photometric stellar calibration of the Gen III system using the catalogue V magnitude (Fig. (2.15) and the catalogue R magnitude (Fig. 2.16). The linear fit where the catalogue V magnitude is used has an intercept with an error of 0.20 Magnitude, almost twice the error of the intercept when the catalogue R magnitude is used. The catalogue R is for us the best choice for the photometric stellar calibration; nevertheless, we chose to use stellar V magnitudes for calibration. This is justified first by the fact that the luminous efficiency for meteors has only been estimated in the V band (Ceplecha et al., 2000, Koten et al., 2006). Secondly, we estimated the color term between Johnson-Cousins V bandpass and R bandpass using actual meteor spectra (Borovicka et al., 2005) by performing synthetic photometry. In this procedure, we multiplied the meteor spectrum by

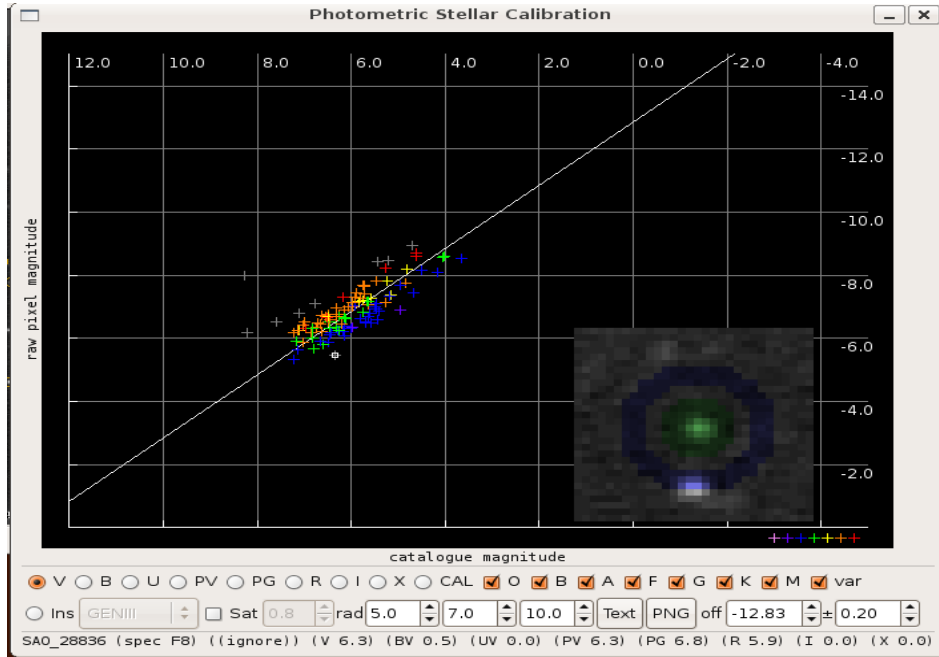


Figure 2.15: Photometric stellar calibration for Gen III camera on April 20, 2007 at 08:23:56 UTC at Tavistock. The stellar V catalogue is used. The linear fit has an intercept with an error of 0.20 Magnitudes.

the appropriate bandpass, and integrated to get a total meteor intensity in each band. Each intensity I was converted into a magnitude M using $I = 10^{(M/-2.5)}$ (see table 2.5). The difference between the R and V magnitudes gives an average correction factor which can be added to a calculated meteor R magnitude to obtain the V magnitude (we use the average value of $V-R$ to correct the lightcurve). This is the correct technique for obtaining V magnitudes from a calibration using R stellar magnitudes; we found, however, that it agreed closely with meteor magnitudes calculated directly using the V magnitude in the stellar calibration (Fig. 2.17). For this reason, we used the simpler procedure of calibrating each image with V magnitudes directly.

Having addressed the issue of photometric calibration, we need to look at the error in the meteor magnitudes. For each meteor, a stellar calibration is performed using a linear fit on a plot of instrumental stellar magnitude (log-sum-pixel) versus catalogue V magnitude to find the relationship between log sum pixel and magnitude. The slope of this fit is forced to be unity as the relative change in catalogue

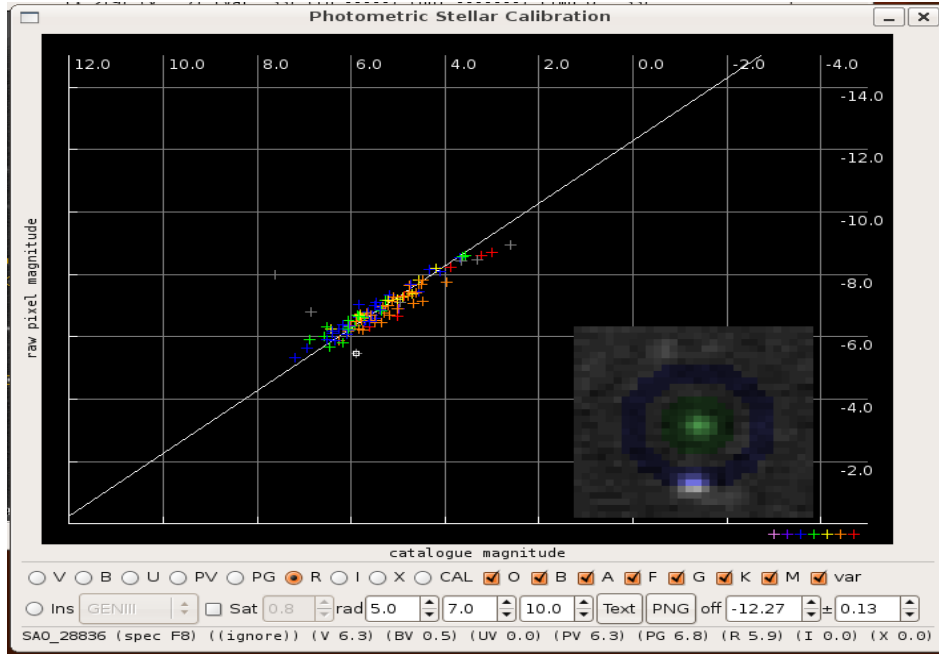


Figure 2.16: Photometric stellar calibration for Gen III camera on April 20, 2007 at 08:23:56 UTC at Tavistock. The stellar R catalogue is used. The linear fit has an intercept with an error of 0.13 Magnitudes.

Table 2.5: Table of synthetic photometric magnitudes using observed video meteor spectra. Values of multiplication of the meteor with the V bandpass and the R bandpass are given. The color term (V-R) is shown for each meteor. Meteor spectra come from Borovicka et al. 2005. The average of $\text{Mag}(V-R)$ is 0.7538 ± 0.0898 .

Spectra	Multiplication V bandpass	Multiplication R bandpass	Mag (V-R)
S557	2.68E+09	5.51E+09	0.7844
SZ1054	7.77E+09	1.98E+10	0.8152
SZ1098	1.52E+09	3.57E+09	0.9257
SZ1315	5.58E+08	1.12E+09	0.7544
SZ1422	2.66E+09	5.79E+09	0.8456
SZ1711	2.27E+09	4.18E+09	0.6646
SZ2197	1.13E+09	3.00E+09	0.6609
SZ2199	1.70E+10	3.37E+10	0.7405
SZ1350	2.58E+09	4.83E+09	0.6824

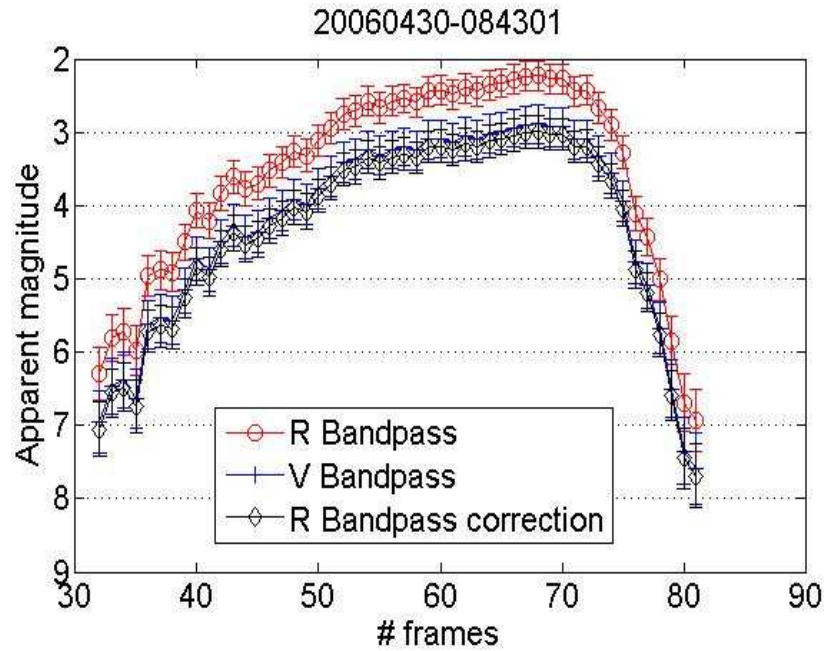


Figure 2.17: Lightcurve of the meteoroid 20060430-084301, determined using both catalog V magnitude and catalog R magnitude. When the R magnitude curve is corrected using the V to R conversion, it agrees with the V magnitude curve.

magnitude and instrumental magnitude are proportional. Our fit establishes the unknown intercept of this linear fit. The typical error for a star is 0.1-0.3 magnitudes defined as its deviation from this best fit line (see Fig. 2.13). At fainter magnitudes, this error is dominated by counting statistics and shot noise in the intensifier. At brighter magnitudes, the error is primarily due to uncertainty in the photometric calibration. The total error is determined using standard error techniques, where the standard deviation of the photon count is governed by Poisson statistics. This gives an error in the photometric magnitude of $2.5/\sqrt{N}$ (where N is the pixel intensity sum, proportional to the number of photons), to which the error from the photometric calibration is added. The magnitude of the meteor is calculated from the calibration and corrected to an absolute magnitude (i.e. the magnitude of the meteor if its range was 100 km from the observer: McKinley, 1961):

$$M_a = M_v + 2.5 \log_{10}(R/100) \quad (2.1)$$

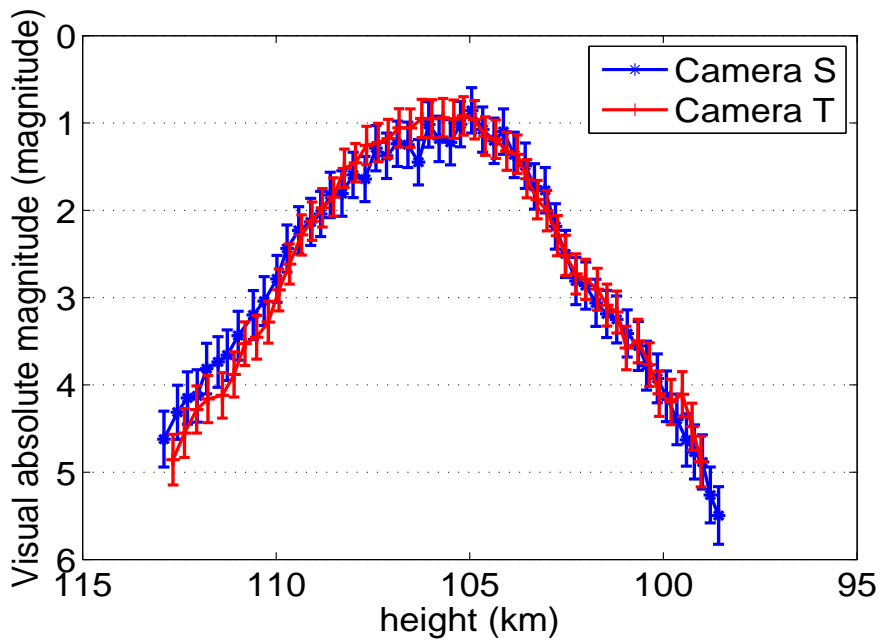


Figure 2.18: The absolute lightcurves of the meteor 20060503-091349 obtained after applying the different photometric techniques (The correction for range has been applied).

where M_a is the absolute magnitude, M_v the apparent magnitude and R the range in km at which the meteor occurred.

In the case of the 9 Gen III meteors which saturated the camera in our sample, a saturation correction (of up to +1.3 magnitudes) was applied to the apparent magnitude before it was converted to an absolute magnitude (see Chapter 4 for details). Figure (2.18) shows the lightcurve of the meteor 20060503-091349 from two Gen III.

Table 2.6: Average of luminous efficiency according to the meteoroid velocity

	velocity		
	$v < 20$ km/s	$20 \text{ km/s} \cdot v < 60$ km/s	$60 \text{ km/s} \cdot v < 100$ km/s
$\tau(\text{tau})$	0.0202	0.0109	0.0028

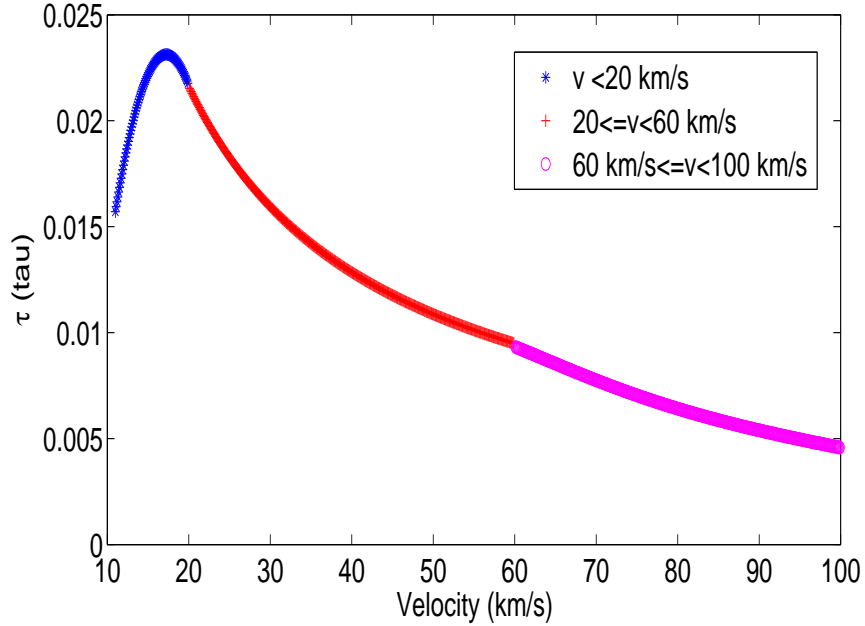


Figure 2.19: Luminous efficiency versus velocity. The three groups according to the meteoroid velocity are shown.

Luminous efficiency

The luminous efficiency (τ) used in this work is the one described by Hill et al. (2005). It depends on velocity and it is divided in 3 groups according to the meteoroid velocity ($v < 20$ km/s, $20 \text{ km/s} \cdot v < 60$ km/s, and $60 \text{ km/s} \cdot v < 100$ km/s). The form of luminous efficiency (τ) is shown in Fig. 2.19, and on average, it is given in functional form as (see table 2.6):

The luminous efficiency is given by the following equation:

$$\tau = 2.0 \times 7.667 \times \frac{x}{v^2} \quad (2.2)$$

where v is the meteoroid velocity and x an intermediate variable whose value is given by:

For $v < 20$ km/s ;

$$x = \left[2.1887e^{-3} v^2 + 4.2903 \times 10^{-4} v^3 \right] + 1.2447 \times 10^{-5} v^4 \quad (2.3)$$

For 20 km/s \cdot $v < 60$ km/s;

$$x = 0.01333 v^{1.25} \quad (2.4)$$

For 60 km/s \cdot $v < 100$ km/s

$$x = \left[12.835 + 6.7672 \times 10^{-1} v \right] + \left[1.163076 \times 10^{-2} v^2 + 9.191681 \times 10^{-5} v^3 \right] + 2.7465805 \times 10^{-7} v^4 \quad (2.5)$$

2.4 Ablation Model

To measure density, we need to compare the observations with a model of atmospheric entry. In our work, we use the dustball model of Campbell-Brown and Koschny (2004). Where the traditional dustball model suggests that the light production starts as soon as the small grains are all released, the heating of the meteoroid, modeled through Clausius-Clapeyron formalism by Campbell-Brown and Koschny, allows one to consider ablation even before the boiling temperature is reached. The dustball model of Campbell-Brown and Koschny allows the user to enter any number of grains and their masses, without necessarily assuming a power law distribution. This is a considerable advantage, since the computing time may be

reduced significantly by representing a distribution of grain sizes as a small number of distinct sizes.

The model considers three sources of energy: energy imparted to the meteoroid by collisions with atmospheric atoms, the energy lost from the meteoroid by radiation, and the energy lost through evaporation of the meteor material. The mass loss is calculated using the Knudsen-Langmuir formula, combined with the Clausius-Clapeyron equation. A term proportional to kinetic energy transfer, like the classical formula, is also added to simulate spallation when the meteoroid is very hot. For more details of the ablation model, see Chapter 1 and Campbell-Brown and Koschny (2004).

2.5 Method of analysis

For each meteor, we extracted the velocity and the radiant using the MILIG trajectory code as described above. We extracted the lightcurve of each meteor which matched our criteria. We applied a correction for saturation (Kikwaya et al. 2010; Chapter 4) to nine of them. We then applied our ablation model to simultaneously fit the observed lightcurve and deceleration (Chapter 3 and Chapter 5).

Among the parameters used in the model, we have chosen some to remain fixed and some to remain free. Fixed parameters include the fusion point of the meteoroid grains, which is taken to be 100 K less than the boiling point of the meteoroid grains (the boiling temperature remains free); the condensation coefficient ψ , which is fixed to 0.5 (condensation coefficient of stone), the emissivity of the meteoroid (fixed to 0.9), and the atmospheric density, provided by the MSISE 90 model (Hedin, 1991) appropriate to the date and location of the observations.

We base the goodness of fit on the reduced chi-squared between the model and observed curves for both the lightcurve and the deceleration curve. This takes into account the size of the error bars in the measured values. The chi-squared is given

by:

$$\chi^2 = \sum_i^n \frac{(O_i - M_i)^2}{\sigma_i^2} \quad (2.6)$$

where O is the observed value, M is the modeled value, σ is the error value of observed value, and i is the number of the observed value. The reduced chi squared χ_c^2 is given by χ^2 / DOF , DOF being the number of degrees of freedom (the difference between the the number of observed points and the number of free parameters).

To fit the observed decelerations and lightcurves, we search the entire free parameter space for each meteor in two stages: a broad search and a refined search. The first stage in the solution procedure helps to identify the regions in parameter space in which solutions are concentrated. If all good solutions found during the broad search are grouped within less than 1000 kg/m^3 (the typical range of density error reported in different works: Babadzhanov (2002), Bellot Rubio et al. (2002), and Chapter 3), we take the best solution among them, by which we mean the one with a reduced chi-squared closest to 1 indicating that our model and observations are in accord with the size of the observational errors. That is, the experimental variance is close to the theoretical variance. In general, our $\lesssim 1000 \text{ kg m}^{-3}$ search range encompasses the regions where $\chi_c^2 < 1$. In the case where the good solutions are grouped in several different regions, we choose the best solution from each group and we work explicitly on each, eliminating any which are unphysical. The reason we proceed by two stages is the difficulty in determining the grain distribution; if the number of solutions covering a reasonable range of each of the other free parameters is merely prohibitive, the number of possible grain distributions is essentially infinite.

In the broad search, we need a rough grain distribution to begin. We calculate an approximate mass distribution index using the work of Murray et al. (2000) as a starting point; in this work, they associated the shape of meteor lightcurves (characterized by the F-parameter) to a mass distribution index of the constituent

grains.

The chosen grain mass distribution may not be the best mass distribution for the grains of any of our meteoroids, but it provides a starting point. With this grain mass distribution, grains are distributed in several bins according to the method described by Borovicka et al. (2007), and summarized below.

Once the best solution from the broad search is found, a better grain distribution is obtained by manual adjustment until we reach the best fit to the observed lightcurve and deceleration. The best solution from the broad search is the solution with χ^2 reduced closest to 1. In the broad search, chi-squared relied only on the curves overlapping by four fifths of all points for the lightcurve and two thirds of the points for the deceleration. This was done to capture all possible good solutions, and this is why good fits in the broad search did not always provide really good solutions.

This mass distribution will be considered the final mass distribution of the meteoroid, and the density of this solution we take to be the density of the meteoroid. To evaluate the uncertainty in the density, we once again search the entire free parameter space with higher resolution in density over a range of $\pm 1000 \text{ kg m}^{-3}$ centred on the best solution in the broad search, using the new grain mass distribution. All solutions from the refined search are sorted and those with reduced chi-squared less than 1 will constitute the density distribution of the meteoroid.

2.5.1 Broad search

Free parameters

The free parameters used in our ablation model include:

- ² grain mass (to which the number of grains is tied) (units of kg)
- ² bulk density of the meteoroid (units of kg m^{-3})
- ² the heat of ablation (Q) (units of J/kg)

- 2 the boiling point of the meteoroid grains (T_{boil}) (units of K)
- 2 the temperature at which the grains are released (T_{lim}) which is physically less than T_{boil} (units of K)
- 2 the specific heat (C_p) (units of $\text{J kg}^{-1} \text{K}^{-1}$)
- 2 the average molar mass of meteoroid material (atomic mass units)
- 2 the thermal conductivity of the meteoroid (units of $\text{W m}^{-1} \text{K}^{-1}$)

Our methodology is as follows:

For the broad search, we allow the density to vary from 100 kg m^{-3} , corresponding to very porous carbonaceous materials (in Chapter 3 we started at 500 kg m^{-3}) to 8000 kg m^{-3} , corresponding to iron. This covers the full range of physically expected densities for any reasonable choice of starting materials. We increased the density by a step of 300 kg m^{-3} . The heat of ablation is of the order of 10^6 J kg^{-1} (see Ceplecha et al., 1998), though the actual value depends on the composition of the meteoroid. Babadzhanov (2002) used $2.8 \times 10^5 \text{ J kg}^{-1}$ for heat of fragmentation supposed to be less than the heat of ablation. Bellot Rubio et al (2002) found that this heat of fragmentation was too low. They thought that it should be around $5.5 \times 10^6 \text{ J kg}^{-1}$. In our work, we allow the heat of ablation to range from 2×10^6 to $9 \times 10^6 \text{ J kg}^{-1}$ to remain in the vicinity of 10^6 J kg^{-1} , used by other authors (Hawkes and Jones, 1975, Borovicka et al. 2007, Kikwaya et al. 2009).

Physically, the fragmentation temperature (T_{lim}) must be less than the boiling temperature (T_{boil}), otherwise the grains will ablate before they separate. Knowing that iron (the densest element we expect to encounter as a major element in the composition of the meteoroid) reaches its boiling temperature around 2000 K, we choose fragmentation temperatures ranging from 900 K to 1600 K, and set the boiling temperature to vary between 1400 K to 2300 K.

The thermal conductivity is expected to be small, since small meteoroids are known to have considerable porosity (Campbell-Brown and Koschny, 2004; Popova

2005). We allow it to range between 0.1 and 1.0 W/m K.

We varied the molar mass from 20 to 56 atomic mass units (amu), a range which spans atoms ranging from sodium to iron. We find that most solutions were not very sensitive to molar mass changes if the value was over 36 amu. The range of specific heat goes from 600 J/kg K to 1400 J/kg K, which correspond to the values used by Campbell-Brown and Koschny (2004).

In some ablation models, Γ (drag coefficient) and Λ (heat transfer coefficient) are assumed from the beginning. Examining the Draconids, Borovicka et al. (2007) set Γ and Λ to 1. Fisher et al. (2000) assumed also Γ and $\Lambda = 1$ (usually Γ and Λ are fixed to specific values to limit the computation time). Campbell-Brown and Koschny (2004) assumed $\Gamma = 1$ and $\Lambda = 0.5$. In our work, when doing the broad search, we fixed Γ and Λ at 1, following these earlier studies. After finding the best solutions, we adjusted them in concert with the mass to improve the model fits. At this stage in our solution procedure, we allow Γ and Λ to vary from 0.7-1.0.

Mass grain distribution

Once the fragmentation temperature (T_{lim}) is reached, the meteoroid mass at that moment separates into a number of individual grains of masses in the interval (m_l , m_u), where m_u is the upper grain mass limit and m_l is the lower grain mass limit.

We assume a power-law mass distribution in the form:

$$n(m) = Cm^{-s} \tag{2.7}$$

with $m_l < m < m_u$. $n(m)$ is the cumulative number of grains of mass m or larger, s is the mass distribution index, and C is a constant. We sorted the grains into mass bins of masses m_0, m_1, \dots, m_k , with m_0 equal to m_u following the procedure proposed by Borovicka et al. (2007). The mass of all grains within the i th bin was set to:

$$m_i = m_0 p^i \quad (2.8)$$

where p , the mass sorting parameter, was chosen to be $10^{-0.1} = 0.7943$. In principle the choice of p is arbitrary, but there are certain limits. If the grains are small (from 10^{-10} kg to 10^{-12} kg like in the case of Draconids, Borovicka et al. 2007) and there is a large number of grains, p can be small (i.e. $10^{-0.1}$). If however, some grains are relatively large in comparison with the total mass of the meteoroid and the mass span is large (i.e. m_l is much smaller than m_u), p must be larger (even $10^{0.5}$), otherwise the number of grains in some mass bins would be, mathematically, less than 1, which is not possible since the number of grains in each bin must be an integer.

The number of mass bins is:

$$k = \log(m_u/m_l) / \log p \quad (2.9)$$

and the number of grains in the i th bin is:

$$n_i = n_0 \left(\frac{m_0}{m_i} \right)^{s-1} = n_0 p^{(1-s)i} \quad (2.10)$$

Since the total mass of grains must be equal to the meteoroid mass,

$$m_f = \sum_{i=0}^k n_i m_i = n_0 m_0 \sum_{i=0}^k p^{(2-s)i} \quad (2.11)$$

The number of grains in the largest mass bin is

$$n_0 = \frac{m_f}{m_0(k+1)} \quad (2.12)$$

for $s = 2$ and

$$n_0 = \frac{m_f}{m_0} \frac{1 - p^{(2-s)}}{1 - p^{(2-s)(k+1)}} \quad (2.13)$$

for $s \in 2$.

This technique of distributing grains in bins can be used when the mass distribution index is known. To evaluate the mass index for the broad search, we used the work of Murray and Beech along with the observed F-parameter for each meteor lightcurve (see Fleming et al., 1993, Murray et al., 2000, Koten et al. 2006, Koten et al. 2007). The F-parameter describes the shape of the lightcurve and is defined as the ratio of the distance from the beginning of the lightcurve to the point of maximum brightness and the entire length of the lightcurve, beginning and ending at a magnitude ΔM fainter than the peak given numerically as:

$$F_{\Delta M} = \frac{H_{B\Delta M} - H_{max}}{H_{B\Delta M} - H_{E\Delta M}} \quad (2.14)$$

where ΔM is usually one of 0.25, 0.5, 0.75, 1.00, ..., 2.5, 2.75, 3.0. $H_{B\Delta M}$ and $H_{E\Delta M}$ are heights where the meteor brightness is equal to $M_{max} + \Delta M$ and M_{max} is the maximum brightness. We calculated the F-values at $\Delta M = 0.75$ ($F_{0.75}$). Lightcurves for which $F = 0.5$ are perfectly symmetrical, with the maximum exactly in the middle of the trajectory. Meteors with $F < 0.5$ reach their maximum brightness during the early part of the trajectory, while $F > 0.5$ gives a lightcurve skewed toward the terminal point (Koten et al., 2006). Koten et al. (2006) suggested that single-body meteors described by classical meteor theory should have $F \gg 0.7$; for the dust-ball model F is expected to be nearly 0.5 (symmetrical lightcurves) (Hawkes & Jones 1975).

For our meteor case study (meteor 20060503-091349), $H_{B0.75}$ and $H_{E0.75}$ were respectively 108.1 km and 103.5 km, and H_{max} was 104.9 km, giving $F_{0.75} = 0.67$. The mass distribution index was found to be 2.80, based on the work of Beech and Murray. The photometric mass of 7.65×10^{-6} kg was distributed in bins, with upper and lower mass bins of $m_u = 1.4 \times 10^{-10}$ and $m_l = 6.6 \times 10^{-11}$ kg [the latter is close to the lowest mass grain capable of ablating, about 10^{-12} kg (see Jones and Kaiser, 1966)]. Using equation (2.8) and equation (2.13), the total observed photometric

Table 2.7: Grain mass distribution for meteor 20060503-091349 at broad search

number of grains	mass of each grain (kg)
39278	6.60×10^{-11}
15358	1.11×10^{-10}
10146	1.40×10^{-10}

mass was distributed in three bins (see table 2.7).

Using this mass grain distribution and the range of values for each free parameter as previously described, we computed about one hundred thousand solutions, and compared the computed lightcurve and deceleration with the observed lightcurve (figure 2.18) and deceleration (figure 2.11) for our example meteor test case. After the broad search, figure (2.20) gives the distribution of all solutions with $\chi^2 < 1$, showing local minima around densities of 680 kg m^{-3} , 920 kg m^{-3} and 1220 kg m^{-3} for meteor 20060503-091349.

Since all local minima are grouped within an interval of density less than 800 kg m^{-3} , we grouped them all together. We selected the solution having reduced χ^2 closest to 1 both on lightcurve and deceleration as the starting point for the refined search. For the case where local minima are spread over more than 1000 kg m^{-3} , each of them is examined until all but one are eliminated on the basis of physical inconsistencies particularly the boiling temperature being lower than the fragmentation temperature.

After the broad search, the solution for meteor 20060503-091349 with χ^2 closest to 1 both on the lightcurve and the deceleration had a density value of 920 kg m^{-3} . The values found for the other free parameters for the test solution (solution for meteor 20060503-091349) are summarized in the table (2.8).

Refined search

Once the broad search defined a best fit interval, we refined the solution. At this stage, we worked manually on the best solution found during the broad search.

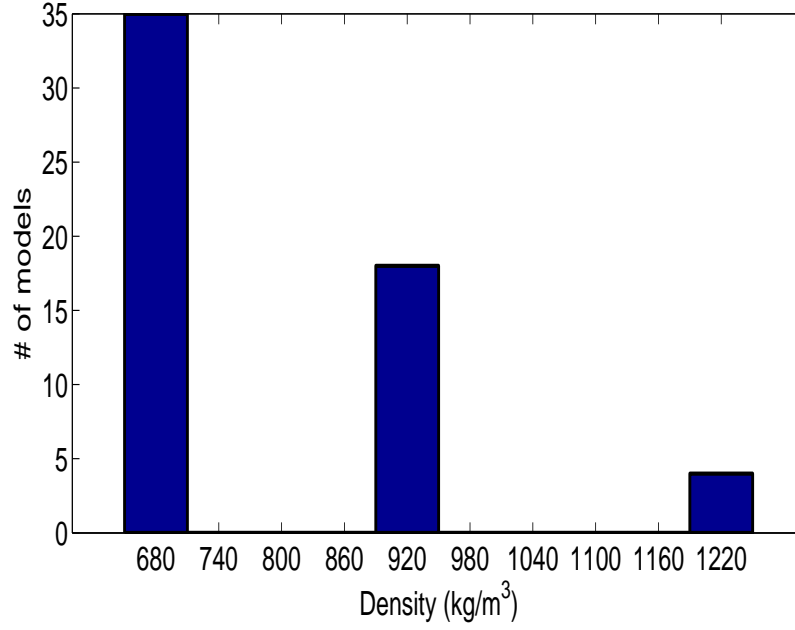


Figure 2.20: All solutions with $\chi^2 < 1$ after the broad search.

Table 2.8: Values of free parameters for the best fit to the lightcurve and the deceleration for meteor 20060503-091349 found in the broad search

Free parameter	Value
Heat of ablation	9.0 ± 10^6 J/kg
T _{lim}	1000 K
T _{boil}	1800 K
Specific heat	$1000 \text{ J kg}^{-1} \text{ K}^{-1}$
Molar mass	36 atomic unit
Thermal Conduct	$0.5 (\text{J m}^{-1} \text{ s}^{-1} \text{ K}^{-1} \text{ or } \text{W m}^{-1} \text{ K}^{-1})$

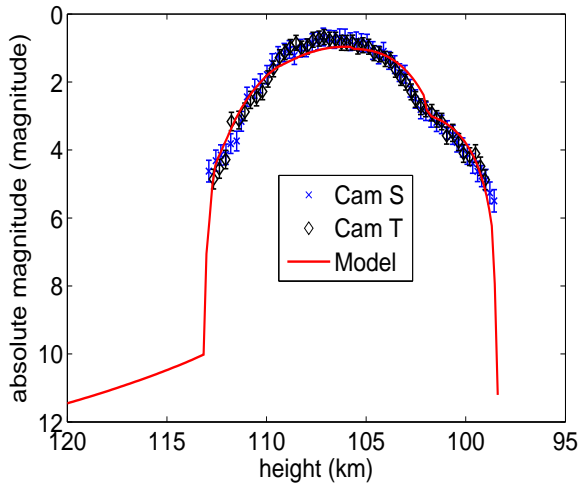


Figure 2.21: The best lightcurve fit for the meteor 20060503-091349.

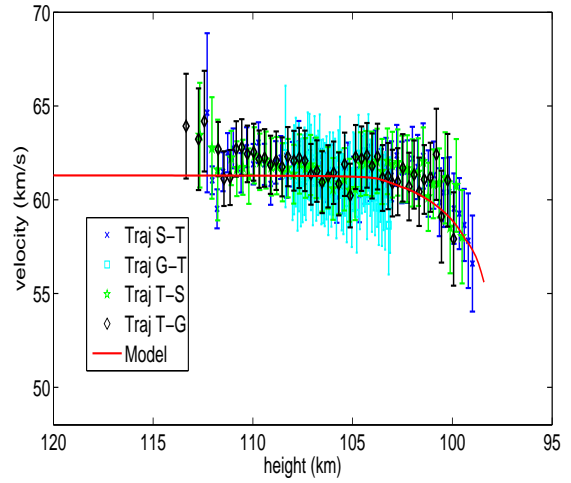


Figure 2.22: The best deceleration fit for the meteor 20060503-091349.

Table 2.9: Grain mass distribution for meteor 20060503-091349 after manual adjustment in the refined search stage. This is taken as the final mass distribution

number of grains	mass of each grain (kg)
75767	$0.93 \text{ } \mathcal{E} \text{ } 10^{-11}$
55130	$1.11 \text{ } \mathcal{E} \text{ } 10^{-10}$
1198	$1.15 \text{ } \mathcal{E} \text{ } 10^{-09}$

We manually modified the mass grain distribution of the meteoroid and slightly perturbed the other free parameters until the modeled lightcurve and deceleration fit the observed lightcurve and deceleration (the reduced χ^2 should be less than 1 and four fifth of the points overlap in the model solution both for the lightcurve and the deceleration within error). We have an advantage over the usual meteor modelling method, since the time spent in trial and error is greatly reduced by starting with a good solution; also, we have ruled out other local minima which the usual trial and error method might miss and not mention.

For meteor 20060503-091349, the best solution is given in figures 2.21 for the lightcurve and 2.22 for the deceleration. The best final mass grain distribution is given in table 2.9. The corresponding final best estimate of density is 970 kg m^{-3} , and the values of other free parameters are given in table 2.10.

Table 2.10: Values of free parameters from the best solution for meteor 20060503-091349 after manual adjustment in the refined search stage.

Free parameter	Value
Heat of ablation	6.5×10^6 J/kg
T _{lim}	930 K
T _{boil}	1900 K
Specific heat	1400 J/kg K
Molar mass	36 atomic unit
Thermal Conduct	0.5 (J/m s K or W/m K)

The last step of our investigation is to use the final mass grain distribution from the refined search for a new, higher resolution search over the entire free parameter space: the step size in density is reduced to 100 kg m^{-3} . All solutions are sorted by reduced χ^2 , and those solutions which have $\chi^2 < 1$ simultaneously on lightcurve and deceleration are possible physical descriptions of the meteoroid.

The density distribution of meteor 20060503-091349 (figure 2.23) suggests that the lowest possible density is 570 kg m^{-3} , and the highest is 1170 kg m^{-3} . We write that meteor 20060503-091349 had a density of $970_{-400}^{+200} \text{ kg m}^{-3}$ (970 kg m^{-3} is the best solution, meaning that his χ_c^2 value is the closest to 1). As an aside, if the saturation correction had not been applied to the light curve, meteor 20060503-091349 would have a calculated density of $480_{-130}^{+170} \text{ kg m}^{-3}$, significantly different (figure 2.24). The heliocentric meteoroid orbits were computed using the methods of Ceplecha (Ceplecha, 1987). The results are summarized in table 2.11.

The final step is to compare the density found to the orbital parameters. The calculation of the Tisserand parameter gives an idea about the origin of the meteoroid and suggests clues as to its chemical composition. This is discussed in more detail in chapters 3 and 5.

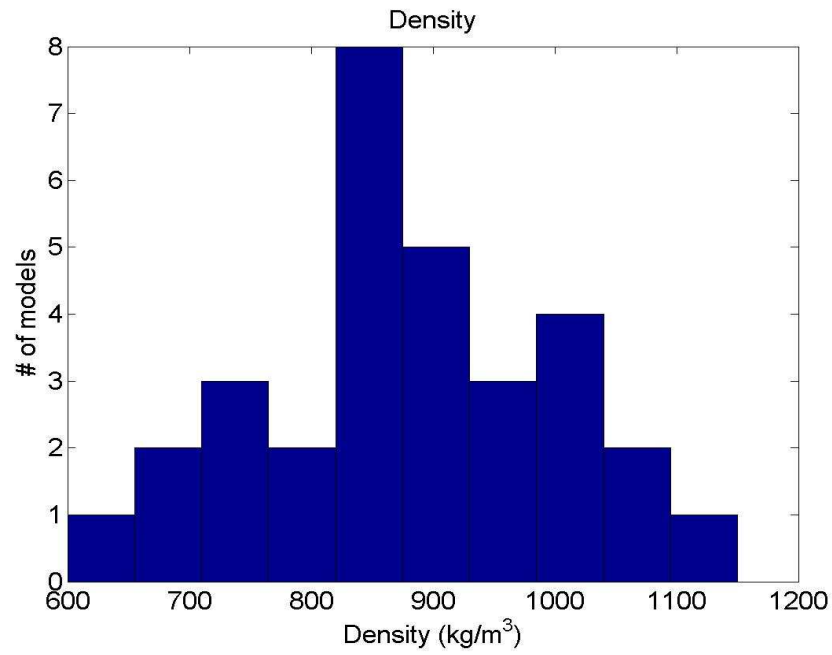


Figure 2.23: The density distribution of meteor 20060503-091349. The best solution is 970_{-200}^{+400} kg m⁻³.

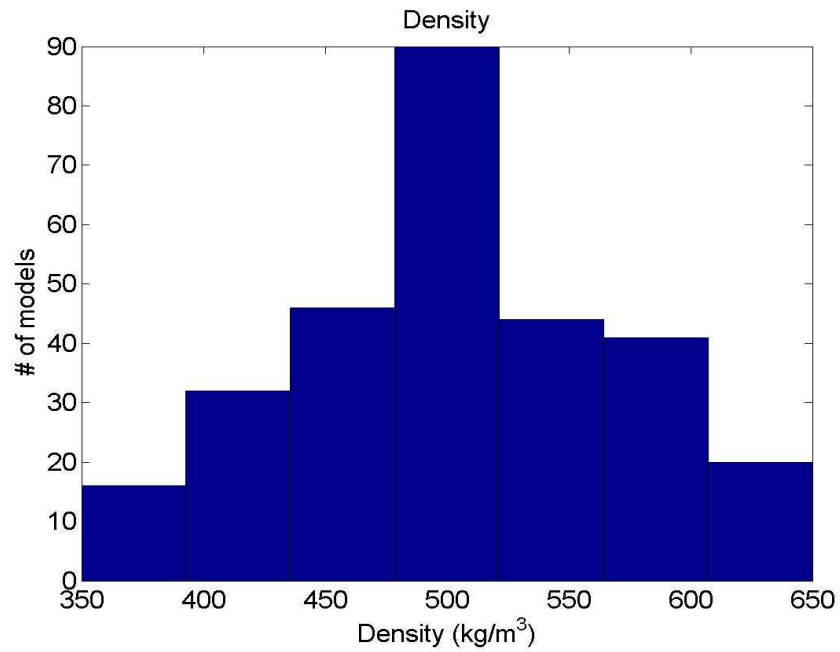


Figure 2.24: The density distribution of meteor 20060503-091349 when no saturation correction is applied to the light curve. The best solution is 480_{-350}^{+650} kg m⁻³.

Table 2.11: Properties of meteoroid 20060503-091349, according to our ablation model. Maximum height refers to the height of maximum brightness. Angular elements are J2000.0 (uncertainties on $\cos Z$ and Q are not reported because these two values are considered to be precised measurements).

		Value
Date (UTC)(YYYYMMDD:HH:MM:SS)		20060503:09:13:49
Observed photometric mass (kg)		(7.65 § 0.02) £ 10 ⁻⁶
Observed peak magnitude (magnitude)		+0.86 § 0.26
Perihelion (AU)	q	0.308 § 0.002
Aphelion (AU)	Q	22.492 § 2.383
Semi-major axis (AU)	a	11.400 § 1.192
Eccentricity	e	0.973 § 0.003
Inclination (±)	i	139.160 § 0.222
Argument of periapsis (±)	ω	114.127 § 0.366
Longitude of the ascending node (±)	Ω	222.725 § 0.000
Velocity (geocentric)(km s ⁻¹)	V_g	60.111 § 0.102
Velocity (helion) (km s ⁻¹)	V_h	41.015 § 0.099
Velocity (infinity) (km s ⁻¹)	V_∞	61.30 § 0.99
Beginning height (km)	H_{beg}	112.90 § 0.11
Maximum height (km)	H_{max}	104.95 § 0.29
Ending height (km)	H_{end}	98.57 § 0.20
Average Range (km)	$Range_{avg}$	122.77 § 0.53
Radiant Right asc (geocentric) (±)	α_{geo}	278.005 § 0.105
Radiant Declination (geocentric) (±)	δ_{geo}	i 37.762 § 0.083
cos zenithal angle	COSZR	0.277
Angle of intercept (±)	Q	20.6
Tisserand Parameter	T_j	i 0.059 § 0.085

Bibliography

- [1] Babadzhanov, P. B. 2002, *A&A*, 384, 317
- [2] Bellot Rubio, L. R., Martinez Gonzalez, M. J., Ruiz Herrera, L., et al. 2002, *A&A*, 389, 680
- [3] Borovicka, J. 1990, *Bull. Astr. Inst. Czechosl.*, 41, 391
- [4] Borovicka, J. 2005, *Asteroids, Comets, and Meteors*. (eds. D.Lazzaro, S. Ferraz-Mello, J.A. Fernandez), Cambridge Univ. Press., *Proceedings IAU Symposium No.* 229, 249
- [5] Borovicka, J., Kotten, P., Spurny, P., et al. 2005, *Icarus*, 174, 15
- [6] Borovicka, J., Spurny, P., & Kotten, P. 2007, *A&A*, 473, 661
- [7] Campbell-Brown, M. D., & Koschney, D. 2004, *A&A*, 418, 751
- [8] Campbell-Brown, M. D., Close, S. 2007, *MNRAS*, 382, 1309
- [9] Ceplecha, Z. 1987, *BAICz*, 38, 222
- [10] Ceplecha, Z., Borovicka, J., Elford, W. G., et al. 1998, *Space Science Rev.*, 84, 327
- [11] Ceplecha, Z., Borovicka, J., & Spurny, P. 2000, *A&A*, 357, 1115
- [12] Fleming, D., Hawkes, R. L., Jones, J. 1993, *Meteoroids and their Parent Bodies*, 261

- [13] Hawkes, R. L., & Jones, J. 1975, MNRAS, 173, 339
- [14] Hawkes, R. L., & Jones, J. 1978, MNRAS, 185, 727
- [15] Hawkes, R. L., & Jones, J. 1986, QJR, Astron. Soc., 27, 569
- [16] Hawkes, R. L., Bussey, J. E., Macphee, S. L., et al. 2001, in Warmbein B., ed., Proc. Meteoroids 2001 Conference., ESA Publications, Noordwijk, 281
- [17] Hawkes, R. L. 2002, *Meteors in the Earth's atmosphere*, Cambridge Univ. Press, Cambridge, 97
- [18] Hedin, A. 1991, J. Geophys. Res., 96, 1154
- [19] Howell, B. H. 2000, *Handbook of CCD Astronomy*, Cambridge Univ. Press, Cambridge
- [20] Jacchia, L.G. 1957, AJ, 62, 358
- [21] Jacchia, L. G., & Whipple, F. L. 1961, SCoA, 4, 97
- [22] Jacchia, L. G., Verniani, F., Briggs, R. E. 1967a, *Smithsonian Contr. Astrophys.*, 10, 1
- [23] Jacchia, L. G., Verniani, F., Briggs, R. E. 1967b, *Smithsonian Contr. Astrophys.*, 11, 1
- [24] Jones, J., & Hawkes, R. L. 1975, MNRAS, 171, 159
- [25] Kikwaya, J. B., Campbell-Brown, M. D., Brown, P. G., et al. 2009, A&A, 497, 851
- [26] Kikwaya, J. B., Weryk, R. J., Campbell-Brown, M. D., et al. 2010, MNRAS, 404, 387
- [27] Koten, P., Borovicka, J., Spurny, P., et al. 2004, A&A, 428, 683

- [28] Koten, P., Spurny, P., Borovicka, J., et al. 2006, M&PS, 41, 1271
- [29] Koten, P., Borovicka, J., Spurny, P., et al. 2007, A&A, 466, 729
- [30] Murray, I. S., Beech, M., Taylor, M. J., et al. 2000, EM&P, 82/83, 351
- [31] Murray, I., Beech, M., Taylor, M., et al. 2000, EM&P, 82/83, 351
- [32] Myers, J. R., Sande, C. B., Miller, A. C., et al. 2001, Sky 2000 Catalog v4, Goddard Space Flight Center, Ycat 5109
- [33] Romanishin, W. 2001, *An Introduction to Astronomical Photometry Using CCDs.*, University of Oklahoma, 175p.
- [34] Seidelmann, P. K., & Urban, S. E. 2010, AAS, 42, 522
- [35] Whipple, F. L. 1938, Proc. Amer. Phil. Soc., 79, 499

Chapter 3

Physical characteristics of very small meteoroids

Originally published as:

Kikwaya, J.B., Campbell-Brown, M.D., Brown, P.G., Hawkes, R.L.; Weryk, R.J. (2009), Physical characteristic of very small meteoroids, *Astronomy and Astrophysics*, **497**, 851-867.

3.1 Introduction

An important physical property of meteoroids is their density. Knowing it can help determine the physical structure and potentially the chemical composition of their parent bodies. However, determining meteoroid density is not an easy task. It might be easy to find the density of a solid, uniform sphere ablating in the atmosphere (assuming the body enters the atmosphere as a solid with a spherical shape, ablates uniformly, and remains a single solid body during the whole of its flight), but ablation modeling is complicated by the fact that meteoroids fragment and have unknown shapes, structures, and chemical compositions.

When a meteoroid comes into contact with the earth's atmosphere, it ablates and generates electromagnetic radiation, including visible light. The height of ablation is influenced by many factors, including the entry angle, the speed of the meteoroid, its mass, the energy required to ablate the material of which it is composed, its boiling point, its structure, and its bulk density (Campbell-Brown and Koschny, 2004).

It has long been known that the ablation behaviour among meteoroids differs considerably. These differences are reflected in different beginning heights, lightcurve shapes and, for larger meteoroids, in end height differences for meteoroids of similar speed and mass (see Ceplecha et al. 1998 for a complete discussion). It has long been assumed that these differences have to do with the physical characteristics of each meteoroid, including its composition, structure, bulk density and size: for example Koten et al. (2004) used the lightcurves and heights of video meteors to find significant differences among meteors from major showers. They argue that this suggests the parent bodies have different chemical compositions or physical structure.

The interpretation of all of these data is substantially complicated by the process of fragmentation. Besides the question of whether or not small meteoroids undergo fragmentation, the process of fragmentation itself remains an open question. Does

fragmentation occur before the onset of, or during rapid vaporization? Does it happen at a critical temperature or a critical pressure?

Campbell et al. (2000) argued that fragmentation occurs before the process of ablation starts. Only after grains have been released from the main mass do they undergo intensive ablation. This is consistent with the dustball meteoroid model (Hawkes and Jones, 1975), in which meteoric bodies are assumed to be composed of grains held together by a lower boiling point ‘glue’: when the binding melts, the grains are released. Further support for the dustball model comes from the weak dependence of the beginning height, maximum height and trail length of the visible meteor on the mass of the meteoroid, as found in studies by Campbell et al. (2000), Koten et al. (2004), Hapgood et al. (1982) (for Perseids fainter than $Mv = 0$) and Beech (1986) (for Draconid meteors). The dustball model predicts that grains of different masses which are ejected from the meteoroid will decelerate at different rates, producing physical wake from the spread in the grains. Fisher et al. (2000) confirmed that half of the video meteors they investigated showed this wake when observed with short effective exposures.

Clearly, the mechanism of fragmentation for meteoroids is complex and much of contemporary meteoroid ablation modelling concentrates on attempting to formalize the process. Campbell-Brown and Koschny (2004) suggested that fragmentation occurs when the temperature of the surface is high enough to disrupt the binding matrix of the meteoroid; the top layer of the meteoroid (to a depth determined by the assumed thermal conductivity) is released all at once.

In a study of six Draconid meteors for which deceleration and photometric measurements were available for the first time, Borovicka et al. (2007) suggested that grain separation started after the surface of the meteoroid received a certain energy flux, calculated to be 10^6 J m^{-2} ; this is physically equivalent to requiring the surface to reach a particular temperature. The meteoroid then gradually fragments into grains over the first half of its trajectory, a process Borovicka et al. (2007) call

thermal erosion. Meteoroids resistant to this process may disrupt at low dynamic pressures.

Beech and Murray (2003) used the dustball model to generate synthetic Leonid lightcurves. They matched different shapes of lightcurves to synthetic lightcurves generated by a power law distribution of grains, from 10^{-10} kg up to 10% of the total mass (which was taken to be 10^{-6} kg), varying the mass distribution index between 1.0 to 2.0. They suggested that the 1999 Leonid meteoroids were relatively rich in larger-mass fundamental grains.

While several studies of the overall physical structure of meteoroids have produced qualitative support for the dustball model, quantitative measurements of the bulk density of meteoroids are more difficult to make, again due to the variety of ways fragmentation may be handled in modelling. Ceplecha (1968) calculated the density of small meteoroids and classified them into four categories (A,B,C,D) based on a parameter, K_B , which depends on the atmospheric density at the beginning of the luminous trajectory, the initial velocity and the elevation of the radiant. Categories A through D were attributed to meteoroids having densities from 2700 to 180 kg m^{-3} .

Babadzhanov (2002) examined 413 photographic super-schmidt meteors and applied a model which assumed quasi-continuous fragmentation (QCF). They found meteoroid densities between 400 kg m^{-3} and 7800 kg m^{-3} . Bellot Rubio et al. (2002) questioned the validity of these high densities for small meteoroids. They singled out two questionable assumptions which led Babadzhanov (2002) to these results. The first is the fact that QCF is based essentially on fitting a model to the lightcurve, without taking into consideration the dynamical properties of the meteoroids, particularly the deceleration. The second was that the specific energy of fragmentation used by Babadzhanov (2002) was underestimated by at least a factor of 10. Bellot Rubio points out that, with such a small heat of fragmentation, the meteoroid will always fragment before reaching the “real” heat of ablation. Analyz-

ing the same meteors using the single body theory (assuming none of the meteoroids fragment), Bellot Rubio et al. (2002) found densities ranging from 400 kg m^{-3} to 4800 kg m^{-3} . Since the characteristics of fragmentation are often observed in the lightcurves of small meteoroids as transient increases in brightness (including in the sample analysed by Bellot-Rubio et al. (2002)), Borovicka (2005) pointed out that this is a shortcoming of Bellot Rubio's work. Clearly, the lightcurves of meteoroids should be fit with a model that takes into account the dynamical properties of the meteoroids.

In this work, we adopt the dustball model as a first approximation to the physical structure of a meteoroid. We use the numerical model of ablation developed by Campbell-Brown and Koschny (2004). This model is applied to high resolution measurements of lightcurves and astrometry for a suite of faint meteors observed from two stations. In particular, our measurement precision is high enough to allow routine observation of deceleration for faint (magnitude $+7$) meteors. This particular model uses eight free parameters to produce a theoretical lightcurve, and allows the velocity to vary with height along the meteoroid trajectory. We explore the solution space of all possible parameters and compute for each meteor hundreds of thousands of solutions whose lightcurves and decelerations are then compared to those observed. We find density limits for each meteor within which a solution can be found; from the number of solutions at each modeled density, we get a statistical measure of the density for each meteoroid and a measure of its error.

3.2 Observations and Equipment

Data were collected during two different observing runs; one over three nights in Canada in May 2004, and one over seven nights in Sweden in October 2007. Second generation (Gen II) Litton microchannel plate image intensifiers with S-20 spectral response were used. Gen II intensifiers have a spectral response from 340 - 870

nm and have less sensitivity in the red, and shorter tube lifetimes, than Gen III intensifiers but are otherwise comparable. They are significantly more sensitive than Gen I intensifiers, and less susceptible to blooming when imaging bright point objects. Gen II intensifiers were used simply because they were simpler to integrate with the large lenses used in these campaigns. We used catadioptric lenses with 155 mm focal length and $f/0.75$ for both stations.

In the first campaign, two Deep Gen II cameras were installed at two different sites, which we call Elginfield Observatory ($43^{\circ} 11' N$, $81^{\circ} 18'90 W$) and the Silo site ($43^{\circ} 12'23 N$, $81^{\circ} 22'62 W$). The baseline between the two stations is 5.5 km and the cameras were pointed at the zenith, in order to cover a very large common volume of the sky. The baseline is much shorter than that typically used in video meteor observations, where cameras with fields of view (FOV) of 25 to 40 degrees are separated by 30 to 60 km. This short baseline for our cameras, with their fields of view of 6 degrees, was motivated by the desire to maximize the number of two-station meteors completely observed by maximizing the common volume observed by the cameras: this also minimizes the height bias of the system. A longer baseline improves the precision, but produces almost no useful two station meteors, as seen by the results in the second campaign. The computation of different height precisions from different baseline values for two different camera FOVs shows that the deep GenII with a FOV of 6 degrees, a baseline of 5.5 km and resolution of 0.008 degrees per pixel produces a height precision within 10% of that obtained with a baseline of 45.5 km and a typical LLLTV resolution of 0.054 degrees per pixel corresponding to a FOV of 35 degrees. Recognizing that the height errors alone are not the only uncertainty and that geometry comes into play in the trajectory solution, we examined all four events in detail from the short baseline campaign and introduced typical meteor measurement errors (of order 1 pixel) to all measured points in a monte carlo simulation run 10000 times. We find that in average the radiant error is 1.6 degrees; the height error 0.6 km and the velocity error 0.8 km/s.

This demonstrates that the shorter baseline is compensated by the higher resolution in terms of overall trajectory precision relative to typical LLLTV baselines.

In the second campaign, cameras were placed at Peera in Finland ($68^{\circ} 53'39$ N, $21^{\circ} 3'34$ E) and at Kiruna in Sweden ($67^{\circ} 51'60$ N, $20^{\circ} 25'98$ E). The baseline between the two stations is 117 km. The main purpose of the second campaign was to look for simultaneous events with the EISCAT tristatic radar, so the geometry was not optimal for our purposes, but some of the data are still useful for this study.

The field of view of the images was $5.4^{\circ} \times 4.1^{\circ}$. The pixel dimensions of the video system are 720x480 pixels, producing a resolution of $\approx 30''/\text{pixel}$.

For a meteor 100 km from the camera, the systems had a resolution of ≈ 13 meters per pixel with the full field of view being equivalent to linear dimensions of 9.5×7.1 km. We find that this is sufficient resolution at our small meteoroid sizes to show even very small decelerations. We used the CCD in an interlaced mode with 60 video fields (or 30 video frames) per second. The limiting stellar magnitude of the video camera system was around +11 per field.

3.3 Data and Analysis

In the first run in London Ontario (Canada), we detected a total of 17 meteors in almost 18 hours, where 13 were simultaneous on both cameras. In the second run in October 2007, 35 meteors in 49 hours were detected and among them, 29 were simultaneously seen on both stations. We examined data for each simultaneous meteor, took the time the event occurred and checked if the meteor ended on the field of view of at least one of the two stations. The end of the trail is particularly critical, since most of the deceleration occurs at the end of a meteor's trajectory. We add to this criterion the requirement that the event should start in the field of view of at least one station as this gives a complete lightcurve for better estimation of the photometric mass of the meteor.

Most of the meteors, as seen from both sites, either started in the field of view but ended outside, or started outside and ended in the field of view of one camera (Figure 3.1 and Figure 3.2). Some completely crossed the field of view (Figure 3.3). Some even crossed the entire field of view in just one frame, making it virtually impossible to get an astrometric solution. All these meteors failed to satisfy our two criteria and were eliminated. Among the 13 meteors seen simultaneously on both sites in the first observing run, only four satisfied the conditions of starting and ending in the field of view of at least one of the two cameras. From the second observing run, with the narrow field of view and the long baseline between the two stations, only two of the 29 simultaneous meteors satisfied the criteria and were selected.

The astrometric positions of meteors are calibrated using the stars in the field of view. The pixel locations of the stars are found using a centre-of-mass algorithm, and are compared against the SKY2000v4 catalogue (Myers et al. 2001). The right ascension and declination are converted into local zenith and azimuth angles (the camera is fixed to that reference frame). A third order linear least squares fit is used; however, in order to fit a frame close to or including the zenith, rotation is used to re-reference each point so that no singularities occur. All of the star coordinates are referenced about the centre of the frame. After this, they are projected onto an xy plane, and then fitted against the pixel locations. While a second order fit may be adequate, a third order fit allows for better lens distortion corrections. Errors in the resulting fit are calculated based on the angular separation between the catalogue and fitted coordinates, so that each star has a single error associated with it. This is more meaningful than quoting separate errors for azimuth and zenith angles, since azimuth error is dependent on the zenith angle. On the GenII systems used in this study, typical errors of 0.002 degrees are found, which corresponds according to our resolution to ≈ 0.3 pixels.

The meteor positions are manually measured by selecting a point on the leading

edge of the meteor. We find that selecting positions manually will result in errors (due to lack of sub-pixel precision) of order 1-2 pixels; this is the dominant source of error in our measurements.

After each frame has been flat fielded, the photometric magnitudes are computed by a log-sum-pixel approach with background subtraction (see Hawkes, 2002). That is, each star has a defined disc covering the whole star and a surrounding ring representing the background. The median value in the ring is subtracted from the disc (taking into account pixel areas), and the magnitude of the star is computed as the logarithm of the sum of the pixel intensities in the disc. A typical error of 0.1-0.2 magnitudes is found for each star. For all the stars in the image, a linear fit relates these magnitudes against catalogue visual magnitudes (from SKY2000v4 (Myers et al. 2001)). Because the magnitude base is fixed, the slope value of this fit is fixed at unity, and the offset determines the calibration.

The photometric mass is found using the standard integral of the lightcurve (see Hawkes, 2002 for details). Here we use value for the luminous efficiency related to velocity from the study by Hill (Hill et al. 2005).

Photometric errors are determined using standard error techniques, where the standard deviation of the photon count is governed by Poisson statistics. This gives an error in the photometric magnitude of $2.5/\sqrt{N}$ (where N is the pixel intensity sum, proportional to the number of photons), to which the error from the photometric calibration is added.

We used code from Borovicka (1990) called Milig to compute the in-atmosphere trajectory of all simultaneous meteors, providing the distance, the velocity and also the height of the meteor versus time along the trajectory. Once the trajectory line has been identified, the velocity can be computed from each station for each pair of points on the trajectory. Small errors in the determined position of the meteor in each frame will produce large random errors on the velocity at each point. In order to reduce this noise on the measurement of velocity versus time (or height), we



Figure 3.1: Meteor captured in Kiruna (Sweden) on October 11 2007 at 02:55:32 UTC.



Figure 3.2: Meteor captured in Kiruna (Sweden) on October 09 2007 at 01:37:25 UTC.



Figure 3.3: Meteor captured in Kiruna (Sweden) on October 06 2007 at 01:54:42 UTC crossing the entire field of view

use a filtering technique which consists of calculating the speed using every third or fourth point instead of every point in the original measurements (Figure 3.4). The meteor clearly shows deceleration (Figure 3.5) and the good agreement between the velocities from each site indicates the solution is robust.

To find the approximate initial, out-of-atmosphere velocity, which is needed as initial input into our model, we make use of the fact that the image resolution of our systems is similar to that of the Super-Schmidt photographic meteors. Following Whipple and Jacchia (1957) the pre-atmospheric velocity of the meteoroid was computed following the empirical expression he suggested relating distance (D) to time (t) (equation 3.1).

$$D = A + Bt + Ce^{kt} \quad (3.1)$$

The velocity at any time can be found from the time derivative of the expres-

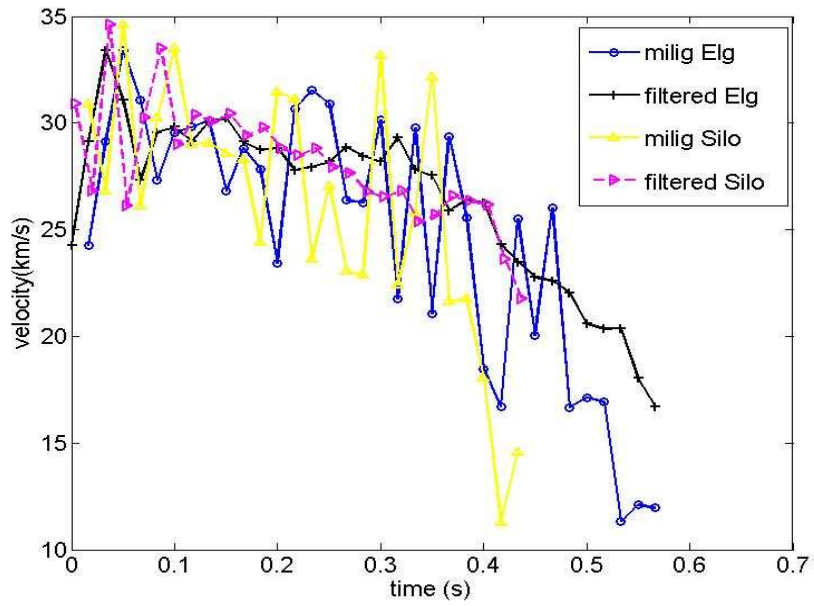


Figure 3.4: An example showing the velocity of a meteor before and after the filtering (smoothing) technique.

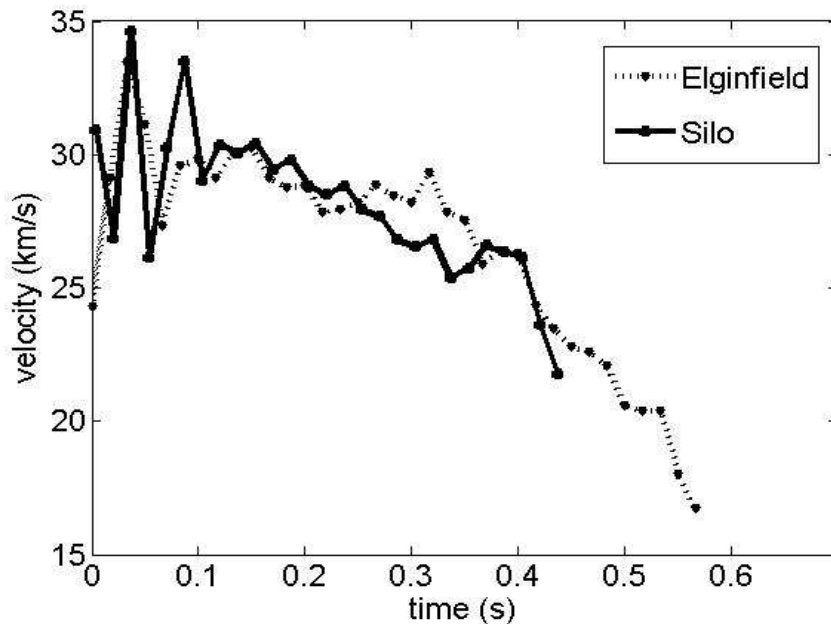


Figure 3.5: The velocity of meteor ELSL11 as measured from both sites along its trajectory.

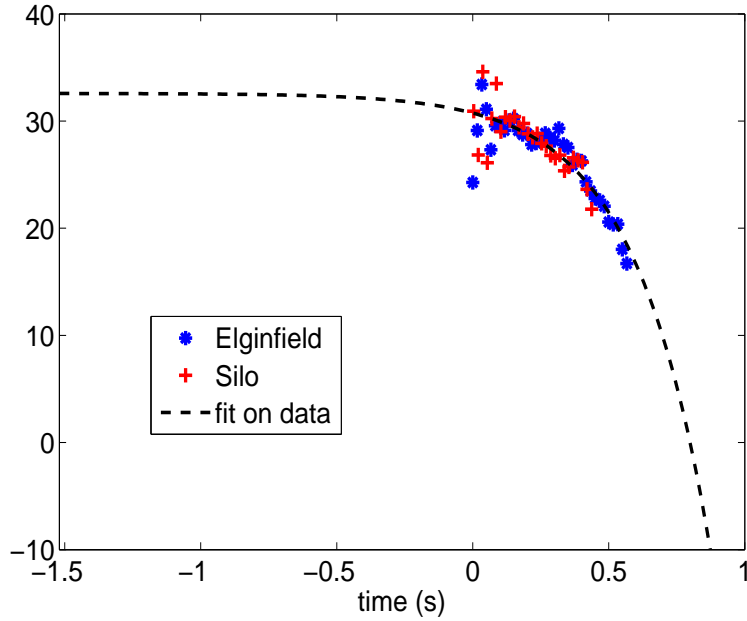


Figure 3.6: Velocity of meteor ELSL11 from both sites along its trajectory.

sion, equation 3.2. The pre-atmospheric velocity can be found by evaluating the expression with t set to minus infinity. The second derivative of equation 3.1 gives the deceleration, and k is the slope of the logarithm of the deceleration. When k is known, B and C can be determined by the method of least squares. The velocity approaches the pre-atmospheric velocity asymptotically as t approaches minus infinity; the error in the fit can be estimated from the error in the fit parameter (Figure 3.6).

$$\frac{dD}{dt} = B + Cke^{kt} \quad (3.2)$$

From the positional measurements at each station, the pre-atmospheric velocity and the radiant were computed according to Borovicka (1990), while the heliocentric meteoroid orbits were computed using the methods of Ceplecha (1987). We note that, due to the geometry used, the meteors captured during the Swedish campaign have relatively greater uncertainty in their solutions due the fact of having only a

few measured points for the entire trajectory.

3.4 Ablation Model

In our work, we use the dustball model of Campbell-Brown and Koschny (2004). Where the traditional dustball model suggests that the light production starts as soon as the small grains are all released, the heating of the meteoroid, modeled through Clausius-Clapeyron formalism by Campbell-Brown and Koschny, allows one to consider ablation even before the boiling temperature is reached. The dustball model of Campbell-Brown and Koschny allows the user to enter any number of grains and their masses, without necessarily assuming a power law distribution. This is a considerable advantage, since the computing time may be reduced significantly by representing a distribution of grain sizes as a small number of distinct sizes.

The model considers three sources of energy: energy imparted to the meteoroid by collisions with atmospheric atoms, the energy lost from the meteoroid by radiation, and the energy lost through evaporation of the meteor material. The mass loss is calculated using the Knudsen-Langmuir formula, combined with the Clausius-Clapeyron equation. A term proportional to kinetic energy transfer, like the classical formula, is also added to simulate spallation when the meteoroid is very hot. For more details the ablation model itself, see Campbell-Brown and Koschny (2004).

3.5 Results

For each meteor, we extracted the velocity and the radiant using the trajectory code of Borovicka (1990). We extracted the lightcurve of each of the six meteors with complete lightcurves. No correction for photometric saturation was needed since none of these six meteors were bright enough to have any saturated pixels. We applied our ablation model to simultaneously fit the observed lightcurve and deceleration.

Among the parameters used in the model, we have chosen some to remain fixed and some to remain free. Fixed parameters include the fusion point of the meteoroid grains, which is taken to be 100 K less than the boiling point of the meteoroid grains (the boiling temperature remains free); the condensation coefficient ψ , which is fixed to 0.5 (condensation coefficient of stone), the emissivity of the meteoroid (fixed to 0.9), and the atmospheric density, provided by the MSISE 90 model (Hedin, 1991).

To fit the observed decelerations and lightcurves, using the model output we search the entire free parameter space for each meteor. This first stage in the solution procedure helps to identify the regions in which solutions are concentrated. The main difficulty with this approach is the grain distribution; while the number of solutions covering a reasonable range of each of the other free parameters is merely prohibitive, the number of possible grain distributions is essentially infinite. As a first approximation, we have chosen to represent each meteor at this step as a collection of grains all having the same size. For each meteoroid, we chose masses of grains (from the smallest grains which will still ablate independently to the total meteoroid mass), and fixed the number of those grains so that the total mass of the meteoroid corresponded to the total photometric mass of the meteor. The shape of the lightcurves found in this way will almost certainly be wrong, but as we get close to a good solution, we expect one of the grain sizes will produce a curve with significant overlap to the measured lightcurve.

We extract from each solution set the best model fit, which we define here to mean the one with the smallest χ^2 value (the χ^2 here is the standard one where the smallest number indicates the best fit). We allow the theoretical lightcurve and the measured lightcurve to have one fourth of points which do not overlap to within the measured error margins. At this stage, for each of these potential solutions, we adjust the mass and number of grains by hand in order to find the best fit to the observed lightcurve and deceleration.

3.5.1 Free parameters

The free parameters used in our ablation model include:

- ² grain mass (to which the number of grains is tied)
- ² density of the meteoroid
- ² the heat of ablation (T_{lim})
- ² the boiling point of the meteoroid grains (T_{boil})
- ² the temperature at which the grains are released
- ² the specific heat (C_p)
- ² the average molar mass of meteoroid material
- ² the thermal conductivity of the meteoroid

Our methodology is as follows:

First, we allow the density to vary from 500 kg m^{-3} (very porous carbonaceous materials) to 8000 kg m^{-3} (iron meteoroid). We used seven steps in the density. The heat of ablation is of the order of 10^6 J kg^{-1} (see Ceplecha et al., 1998). The actual value depends on the composition of the meteoroid. Babadzhanov(2002) used $2.8 \times 10^5 \text{ J kg}^{-1}$ while Bellot Rubio et al (2002) thought that it should be around $8 \times 10^6 \text{ J kg}^{-1}$. Following Bellot Rubio et al. (2002), we allow the heat of ablation to range from 2×10^6 to $9 \times 10^6 \text{ J kg}^{-1}$.

Physically, the fragmentation temperature (T_{lim}) must be less than the boiling temperature (T_{boil}), otherwise the grains will ablate before they separate. Knowing that iron (the densest element we expect to encounter as a major element in the composition of the meteoroid) reaches its boiling temperature around 2000 K, we choose fragmentation temperatures ranging from 900 K to 1600 K, and set the boiling temperature to vary between 1400 K to 2300 K.

The thermal conductivity is expected to be small considering the physics of small meteoroids with considerable porosity (Campbell-Brown and Koschny, 2004, Popova, 2005). We choose it to range between 0.1 to 1.0 W/m K.

We varied the molar mass from 20 to 56 atomic mass units (amu), covering atoms ranging from sodium to iron. We find that most solutions were not very sensitive to molar mass changes if the value was over 36 amu. The range of specific heat goes from 600 J/kg K to 1400 J/kg K, which correspond to the values used by Campbell-Brown and Koschny (2004).

In some ablation models, Γ (drag coefficient) and Λ (heat transfer coefficient) are assumed from the beginning. Examining the Draconids, Borovicka et al. (2007) set Γ and Λ to 1. Fisher et al. (2000) assumed also Γ and $\Lambda = 1$. Campbell-Brown and Koschny (2004) assumed $\Gamma = 1$ and $\Lambda = 0.5$. In our work, when doing the huge search of solutions, we left Γ and Λ to be 1 following these earlier studies. After finding the regions near the best solutions, we adjusted them in concert with the mass to improve the model fits. At this stage in our solution procedure, we allow Γ and Λ to vary from 0.7-0.9.

To demonstrate our procedure in detail we take meteor ELSL11 as a first example, showing explicitly how we evaluated the interval of possible values for each parameter. Other meteor events will be discussed only briefly.

3.5.2 Evaluation of Density

Case Study of Meteor ELSL11

We start with the observed lightcurve and deceleration (plot of velocity versus height) of meteor ELSL11. The investigation will consist of finding all the modeled lightcurves and decelerations which will match the observed curves. The solution will combine the eight free parameters described above with those which have been fixed (air density, emissivity, etc). A reasonable determination of each parameter is defined.

Table 3.1: Initial grain mass distributions used for meteor ELSL11 in the first stage of analysis.

Number of size bins	Number of grains	Grain mass (kg)
1	121078	1.02×10^{-12}
1	60837	2.03×10^{-12}
1	9216	1.34×10^{-11}
1	7395	1.67×10^{-11}
1	693	1.78×10^{-10}
1	93	1.32×10^{-9}

It is relatively easy to choose a range of values for each parameter, except for the grain mass. This fact will lead us to approach the real meteoroid grain mass distribution through two steps. We know that the reasonable number of grains in a meteoroid is in the thousands, and the mass of individual grains could range from 10^{-12} kg (approximately the smallest size which will ablate) to 10^{-8} kg (about one tenth the total mass for our sample events). The number of sizes of grains involved for any meteoroid is almost certainly more than one; however, in the first step, we consider the meteoroid to be composed of only one size of grain, the mass of which we can alter from 10^{-12} kg to 10^{-9} kg.

For meteor ELSL11, we present the grain mass distributions which were initially modeled in table 3.1. The photometric mass was taken to be the initial mass. Considering the grain mass ranging from 10^{-9} kg to 10^{-12} , we divided the initial photometric mass to have the number of grains. Our goal is to find those grain mass distributions which offer good fits between the modeled lightcurve and deceleration curve, and the observed curves. The second step will then be to use these solutions as starting points and to refine these solutions by finding a grain mass distribution which produces a good fit for the meteor event as defined by the χ^2 fit between the model and the observations. For ELSL11, the values of other parameters used in the modelling are given in table 3.2.

Using every combination of all these values of the free parameters, we generated

Table 3.2: Values for the parameters (other than grain mass) used in the modelling. T_{lim} is the temperature at which fragmentation occurs, T_{boil} the boiling point of the grains, C_p the specific heat, Mmass the molar mass, and Thermal Cond the thermal conductivity of the bulk meteoroid (Meteor ELSL11).

Density (kg/m ³)	Heat of ablation (J/kg)	T_{lim} (K)	T_{boil} (K)	C_p (J/kg K)	Mmass (amu)	Thermal Cond (W/m K)
500	2 E6	900	1500	800	20	0.2
1000	4 E6	1200	1700	1000	30	0.5
2000	5 E6	1350	1800	1200	36	0.7
4000	7 E 6	1600	2000			1.0
6000						
7500						
8000						

151200 different theoretical lightcurves and decelerations. Each was then compared to the observed ones through the goodness-of-fit using standard χ^2 . A perfect fit to both curves would have a χ^2 value equal to zero.

We sorted these 151200 solutions by the χ^2 values, as compared to both the observed lightcurve and the observed deceleration curve. For this event, we rejected any solution with χ^2 less than 0.016. This value is chosen by noting that for this particular event the number of degrees of freedom is 51 and the average sigma (error bar) on the lightcurve is 0.15 magnitudes. As such, this value for the χ^2 produces a statistically significant difference between the model and observed lightcurve values (see Bevington and Robinson, 2003). We ended up with two major concentrations of solutions: one around a density of 1000 kg m⁻³ and another around a density of 8000 kg m⁻³.

For each group of solutions, we find the one with the smallest χ^2 . In our example, the first group of solutions, with densities concentrated around 1000 kg m⁻³, has the best solution at model number 107935 with grain mass 1.78 E-10 kg, heat of ablation 7.0E6 J/kg, fragmentation temperature 1700 K, boiling temperature 2000 K, specific heat 800 J/kg K, molar mass 30 atomic units, and thermal conductivity 1.0 W/m K. The second set of solutions around 8000 kg m⁻³ has a grain mass bigger

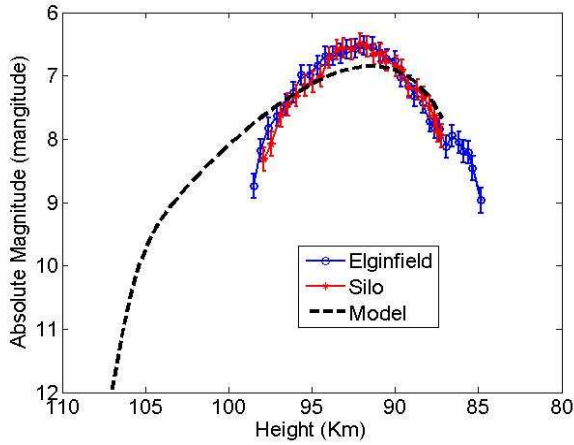


Figure 3.7: Lightcurve of the best single grain mass solution around 1000 kg m^3 for ELSL11.

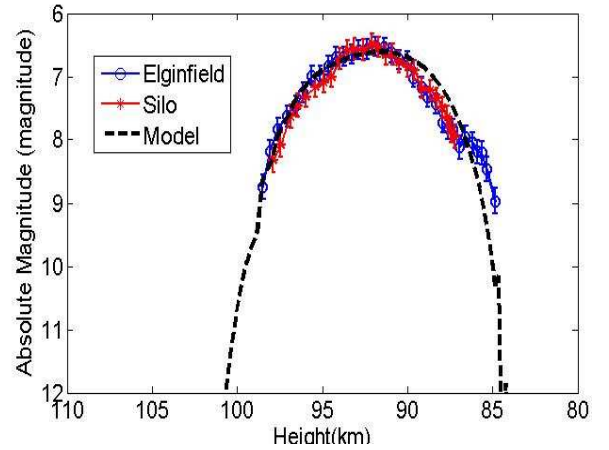


Figure 3.8: Lightcurve of the best single grain mass solution around 8000 kg m^3 for ELSL11.

than the one for the low density solution ($1.32 \text{ E-}09 \text{ kg}$). The heat of ablation is the same, the fragmentation temperature differs by just 100 K, as does the boiling temperature. The specific heat is the same for both solutions. The best molar mass is 36 atomic units for the 8000 kg m^{-3} solution, compared to 30 atomic units for the low density solution. For the thermal conductivity, the best value for the 8000 kg m^{-3} solution is half that of the 1000 kg m^{-3} solution.

In examining the modelled lightcurves and velocity profiles for the two best solutions (a low density solution around 1000 kg m^{-3} and high density solution around 8000 kg m^{-3}) we find that the high density solution matches the observed data better than the low density solution. The low density solution shows the light production stopping at 87 km; the observed data go down to 83 km. Figures 3.7 and 3.8 show the lightcurves of the high and low density solutions; figures 3.9 and 3.10 show the decelerations for the two solutions.

The next step in our solution procedure is to use these two best model fits as starting points, and to refine the grain masses, heat transfer and drag coefficients to find the best possible solution in the phase space region. This step was done by hand, adding and subtracting grains of different masses while keeping the other parameters constant. At each step, both the lightcurve and deceleration produced

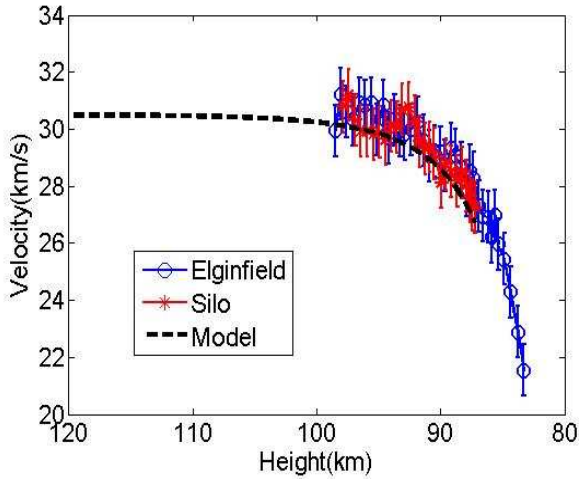


Figure 3.9: Deceleration of the best single grain mass solution around 1000 kg m^3 for ELSL11.

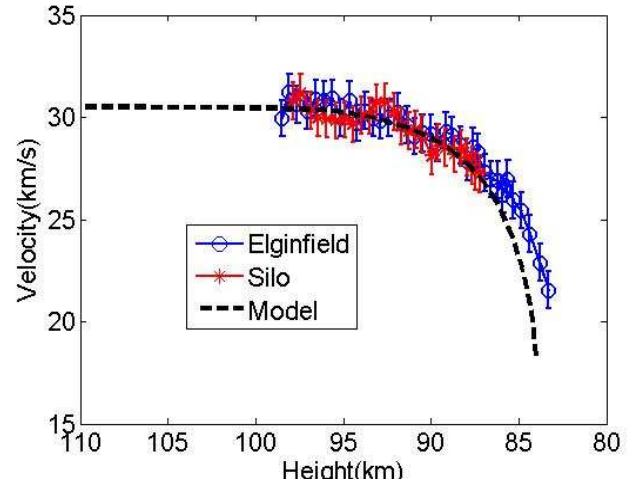


Figure 3.10: Deceleration of the best single grain mass solution around 8000 kg m^3 for ELSL11.

by the model were compared to the observed curves.

The starting values of the parameters for the high density solution were those of the best fit, listed in the previous section. The shape of the lightcurve is clearly not single body, meaning that more than one size of grain is needed to model it properly. We attempted to find a better solution using three different grain masses. We were able to find a model which is very close to the observed data (Figures 3.11 and 3.12). The parameters for this fit are given in Table 3.3.

For the low density solution, we began by modifying the number and size of the grains involved. As with the high density solution, we used three grain sizes. The initial attempt used the same parameters as the single grain size model, but had 450 grains with masses of $1.10 \times 10^{-11} \text{ kg}$, 430 grains with a mass of $1.35 \times 10^{-10} \text{ kg}$, and 30 grains with a mass of $1.93 \times 10^{-9} \text{ kg}$. The peak magnitude produced by this model was too small, so we then increased the mass of the grains in the middle bin from $1.35 \times 10^{-10} \text{ kg}$ to $2.35 \times 10^{-10} \text{ kg}$. This matched the maximum magnitude, but the model produced more light than observed at higher and lower altitudes, and did not penetrate as far into the atmosphere as the observed meteor. To correct for the latter, we increased the mass of the largest grains to $2.53 \times 10^{-9} \text{ kg}$. The lightcurve

Table 3.3: Table summarizing parameters involved in the final stage of the high density solution model for ELSL11. Den is density, Qf is heat of ablation, Cps is specific heat, Thermal Cond is thermal conductivity.

# grains	Grain mass (kg)	Den kg/m ³	Qf (J/kg)	T_{im} (K)	Tboil (K)	Cps (J/kg K)	Molar mass au	Thermal Cond. W/m K
450	1.10E-11	8000	7000000	1600	2100	800	36	0.5
430	1.35E-10							
30	1.993E-09							

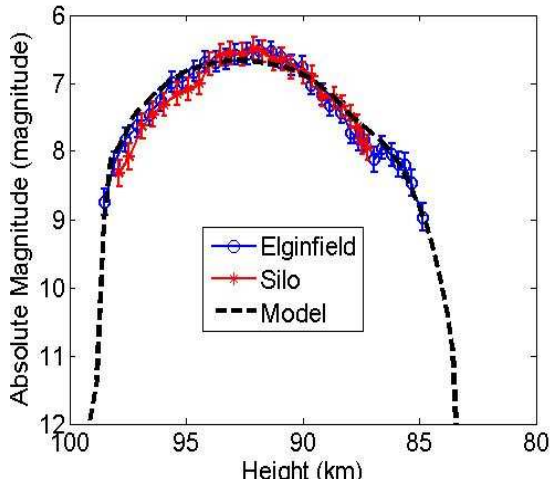


Figure 3.11: Lightcurve for ELSL11 with the model fit for a density of 8000 kg m^{-3} using parameters from table 3.3.

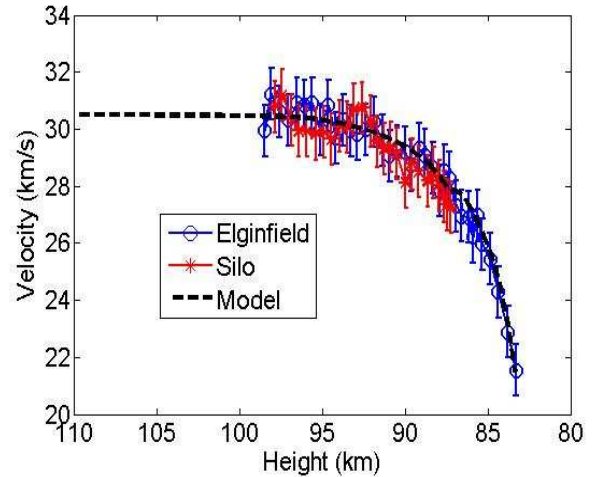


Figure 3.12: Deceleration for ELSL11 for a density of 8000 kg m^{-3} using parameters from table 3.3.

for this model is compared to the observed lightcurve in Figure 3.13; the parameters used are given in table 3.4.

In all three of the solutions where grain numbers and masses were varied, the model solution reaches the detection threshold earlier than the observed lightcurve. This could be corrected if the fragmentation temperature is increased, releasing the grains just prior to the height where the meteor becomes visible. In order to match the observed starting height, it was necessary to raise the fragmentation temperature from 1700 K to 3000 K. In order to keep the fragmentation temperature lower than the boiling temperature, we also had to raise the boiling temperature to 3300 K, and we set the fusion temperature to 3200 K for consistency. We used the same grain mass distribution as in the previous solution. The parameters for this modified solution are given in table 3.5, and the model is compared to the observed lightcurve in Figure 3.14.

The solution around 1000 kg m^{-3} is still a poor fit, and it seems physically unrealistic to have a low density meteoroid with a fragmentation temperature as high as 3000 K. We therefore reject the low density solution, and proceed to refine the density measurement assuming that the meteoroid's density is close to 8000 kg m^{-3} .

Table 3.4: Distribution of grains for the solution around 1000 kg m^{-3} using three grain masses.

# grains	Grain mass (kg)	Den (kg/m^3)	Qf (J/kg)	T_{lim} (K)	Tboil (K)	Cps (J/kg K)	Molar mass (au)	Thermal Cond. (W/m K)
450	1.10 E-11	1000	7000000	1700	2000	800	30	1
430	2.35 E-10							
30	2.53 E-09							

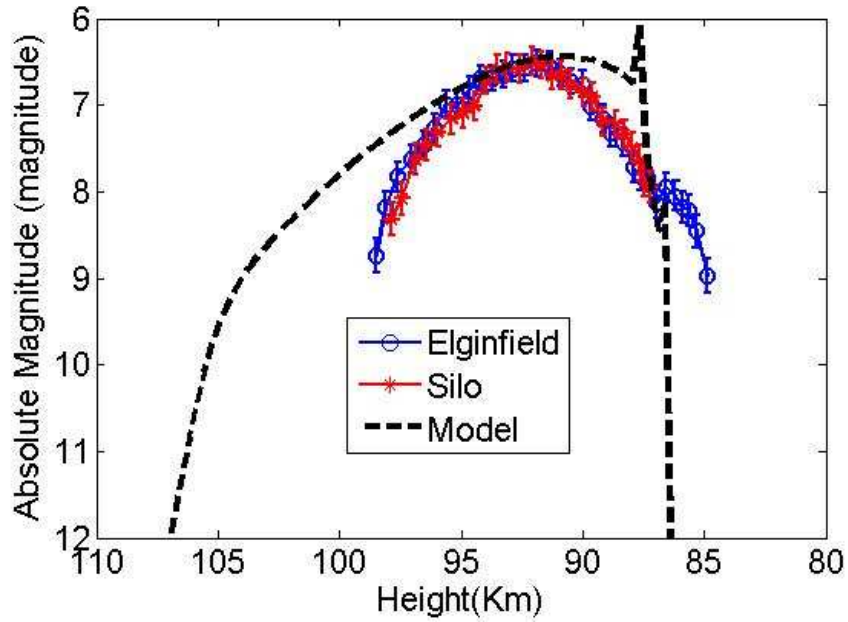


Figure 3.13: Modified solution for 1000 kg m^{-3} using three grain masses. The sudden jump in the predicted light output from the model indicates a sudden fragmentation event.

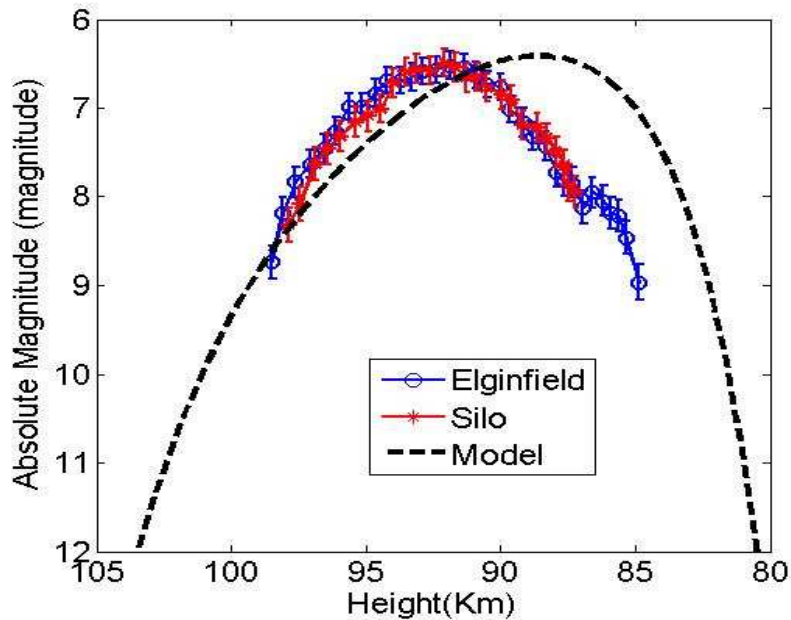


Figure 3.14: Modified solution for 1000 kg m^{-3} , with three grain sizes and modified temperatures of fragmentation, boiling and fusion.

Table 3.5: Distribution of grains for the solution around 1000 kg m^{-3} , with three grain sizes and modified temperatures of fragmentation, boiling and fusion.

# grains	Grain mass (kg)	Den (kg/m^3)	Qf (J/kg)	T_{im} (K)	Tboil (K)	Cps (J/kg K)	Molar mass (au)	Thermal Cond. (W/m K)
450	1.10 E-11	1000	7000000	3000	3300	800	30	1
430	2.35 E-10							
30	2.53 E-09							

m^{-3} .

The point of the first search over the eight different parameters is to identify broadly the different regions where the possible solutions fall, to work on the best solution from each region, to determine where among all the different concentrations of solutions the best solution lies, and determine the likely mass distribution of the grains in the meteoroid. We will now fix the grain distribution, and perform a second search with greater resolution in the density parameter, which is the parameter of greatest interest to us. We allow the other parameters (apart from grain masses) to vary as shown in table 3.6.

Using every possible combination of the parameters in the table, we computed 432000 modeled solutions. We compared each of these to the observed lightcurves and deceleration of ELSL11. For this search, we set a stricter limit on the χ^2 value of 0.08 for both the lightcurve and deceleration comparison; this roughly corresponds to a solution which fits inside the error bars of both plots. We ended up with 234 different good solutions (solutions with χ^2 less than or equal to our limit) with densities from 5000 kg m^{-3} to 8000 kg m^{-3} for ELSL11. The greatest number of good solutions falls between a density of 5500 kgm^{-3} and 6500 kgm^{-3} . Among these 234 solutions, the best one (with the smallest χ^2 both on the lightcurve and the deceleration) has a density of 5500 kgm^{-3} with a total mass of $1.36\text{E} 10^{-7} \text{ kg}$. All other parameters associated with this particular solution are summarized in table 3.7.

To determine the range of probable densities in our final model fits, we adopt the best fit value and expressed the density of ELSL11 by an asymmetrical error bar as $5500 + 2500 /- 500 \text{ kg m}^{-3}$, expressing the full range of possible density fits for our chosen χ^2 cut.

This detailed example serves to outline our methodology as we try to fit our model to the available metric and photometric observations. In the next sections, we will briefly summarize our findings for the additional 5 meteor events for which

Table 3.6: Variation of parameters used modeling lightcurves and decelerations for ELSL11 in the second stage search. The mass column does not give the variation of grain sizes, but the actual grain distribution used in every model.

mass (kg)	density (kg/m ³)	Heat of Abl (J/kg)	T lim (K)	T boil (K)	Specific heat (J/kg K)	molar mass (au)	thermal conduc (W/m K)
450x1.10 10 ⁻¹¹	3500	5 10 ⁶	900	1800	700	20	0.2
430x1.35 10 ⁻¹⁰	4000	6 10 ⁶	1000	1900	800	30	0.3
30x1.93 10 ⁻⁰⁹	4500	7 10 ⁶	1100	2000	900	36	0.5
	5000	8 10 ⁶	1200	2100	1000	56	0.7
	5500	9 10 ⁶	1400	2200	1100		0.9
	6000		1450	2300	1200		
	6500		1500				
	7000		1550				
	7500		1600				
	8000		1800				
	8500						
	9000						

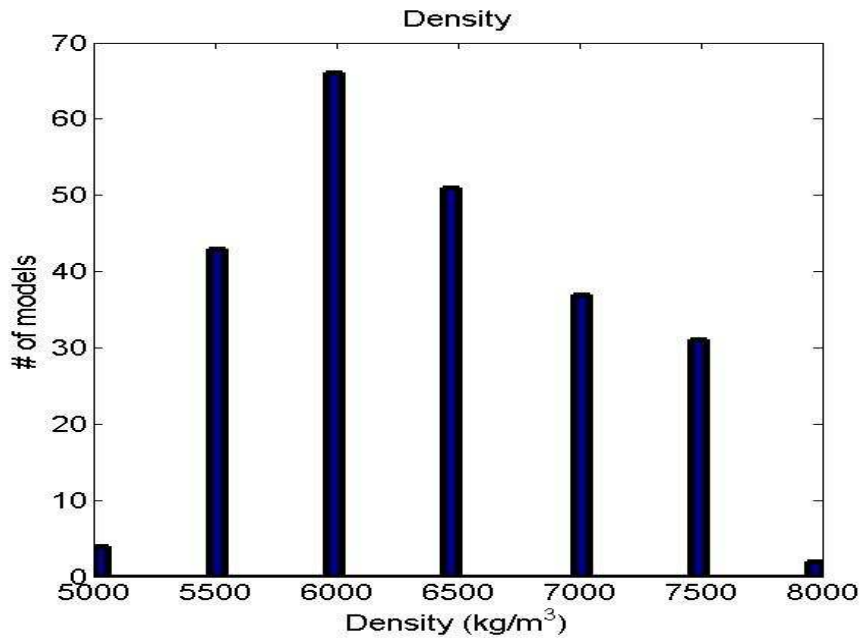


Figure 3.15: Plot of the best density solutions for ELSL11. The best solution falls at 5500 kg m^{-3} . The left bound is 5000 kg m^{-3} and the right bound is 8000 kg m^{-3}

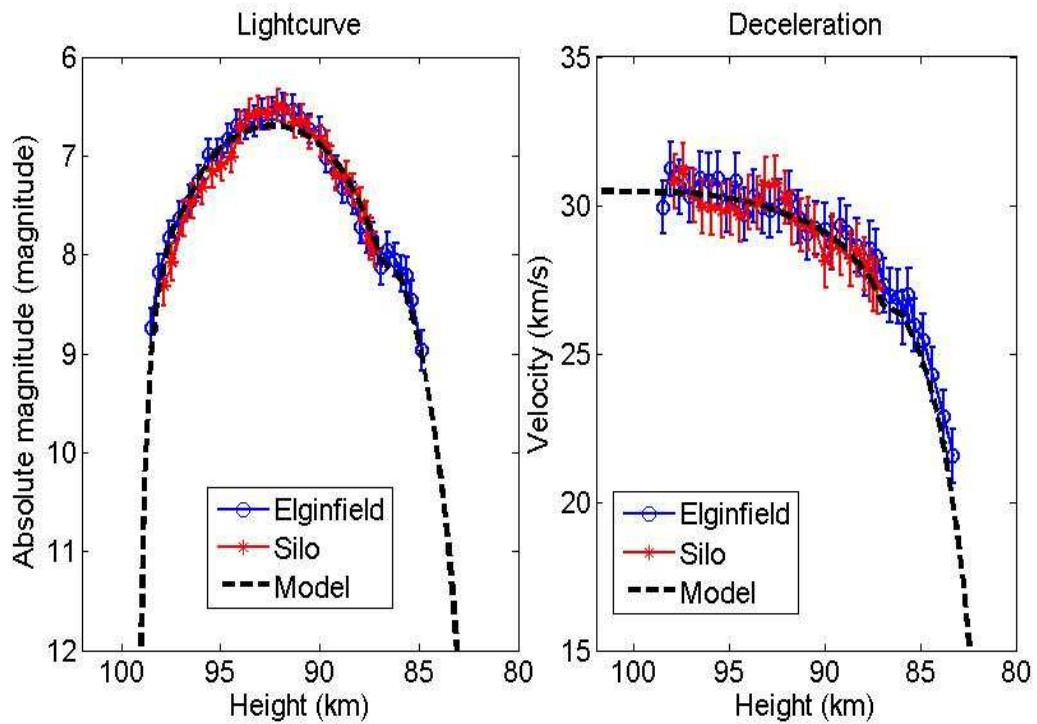


Figure 3.16: The best model of meteor ELSL11, with a density of 5500 kg m^{-3} .

Table 3.7: Values of parameters producing the best model solution among 234 solutions found to describe meteor ELSL11.

mass (kg)	density (kg/m ³)	heat of abl (J/kg)	T lim (K)	T boil (K)	specific heat (J/kg K)	molar mass (au)	thermal conduc (W/m K)
450 x 1.10 10 ⁻¹¹	5500	8 10 ⁶	1400	2300	1100	36	0.5
430 x 1.3 10 ⁻¹⁰							
30 x 1.93 10 ⁻⁹							

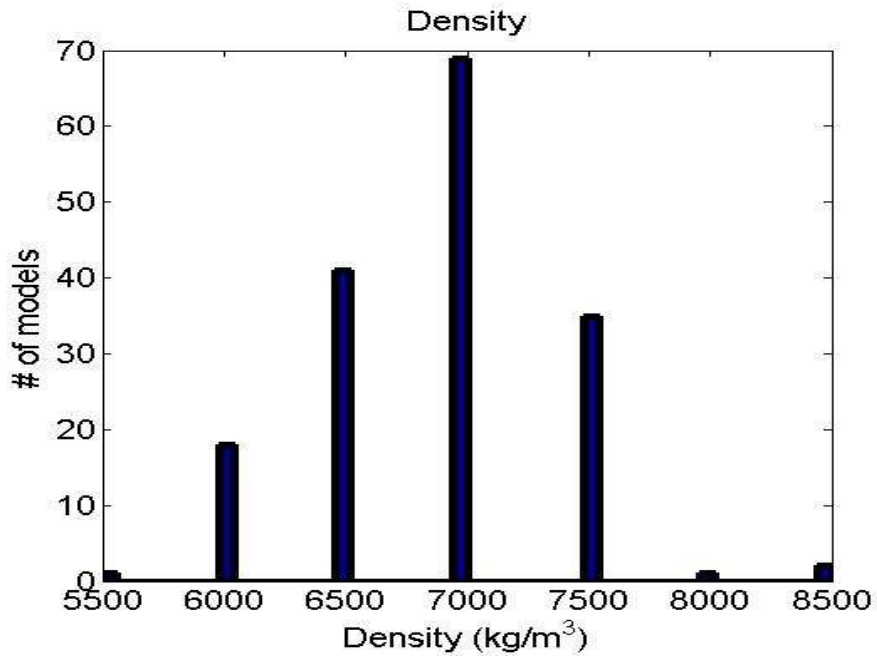


Figure 3.17: Plot of accepted solutions for ELSL01. The best solution falls at 7000 kg m⁻³. The left bound is 5500 kg m⁻³ and the right bound is 8500 kg m⁻³

we were able to apply this detailed approach.

Meteor ELSL01

Using the mass distribution in table 3.8, we modeled a 352800 combinations of the free parameters, with densities concentrated around 7000 and 8000 kg m⁻³. For this event, statistically significance required the solutions to have a χ^2 less than or equal to 0.078 on the lightcurve and less than or equal to 0.1 on deceleration; a total of 167 solutions matched the observed data (figure 3.17). Among these solutions, the best one has a density of 7000 kg m⁻³ (plotted in Figure 3.18); the values of the other parameters are given in table 3.9. The total mass of ELSL01, which had a velocity of 11.3 km s⁻¹, close to the earth escape velocity, was modeled to be 4.36 $\times 10^{-6}$ kg. The density of ELSL01 was found to be 7000 + 1500 / - 1500 kg m⁻³.

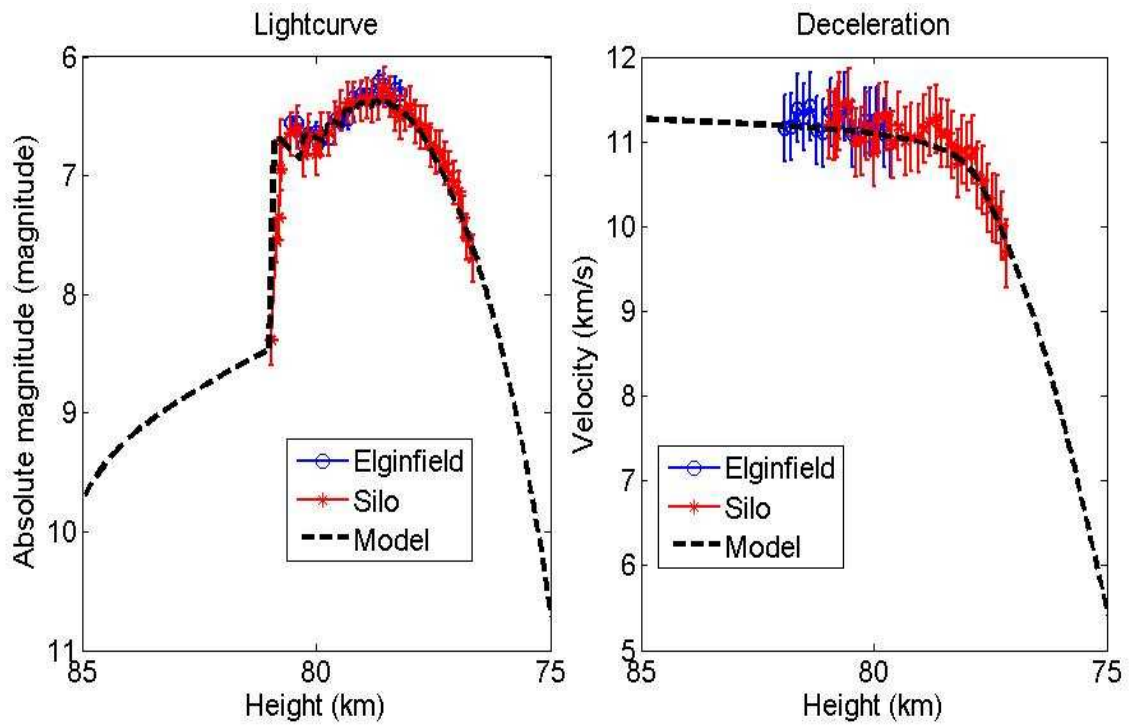


Figure 3.18: Lightcurve and deceleration of ELSL01, with best model.

Meteor ELSL09

Using the grain mass distribution in table 3.8, we computed 483000 solutions with density ranging from 250 kg m^{-3} to 3000 kg m^{-3} . We found 147 solutions whose lightcurves and decelerations matched the observed ones with a statistically significant value of standard χ^2 of better than 0.06 on both lightcurve and deceleration (figure 3.19). Among these good solutions, the one having the smallest standard chi-square had a density of 900 kg m^{-3} (figure 3.20) with a total modeled mass of $7.63 \times 10^{-8} \text{ kg}$. Values of the other parameters for this particular solution are summarized in table 3.9. The best fit density for ELSL09 is $900 + 250 \text{ /- } 150 \text{ kg m}^{-3}$.

Meteor ELSL12

With the grain mass distribution in table 3.8, we effected a search to find a more precise determination of the density which was computed using a standard χ^2 cutoff

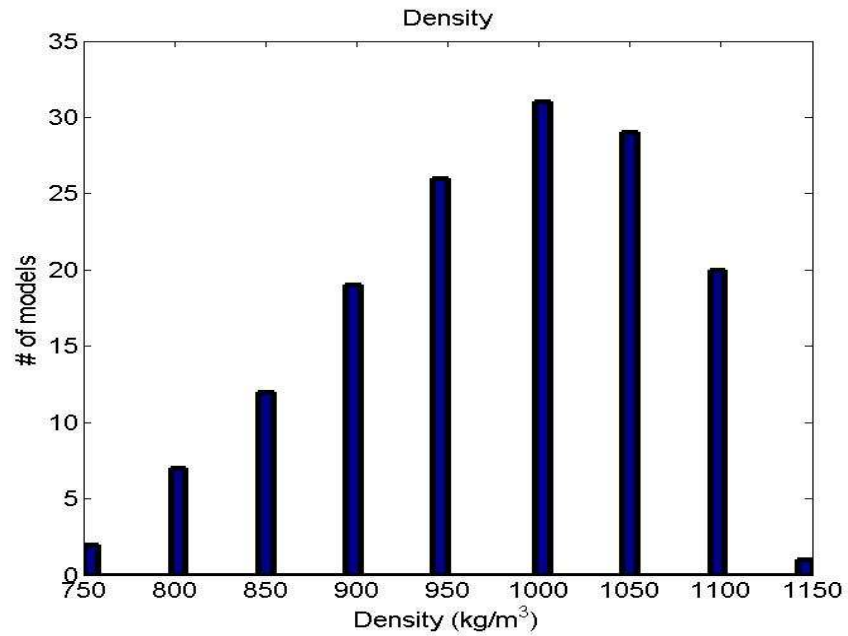


Figure 3.19: Plot of best solutions for ELSL09. The best solution falls at 900 kg m^{-3} . The left bound is 750 kg m^{-3} and the right bound is 1150 kg m^{-3}

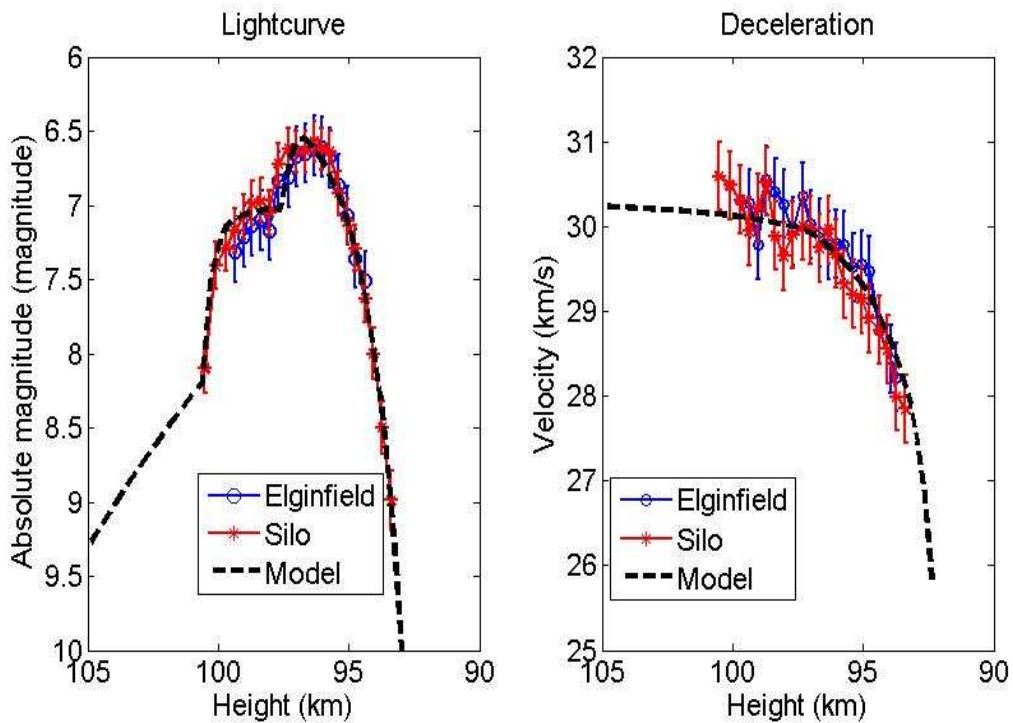


Figure 3.20: Lightcurve and deceleration of ELSL09 together with the best model fit.

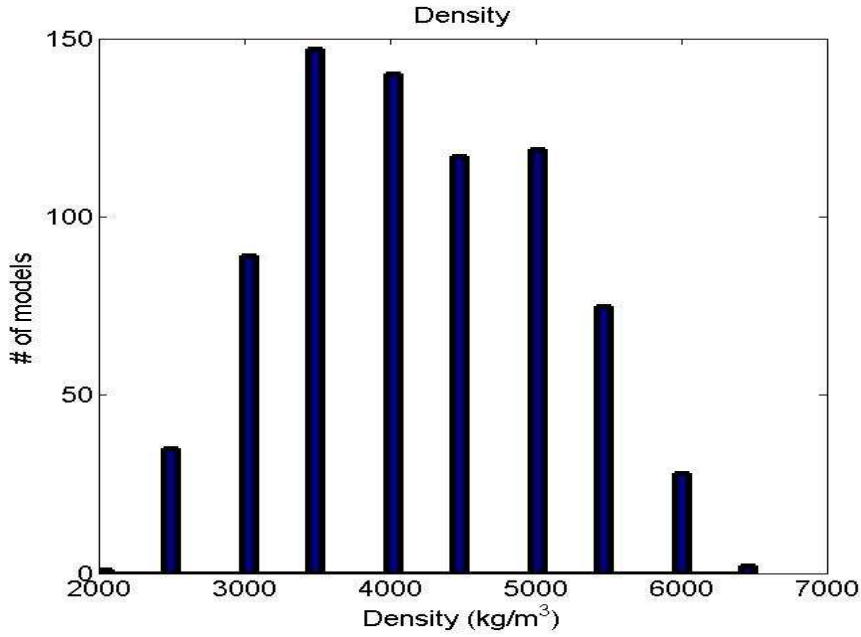


Figure 3.21: Plot of good solutions for ELSL12. The best solution falls at 4500 kg m⁻³. The left bound is 2000 kg m⁻³ and the right bound is 6500 kg m⁻³

of 0.15 or less on the lightcurve and 0.1 on the deceleration. This left 753 solutions and gives the density distribution shown in figure 3.21. Among all of these solutions, the best one had a density of 4500 kg m⁻³ (shown in figure 3.22) with a total modeled mass of 4.41×10^{-8} kg. The values of the other parameters in the best model are specified in table 3.9. The density of ELSL12 was found to be 4500 ± 2000 kg m⁻³.

Meteor PEKI08

The second search was based on 330750 different models using the grain mass distribution in table 3.8. The modeled densities ranged from 200 kg m⁻³ to 1200 kg m⁻³. Only models having a standard χ^2 less than or equal to 0.04 on the lightcurve and 0.01 on the deceleration were considered. 1525 solutions satisfied the conditions, shown in Figure 3.23. Among them, the best one had a density of 600 kg m⁻³ (figure 3.24) with a total modeled mass of 1.40×10^{-7} kg. Other parameter values are given in table 3.9. The density of PEKI 08 was found to be 600 ± 200 kg m⁻³.

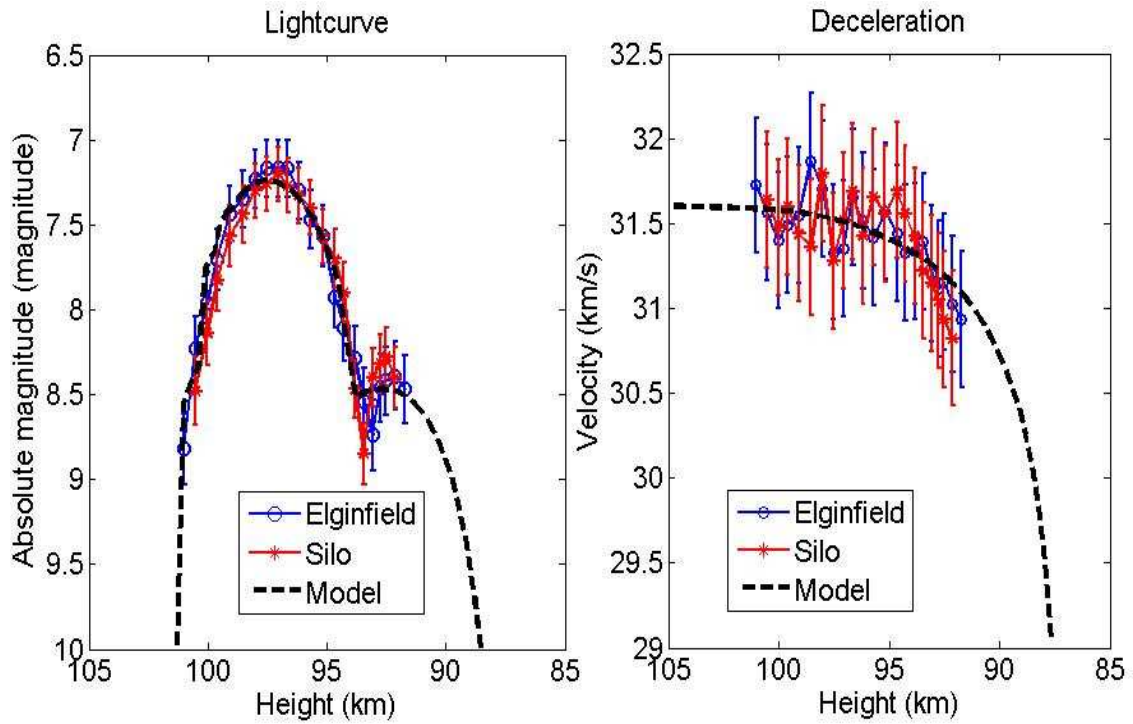


Figure 3.22: Lightcurve and deceleration of ELSL12, shown together with the best fitting model.

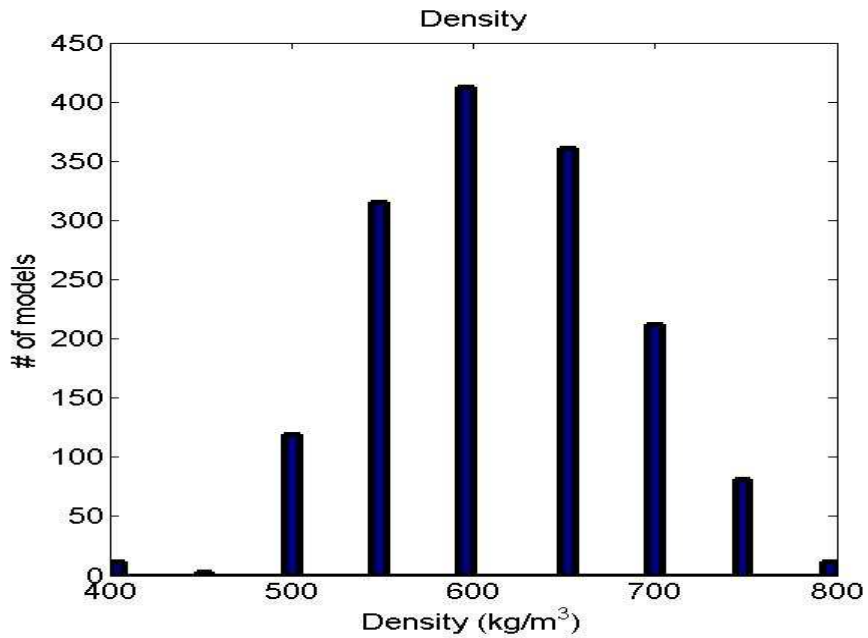


Figure 3.23: Plot of good solutions for PEKI08. The best solution falls at 600 kg m⁻³. The left bound is 400 kg m⁻³ and the right bound is 800 kg m⁻³

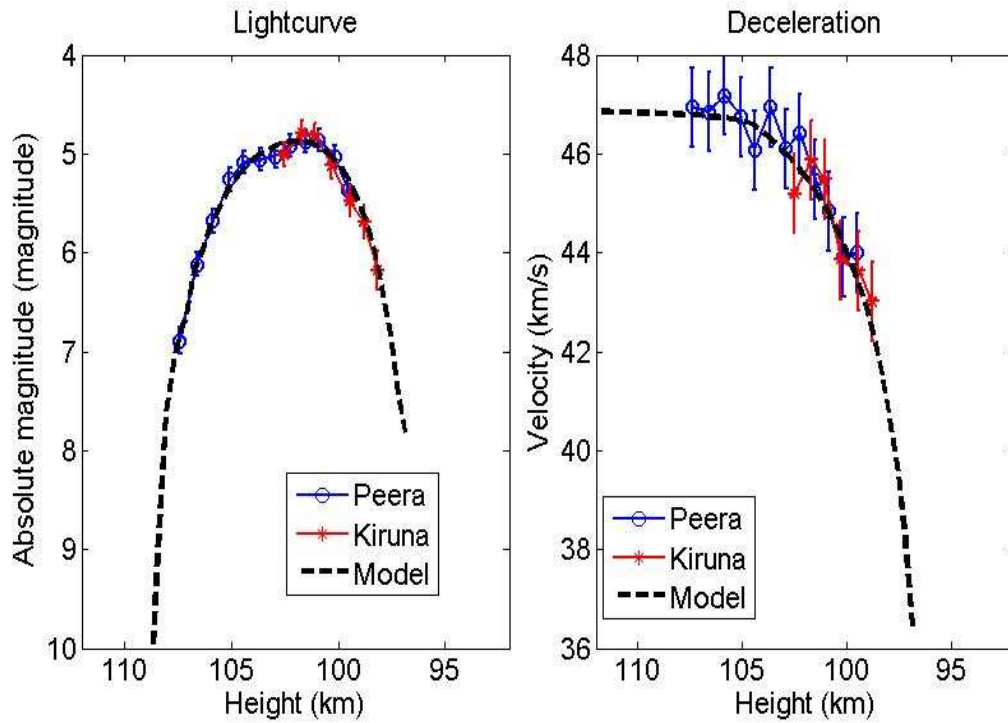


Figure 3.24: Lightcurve and deceleration of PEKI08, with the best fitting model.

Meteor PEKI09

Using the mass distribution in table 3.8 and the resolution on the density parameter from 200 kg m^{-3} to 1500 kg m^{-3} with a step of 50 kg m^{-3} , 330000 model solutions were computed. These were required to have a standard χ^2 on lightcurve and deceleration less than or equal to 0.07. A total number of 2994 solutions satisfied this particular condition, and the density distribution is plotted in Figure 3.25. Among these good solutions, the best one had a density of 500 kg m^{-3} (plotted in figure 3.26) and its total modeled mass was $1.77 \cdot 10^{-7} \text{ kg}$. Table 3.9 shows the values of other parameters of the best solution. The good solutions range from 200 kg m^{-3} to 800 kg m^{-3} and the best solution with the smallest χ^2 is 500 kg m^{-3} . The density of PEKI09 is estimated as $500 + 300/- 300 \text{ kg m}^{-3}$.

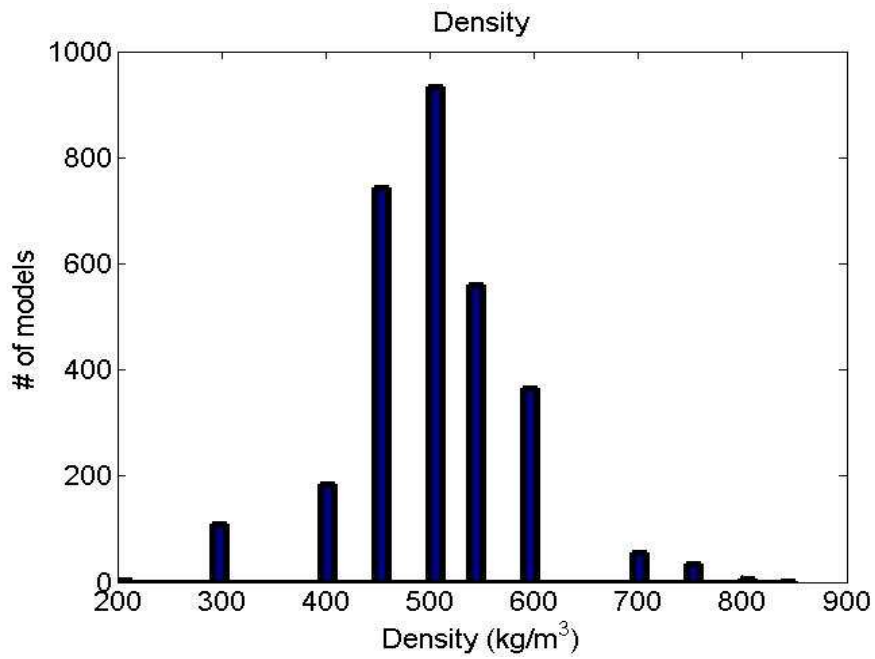


Figure 3.25: Plot of good solutions for PEKI09. The best solution falls at 500 kg m^{-3} . The left bound is 200 kg m^{-3} and the right bound is 800 kg m^{-3}

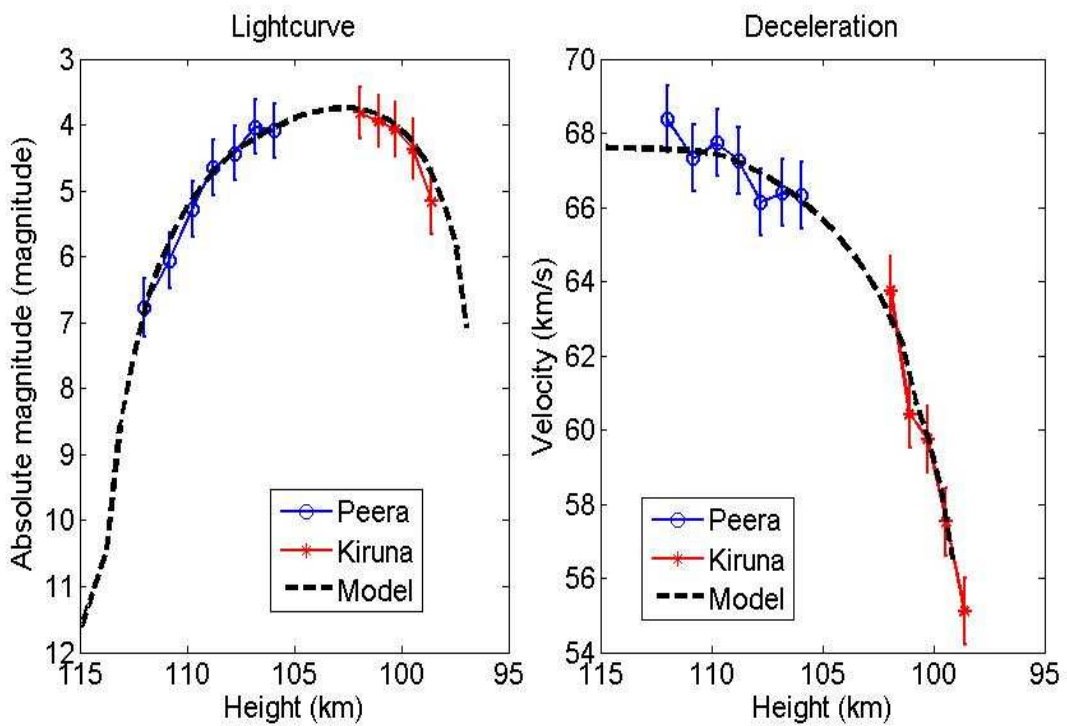


Figure 3.26: Lightcurve and deceleration of PEKI09, with the best fitting model.

Table 3.8: Summary table for the six meteors modelled in detail in this study. A value of 1 under the size column means there is only one size of grains used in the modelling, 1,2 two sizes in the composition of the meteoroid and 1,2,3 three sizes of grains in the composition of the meteoroid.

Name	Modeled mass (kg)	Grain mass (kg)	# grains	size	dens (kg/m ³)	Qf (J/kg)	T_{lim} (K)	T_{boil} (K)	C_p (J/Kg K)	Mmass (au)	Ther Cond (W/m K)
ELSL01	4.36 £ 10 ⁻⁷	1.50 10 ⁻¹⁰	3550	1	7200	5 10 ⁶	1500	2100	1000	36	0.2
		4.50 10 ⁻⁹	470	2							
ELSL09	7.63 £ 10 ⁻⁸	1.0 10 ⁻¹¹	8	1	900	5 10 ⁶	1400	2100	1100	30	0.3
		9.7 10 ⁻¹⁰	87	2							
ELSL11	1.36 £ 10 ⁻⁷	1.10 10 ⁻¹¹	450	1	5500	8 10 ⁶	1400	2300	1100	36	0.5
		1.3 10 ⁻¹⁰	430	2							
		1.93 10 ⁻⁹	30	3							
ELSL12	4.41 £ 10 ⁻⁸	3.16 10 ⁻¹¹	900	1	4500	5 10 ⁶	1400	2100	1200	36	0.2
		2.02 10 ⁻⁹	8	2							
PEKI08	1.40 £ 10 ⁻⁷	1.78 10 ⁻¹⁰	787	1	600	7 10 ⁶	1300	2200	1300	36	0.7
PEKI09	1.77 £ 10 ⁻⁷	1.78 10 ⁻¹⁰	998	1	500	9 10 ⁶	1200	2300	1200	20	0.2

Table 3.9: Summary table of the six meteors and their statistical densities as given by the method. A value of 1 in the size column means there is only one size of grains in the composition of the meteoroid, 1,2 two sizes in the composition of the meteoroid and 1,2,3 three sizes of grains in the composition of the meteoroid

Name	Modeled mass (kg)	Grain mass (kg)	# grains	size	density (kg/m ³)
ELSL01	4.36 £ 10 ^{i 6}	1.50 10 ^{i 10}	3550	1	7000+1500 /-1500
		4.50 10 ^{i 9}	470	2	
ELSL09	7.63 £ 10 ^{i 8}	1.0 10 ^{i 11}	8	1	900+200 /-250
		9.7 10 ^{i 10}	87	2	
ELSL11	1.36 £ 10 ^{i 7}	1.10 10 ^{i 11}	450	1	5500+2500 /-500
		1.3 10 ^{i 10}	430	2	
		1.93 10 ^{i 9}	30	3	
ELSL12	4.41 £ 10 ^{i 8}	3.16 10 ^{i 11}	900	1	4500+2000 /-2500
		2.02 10 ^{i 9}	8	2	
PEKI08	1.40 £ 10 ^{i 7}	1.78 10 ^{i 10}	787	1	600+200 /-200
PEKI09	1.77 £ 10 ^{i 7}	1.78 10 ^{i 10}	998	1	500+300 /-300

3.6 Discussion

Our analysis emphasizes that when it comes to modeling meteoroid behaviour, where many free parameters are involved, we should not in general expect to find a unique solution matching the lightcurve, or even both the lightcurve and the deceleration. Different combinations of free parameters can produce modeled lightcurves and decelerations falling within the observed error bars. If solutions closely matching the observations can be found for both high and low densities, the data often are not sufficiently restrictive to uniquely determine the meteoroid density. We found, for the six meteors we observed, that good solutions were concentrated in a relatively small portion of the density space, meaning that a meaningful density and an estimate of the error could be found. In our case, the fact that the number of good fits falls to zero for densities higher and lower than the best fit density gives the ultimate boundaries to the meteoroid density, though these may be somewhat conservative.

Our analysis revealed similar behaviour to that found by Borovicka et al. (2007). Both works showed that meteoroids fragment gradually near the onset of detectable light production into constituent grains whose masses vary in a very narrow range between 10^{-9} and 10^{-12} . In both studies, the disruption occurs with an energy around 10^6 J kg $^{-1}$. The grain distribution used in our study (between one and three discrete sizes of grain) is in contrast to that used in other studies, many of which use the more physical assumption of a power law (Borovicka et al. 2007, Beech, 1986, Beech and Murray, 2003). The lightcurves produced by this simplification are almost as smooth as the power-law generated curves, and deliver a considerable gain in computation time, since particles of the same size released at the same time can be simulated as a single particle and their luminosity later multiplied. Computation time was of critical importance in our study, since hundreds of thousands of models had to be run for each meteor.

In this work, we obtained the density of each meteoroid after fitting both its lightcurve and deceleration. This was done for first time by Borovicka et al. (2007) for six Draconids. They found an estimated density of 300 kg m $^{-3}$ for Draconids in full agreement with Ceplecha (1988) and Revelle (2001). The meteoroids in our work had a range of densities going from 500 kg m $^{-3}$ to 7000 kg m $^{-3}$, overlapping with values obtained by Babadzhanov (2002) and Bellot Rubio et al. (2002).

Three of the six meteoroids have very high density (ELSL01, ELSL11, ELSL12). They fall well within the range of density defined by Babadzhanov (2002) whose investigation on density of meteoroids took into account the fragmentation process. But they are significantly higher than the range defined by Bellot Rubio et al. (2002). Some of the ablation for these higher density meteoroids may be occurring as liquid droplets, rather than as discrete grains (Lebedinets and Portnyagin, 1968). Association of these high density meteoroids with asteroidal objects is further supported by their orbits which have Tisserand values greater than 3, consistent with an asteroidal origin. These events may represent the iron meteoroid population identified

at slightly larger sizes spectrally by Borovicka et al. (2005); our work suggests that this iron meteoroid population may extend down to even smaller masses. Among the meteors we believe underwent fragmentation (and had more than one size of grain), ELSL09 does have a low density. Thus, we cannot automatically associate fragmentation with high values of density. This suggests that when the model is based not only on the observed lightcurve, but also on the observed deceleration behaviour of the meteoroid, there is no exclusive bias against finding low densities with the model. We can also address the disagreement of Bellot Rubio et al. (2002) with Babazhanov's work (Babazhanov, 2002) concerning the value of heat of ablation. Babazhanov (2002) assumed the heat of ablation to be fixed to $2.8 \times 10^5 \text{ J kg}^{-1}$ (latter, he brought it to $2 \times 10^6 \text{ J kg}^{-1}$), but in our study we found different heats of ablation involved in good model fits of different meteoroids. This shows that the heat of ablation cannot be assumed, but should be fitted as a free parameter. The density of three other meteoroids (ELSL09, PEKI08, PEKI09) fell well inside both the ranges defined by Bellot Rubio et al. (2002) and Babazhanov (2002). All of these meteors fragmented, but had densities at the lower end.

The heights of meteors of the Swedish campaign (at different season and latitude) are significantly higher than the Canadian one. This is partly the result of the observing geometry and may also reflect our detection bias given the volume sampled from both sites. While one of our six events has a nominally hyperbolic orbit, the precision of the velocity measurement (given the paucity of data points for the Swedish campaign data) together with the large extrapolation between the observed and extra-atmosphere velocity suggests to us rather that this is measurement uncertainty.

3.7 Conclusion

In this work we have, for the first time for meteoroids in the size range of 10^{-7} to 10^{-8} kg, used both the dynamic and photometric observations of meteoroids to determine their densities, using a full simulation of ablation including fragmentation. We have exhaustively searched the parameter space to ensure that the density limits we determine from the model fully characterize the possible range of density. Previous studies of meteoroid density have relied on finding a single model which matches the observations, without searching for other combinations of the free parameters which might yield equally good fits. The number of meteors for which we have applied this modelling technique has been limited and we have analysed these in detail mainly to demonstrate the method at this stage. We note that our findings in terms of meteoroid physical properties should not be taken to represent the meteoroid population as a whole as our sampling is very biased by the requirements of complete trails.

Among 13 meteors in the first observing run and 29 meteors in the second run, only six satisfied the criteria of both starting and ending in the field of view of at least at one of the two stations (the necessary criteria to guarantee a complete lightcurve for an accurate photometric mass of the meteoroid). Among the six meteors, three with relatively low velocity were found to have very high densities. Taking into account fragmentation in determining the density of meteoroid does not, however, necessarily lead to higher values of meteoroid density, particularly when the heat of ablation of the meteoroid material is kept as a free parameter. The proportion of small meteoroids with high densities may be underestimated. It is possible these nearly pure iron meteoroids represent the impact pulverized remains from asteroids with ordinary chondrite compositions, a process which has been demonstrated in the lab to produce small, nearly pure iron particulates (Horz et al. 2005). Instruments with a narrow field of view and very high sensitivity are able to record these very faint meteoroids. Apart from the small number statistics in this study, our observations

were biased toward slow, dense meteoroids which ablate low in the atmosphere and therefore have shorter trails, more likely to begin and end in the field of view.

Precise measurements of deceleration provide a very important constraint in determining meteoroid density. For small meteoroids, both the photometric and dynamic data are needed to adequately constrain ablation models. High velocity meteoroids typically only show deceleration at the very end of their trajectory, with most of the energy transfer being used for ablation and very little going in to changing the velocity, making deceleration difficult to measure. The equipment used in this investigation is capable of detecting very small decelerations, but the number of usable meteors is small because of the very small fields of view. The next step will be to see if standard meteor video cameras, with fields of view in the 15 to 30 degree range, can measure the deceleration with enough accuracy to constrain the model parameters, particularly density. If so, many more meteor densities will be determined, giving the statistics needed for an analysis of the average composition of meteoroids.

Bibliography

- [1] Babadzhanov, P. B. 2002, *A&A*, 384, 317
- [2] Beech, M. 1986, *AJ*, 91, 159
- [3] Beech, M., & Murray, I. S. 2003, *MNRAS*, 345, 696
- [4] Beech, M., Illingworth, A., Murray, I. S. 2003, *M&PS*, 38, 1045
- [5] Bellot Rubio, L. R., Martinez Gonzalez, M. J., Ruiz Herrera, L., et al. 2002, *A&A*, 389, 680
- [6] Bevington, P. R., & Robinson, D. K. 2003, *Data Reduction and Error Analysis for the Physical Science*, McGraw-Hill, New York, 313p
- [7] Borovicka, J. 1990, *Bull. Astr. Inst. Czechosl.*, 41, 391
- [8] Borovicka, J., Kotten, P., Spurny, P., et al. 2005, *Icarus*, 174, 15
- [9] Borovicka, J. 2005, *Proceedings of the International Astronomy Union*, Cambridge University Press, 249
- [10] Borovicka, J., Spurny, P., & Kotten, P. 2007, *A&A*, 473, 661
- [11] Campbell, M., Brown, P., Leblanc, A., et al. 2000, *M&PS*, 35, 1259
- [12] Campbell-Brown, M. D., & Koschny, D. 2004, *A&A*, 418, 751
- [13] Ceplecha, Z. 1968, *SAO Special Report*, 279, 1

- [14] Ceplecha, Z. 1987, *Bull. Astron. Inst. Czech.*, 38, 4, 222
- [15] Ceplecha, Z. 1988, *Bull. Astron. Inst. Czech.*, 39, 4, 221
- [16] Ceplecha, Z., Borovicka, J., Elford, W. G., et al. 1998, *Space Science Rev.*, 84, 327
- [17] Fisher, A. A., Hawkes, R. L., Murray, I. S. 2000, *Planetary and Space Science*, 48, 911
- [18] Hapgood, M., Rothwell, P., Royrvik, O. 1982, *MNRAS*, 201, 569
- [19] Hawkes, R. L. & Jones, J. 1975, *MNRAS*, 173, 339
- [20] Hawkes, R. L. 2002, *Meteors in the Earth's atmosphere.* ed. Edmond Murad and Iwan P. Williams, 97
- [21] Hedin, A. 1991, *J. Geophys. Res.*, 96, 1154
- [22] Hörz, F., Cintala, M. J., See, T. H., et al. 2005, *M&PS*, 40, 1329
- [23] Koten, P., Borovicka, J., Spurny, P., et al. 2004, *A&A*, 428, 683
- [24] Lebedinets, V. N., Portnyagin, Yu. I. 1968, *Soviet Astronomy AJ*, 11, 700
- [25] Hill, K. A., Rogers, L. A., Hawkes, R. L. 2005, *A&A*, 444, 615
- [26] Myers, J. R., Sande, C. B., Miller, A. C., et al. 2001, *yCat* 5109.
- [27] Popova, O. P., 2004, *EM&P*, 95, 303
- [28] Revelle, D. O. 2001, in *Proc. Meteoroids 2001 Conf.*, ed. B. Warmbein, Kiruna, Sweden, ESA-SP, 495, 513
- [29] Whipple, F. L., & Jacchia, L. G. 1957, *Smithsonian Contr. Astrophysics*, 1, 183

Table 3.10: Summary table for the first observing campaign near London Ontario (Canada). Hb is beginning height, Hi is initial height (actual height as appeared on the field of view), He is ending height and Hf is final height (actual height as appeared on the field of view). The velocity is the no-atmosphere velocity computed as outlined in the text.

Name	Date	Time (UTC)	Velocity (km/s)	Positions on FOV			
				Hb(km)	Hi (km)	He (km)	Hf (km)
ELSL01	20040517	04:56:04	11.3 \$ 0.9	81.91	81.9	77.2	77.2
ELSL02	20040517	06:35:18	31.8 \$ 0.7		102.1		98.2
ELSL03	20040520	05:46:48	17.7 \$ 1.2		95.5		81.7
ELSL04	20040520	08:01:42	31.7 \$ 1.1		97.5		97.4
ELSL05	20040527	05:10:42	11.6 \$ 1.5		80.2	76.6	76.6
ELSL06	20040527	05:30:38	35.6 \$ 0.9		102.6		97.9
ELSL07	20040527	06:05:21	14.5 \$ 1.3		89.4	85.6	85.6
ELSL08	20040527	06:42:38	14.8 \$ 0.8		95.8	91.2	91.2
ELSL09	20040527	07:35:40	30.3 \$ 0.9		100.5	93.4	93.4
ELSL10	20040527	07:51:43	24.3 \$ 1.2		89.2	84.7	84.7
ELSL11	20040527	08:19:27	30.5 \$ 0.8		98.5	83.3	83.3
ELSL12	20040527	08:32:51	31.6 \$ 0.9		101.1	90.9	90.9
ELSL13	20040527	08:33:42	31.1 \$ 1.3		98.3		93.5

Table 3.11: Summary table of the second observing campaign from Kiruna (Sweden) and Peera (Finland). Hb is beginning height, Hi is initial height (actual height as appeared on the field of view), He is ending height and Hf is final height (actual height as appeared on the field of view). The velocity is the no-atmosphere velocity computed as outlined in the text.

Name	Date	Time (UTC)	Velocity (km/s)	Positions on FOV			
				Hb(km)	Hi (km)	He (km)	Hf (km)
PEKI01	20071006	01:54:42	63.7 \$ 1.6		105.4		102.6
PEKI02	20071008	20:45:52	14.9 \$ 0.9		92.6		88.1
PEKI03	20071008	22:17:01	28.9 \$ 1.2		100.7		96.7
PEKI04	20071008	23:08:30	38.4 \$ 1.2		106.1	96.3	96.3
PEKI05	20071009	01:36:48	59.6 \$ 1.4		101.1		97.1
PEKI06	20071009	01:37:25	50.8 \$ 0.9		105.5	97.8	97.8
PEKI07	20071009	01:45:58	34.3 \$ 1.3	103.1	103.1		91.7
PEKI08	20071009	01:49:48	46.9 \$ 0.8	107.4	107.4	98.2	98.2
PEKI09	20071009	01:55:13	67.9 \$ 0.9	112.0	112.0	98.6	98.6
PEKI10	20071009	02:32:20	60.8 \$ 1.3		108.7		102.4
PEKI11	20071010	01:03:45	57.7 \$ 0.9		104.1	93.5	93.5
PEKI12	20071010	01:47:22	26.7 \$ 0.7		99.7		93.7
PEKI13	20071010	01:49:10	31.3 \$ 1.6		99.9		91.5
PEKI14	20071010	21:30:38	41.2 \$ 0.8		103.3		95.3
PEKI15	20071010	21:45:44	38.4 \$ 0.9		104.3	93.7	93.7
PEKI16	20071010	22:07:01	62.4 \$ 1.3		109.2		101.4
PEKI17	20071010	22:33:32	35.7 \$ 0.8		101.5		87.5
PEKI18	20071010	22:51:37	23.6 \$ 1.2	99.9	99.9		91.6
PEKI19	20071010	23:03:20	29.2 \$ 0.9	101.7	101.7		96.8
PEKI20	20071011	01:00:16	no solution	—	—	—	—
PEKI21	20071011	02:53:28	41.3 \$ 1.3	103.5	103.5		96.3
PEKI22	20071011	02:55:32	22.5 \$ 0.9	98.9	98.9		93.4
PEKI23	20071011	02:57:54	79.7 \$ 1.8		122.4		108.5
PEKI24	20071011	03:08:40	63.4 \$ 1.2		106.4		97.6
PEKI25	20071012	19:49:53	34.4 \$ 0.8	104.2	104.2		95.9
PEKI26	20071012	20:00:28	26.1 \$ 0.9		99.9		96.1
PEKI27	20071012	20:14:15	51.3 \$ 1.5		105.4	93.5	93.5
PEKI28	20071013	00:04:16	64.5 \$ 1.3		110.2		96.7
PEKI29	20071013	00:09:26	31.2 \$ 0.9		100.3		97.7

Table 3.12: Table summarizing orbital elements of all 42 meteors. alp geo and del geo are respectively geocentric right ascension and declination at the epoch J2000.0. TJ is Tisserand parameter with respect to Jupiter. PEKI20 is the case of meteors which crossed the entire field of view making it difficult to compute any trajectory solution.

Name	Radiant				Orbital elements							TJ
	α_g (°)	δ_g (°)	a (AU)	e	i (°)	ω (°)	Ω (°)	q per (AU)	q aph (AU)			
ELSLO1	214.5 ± 0.4	1.5 ± 1.3	1.06 ± 0.04	0.1 ± 0.2	1.2 ± 0.8	47.9 ± 0.8	236.6 ± 0.1	0.99 ± 0.01	1.14 ± 0.08	5.804		
ELSLO2	257.8 ± 1.1	-22.1 ± 1.1	1.3 ± 0.1	0.84 ± 0.01	1.4 ± 1.7	317.5 ± 1.9	56.66 ± 0.03	0.21 ± 0.02	2.4 ± 0.2	4.542		
ELSLO3	215.0 ± 1.4	32.4 ± 1.1	2.9 ± 0.8	0.7 ± 0.1	14.7 ± 1.5	207.9 ± 1.2	59.5 ± 0.1	0.965 ± 0.005	4.8 ± 1.5	2.825		
ELSLO4	239.5 ± 1.4	-43.3 ± 1.1	4.2 ± 1.3	0.88 ± 0.04	23.5 ± 1.2	94.9 ± 2.3	239.6 ± 0.1	0.5 ± 0.1	7.9 ± 2.6	2.021		
ELSLO5	179.5 ± 2.9	25.25 ± 2.02	2.6 ± 1.3	0.6 ± 0.2	1.9 ± 1.5	181.8 ± 1.9	66.2 ± 0.1	1.0 ± 0.3	4.1 ± 2.7	3.131		
ELSLO6	260.3 ± 1.1	-13.3 ± 1.1	3.6 ± 0.9	0.92 ± 0.02	15.2 ± 1.7	299.2 ± 2.4	66.2 ± 0.1	0.29 ± 0.02	6.8 ± 1.7	2.074		
ELSLO7	82.76 ± 2.8	64.8 ± 4.1	1.3 ± 0.1	0.32 ± 0.07	10.9 ± 3.0	127.4 ± 4.3	66.241 ± 0.001	0.918 ± 0.006	1.8 ± 0.3	4.930		
ELSLO8	201.3 ± 3.5	61.8 ± 1.2	1.7 ± 0.2	0.42 ± 0.06	14.2 ± 1.6	178.5 ± 1.4	66.3 ± 0.1	1.01 ± 0.01	2.5 ± 0.3	4.064		
ELSLO9	259.6 ± 1.1	-6.3 ± 1.1	1.9 ± 0.2	0.80 ± 0.02	19.2 ± 1.4	292.4 ± 2.4	66.3 ± 0.1	0.39 ± 0.02	3.5 ± 0.4	3.422		
ELSLO10	304.3 ± 1.1	14.9 ± 1.1	0.644 ± 0.007	0.65 ± 0.02	41.9 ± 4.1	346.7 ± 1.1	66.31 ± 0.01	0.22 ± 0.01	1.07 ± 0.01	8.472		
ELSLO11	272.8 ± 1.4	41.9 ± 1.1	2.1 ± 0.2	0.57 ± 0.05	47.5 ± 1.2	225.1 ± 3.1	66.33 ± 0.01	0.91 ± 0.01	3.3 ± 0.5	3.182		
ELSLO12	307.9 ± 1.5	44.7 ± 1.1	1.01 ± 0.05	0.03 ± 0.02	59.9 ± 1.7	272.4 ± 3.1	66.34 ± 0.01	0.99 ± 0.005	1.04 ± 0.05	5.590		
ELSLO13	318.1 ± 1.1	8.6 ± 1.1	0.56 ± 0.06	0.84 ± 0.02	72.7 ± 1.4	354.7 ± 0.7	66.34 ± 0.01	0.09 ± 0.01	1.04 ± 0.01	9.392		
PEKI01	84.6 ± 1.1	-3.02 ± 1.1	8.8 ± 0.1	0.9 ± 0.1	129.1 ± 1.8	55.3 ± 5.3	12.3 ± 0.1	0.79 ± 0.03	16.8 ± 0.4	-0.124		
PEKI02	326.1 ± 1.2	-6.3 ± 2.8	2.6 ± 0.6	0.64 ± 0.09	1.8 ± 0.9	207.5 ± 1.3	195.1 ± 0.5	0.9 ± 0.1	4.3 ± 1.2	3.086		
PEKI03	22.9 ± 1.1	2.3 ± 1.1	2.6 ± 0.3	0.83 ± 0.02	6.67 ± 1.04	103.2 ± 2.2	15.148 ± 0.001	0.44 ± 0.01	4.8 ± 0.6	-0.287		
PEKI04	156.7 ± 2.1	61.5 ± 1.1	0.99 ± 0.06	0.35 ± 0.02	74.9 ± 2.2	67.9 ± 9.4	194.4 ± 0.1	0.64 ± 0.04	1.33 ± 0.08	5.466		
PEKI05	80.6 ± 1.1	8.7 ± 1.1	1.8 ± 0.3	0.75 ± 0.03	145.9 ± 2.4	108.3 ± 6.7	15.3 ± 0.1	0.44 ± 0.04	3.1 ± 0.6	2.244		
PEKI06	77.2 ± 1.2	34.6 ± 1.1	0.88 ± 0.04	0.79 ± 0.02	144.2 ± 2.9	328.3 ± 2.9	195.3 ± 0.1	0.2 ± 0.1	1.6 ± 0.1	5.499		
PEKI07	175.7 ± 2.1	61.01 ± 1.04	1.1 ± 0.1	0.4 ± 0.1	61.6 ± 2.4	81.7 ± 4.5	195.3 ± 0.1	0.69 ± 0.03	1.5 ± 0.1	5.128		
PEKI08	77.98 ± 1.52	48.43 ± 0.06	0.85 ± 0.04	0.65 ± 0.02	111.7 ± 2.2	321.1 ± 3.5	195.3 ± 0.1	0.30 ± 0.02	1.41 ± 0.06	5.890		
PEKI09	82.5 ± 1.8	57.2 ± 1.1	-1.8 ± 0.3	1.49 ± 0.09	120.8 ± 1.5	220.4 ± 2.6	195.3 ± 0.1	0.86 ± 0.02	—	-3.554		
PEKI10	85.9 ± 1.1	4.59 ± 1.01	1.9 ± 0.4	0.67 ± 0.05	140.6 ± 2.1	86.9 ± 7.3	15.3 ± 0.1	0.62 ± 0.04	3.1 ± 0.7	2.043		
PEKI11	91.5 ± 1.4	43.7 ± 1.1	1.19 ± 0.09	0.45 ± 0.03	137.6 ± 1.9	275.6 ± 7.9	196.3 ± 0.1	0.66 ± 0.04	1.7 ± 0.2	3.739		
PEKI12	0.1 ± 1.4	41.6 ± 1.1	2.5 ± 0.3	0.73 ± 0.03	27.3 ± 1.1	257.8 ± 2.3	196.3 ± 0.1	0.66 ± 0.01	4.3 ± 0.6	2.922		
PEKI13	351.9 ± 3.4	72.45 ± 1.03	2.0 ± 0.4	0.6 ± 0.1	48.9 ± 2.3	232.6 ± 4.2	196.3 ± 0.1	0.86 ± 0.01	3.15 ± 0.71	3.252		
PEKI14	30.6 ± 1.3	37.9 ± 1.1	4.4 ± 1.4	0.94 ± 0.01	47.8 ± 1.9	300.4 ± 2.7	197.09 ± 0.01	0.27 ± 0.02	8.6 ± 2.7	1.603		
PEKI15	156.3 ± 2.2	62.16 ± 1.03	0.96 ± 0.05	0.30 ± 0.02	75.7 ± 1.7	65.8 ± 9.2	197.1 ± 0.1	0.67 ± 0.04	1.26 ± 0.06	5.619		
PEKI16	162.5 ± 1.3	40.07 ± 1.01	-2.1 ± 0.6	1.2 ± 0.1	109.4 ± 1.9	98.4 ± 3.7	197.1 ± 0.1	0.52 ± 0.03	—	-2.756		
PEKI17	213.1 ± 3.2	71.35 ± 1.03	2.8 ± 0.5	0.6 ± 0.1	57.7 ± 1.1	156.8 ± 2.6	197.1 ± 0.1	0.97 ± 0.01	4.5 ± 0.9	2.484		
PEKI18	262.89 ± 2.4	63.9 ± 1.1	2.1 ± 0.3	0.5 ± 0.1	34.4 ± 1.8	176.1 ± 1.8	197.1 ± 0.1	0.9 ± 0.1	3.2 ± 0.6	3.384		
PEKI19	19.02 ± 1.06	14.76 ± 1.05	3.2 ± 0.5	0.86 ± 0.02	6.28 ± 1.08	281.4 ± 2.2	197.150 ± 0.001	0.45 ± 0.02	5.9 ± 0.9	-0.814		
PEKI20	—	—	—	—	—	—	—	—	—	—		
PEKI21	200.2 ± 4.4	76.54 ± 1.02	5.0 ± 2.5	0.8 ± 0.1	67.3 ± 1.5	166.8 ± 2.4	197.3 ± 0.1	0.9 ± 0.1	9.1 ± 4.9	1.494		
PEKI22	309.9 ± 2.0	58.6 ± 1.1	2.5 ± 0.3	0.62 ± 0.05	29.7 ± 1.4	206.3 ± 1.6	197.3 ± 0.1	0.9 ± 0.1	4.1 ± 0.7	3.025		
PEKI23	99.6 ± 1.1	23.1 ± 1.1	-1.3 ± 0.3	1.7 ± 0.2	179.9 ± 0.5	203.9 ± 5.2	198.1 ± 5.1	0.95 ± 0.01	—	-5.374		
PEKI24	127.6 ± 1.1	25.34 ± 1.01	1.5 ± 0.2	0.6 ± 0.1	167.2 ± 2.1	93.5 ± 8.0	197.3 ± 0.1	0.6 ± 0.4	2.5 ± 0.4	2.629		
PEKI25	176.7 ± 3.6	73.33 ± 1.03	1.2 ± 0.1	0.21 ± 0.04	62.8 ± 1.4	134.4 ± 9.7	198.01 ± 0.01	0.94 ± 0.02	1.4 ± 0.1	4.763		
PEKI26	31.88 ± 1.05	8.6 ± 1.1	1.4 ± 0.1	0.72 ± 0.02	3.9 ± 1.1	117.5 ± 2.1	19.01 ± 0.01	0.39 ± 0.02	2.4 ± 0.2	4.433		
PEKI27	133.9 ± 2.8	68.70 ± 1.02	2.5 ± 0.7	0.6 ± 0.1	94.8 ± 1.7	174.0 ± 3.6	199.02 ± 0.01	0.9 ± 0.3	4.1 ± 1.4	1.987		
PEKI28	71.9 ± 1.5	48.38 ± 1.01	-3.1 ± 1.2	1.2 ± 0.1	123.7 ± 1.9	258.4 ± 3.9	199.2 ± 0.1	0.6 ± 0.3	—	-2.245		
PEKI29	35.09 ± 1.03	6.9 ± 1.05	1.8 ± 0.2	0.8 ± 0.2	8.9 ± 1.4	122.3 ± 2.2	19.2 ± 0.1	0.3 ± 0.2	3.4 ± 0.4	3.586		

Chapter 4

A model for saturation correction in meteor photometry

Originally published as:

Kikwaya, J.B., Weryk, R.J., Campbell-Brown. M, Brown, P.G. (2010). A model for saturation correction in meteor photometry, *Monthly Notices of the Royal Astronomical Society*, **404**, 387-398.

4.1 Introduction

Our knowledge of meteoroids, particularly regarding their physical properties (composition, structure, etc.) has improved in the last century thanks to successive improvements in radio and optical instruments (radar, photographic Super-Schmidt and low light level television systems, for example). Determining the physical properties of meteoroids generally depends on observing the deceleration and mass ablated as a function of time; in other words it requires precise observations of position and brightness or ionization at many points along the meteor trail.

Radio observations have the advantage of observing in daytime and through clouds. However, transverse backscatter systems provide ionization information for only one point (or, with special systems, a handful of points); they are therefore of little use for compositional studies. Radial scatter (High Power Large Aperture, or HPLA) systems can measure ionization at many points (Campbell-Brown & Close, 2007), and can be used to generate ionization curves, but the observing biases and calibration from scattered power to mass are still poorly understood.

Some of the most complete studies of the complex physical structure of meteoroids have come from the analysis of optical meteors recorded by Super-Schmidt cameras (Jacchia & Whipple, 1961). Jacchia, Verniani & Briggs (1967a,b) provided precise information on the orbits, trajectories, decelerations and light curves of over four hundred meteors down to about a magnitude of +3. From these analyses, the idea of a meteoroid as a conglomerate of tiny grains began to emerge. Differential deceleration (inferred from the presence of wake), irregularities in light curves and shorter trail lengths further supported the idea that meteoroids are conglomerates of tiny grains.

However, Super-Schmidt cameras are restricted to meteors brighter than a magnitude of +3. A complete understanding of the physical structure of meteoroids and how they ablate can only be obtained by extending optical techniques to fainter meteors. This became possible with the introduction of low-light-level electro-optical

techniques in the 1960s, modern versions of which have limiting magnitudes from +6 to +9 (see Hawkes and Jones, 1986).

The sensitivity of image intensified video is much greater than photographic film, but it has drawbacks. TV systems typically have much lower resolution than photographic film, resulting in larger errors in computed trajectories and orbits. Photometry is also more difficult: video is typically digitised as 8-bit grayscale images, meaning each pixel can have a value from 0 to 255. A pixel saturates when too many photoelectrons are collected on one pixel, exceeding its full well capacity (Howell, 2000). When this happens, blooming can occur as the image of a bright object spills onto neighbouring pixels, but the maximum pixel value is truncated at 255. The cross section of an unsaturated meteor is generally assumed to be Gaussian, but a saturated meteor is clipped above a pixel intensity of 253 ADUs. In general, the brightness of a meteor which saturates a CCD detector will be underestimated due to the clipping. This will also cause the photometric mass to be underestimated.

The mass distribution index of meteoroids is important when estimating the hazard to spacecraft. Mass distribution indices of sporadic meteors can be calculated by plotting the distribution of masses of observed meteors (eg Hawkes & Jones, 1975, who found $s = 2.02 \pm 0.04$ for TV meteors), or by counting the number of meteors observed with different limiting magnitudes (Clifton 1973, $s=2.26$; Cook et al. 1980, $s=2.33$). These two techniques have produced significantly different values for the mass distribution, and part of the difference may be due to saturation effects in mass calculations.

Density is an important property of meteoroids since it can help to determine their physical characteristics, particularly composition and structure. Because the photometric mass of a meteoroid is involved in the computation of its density, accurate photometric masses are critical to determining the density of the meteoroid. If the saturation correction is not applied for bright, saturated meteors, the photometric mass will be underestimated and the density derived will tend to be overes-

timated.

Swift, Suggs & Cooke (2004) developed a program, METEOR44, to determine the unique saturation correction for a particular camera/lens set. In their setup, an artificial, fixed star of variable brightness is created in the laboratory using a turning wheel with a neutral density filter of varying density. Standard photometric routines are used to determine the magnitude of this artificial star and a power law function is applied to fit the magnitude versus filter transparency. This power law can then be used to find the true magnitude of a meteor. Swift, Suggs & Cooke (2004) applied this technique to one night of observations during the 2001 Leonid storm. The masses thus obtained were shown to be significantly different from those obtained with no saturation correction. The advantage of this technique is that a large dynamic range of brightnesses/saturation corrections can be measured under controlled conditions. The main difficulty with this method is that it is time consuming to set up (unless a dedicated lab setup is maintained), and must be redone each time the camera or intensifier settings are changed. Furthermore, the method uses only a point source in the calibration; most meteors have significant angular velocity and the spread of the meteor across the detector is not taken into account. Extended sources are also difficult to accurately replicate in the laboratory.

In this work, we will instead model the response of an image intensified video instrument, taking into account the angular speed of the meteor, the background of the image and the width of the meteor. The goal is to correct the clipped profile of a saturated meteor to account for the light which is missed. The model will be tested against actual meteor data taken with image intensified video cameras.

4.2 Observations and Equipment

Data were collected on two nights: October 31st, 2008 and November 6, 2008 from 04:00 to 10:00 UTC. Third generation (Gen III) ITT NiteMate microchannel plate

image intensifiers with 18 mm GaAs detectors were used (for technical details about these Gen III intensifiers, see Hawkes et al., 2001). These were lens coupled to Cohu 4910 series video CCD cameras, which are high performance, relatively sensitive, monochrome CCD cameras with analog output (Hawkes et al., 2001). We used two of these systems, identified as T and Q, on each of which a 25mm Fujinon f/0.85 lens was used as the objective.

Gen III intensifiers are similar to Gen II, in that they are less susceptible to blooming than first generation intensifiers when imaging bright point objects. The main improvement over previous generations is tube lifetime, sensitivity at longer wavelengths and the elimination of persistence from one video frame to another, making it possible to accurately measure the light from the meteor in each frame.

The observations took place at Elginfield, Ontario, Canada ($43^{\circ} 11'58$ N, $81^{\circ} 18'90$ W), near London, Ontario. The two cameras, T and Q, had a common pointing direction of 42° altitude and 181° astronomical azimuth. Since no major showers were active, a convenient direction was chosen which was easily found with both cameras, since they had to be pointed identically. The 8-bit, 640x480 pixel images were streamed directly to computer at the standard NTSC rate of 30 interlaced frames per second. No compression routines were involved in the storage of the image data. Individual deinterlaced fields (60 per second) were used in this work (see also Hawkes et al., 2001).

The field of view of each system was $34.4^{\circ} \times 24.9^{\circ}$, producing a resolution of 0.05° per pixel ($3.1'$ per pixel). For a meteor occurring at an altitude of 100 km, one pixel represents 94 m. The limiting stellar magnitude of each video camera system was between +7.5 to + 8 with the lens iris fully opened.

4.3 Data and Reduction

At the beginning of each night of observations, we set the gain of each camera (T and Q) identically. The f-stop on each of them was set to $f/0.85$ and the cameras were identically focused. Line profiles of pixel brightness across images produced by each camera were compared in real-time to verify that the background was the same, so that the two cameras would have identical detection probabilities. On the first night, the gain of both cameras was set so that the background was 50 ADUs; on the second night, in order to obtain more background stars for calibration on camera Q, we increased the gain on both cameras so that the background was 70 ADUs.

To collect data for this saturation study, the lens aperture on camera Q was reduced two stops, to $f/2$, decreasing sensitivity by a factor of 4. With this arrangement, a very bright meteor which saturated camera T might not saturate camera Q. Our approach is to collect meteors where the light curve can be found with no saturation correction from the camera Q observation, and this can be used to correct the saturated part of the light curve from the camera T data. This will then be compared to the predicted correction from the saturation model. As well, we will examine a smaller number of common events saturated on both cameras (but to different degrees) and apply model corrections to both cameras to check for agreement.

On the first night of observations (October 31, 2008) we collected 256 meteors, and on the second night (November 06, 2008) 260 meteors were captured. The value of each pixel within a meteor trail determined whether or not a particular meteor was considered saturated. Since our system generates 8-bit images, any pixel with a value of 255 is saturated; but analysis showed that saturation in our system occurs sooner, at pixel values of 253, because of the digitization process. In Fig. 4.1, Fig. 4.3 and Fig. 4.4, all pixels with values greater than 253 appear in solid gray to clearly discriminate them from unsaturated pixels. Based on the saturation data,



Figure 4.1: Meteor recorded on October 31, 2008 at 09:38:50 UTC, which saturated camera T



Figure 4.2: Same meteor captured on October 31 2008 at 09:38:50 UTC on camera Q, which was not saturated.

we sorted the meteors into three different groupings. The first group consisted of all the meteors that saturated camera T and did not saturate camera Q (Fig. 4.1 and Fig. 4.2): there were 30 meteors in this group. The second group (7 meteors) were very bright meteors which saturated both cameras T and Q (Fig. 4.3 and Fig. 4.4). The third group contains all the faint meteors which did not saturate either of the cameras. Group III contained 479 meteors, or nearly 93% of the sample. This shows that most light curves collected with these cameras do not require saturation corrections: this work affects only the brightest meteors. The fraction of bright meteors will be higher during showers, which tend to have more large particles, so typical shower data would have a greater fraction of affected meteors. We should note, however, that the brighter meteors often penetrate deeper and show more deceleration so are more frequently used in physical studies requiring such data.

We were particularly interested in meteors belonging to groups I and II. In the case of group I, we can correct the saturated light curve from camera T with the model, and compare the result with the unsaturated light curve from camera Q to verify that the model correction is valid. For group II, where both cameras were saturated, we can correct both light curves with the model and confirm that the results are consistent.

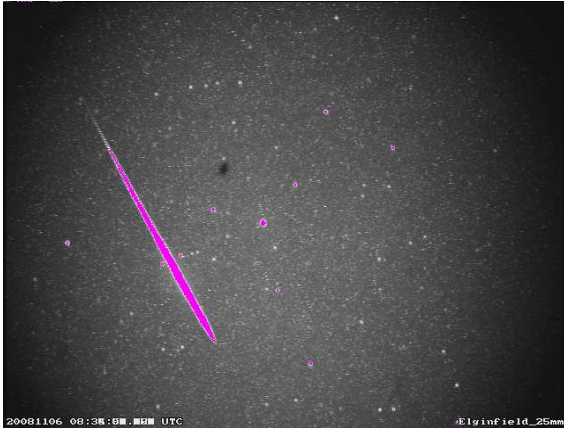


Figure 4.3: Meteor recorded on November 06, 2008 at 03:34:58 UTC, which saturated camera T



Figure 4.4: Same meteor captured on November 06 2008 at 03:34:58 UTC; it also saturated camera Q

We used standard routines for the meteor photometry. For both group I and group II meteors, each frame is flat fielded, and the photometric magnitude of the meteor is computed by calibrating the log-sum-pixel of the meteor with those of surrounding stars (see Hawkes et al., 2001; Hawkes, 2002). The log sum pixel of each star is calculated by taking a disc covering the whole star and a surrounding ring representing the background. The median value of pixels in the ring is subtracted from the disc (taking into account pixel areas), and the instrumental magnitude of the star is computed as the logarithm of the sum of the pixel intensities in the disc: these are compared to catalog V magnitudes (from SKY2000v4, Myers et al., 2001) with a linear fit to obtain the calibration. The linear fit has a fixed slope of unity, and the offset of the line gives the calibration of the system. A typical error of 0.1-0.3 magnitudes is found for each star. At fainter magnitudes, this error is dominated by counting statistics and shot noise in the intensifier. At brighter magnitudes, the error is primarily due to uncertainty in the photometric calibration. Photometric measurement errors are determined using standard error techniques, where the standard deviation of the photon count is governed by Poisson statistics. This gives an error in the photometric magnitude of $2.5/\sqrt{N}$ (where N is the pixel intensity sum, proportional to the number of photons), to which the error

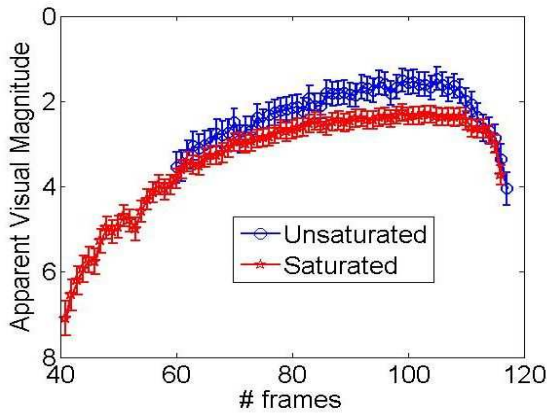


Figure 4.5: Observed light curve of meteor 20081031-093850; saturated, from camera T, and unsaturated, from camera Q

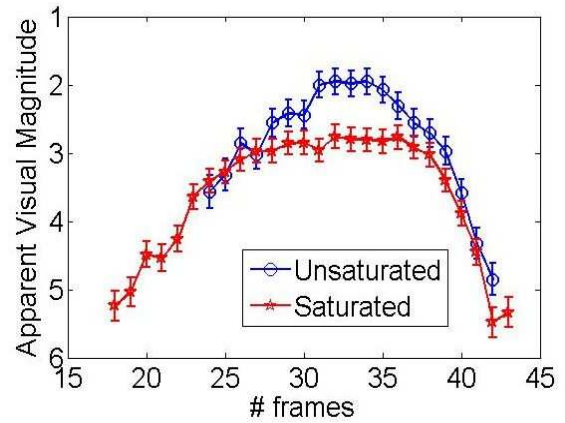


Figure 4.6: Observed light curve of meteor 20081106-081528; saturated, from camera T, and unsaturated, from camera Q

from the photometric calibration is added. The light curves are kept in apparent, rather than absolute, magnitudes, since the range to the two cameras is identical.

As an example, the light curve of meteor 20081031-093850, a group I member which occurred on October 31, 2008 at 09:38:50 UTC, is shown in Fig. 4.5. The saturated light curve from Camera T has a peak magnitude of $+2.3 \pm 0.3$, while the unsaturated light curve from camera Q has a peak magnitude of $+1.5 \pm 0.3$. A maximum correction of 0.8 magnitudes, added to the saturated light curve, is needed to make the two curves agree. Meteor 20081106-081528 shows a difference of 0.9 magnitudes at peak magnitude between the saturated light curve from camera T and the unsaturated light curve from camera Q (Fig. 4.6). For this meteor, saturation occurs at a magnitude of about $+2.8$: from frame 27 to 38 the saturated light curve shows a plateau which is not seen in the unsaturated curve.

Table 4.1 gives the relevant information for the 30 meteors of group I for which we apply model corrections.

4.4 Saturation Correction Model

When the individual frames of an unsaturated meteor are studied, we find that their transverse cross sections have a Gaussian profile. This is consistent with the fact

Table 4.1: Saturation correction for all 30 group I meteors. Max saturated (observed) is the brightest mag among all saturated photometrically measured points on the meteor light curve, Max unsaturated (observed): the brightest point among all unsaturated points, Max deviation at peak correction: deviation between the observed apparent magnitude and the modelled corrected magnitude (the average deviation is smaller), Peak correction: the largest correction applied to the saturated light curve by the model correction.

Name	Angular velocity (pixels/second)	Max saturated (observed) (visual magnitude)	Max unsaturated (observed) (visual magnitude)	Max deviation at peak correction (magnitude)	Peak correction (magnitude)
20081031-025809	220.7	2.6 \$ 0.1	1.9 \$ 0.2	0.7 \$ 0.2	0.9 \$ 0.1
20081031-044135	193.3	2.9 \$ 0.2	2.5 \$ 0.2	0.3 \$ 0.3	0.5 \$ 0.2
20081031-045229	367.0	1.9 \$ 0.2	1.6 \$ 0.2	0.3 \$ 0.3	0.5 \$ 0.2
20081031-061407	341.0	1.9 \$ 0.2	1.3 \$ 0.2	0.7 \$ 0.3	0.9 \$ 0.2
20081031-072447	338.0	1.9 \$ 0.2	1.3 \$ 0.2	0.6 \$ 0.3	0.9 \$ 0.2
20081031-080212	354.1	2.3 \$ 0.1	1.5 \$ 0.2	0.7 \$ 0.3	1.1 \$ 0.2
20081031-083454	256.3	2.4 \$ 0.2	1.9 \$ 0.2	0.3 \$ 0.3	0.5 \$ 0.2
20081031-083900	227.1	2.7 \$ 0.2	2.3 \$ 0.2	0.3 \$ 0.2	0.4 \$ 0.2
20081031-093448	174.0	2.9 \$ 0.1	2.5 \$ 0.2	0.4 \$ 0.3	0.3 \$ 0.1
20081031-093850	392.6	2.3 \$ 0.2	1.5 \$ 0.3	0.8 \$ 0.3	0.8 \$ 0.2
20081106-051738	417.0	2.8 \$ 0.2	2.6 \$ 0.2	0.3 \$ 0.2	0.6 \$ 0.2
20081106-053718	376.9	2.9 \$ 0.2	2.2 \$ 0.2	0.7 \$ 0.3	1.1 \$ 0.2
20081106-062345	340.3	3.2 \$ 0.2	2.3 \$ 0.1	0.8 \$ 0.2	1.2 \$ 0.2
20081106-064748	438.0	3.2 \$ 0.2	2.3 \$ 0.1	0.8 \$ 0.2	0.9 \$ 0.2
20081106-072145	339.0	2.9 \$ 0.2	2.3 \$ 0.2	0.5 \$ 0.3	0.7 \$ 0.2
20081106-073324	360.0	3.5 \$ 0.2	3.2 \$ 0.2	0.2 \$ 0.3	0.4 \$ 0.2
20081106-073649	360.0	3.2 \$ 0.2	2.8 \$ 0.2	0.5 \$ 0.3	0.7 \$ 0.2
20081106-074239	418.6	2.8 \$ 0.2	1.7 \$ 0.2	1.4 \$ 0.2	1.8 \$ 0.2
20081106-081528	396.8	2.8 \$ 0.2	1.9 \$ 0.2	0.8 \$ 0.2	0.9 \$ 0.2
20081106-082229	387.3	2.5 \$ 0.2	1.5 \$ 0.2	0.9 \$ 0.2	1.1 \$ 0.2
20081106-082820	363.0	3.3 \$ 0.2	2.9 \$ 0.2	0.3 \$ 0.3	0.4 \$ 0.2
20081106-083743	447.0	3.2 \$ 0.2	2.5 \$ 0.2	0.4 \$ 0.2	0.5 \$ 0.2
20081106-092831	300.9	3.5 \$ 0.2	2.9 \$ 0.2	0.4 \$ 0.3	0.5 \$ 0.2
20081106-093156	444.0	2.8 \$ 0.2	1.9 \$ 0.2	0.8 \$ 0.3	1.0 \$ 0.3
20081106-093831	402.0	3.2 \$ 0.2	2.6 \$ 0.2	0.5 \$ 0.2	0.6 \$ 0.2
20081106-094920	450.0	2.5 \$ 0.2	1.6 \$ 0.1	0.9 \$ 0.2	1.1 \$ 0.2
20081106-095543	306.0	3.2 \$ 0.2	2.7 \$ 0.2	0.5 \$ 0.3	0.7 \$ 0.2
20081106-100426	324.0	3.1 \$ 0.2	2.5 \$ 0.1	0.6 \$ 0.2	0.7 \$ 0.2
20081106-100524	423.0	3.0 \$ 0.2	2.4 \$ 0.2	0.5 \$ 0.2	0.6 \$ 0.2
20081106-101620	444.0	2.5 \$ 0.3	1.6 \$ 0.1	0.8 \$ 0.4	0.9 \$ 0.3

that a point source will have a Gaussian point spread function (PSF) and a meteor can be treated as a moving point source. In this work, we develop a new numerical model to correct the effects of saturation in bright meteor images. We will test the model using data from our specific Gen III image intensifiers coupled to video rate CCD cameras, but the approach is general and can be applied to most camera (except all-sky images since, with these systems, the meteor overhead appears much bigger than the one near the horizon).

Our frame-grabbers (based on the Brooktree 878 chipset) produce NTSC resolution images in an 8-bit YUV colour-space. Y (the luma component, as opposed to UV which are the chroma components) is defined in the interval 16-235, however our specific frame grabbers allow the range 16-253. Pixel intensities greater than 253 ADUs are clipped to 253, which means that any photometric measurements of clipped meteors will be underestimates.

The saturation correction has two components: one generates artificial meteor images by smearing out a Gaussian profile to mimic a recorded meteor, and the other is a model which calculates the correction term to be applied to these synthetic events because of saturation. We can test the model on the data collected: the artificial meteors are used to explore how the correction is influenced by the input parameters, outside the range of the collected data.

4.4.1 Synthetic lightcurve

To make light curves for testing, we use three principal inputs: the meteor angular speed (in pixels/second), the meteor width and the image background. Knowing the field rate of our camera, we determined the meteor angular speed by measuring the distance the meteor travelled in one field multiplied by the field rate. The entire image background is given by the average pixel intensity of the image background. The Gaussian standard deviation (width, σ) of the meteor is estimated to be approximately one pixel. From other studies (Kaiser et al., 2004) optical trail

width is less than » 10 meters, much smaller than one pixel. In our simulated data, the background has a constant value, so the position of the meteor in the field is unimportant.

Our simulator uses each field (field being a deinterlaced frame and having a rate twice the frame rate, in our case 60 fields/sec). The image size is set by default to 640x480 pixels, the same as our recorded data. The time step for sliding the point source in the computation is set by default to 0.0001 second and the frame rate to 60000/1001 second (60 fields per second). The time step of 0.0001 is chosen to provide enough steps to make the simulated trail smooth. The bit depth of images created was 8 bits and the Gaussian sigma was 1 pixel, to match the measured meteor widths.

At the beginning of the computation, an image 640x480 pixels with the background value is created and a synthetic meteor starts at the position (x,y)=(50,50) on the first field. This particular position is near the top left corner of the image; the direction of the meteor is set to -20 degrees (going toward the bottom right corner) to ensure that the entire meteor will remain inside the image for our range of required model angular speeds. The exact position and direction of motion is arbitrary.

To ensure that the change in meteor brightness with time were not missed, we choose an arbitrary function to simulate a lightcurve (Fig. 4.7). In our model, the function we chose is given by the expression (4.1). Any smooth shape that covers the desired dynamic range can be used.

$$M = 7.0 + 10.0 \sin\left(\frac{2.0 \pi t}{5.0}\right) \quad (4.1)$$

The function gives the magnitude of the simulated meteor as a function of time t (for $t=0$, the magnitude value is 7, close to the faintest magnitude found in real lightcurves given by our GenIII cameras).

The total intensity (sum of all meteor pixels in one field) is calculated from the

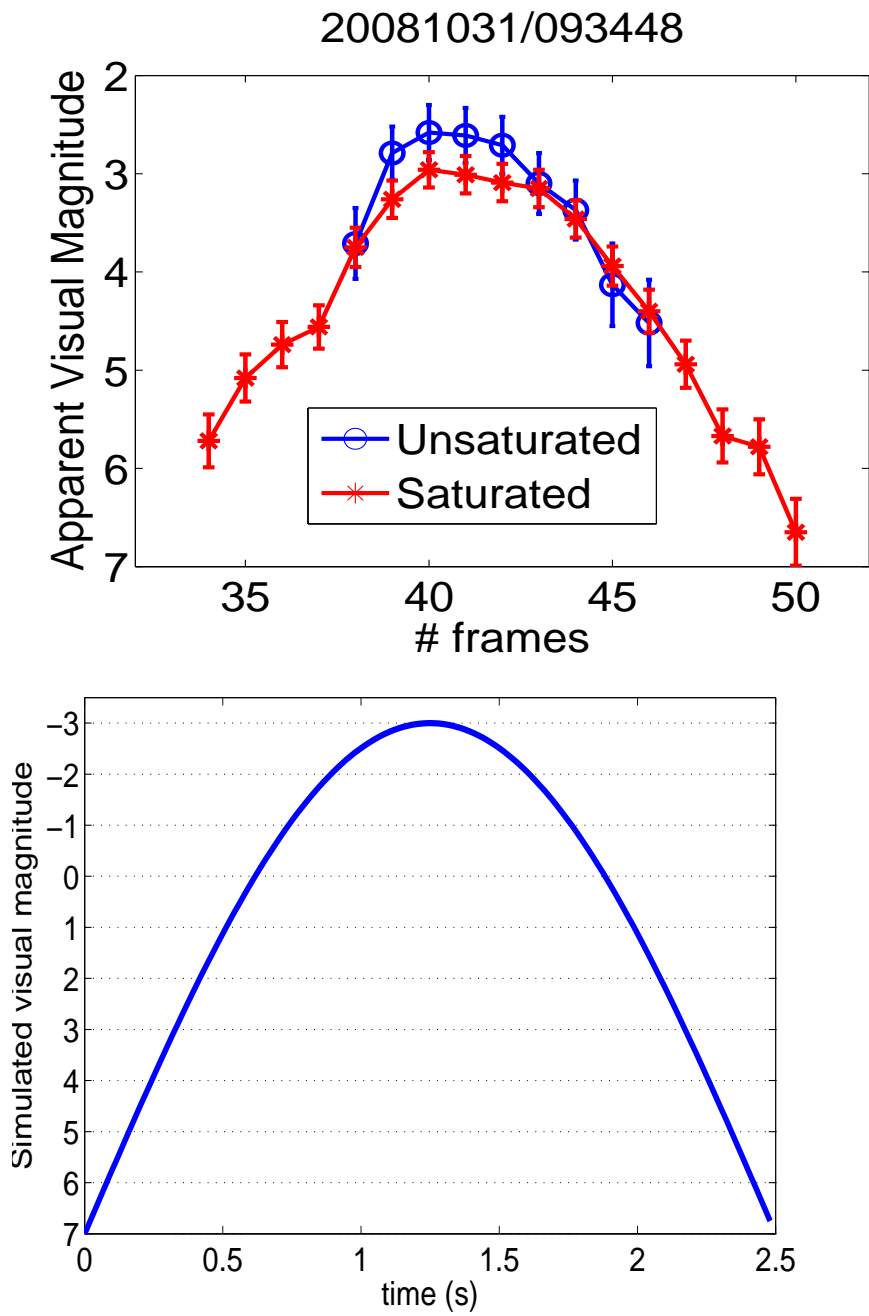


Figure 4.7: Top: Lightcurve of meteor 20081031-093438. Its shape demonstrates the gradual increase and decrease of a typical observed light curve: note the saturation effect on the more sensitive camera). Bottom: our function ($M = 7.0 ; 10.0 \times \sin(\frac{2.0 * \pi * t}{5.0})$) reproduces the general shape of the meteor lightcurve.

magnitude using equation (4.2) where M' is the uncalibrated magnitude (equal to M minus the appropriate stellar calibration offset for this camera).

$$\sum I = 10^{(M' / -2.5)} \quad (4.2)$$

At each time step to the end of the field exposure, we draw a Gaussian whose amplitude A is given by (4.3) and spread the total intensity over a ten pixel radius of the per-step meteor position using (4.4) where P is the ADU pixel value at the distance r . We choose 10 pixels, as the numerical values this far from the center using our Gaussian expression become negligible. The position is then updated at each step and the process repeated. Because of the small width, there is little change in pixel value beyond a few pixels. When the frame is complete, the pixels are clipped to 253, to mimic the real data. See Fig. 4.8 for the algorithm.

$$A = \frac{\sum I}{2 \pi \sigma^2} \quad (4.3)$$

$$P = A e^{(-0.5 * \frac{r^2}{\sigma^2})} \quad (4.4)$$

4.4.2 Numerical saturation model

The saturation model can now be applied to the simulated data to investigate the effects of the input parameters on the saturation correction. For both the simulated and real data, the apparent magnitude, background value, meteor angular speed, frame rate, and Gaussian width of the meteors are required for input. The model creates a single artificial meteor frame by smearing a Gaussian in a small (20 x 20 pixel) sub-frame, using the apparent magnitude to generate the intensity profile. This profile is clipped to simulate saturation, and its clipped magnitude is compared to the input. If the input is unsaturated, this model output will be the same as the input. If the input is saturated, the model output will be too small. If saturation is

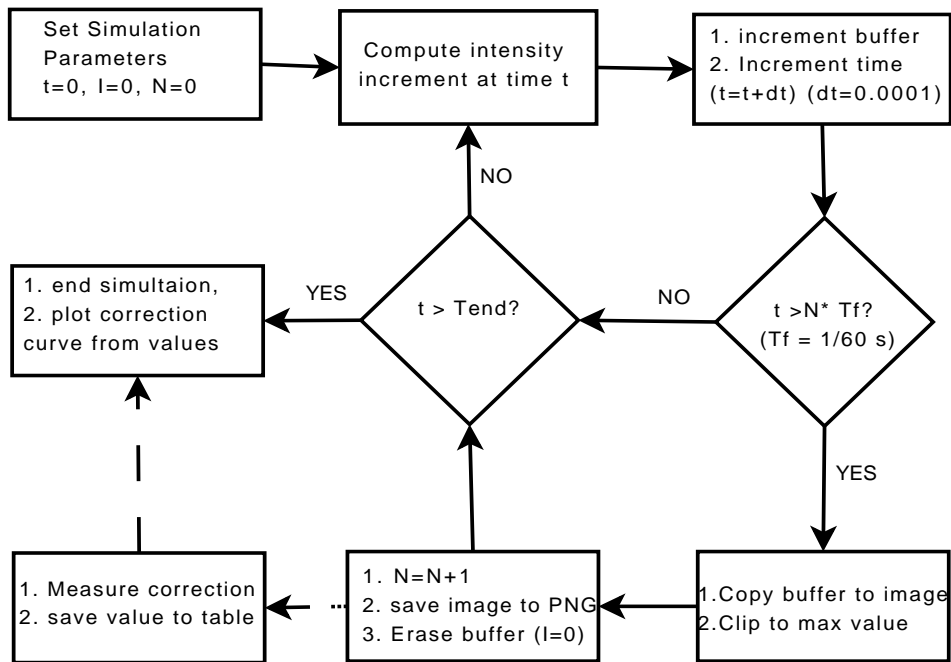


Figure 4.8: Diagram detailing the procedure used to create the artificial light curve. T_f is time of a deinterlaced frame (16 ms), N is the current frame number, dt is the time step, T_{end} is the light curve total time and I represents intensity of the simulated meteor in the virtual frame buffer that has no saturation limit. Two left bottom boxes: once a frame is complete, it is saved and will be used by a separate step while the program continues in the upward direction.

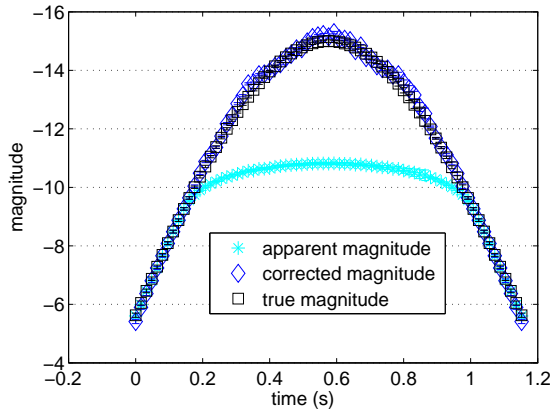


Figure 4.9: Synthetic meteor created with an angular speed of 300 pixels/second, background of 50 ADUs and σ of 1 pixel. The true magnitude is from the synthetic data without applying saturation; the apparent magnitude shows the lightcurve when any pixel with a value more than 253 ADUs has been clipped to 253 ADUs. The corrected magnitude is the apparent lightcurve corrected using our model of saturation correction.

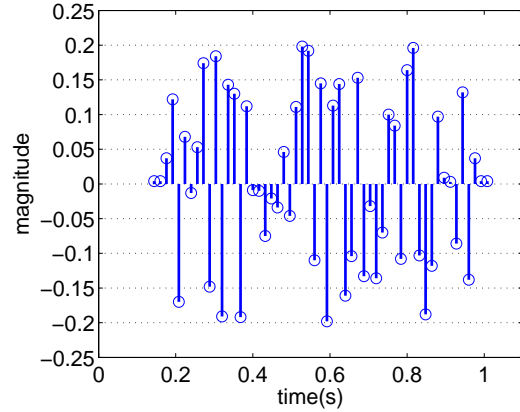


Figure 4.10: Residuals between true magnitude and corrected magnitude of the synthetic lightcurve created with an angular speed of 300 pixels/second, background of 50 ADUs and σ of 1 pixel. The points at the beginning and end, where the correction was close to zero, are not plotted. Our model of saturation correction shows a residual average (rms) of 0.10 magnitudes

present, the artificial meteor is scaled by a small factor using an iterative procedure and the new output is compared until the model output matches the input.

As an illustration, we created a synthetic meteor with an angular speed of 300 pixels per second, a background of 50 ADUs, and a Gaussian standard deviation (σ) of 1 pixel (Fig. 4.9). From the true synthetic lightcurve, by clipping each pixel with a value more than 253 ADUs to 253 ADUs, we extracted the synthetic apparent lightcurve. This is what would be observed by a real-world camera. Using this apparent lightcurve, we were able to compute its corrected synthetic lightcurve using the model. The example shows that the corrected lightcurve is close to the original, unclipped lightcurve to within 0.3 magnitudes (Fig. 4.10).

4.4.3 Effect of input parameters on saturation correction

There are three variables in our model that control where the saturation begins: background brightness, angular meteor speed and meteor width. The average background value in the image must first be measured, as it limits the true dynamic range of the image. For example, if the background level is 50 ADUs, then there are 203 effective ADUs before saturation. If the background is 75 ADUs, then there are only 178 effective ADUs before saturation. Fortunately, the background level is very straightforward to measure. In Figs. 4.11 and 4.12, the angular meteor speed is fixed at 50 pixels per second, the Gaussian σ at 1 pixel, and the background is varied from 10 to 70 ADUs. The apparent magnitudes (ie. what a real-world camera would see) are plotted against the corresponding true unsaturated magnitudes. These values are log-sum-pixels where calibration is not yet applied. This particular simulation, based on background variation, shows that the meteor saturation point (where the measured magnitude diverges from the true magnitude becomes fainter) when the background increases, as expected. Figure 4.12 gives the saturation correction term versus the corresponding apparent magnitude.

The angular speed of the meteor is the next factor affecting the amount of saturation in an image. Because the meteor is a smeared out Gaussian, the faster it moves across the CCD, the more spread out its light will be, meaning that any individual pixel will not integrate as much light (ie: the dwell time over any particular pixel is reduced). Like the background level, the angular speed is also straightforward to measure. To simulate the effects of angular meteor speed with our synthetically generated meteors, we kept the background fixed at 50 ADUs and the meteor Gaussian standard deviation at 1 pixel, and varied the model meteor speed from 50 to 400 pixels/second. The saturation point as a function of meteor angular speed is shown in Fig. 4.13. Figure 4.14 shows that the correction term varies more with speed variation than with background variation. For instance, for an apparent uncalibrated saturated magnitude of -10.0 magnitude (see Fig. 4.14), the correction term goes

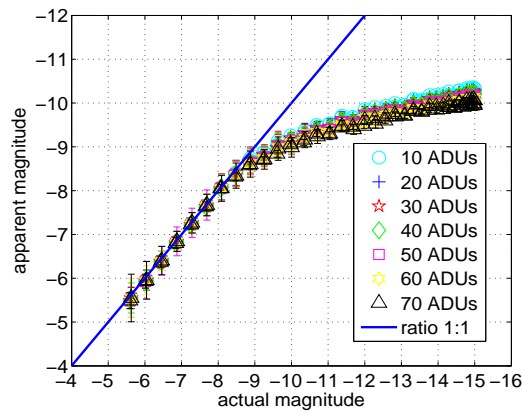


Figure 4.11: Simulated starting saturation point when the background level is varied from 10 ADUs to 70 ADUs. True model magnitude is the magnitude measured taking into account the total amount of light from the model while apparent model magnitude is the model magnitude taking into account the saturation effect. The apparent magnitude is what a camera would record. The Meteor saturation point decreases (becomes fainter) as the background increases.

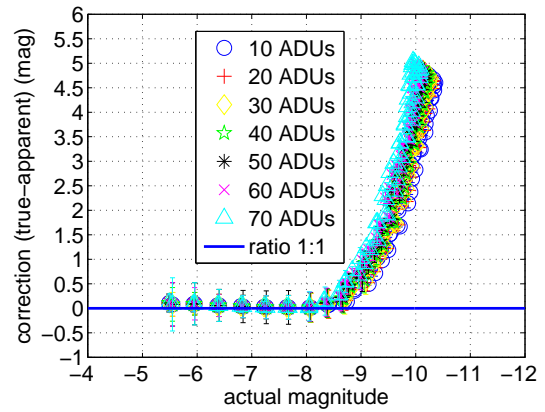


Figure 4.12: Saturation correction for saturated light curve as the background level is varied from 10 ADUs to 70 ADUs. The correction represents the magnitude to be added to the apparent model magnitude to correct the effect of saturation to reach the true input model magnitude. For instance, for an apparent model magnitude of -9.0 magnitude, the correction term goes from about 0.5 magnitude for a meteor with a background of 10 ADUs to almost 1.0 magnitude for a meteor with a background of 70 ADUs.

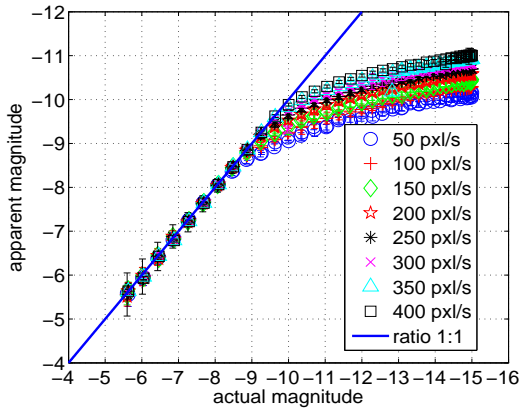


Figure 4.13: Simulated saturation point with varying angular meteor speed from 50 pixels/second to 400 pixels/second. True model magnitude is the magnitude measured taking into account the total amount of light as input from the model and apparent model magnitude is the magnitude which would actually be measured, taking into account the saturation effect. The meteor saturation point decreases (becomes fainter) as the speed decreases, as expected since light spreads over fewer pixel at lower angular speeds.

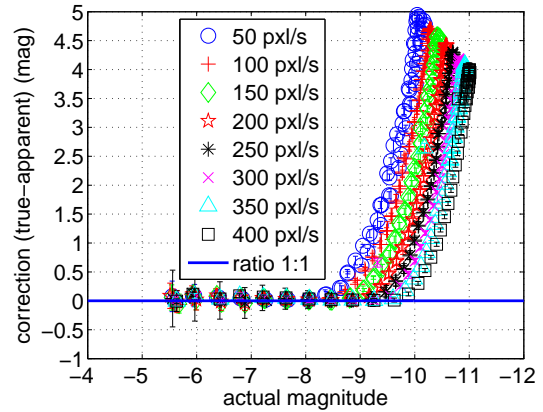


Figure 4.14: Saturation correction for saturated meteor points with varying angular meteor speed from 50 pixels/second to 400 pixels/second. The correction represents the magnitude to be added to the apparent model magnitude to correct the effect of saturation. For instance, for a particular apparent model magnitude, the correction term increases as the meteor speed decreases.

from about 0.5 magnitude for a speed of 400 pixels/second to 2.0 magnitudes for a meteor speed of 200 pixels/second.

Lastly, the width of the Gaussian profile used in the simulated images must correspond to the width of a real meteor. We found by direct measurement of many real meteor images that the vast majority of meteors have a constant Gaussian σ around 1 pixel for our systems; this is consistent with the fact that the luminous region around a meteor (see Kaiser et al., 2004) is much smaller than the pixel resolution (which is of order 100m for the systems used in this study). We give in Figs. 4.15 and 4.16 some results of simulated saturation corrections as the width is varied. We varied the meteor Gaussian width from 0.7 to 1.3 pixels and kept fixed the meteor speed at 250 pixels/second and the background at 50 ADUs. The saturation starting point decreases (becomes fainter) as the meteor width decreases

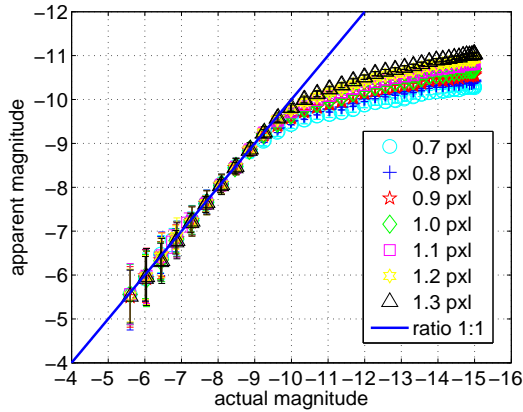


Figure 4.15: Simulated saturation point with varying meteor Gaussian width from 0.7 pixels to 1.3 pixels. True model magnitude is the magnitude measured taking into account the total amount of light and apparent model magnitude is the model magnitude taking into account the saturation effect. Meteor saturation point decreases (becomes fainter) as the meteor width decreases.

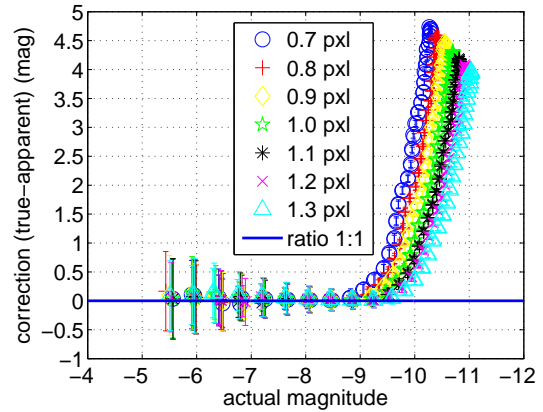


Figure 4.16: Saturation correction for saturated light curve with varying meteor gaussian width from 0.7 pixels to 1.3 pixels. The correction represents the magnitude to be added to the apparent model magnitude to correct the effect of saturation. The correction term increases as the meteor width decreases.

(a meteor with a smaller Gaussian width would start to saturate earlier than a meteor with a bigger Gaussian width). For instance, a meteor with a width of 0.7 pixels starts to saturate around -9.0 uncalibrated magnitude in our simulation, while the one with a width of 1.30 pixels will begin to saturate only around -10.0 uncalibrated magnitude. The correction term, as with angular meteor speed, varies more with meteor width than image background. For an uncalibrated saturated meteor frame of -10.0 magnitude (see Fig. 4.16), the correction term goes from 0.5 magnitude for a meteor width of 1.3 pixels to 2.0 magnitudes for a meteor width of 0.8 pixels.

It is important to note that our model can introduce errors if meteors behave differently than we have assumed. For example, our correction is questionable if a meteor is not a point object (and thus has a non-Gaussian PSF); when it is very bright (causing ringing in the video signal due to camera bandwidth limitations); or when other artifacts are present (such as an extended wake along the meteor trail).

It may be possible to include these effects in a future version of this correction model. However, as we will show in the next section, our numerical model produces good results when applied to typical observed meteors, so deviations would appear to be the exception not the rule. Another effect which must be considered is reciprocity failure, in which the response of a CCD becomes nonlinear before just saturation. However, it seems the camera systems used in this study are not strongly affected by this effect. Hawkes (2002) notes that the intensified and CCD response are "surprisingly" linear even well into the saturation regime (cf Hawkes, 2002, p.110). We neglect non-linear effects, but caution that such effects could be significant for large saturation corrections and/or other camera systems.

4.5 Results

We first compared the simulated saturation correction with the observed group I meteor data. If the model correction makes the saturated light curve agree with the unsaturated one, we will have confidence using it in future studies to correct saturated light curves with our cameras. Each meteor will be simulated (using the observed parameters as input into the model) and the difference between the model saturated and model unsaturated magnitudes will be used to correct the observed saturated light curve. For each saturated curve, we obtain the background level, extracted from the meteor images from camera T, and the angular meteor speed, as the measured change in position of the meteor from one frame to another. The angular meteor speed is nearly constant from frame to frame. The Gaussian σ of the meteors was taken to be 1.0 pixel in all cases.

The magnitudes generated by the model are in instrumental magnitudes: we determine the offset to convert the observed light curve to an apparent visual magnitude by comparison with the stars in the image (around 100 stars for camera T and 80 stars for camera Q), and use the same conversion to calibrate the simulated

light curve.

In practice, the model generates a simulated lightcurve, not the one that we observe. Actually, the shape does not matter as we are interested in the correction only at one specific magnitude. We run the model with the three input values measured on an observed meteor, and obtain a saturated and unsaturated curve. We use interpolation between two values closest to the observed saturated magnitude to find the corresponding unsaturated model magnitude, and take the difference to obtain a correction factor. This is subtracted from the observed saturated magnitude to obtain a corrected magnitude for the saturated curve. In calculating the uncertainty for the corrected light curve, we neglect the uncertainty introduced by errors in the model, since the measurement errors in the observed magnitude are expected to be much greater. We do not discriminate the saturated and unsaturated points in the observed camera T light curve, but calculate correction factors for all of them: the model automatically gives a correction of zero if a point on a light curve is not saturated.

4.5.1 Group I meteors

Application of this procedure to two typical group I meteors are shown. Meteor 20081031-093850 had a measured speed of 393 pixels/s. Figure 4.17 shows the saturation correction calculated for this particular meteor; it shows that the meteor begins to saturate at around +3.0 apparent magnitude. The figure 4.18 also gives the correction term as more and more of the meteor is saturated, up to +2.2 apparent magnitude. The biggest correction term is about 0.8 magnitudes.

Figure 4.19 shows the result when the model correction is added to the observed saturated light curve and compared with the observed unsaturated light curve for the same meteor. Figure 4.20 shows the residuals between the model-corrected saturated curve measured by Cam T and the unsaturated one observed by Cam Q. The first 19 points in this plot are unaffected by the saturation correction since

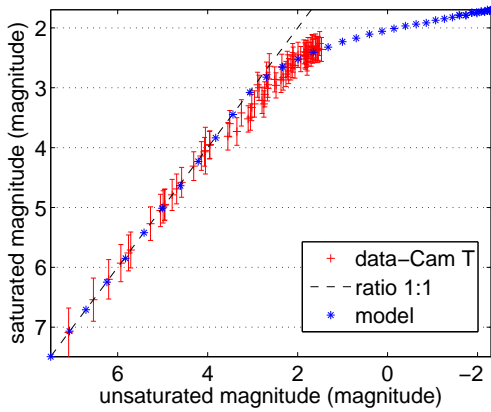


Figure 4.17: Modelled and observed light curve of meteor 20081031-093850

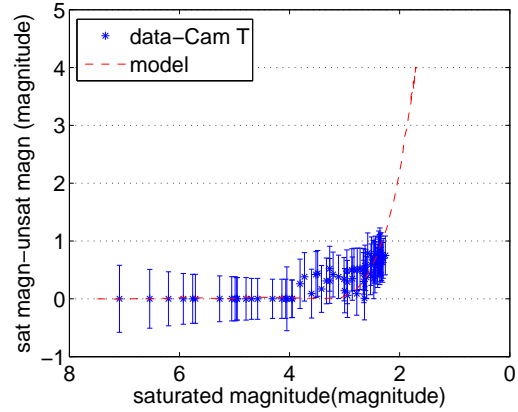


Figure 4.18: Saturation correction relationship for meteor 20081031-093850

the meteor was unsaturated in both cameras at that time. The root mean square (residual average) including the first 19 points is 0.25 magnitudes, showing that our saturation correction has very closely reproduced the unsaturated curve.

The saturated and unsaturated light curves of meteor 20081106-081528, measured by camera T and Q respectively, are plotted in Fig. 4.21, and the saturation correction is given in Fig. 4.22. We note that the meteor becomes saturated in camera T around +3.4 magnitude, 0.4 magnitudes brighter than the previous night; this is because of the change in the background value.

The model-corrected saturated light curve is compared with the observed unsaturated light curve from Cam Q in Fig. 4.23. Figure 4.24 gives the residuals between the model-corrected saturated light curve and the observed unsaturated one. The average value in residuals is about 0.18 magnitudes. Note that the first six points have residuals around 0.0 magnitudes; these are unsaturated points in both cameras.

Table 4.1 gives information for group I meteors. Column 1 gives the name of the meteor, based on the date and time the event occurred. Column 2 gives the observed angular velocity of the meteor in pixels per second as described above. Columns 3 and 4 contain the maximum value of the observed saturated light curve from camera T and the maximum value of the observed unsaturated light curve from camera Q. Column 5 lists the maximum difference between the saturated and

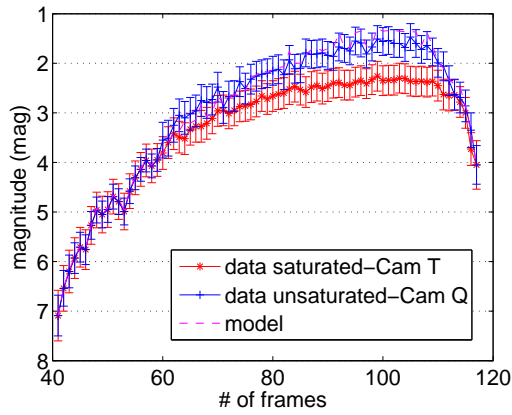


Figure 4.19: Saturated light curve observed by Cam T, observed unsaturated light curve by Cam Q and model-corrected saturated light curve from Cam T of meteor 20081031-093850

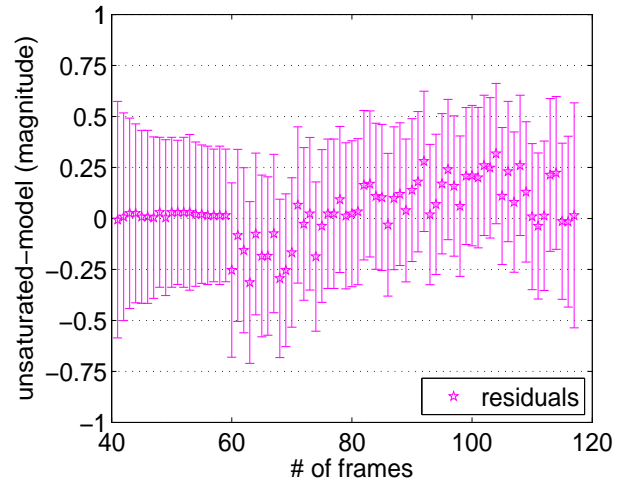


Figure 4.20: Residuals between observed unsaturated light curve measured by Cam Q and model-corrected saturated light curve from Cam T data for meteor 20081031-093850

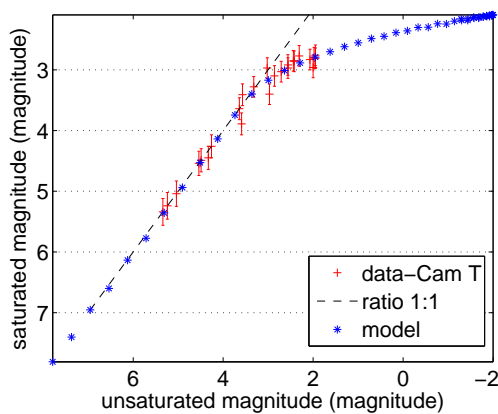


Figure 4.21: Modelled and observed light curves of meteor 20081106-081528

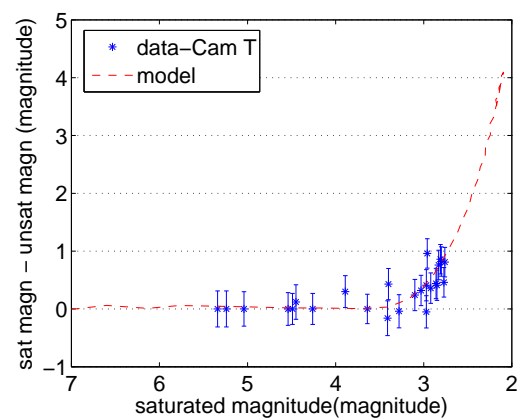


Figure 4.22: Saturation correction relationship for meteor 20081106-081528

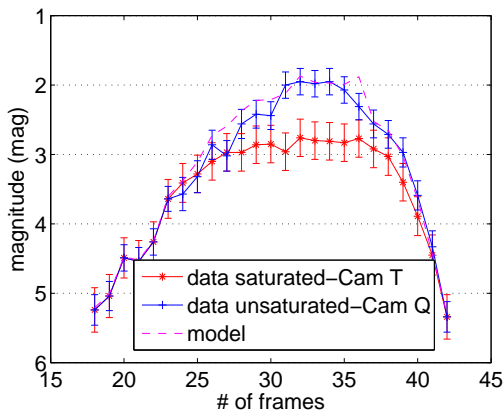


Figure 4.23: Saturated light curve, observed unsaturated light curve and modelled unsaturated light curve of meteor 20081031-093850. The model curve represents the correction of the saturated light curve applying model corrections.

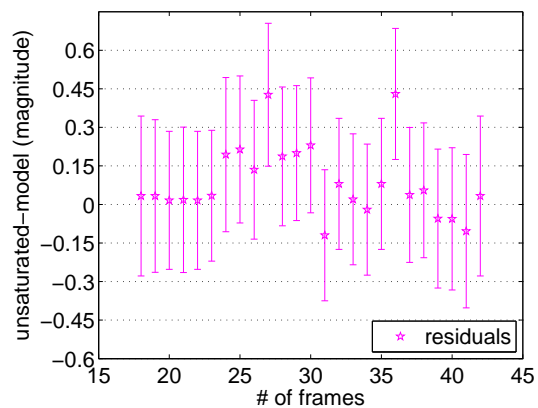


Figure 4.24: Residuals between observed unsaturated light curve from Cam Q and modelled unsaturated light curve for meteor 20081031-093850 based on correction of the observed saturated light curve from Cam T

unsaturated light curves, and column 6 gives the maximum correction value. The difference between column 5 and column 6 gives a measure of the deviation between the observed correction coming from the observed unsaturated light curve and the modelled correction provided by our saturation correction technique.

Table 4.1 shows clearly that the background is strongly related to the starting saturation point, and it must be taken into account in any saturation correction. On October 31, 2008, when the background was set at 50 ADUs, the peak saturated values for camera T occurred between +2.9 magnitude and +1.91 magnitude, while on November 06, 2008 – where the background reached the value of 70 ADUs – the peak saturated values ranged from +3.5 magnitude to +2.4 magnitude.

Table 4.1 shows that the maximum saturation correction for the 30 group I meteors was +1.8 magnitudes. This represents the information that would be lost if the saturation correction were not applied. At the peak correction, the difference between the observed unsaturated value and the corrected value varies, on average, from 0.1 magnitudes to 0.3 magnitudes. This demonstrates the importance of proper saturation correction, its variability and that our saturation correction technique is

an effective way to account for all the light in saturated light curves.

4.5.2 Group II meteors

The main limitation of studying Group I meteors is that there is an upper limit to the brightness of the meteors in this group due to the two stops difference in the lens between the cameras, and we are therefore not testing the saturation correction of the brightest meteors in the sample, since they saturate both cameras. In this case, we don't have a reference unsaturated light curve, but we can still test the consistency of the correction by applying it to both observed saturated light curves. Since the saturation level is different on the two cameras, the corrections applied will be different, but if they produce the same corrected light curve we can have confidence in our technique for brighter meteors too.

For each camera, the determination of the saturation starting point is crucial since points which are unsaturated will not be corrected. This point is estimated from the modelled correction curve. We noticed in the previous analysis that the smallest correction term is around 0.4 magnitudes. The first modelled saturated point whose difference with its equivalent modelled unsaturated point has an absolute value greater than 0.4 magnitudes (meaning that most of the meteor contains pixels with values greater than 253) will be considered the saturation starting point. All observed values fainter than the saturation starting point are unsaturated and therefore are not subject to any correction.

Among the 516 meteors collected on the two nights, we found 7 meteors which saturated both cameras T and Q. Table 4.2 summarizes all the relevant information about these group II meteors. Since we are now applying the model to meteors from camera Q, we must take into account the background level of that camera as well. On October 31, when camera T had a background of 50 ADUs, camera Q had a background of 30 ADUs; on November 6, camera T had a background of 70 ADUs and camera Q 50 ADUs. We again assumed a Gaussian standard deviation σ of 1

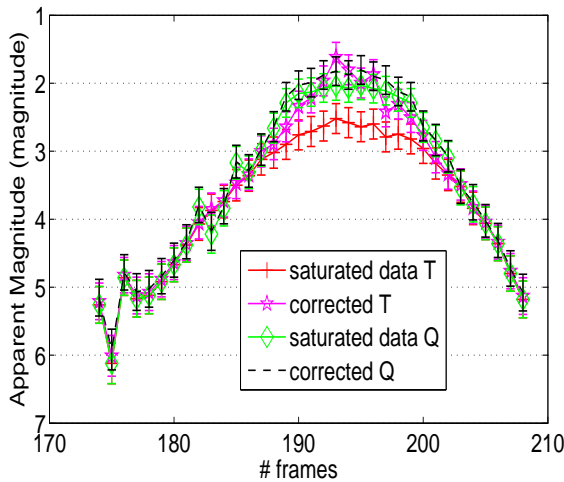


Figure 4.25: Saturation correction applied on both observed saturated light curves from camera T and camera Q for meteor 20081106-063244

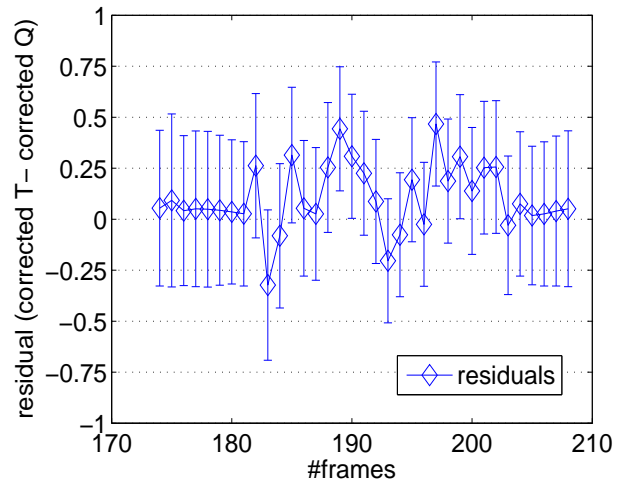


Figure 4.26: Residuals between the model-corrected saturated curves for T and Q.

pixel for all meteors. The angular speed is the same for both cameras. Note that these background differences do not affect measurements of unsaturated meteors.

As an example, 20081106-063244 is a very bright meteor which occurred on November 6, 2008 at 06:32:44 UTC. The angular meteor speed was 456.0 pixels/second. The two light curves and their corrections are shown in Fig. 4.25. The peak observed brightness on camera T is +0.9 magnitude, and on camera Q, +0.2 magnitude. This clearly shows the different saturation levels on the two cameras because of the difference in sensitivity. The maximum deviation between the corrected light curve from camera T and the corrected light curve from camera Q is 0.5 § 0.3 magnitudes, while the average residual between the two corrected light curves is 0.3 § 0.3 magnitudes (Fig. 4.26).

Table 4.2 gives a summary of all seven meteors belonging to group II. The residual average between the two corrected light curves of from cameras T and Q ranges between 0.2 and 0.3 magnitudes. The maximum deviation between the two corrections remains below 0.8 magnitudes, which is larger than the deviation in group I, probably due to the errors introduced when correcting both curves. The maximum

correction for meteors of group II ranges from 0.9 magnitudes to 2.1 magnitudes, a very significant correction because of saturation.

4.6 Discussion and Conclusion

Swift et al. (2004) is the only other work to attempt a correction for meteor saturation in video systems and report the procedure in detail. While we suggest that their technique applied to one night of observations during the 2001 Leonid storm gave different masses from those obtained without it, we need to note they did not take into account variations due to the background value of the camera and the angular meteor speed which do affect the apparent magnitude of a meteor in an intensified video system.

Our model was successful in correcting saturated light curves for group I meteors so that they matched the observed unsaturated curves. Brighter meteors cannot be directly compared with an unsaturated curve, but correction of two saturated curves with different saturation levels for group II meteors showed agreement between the two within error. Our saturation correction based on simulating the saturated meteors shows encouraging results even for very bright meteors.

In our total sample, only 7% of meteors saturated one or both cameras. Considering the small fraction of saturated meteors and the difficulty of reliably producing saturation corrections, it is clear why the full correction has not been attempted. Still, for those meteors which are saturated, our work has demonstrated that some meteors require corrections of up to 2.5 magnitudes, which will introduce order of magnitude errors into calculations of photometric mass if the correction were not applied. Other systems may produce higher fractions of saturated meteors, making the correction even more important. Our technique is also of value because it requires only basic knowledge of the video system and meteor being corrected, so no optical lab is required. Our technique does require the simulations to be redone ev-

Table 4.2: Saturation correction for all 7 meteors of group II. The table shows Max observed saturated (camera T): the brightest magnitude among all observed saturated points from camera T, Max observed saturated (camera Q): the brightest magnitude among all observed saturated points from camera Q, Max correction deviation, Average deviation: deviation between the observed saturated light curve of camera T and the correction applied to the light curve from the camera T and deviation between the observed saturated light curve of camera Q and the correction applied to the light curve from the camera Q, Peak correction: the largest correction applied to the light curve.

Name	Angular velocity (pixels/second)	Max observed saturated (camera T) (visual magnitude)	Max observed saturated (camera Q) (visual magnitude)	Max correction deviation (T and Q) (magnitude)	Average deviation (T and Q) (magnitude)	Peak correction (both T and Q) (magnitude)
20081031-045201	456.0	0.9 \$ 0.2	0.2 \$ 0.2	0.6 \$ 0.3	0.3 \$ 0.3	2.0 \$ 0.2
20081031-051216	498.1	0.9 \$ 0.2	0.2 \$ 0.2	0.8 \$ 0.3	0.2 \$ 0.3	2.1 \$ 0.2
20081031-063441	576.3	0.8 \$ 0.2	0.3 \$ 0.2	0.9 \$ 0.3	0.2 \$ 0.3	1.5 \$ 0.2
20081106-063244	510.0	2.5 \$ 0.2	0.2 \$ 0.2	0.4 \$ 0.3	0.1 \$ 0.3	0.9 \$ 0.2
20081106-083458	525.3	1.3 \$ 0.2	0.8 \$ 0.2	0.6 \$ 0.3	0.3 \$ 0.3	1.4 \$ 0.2
20081106-101402	606.0	1.4 \$ 0.2	1.0 \$ 0.2	0.7 \$ 0.3	0.2 \$ 0.3	2.1 \$ 0.2
20081106-105310	483.0	2.2 \$ 0.2	0.7 \$ 0.2	0.7 \$ 0.3	0.2 \$ 0.3	0.9 \$ 0.2

ery time the camera settings are modified, to account for the change in background level, but since the model must be run for individual meteors this is not a significant drawback.

From our results, we emphasize that fixed corrections for meteor saturation (not taking into account angular velocity and changes in background levels) can be in error by more than several magnitudes in some cases.

Bibliography

- [1] Campbell-Brown, M. D., Close, S., 2007, MNRAS, 382, 1309
- [2] Clifton, K. S., 1973, J.Geophys. Res., 78, 6511
- [3] Cook, A. F., Weekes, T.C., Williams, J.T., Omongain, E., 1980, MNRAS, 193, 645
- [4] Hawkes, R. L., 2002, in *Meteors in the Earth's atmosphere*, Cambridge Univ. Press, Cambridge, p. 97
- [5] Hawkes, R. L., Jones, J., 1975, MNRAS, 173, 339
- [6] Hawkes, R. L., Jones, J., 1986, Q. J. R. Astron. Soc., 27, 569
- [7] Hawkes, R. L., Bussey, J. E., Macphee, S. L., Pollock, C. S., Taggart, L. W., 2001, in Warmbein B., ed., *Proc. Meteoroids 2001 Conference*. ESA Publications, Noordwijk, p. 281
- [8] Howell, B. H., 2000, *Handbook of CCD Astronomy*, Cambridge Univ. Press, Cambridge
- [9] Jacchia, L. G., Whipple, F. L., 1961, *Smithsonian Contr. Astrophys.*, 4, 97
- [10] Jacchia, L. G., Verniani, F., Briggs, R. E., 1967a, *Smithsonian Contr. Astrophys.*, 10, 1
- [11] Jacchia, L. G., Verniani, F., Briggs, R. E., 1967b, *Smithsonian Contr. Astrophys.*, 11, 1

- [12] Kaiser, N., Brown, P., Hawkes, L. K., 2004, *Earth Moon Planets*, 95, 579
- [13] Myers, J. R., Sande, C. B., Miller, A. C., Warren, W. H., Tracewell, D. A.,
2001, *Sky 2000 Catalog v4*, Goddard Space Flight Center, Ycat 5109
- [14] Swift, W. R., Suggs, R. M., Cooke, W. J., 2004, *Earth Moon Planets*, 95, 533

Chapter 5

Bulk density of small meteoroids

Accepted for publication as:

Kikwaya, J.B., Campbell-Brown, M.D., Brown, P.G., (2011), Bulk density of small meteoroids, *Astronomy and Astrophysics*, Accepted: February 2011.

5.1 Introduction

Density is one of the most important physical properties of meteoroids. It is a critical factor in modelling the risk meteoroids pose to spacecraft, and also helps determine the physical structure and potentially the chemical composition of meteoroids' parent bodies, comets and asteroids. However, it is difficult to determine meteoroid density from meteor observations, because the meteoroid does not in general ablate uniformly, and does not remain as a single body during its entire flight in the Earth's atmosphere. It experiences fragmentation, which, along with its unknown shape, structure, and chemical composition, complicates any effort of ablation modeling (Kikwaya et al. 2009).

Other factors influence the ablation of a meteoroid, including its entry angle, speed, mass, ablation energy (energy required to ablate a quantity of mass of the meteoroid), boiling temperature, and bulk density (Campbell-Brown & Koschny 2004). Each meteoroid will have different ablation behaviour due to its composition, structure, bulk density and size. For example, the beginning heights and lightcurve shapes of faint meteors show significant variation, while larger meteors vary in end height (Ceplecha et al. 1998). Koten et al. (2004) showed that the differences in lightcurves and beginning heights among major video meteor showers can be explained by differences in the chemical composition and physical structure of their parent bodies.

Fragmentation complicates even further the determination of the physical properties of meteoroids, particularly density. The fact that meteoroids fragment is shown by the difference between the meteoroid photometric mass and dynamic mass, observed in the photographic Super-Schmidt meteors, and also in the short trail lengths of Draconid meteors (Jacchia, 1955). According to the dustball meteoroid model (Hawkes & Jones, 1975), fragmentation occurs before the process of ablation starts, and the grains undergo intensive ablation after they have been released from the main mass. The dustball model assumes meteoroids are composed of refractory

grains held together by a “glue” with a lower boiling point; when this temperature is reached the grains are released. Fragmentation also explains the production of the physical wake in meteor observations. Grains of different masses, predicted by the dustball model, decelerate at different rates, leading to an elongated luminous region (Borovicka, 2005). Many video meteors observed with short exposures show this wake (Fisher et al., 2000).

The process of fragmentation is complex, and there are several contemporary meteoroid ablation models which try to formalize it. Campbell-Brown & Koschny (2004) presented an ablation model which follows these steps: (a) the surface temperature of the meteoroid reaches a certain critical point; (b) the binding matrix of the meteoroid disrupts (the penetration of the heat through the meteoroid is governed by thermal conductivity); (c) grains are released (fragmentation). Kikwaya et al. (2009) applied this model of ablation to six meteors with masses between 10^{-6} and 10^{-8} kg recorded with narrow-field intensified cameras. They evaluated the bulk density by simultaneously fitting the lightcurve and the deceleration measurements of each of them. They found densities ranging from 500 kg m^{-3} to 7200 kg m^{-3} .

Borovicka et al. (2007) used a meteoroid ablation model based on these assumptions: (a) the separation of the meteoroid grains begins after a certain energy flux (10^6 Jm^{-2}) is delivered to the surface of the meteoroid; (b) the meteoroid gradually fragments into grains during the first half of its trajectory; (c) small dynamic pressures fragment the bulk meteoroid not disrupted in the previous step. This ablation model has been successfully applied to six Draconids for which, for the first time, deceleration and photometric measurements were available.

Jacchia (1955) surprisingly found that the dynamical mass of some faint meteoroids decreases more rapidly than the photometric mass as the meteoroid moves along its trajectory, showing unexpected deceleration. To account for this, he introduced the concept of progressive fragmentation (meteoroids fragment progressively into smaller pieces during atmospheric flight). Bellot Rubio et al. (2002) found that

visible forms of fragmentation (wake and terminal blending) can be present in the lightcurves of some faint meteors showing deceleration anomalies.

Quantitative measurements of the meteoroid bulk density are difficult, since variations in the way fragmentation is handled in modelling will change the inferred bulk density. Ceplecha (1968) estimated the density of small meteoroids, based on evaluating a parameter K_B , which depends on the beginning height of the meteor, the initial velocity and the meteoroid entry-angle. He classified meteoroids into four categories (A, B, C, D), with densities ranging from A (asteroid parent body, 2700 kg m^{-3}) to D (cometary parent body, 180 kg m^{-3}). Babadzhanov (2002) calculated the bulk density of 413 photographic Super-Schmidt meteors using an ablation model based on quasi-continuous fragmentation (QCF). He found values ranging from 400 kg m^{-3} to 7800 kg m^{-3} . Bellot Rubio et al. (2002) pointed out two questionable assumptions (see Kikwaya et al. 2009, for details on the discussion) which led Babadzhanov to estimate these high densities, the most important being the fact that Babadzhanov's (2002) method was only based on fitting the lightcurve, neglecting the meteoroid dynamics. Working on the same data, Bellot Rubio et al. (2002), using the single body theory which neglects fragmentation entirely, found bulk densities ranging from 400 kg m^{-3} to 4800 kg m^{-3} . The complete model of meteoroid ablation must take into account fragmentation and dynamical properties of the meteoroids simultaneously (Borovicka, 2005), as described and applied by Borovicka et al. 2007, and Kikwaya et al., 2009.

From these previous works, we see that estimating the density of a meteoroid is a difficult task, but it is achievable by combining precise observations (both photometric and astrometric measurements) and a complete model of ablation where all the different processes of mass-loss are taken into account (Hill et al. 2005, Popova, 2004, Borovicka et al. 2007, Jones and Kaiser, 1966). Strictly speaking, this type of analysis should produce a bulk density for meteoroids not as a single and unique value, but instead as a range of possible solutions.

The closest direct analog to small meteoroids to have directly measured densities are IDPs. Love et al. (1994) measured the densities of about 150 5-15 μm sized stratospheric IDPs (Interplanetary Dust Particles). Masses were determined using an absolute x-ray analysis technique with a transmission electron microscope, and volumes were found using scanning electron microscope imagery. They found that unmelted chondritic particles have densities between 500 kg m^{-3} and 6000 kg m^{-3} . Almost half of the particles had densities below 2000 kg m^{-3} , and porosity which is significant, but less than 70%. IDPs with densities above 3500 kg m^{-3} contain large sulfide grains. Melted chondritic particles (chondritic spherules) were found to have densities near 3500 kg m^{-3} . They find a peak in IDP density for a debiased exoatmospheric population near 2000 kg m^{-3} , with significant numbers up to $\gg 7000$ kg m^{-3} (see Fig. 5 of Love et al., 1994).

In this work, following Kikwaya et al. 2009, we use the dustball theory as modelled numerically by Campbell-Brown and Koshny (2004), and we apply it to faint (magnitude +2.5 to +6.0) meteors. We have explored the entire solution space of each of 8 free model parameters, and we will produce for each meteor typically hundreds of thousands of solutions. Each solution consists of a lightcurve and deceleration curve (variation of velocity with height) which will be compared to the observed lightcurve and deceleration. We use the reduced χ_c^2 value of the observed versus modeled astrometry and photometry as figure of merit (for a detailed discussion of the use and application of the reduced χ_c^2 value, see Bevington and Robinson, 2003).

5.2 Observations and equipment

Data were collected with two or three stations in seven different runs between 2006 and 2009: one over six nights with two stations in Arizona, USA, in 2006; five runs with two stations over fourteen nights in Canada from 2007 to 2009; and one run

with three stations over two nights in Canada in 2009. Three different systems were used: third generation (Gen III) intensified cameras, a digital Image Intensified CCD camera with an electronically gated image intensifier (referred to hereafter as the gated system), and a high resolution Gen III system, hereafter Cooke camera.

The Gen III cameras use ITT NiteCam model 380i microchannel plate image intensifiers with 18 mm GaAs detectors. These are lens coupled to CoHu 4910 series video CCD cameras, which are high performance, relatively sensitive, monochrome CCD cameras with analogue output (Hawkes et al. 2001, Hawkes, 2002), having 480×640 pixels recording at 30 interlaced frames per second. We used two of these systems, each with a 25-mm Fujinon f/0.85 lens as the objective. A single gated system with integrated intensifier was used, with a 50-mm Fujinon f/0.75 objective lens. The gated camera CCD had a pixel array of 1360×1036 pixels and 14 bit photometric depth. An internal electronic device, set by an external control box, controls both the CCD exposure time and the rate of the gating. The gating rate is much higher than the frame rate, so a meteor is broken into a series of dots (see Figure 5.1). During all seven campaigns which used the gated system, the CCD exposure time was set to 5 frames per second (5 Hz). From 2006 to 2007, we used 200 Hz for the gating, and from 2008 to 2009, to ensure that dots were well separated, we used 100 Hz. The high resolution digital intensified CCD cameras, our third system, used the same Gen III ITT intensifiers as the Gen III system lens coupled to a Cooke pco.1600 CCD camera, which are run with a resolution of 1024×1024 pixels at 20 fps (progressive scan). These cameras have digital output and 14-bit optical depth. Two of these were used, each with 50 mm f/0.95 Navitar objective lens (see tables 5.1 and 5.2).

Table 5.1: Table summarizing all campaigns and their details.

Camp. Duration	# usable nights	# stations	location			baseline	instruments	nb events
			site 1	site 2	site 3			
20060430-20060506	5	2	Kitt Peak	Whipple obs		77.04 km	Gen III camera Gated system Gen III camera	09
			31° 57' 70N 111° 36' 01W	31° 40' 51N 110° 57' 17W				
20070420-20070422	2	2	Elginfield	Tavistock		44.61 km	Gen III camera Gated system Gen III camera	05
			43° 11' 58N 81° 18' 90W	43° 15' 84N 80° 46' 32W				
20070519-20070520	1	2	Elginfield	Tavistock		44.61 km	Gen III camera Gated system Gen III camera	05
			43° 11' 58N 81° 18' 90W	43° 15' 84N 80° 46' 32W				
20070812-20070813	2	2	Elginfield	Tavistock		44.61 km	Gen III camera Gated system Gen III camera	17
			43° 11' 58N 81° 18' 90W	43° 15' 84N 80° 46' 32W				
20080910-20080911	2	2	Elginfield	Tavistock		44.61 km	Gen III camera Gated system Gen III camera	25
			43° 11' 58N 81° 18' 90W	43° 15' 84N 80° 46' 32W				
20090625-20090911	8	2	Elginfield	Tavistock		44.61 km	Cooke camera Gated system Cooke camera	31
			43° 11' 58N 81° 18' 90W	43° 15' 84N 80° 46' 32W				
20090624-20090825	3	3	Elginfield	Tavistock	Brussels	61.36 km 44.61 km 64.14 km	Cooke camera Gated system Cooke camera	15
			43° 11' 58N 81° 18' 90W	43° 15' 84N 80° 46' 32W	43° 44' 88N 81° 12' 42W			

Table 5.2: The instruments used in the data collection.

Name	Intens.	CCD frame rate	lens	(FOV)	Im. size (pxl)	Pxl size (microns)	pixel scale of images	Image (bit)	resol (100 km)	stellar magn. limit	avg meteoroid mass(kg)
Gen III	ITT Nitecam 380i	30 fps	25 mm f/0.85	$34.4^\circ \times 24.9^\circ$	640×480	8.4×9.8	0.05°	8	94m	+9.5	3×10^{-6}
Gated	ITT extended blue	5 fps	50 mm f/0.75	$15.2^\circ \times 11.5^\circ$	1360×1036	6.45×6.45	0.01°	14	20m	+8.0	$\sim 10^{-6}$
Cooke	ITT Nitecam model 380i	20 fps (pco 1600)	50 mm f/0.95	$20.7^\circ \times 20.7^\circ$	1024×1024	8.4×9.8	0.02°	14	35m	+8.0	8×10^{-6}

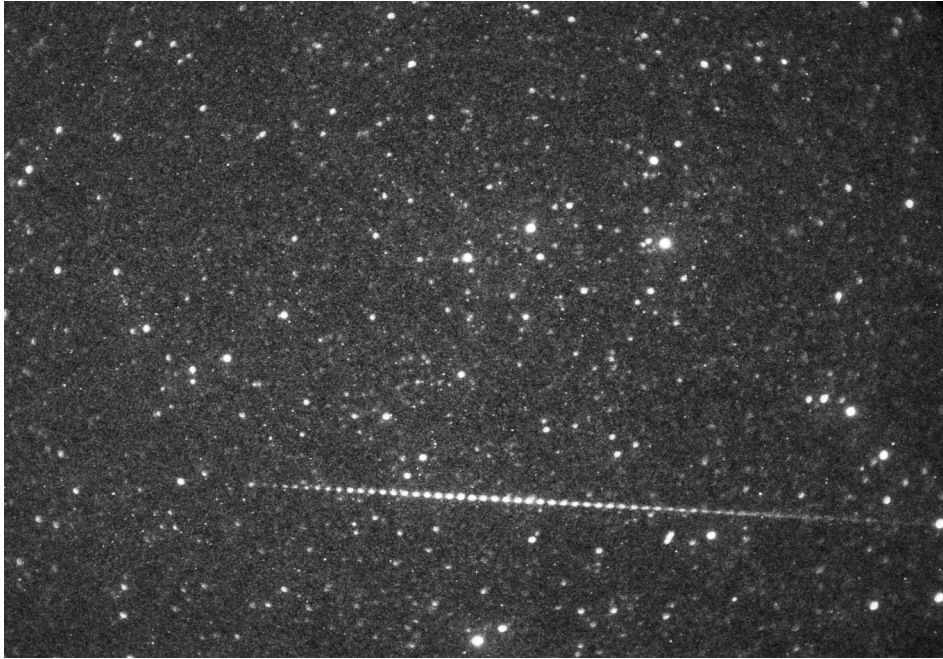


Figure 5.1: Meteor 20090825-065903 recorded with the gated camera on August 25, 2009 at 06:59:03 UTC at Brussels, Ontario, Canada. The frequency of CCD was set to 5 Hz and the frequency of the intensifier gating was 100 Hz.

5.3 Data and reduction

We obtained a total of 107 useful multistation meteors over all seven campaigns from 2006 to 2009. By useful, we mean that the triangulation geometry was good (large angular separation of observing planes from the two stations), and the SNR was high enough to make precise measurements. After each campaign, we searched the data for simultaneous meteors, and checked if the meteor started and ended in the field of view of at least one of the stations: all partial trails were rejected. When the gated camera was used, we also required the meteor to be captured by the gated camera to provide precise astrometric measurements. For photometric measurements, we used only two systems: either the Gen III or high-resolution Cooke systems. The gated camera was not used for photometry because the meteor images in each frame are so close together that their photometric measurements blend into nearby meteor “dots”.

For a better estimate of the photometric mass of the meteor, we added to the

astrometric criteria the requirement that the event should start in the field of view of at least one Gen III or high-resolution system, as this gives a complete lightcurve of the meteor. After applying these criteria, the total number of useful meteors went down to 92.

5.3.1 Astrometry

We used standard astrometric techniques (Kikwaya et al. 2009) to extract the positions of meteors by comparing them to the positions of stars. For the Gen III systems, typical errors of 0.016° are found by comparing plate fits with actual positions, which corresponds, at the Gen III resolution, to ≈ 0.3 pixels. On the gated system, the plate errors were approximately 0.007° (0.6 pixels) and on the Cooke camera system, errors were around 0.012° , or approximately 0.3 pixels.

The astrometric procedures used in Kikwaya et al. (2009) were also used in this study. Briefly, the meteor positions were measured manually and the velocities smoothed by choosing frames 5 to 25 points apart, depending on the system, to clearly show the deceleration. The atmospheric trajectories were calculated using the computer program Milig, based on the algorithm described in Borovicka (1990).

As an example, we compute the trajectory solution with Milig for meteor 20060503-091349, recorded on May 3, 2006 at 09:13:49 UTC in Tucson, Arizona. The deceleration, necessary to constrain the model, was noticeable. The deceleration is more obvious when we calculate the difference between the computed distance (assuming a constant speed) and the observed distance (Fig. 5.2). The smoothed curve of the velocity of the meteor 20060503-091349 is shown in Fig. 5.3. The uncertainty at each point has been calculated for later use in comparing with the model data.

The pre-atmospheric velocity was determined by taking a linear least-squares fit of the first 5 to 25 positions (equal to the number of points used in smoothing the curve). The error on the pre-atmospheric velocity is the standard deviation of the initial velocity on the two or three cameras which recorded it. For meteor

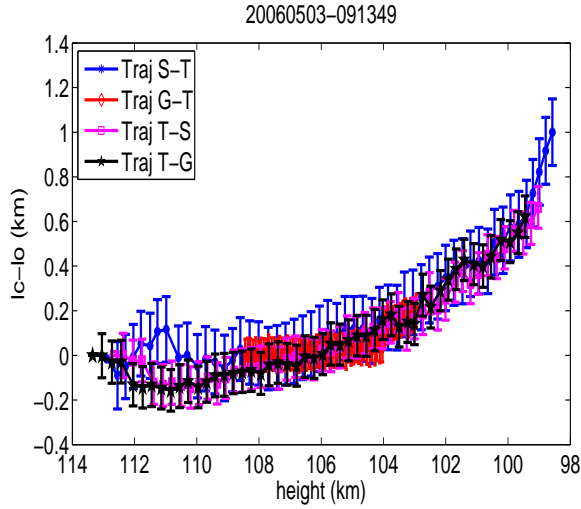


Figure 5.2: Plot showing the deceleration of the meteor 20060503-091349. Here l_o is the observed length of the meteor along its trajectory and l_c is the calculated length assuming a velocity of $v=61$ km/s ($v=\frac{l_c}{t}$, t being the meteor time). Traj S-T is the trajectory solution from camera S computed using the cameras S and T; Traj T-S is the trajectory solution from camera T computed using the cameras S and T. Traj G-T is the trajectory solution from camera G computed using the cameras G and T and Traj T-G is the trajectory solution from camera T computed using the camera G and T.

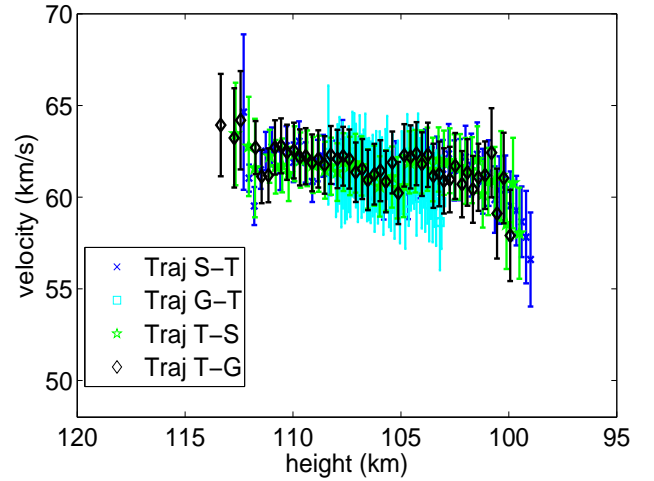


Figure 5.3: Velocity profile of the meteor 20060503-091349. We have inserted error-bars at each point along the trajectory. The first points are simple point-to-point differencing while the remaining points are several points smoothed: 5 for Gen III and 10 for gated camera (see Fig. 5.2 for legend).

20060503-091349, the pre-atmospheric speed was $61.30 \pm 0.99 \text{ km s}^{-1}$.

The uncertainties for each velocity measurement (Fig. 5.3) come from the combination of systematic and random error of the position picks for the meteor in each frame. We found the systematic error by comparing the positions of 10 meteors, reduced separately by 9 people. Each person introduces a different systematic shift, which we found to be 0.6 pixels on average; this was adopted as the systematic error for all the systems. The random error is evaluated from the observed standard deviation of the points (residuals) for a two station solution, since this represents the scatter about a line. The random error depended on the system: for the Gen III cameras, the random error ranged from 0.2 to 0.3 pixels; for the gated camera, it was between 0.4 and 0.6 pixels; and for the Cooke camera, the random error was about 0.5 pixels. We added these two types of error to all measured points of each meteor in a Monte Carlo simulation, which was run between 2500 to 5000 times (each point had a gaussian error distributed according to these values). We were then able to determine the uncertainty in position, height, range and velocity for each meteor taking the camera-meteor-camera geometry explicitly into account.

The heliocentric meteoroid orbits were then computed using the methods of Ceplecha (Ceplecha, 1987).

5.3.2 Photometry

We used standard routines for meteor photometry, comparing the integrated brightness above background of the stars in a flat-fielded image to the brightness of each meteor image (see Kikwaya et al., 2009). A total of about 100 stars are used in each calibration; the V magnitudes are taken from the SKY2000v4 catalog (Myers et al., 2001). Although the Gen III and the Cooke systems have a spectral response closer to the R band than the V band (around 45% quantum efficiency in R compared to 35% in V; also the stellar R magnitudes give a calibration fit with less scatter than the stellar V magnitudes), we use the stellar V magnitudes to calibrate. The luminous

efficiency (see Hill et al., 2005) used to compute the photometric mass of meteors has been estimated in the panchromatic band, and not the red (Ceplecha et al., 2000, Koten et al., 2006). To check for errors introduced when using V magnitudes instead of R, we took a sample of meteor spectra from Borovicka et al. (2005), and worked out an average correction factor to convert the R-band meteor magnitude to a V-band meteor magnitude. This average (V-R) value was 0.72 magnitudes. We calculated light curves in the R-band for a few of our meteors, and used the correction factor to convert these to V magnitudes. We found that the lightcurves were the same within our error as those found using the V-band calibration directly, so we used the V-band calibration for all our meteors.

A typical error of 0.1-0.3 magnitudes is found for each star. It represents the difference between the catalogue value and the calibration. At fainter magnitudes, this error is dominated by counting statistics and shot noise in the intensifier. At brighter magnitudes, the error is mainly due to uncertainty in the photometric calibration. The combination of Poisson error and error in the calibration fit are used to estimate the calibration uncertainty in the meteor magnitudes (see Kikwaya et al. 2010). The lightcurve of each meteor is calculated as apparent magnitude, and converted to absolute magnitude, defined as the apparent brightness the meteor would have at a range of 100 km at the zenith.

The Gen III systems, with 8-bit pixel depth, were subject to saturation effects for meteors +2.3 magnitude and brighter. The maximum pixel value in this case is truncated to 255, and blooming occurs as the excess photoelectrons spill over into neighbouring pixels. This saturation effect flattens the lightcurves of bright meteors, which has serious consequences for attempts to fit the lightcurve. For the nine meteors in our sample which were saturated through part of their lightcurves, a saturation correction (Kikwaya et al., 2010) was applied to extract the true magnitude for those frames. The typical maximum correction to a lightcurve was approximately +1 magnitude, a significant effect. Saturation was not a factor in the Cooke system,

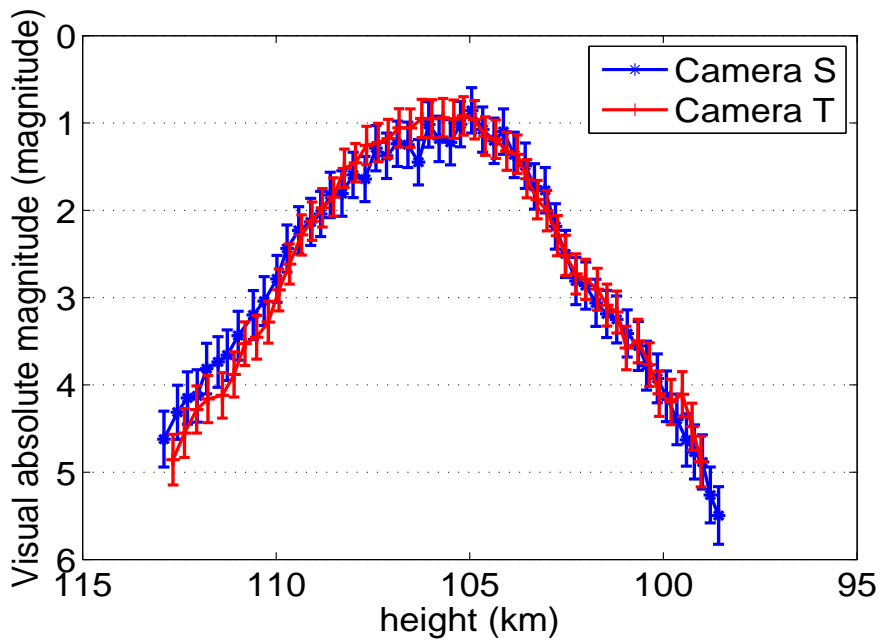


Figure 5.4: The absolute lightcurves of the meteor 20060503-091349 obtained after applying the different photometric techniques (the correction for range has been applied).

because of the much larger bit depth.

Figure 5.4 shows the lightcurve of the meteor 20060503-091349 from two Gen III cameras.

5.4 Ablation Model

We use the dustball model of Campbell-Brown and Koschny (2004). It uses the Clausius-Clapeyron formalism to consider mass loss before the boiling temperature is reached, and allows the user to define the number and size of constituent grains. The model considers three sources of energy:

1. energy imparted to the meteoroid by collisions with atmospheric atoms
2. energy lost from the meteoroid by radiation
3. energy lost through evaporation of the meteoroid material

The equation of the momentum transfer from air molecules which collide with the meteoroid is given by:

$$\frac{dv}{dt} = \frac{\Gamma \rho_a v^2}{m} A \left(\frac{m}{\rho_m} \right)^{2/3} \quad (5.1)$$

where ρ_a is the atmospheric density, ρ_m is the density of the meteoroid, and A is the shape factor of the meteoroid, defined so that $A(m/\rho_m^{2/3})$ is the effective cross sectional area of the meteoroid. Γ is a dimensionless coefficient, varying between 0 and 1 and describing the proportion of momentum from air molecules transferred to the meteoroid. The velocity of the meteoroid, output versus both time and height, provides the deceleration.

The classical meteor ablation model considers mass loss to be proportional to the kinetic energy imparted to the meteoroid. The ablation in our model starts as soon as the surface of the meteoroid reaches the boiling temperature (e.g. Bronshten 1983), which means as the classical model of ablation suggests, when the ‘glue’ evaporates and grains are released. The classical equation of mass loss is then given by:

$$\frac{dm}{dt} = i \frac{A\Lambda}{2L} \left(\frac{m}{\rho_m} \right)^{2/3} \rho_a v^3 \quad (5.2)$$

where Λ , the heat-transfer coefficient, is equal to or less than unity, since the energy expended on ablation cannot exceed the total kinetic energy of the oncoming stream molecules (Bronshten, 1983), and L is the heat of ablation (energy that must be delivered to a mass dm in order to melt and/or vaporize it).

The ablation model we use in our work considers ablation as soon as the meteoroid begins to heat, very high in the atmosphere. The mass loss is then calculated through Knudsen-Langmuir formula combined with the Clausius-Clapeyron equation, adding a term like the classical formula to simulate spallation when the meteoroid is very hot. The mass loss equation is evaluated as:

$$\frac{dm}{dt} = A \left(\frac{m}{\rho_m} \right)^{2/3} \psi \frac{P_a \exp\left(\frac{L\mu}{k_B T_M}\right) \exp\left(-\frac{L\mu}{k_B T_B}\right) i p_v}{\sqrt{\frac{2\pi k_B T}{\mu}}} \quad (5.3)$$

where p_v is the vapor pressure produced by sublimating meteoroid material and ψ is the condensation coefficient, which gives the probability that an ablated meteor atom colliding with the surface will condense. For metals, ψ is 1: following Bronshten (1983), ψ of stone (silicate) is considered to be 0.5. T_B is the boiling temperature of the meteoroid substance at sea level pressure P_a , and T_M is the meteoroid temperature (we note a typographic error in the equation 9 of Campbell-Brown and Koschny (2004) where T_B in the first expression term should be T_M). T is the fusion temperature. L is the heat of ablation, μ the average mass of a meteor atom and k_B the Boltzmann constant. For more details of this particular equation of mass loss and the physical background behind its application, see Campbell-Brown and Koschny (2004).

In our model, we adopt the classical assumption that the luminous intensity is proportional to the kinetic energy lost by the meteoroid (see Campbell-Brown and Koschny, 2004). For small meteoroids, the luminous intensity is proportional to the mass loss rate as given in the following equation:

$$I = \tau \frac{dm}{dt} \frac{v^2}{2} \quad (5.4)$$

where τ is the luminous coefficient, v the meteoroid velocity.

5.5 Analysis

For each of our 92 meteors, we extracted the trajectory and light curve, and applied our ablation model to simultaneously fit the observed lightcurve and deceleration.

Among the parameters used in the model, we have chosen some to remain fixed and some to remain free. Fixed parameters include:

1. the fusion point of the meteoroid grains (we constrain it to be 100 K less than the boiling point of the meteoroid grains)
2. the condensation coefficient ψ [fixed to 0.5: condensation coefficient of stone (silicates)] (Campbell-Brown and Koschny, 2004),
3. the emissivity of the meteoroid (fixed to 0.9)(Campbell-Brown and Koschny, 2004),
4. the terrestrial atmospheric density, provided by the MSISE-90 model (Hedin, 1991).

For each meteor, we search the entire free parameter space in two stages. The first, broad search identifies the regions in which solutions are concentrated. For this first step, we use a relaxed fit criterion requiring agreement between the model and two thirds of common points in the lightcurve and four fifths of the measured points in the deceleration, since the grain distribution is not varied at this step and the shape of the lightcurve may be a poor fit. If all of the good solutions have densities which are grouped within $\pm 1000 \text{ kg/m}^3$ (typical of the range of density errors reported in other works, such as Babadzhanov, 2002, see table 1, Bellot Rubio et al., 2002 see table 2, and Kikwaya et al. 2009 see table 10) we took the best solution among them. Our figure of merit for defining the best model fit is the model with the reduced chi-squared which is closest to unity. If we find good solutions with a wider range in densities, we choose the best solution in each group of similar density and attempt to find a “best” solution within each group. The reason for beginning with this coarse search is the difficulty of determining the grain distribution; if the number of solutions covering a reasonable range of each of the other free parameters is merely prohibitive, the number including all possible grain distributions is essentially infinite.

In the broad search, the approximate grain mass distribution index is estimated using the work of Murray and Beech as a guide: they associated the shape of a

lightcurve (characterized by the F-parameter) to a meteoroid mass distribution index (Murray and Beech, 2000; see table 2). The grain mass distribution may not follow the true mass index of each of our meteoroids, but it provides a starting point for the broad search of parameter space. Murray and Beech (2000) assume the grain mass index is self-similar to the meteoroid population mass distribution as a whole, i.e. that the grain mass index is the same as the meteor mass index, s . With this mass index, grains are distributed into three bins according to the method described by Borovicka et al., 2007. Only three bins are used to minimize computing time, which is already very large.

Once the best “coarse” solution is found in the broad search, the grain masses are further modelled to give the best fit to the shape of the lightcurve and the deceleration. If several best densities were found, this procedure was repeated for each group of densities; in each case, it happened that we could rule out all but one of the density groups at this stage, since no good match could be found for the others. This grain distribution was then taken to be the final distribution for a particular meteoroid. At this point, we have a best fit “coarse” density, but in order to evaluate the error in this density measure, we will once again search the entire free parameter space with a smaller range in density and higher resolution in density (refined search). All solutions from the refined search are sorted by reduced chi-squared using both the lightcurve and deceleration simultaneously, and those with reduced chi-squared of one or less we adopt as the density distribution of the meteoroid.

5.5.1 Broad search

Free parameters

In our first stage, the broad search, the free parameters of our ablation model include:

- ² grain mass and number of grains

- 2 density of the meteoroid
- 2 heat of ablation
- 2 boiling point of the meteoroid grains (T_{boil})
- 2 temperature at which the grains are released (T_{lim})
- 2 specific heat (C_p)
- 2 average molar mass of meteoroid material
- 2 thermal conductivity of the meteoroid

The range of values for each free parameter is described in Table 5.3.

In most models, Γ (drag coefficient) and Λ (heat transfer coefficient) are assumed. Borovicka et al. (2007) set both parameters to unity; this was also the value assumed by Fisher et al. (2000). Campbell-Brown and Koschny (2004) assumed $\Gamma = 1$ and $\Lambda = 0.5$. We treat Γ and Λ differently during the broad search and at the refined one. In the broad search, they are set to unity. When fitting the grain distribution, we manually adjust Γ and Λ to improve the model fit. For the refined search, we allow Γ and Λ to vary from 0.5 to 1.0.

Grain mass distribution

For the initial broad search, we used three grain masses for each meteor. The smallest mass was close to the ablation limit, below which radiation will dominate and the mass loss will be negligible. The other masses, and the number of grains in each bin, were assigned according to the mass distribution index using the method of Borvicka et al. (2007). The total mass was made to agree with the photometric mass determined for each meteor. To determine photometric mass, we used the luminous efficiency as described by Hill et al.(2005).

To determine a trial mass index for each meteor, we used the work of Murray & Beech (2000), who related the F-parameter (a standard measure of the asymmetry

Table 5.3: Free parameters of the model and the range of values used.

Parameter	Range	Step	References
Density (kg m^{-3})	100 - 8000	300	very porous cabornaceous-iron meteoroid
Heat of Ablation (J kg^{-1})	$2\mathbf{E} 10^6$ - $9\mathbf{E} 10^6$	$1 \mathbf{E} 10^6$	Hawkes & Jones, 1975 Bellot Rubio et al. (2002) Boroviccka et al. 2007 Kikwaya et al. 2009
Fragmentation T (K)	900 - 1600	100	Campbell-Brown & Koschny, 2004 Kikwaya et al. 2009
Boiling T (K)	1400 - 2300	200	Campbell-Brown & Koschny, 2004
Thermal conductivity ($\text{W m}^{-1} \text{K}^{-1}$)	0.1 - 1	0.1	Campbell-Brown & Koschny, 2004 Popova, 2005 Kikwaya et al., 2009 Vokrouhlicky & Farinella, 2000
Molar mass (amu)	20, 36, 56		sodium - iron
Specific heat ($\text{J kg}^{-1} \text{K}^{-1}$)	600 - 1400	200	Campbell-Brown & Koschny, 2004

of a light curve) to the mass index of grains which could successfully fit the curve. Although this was often not the final grain distribution, nor a unique solution, it did provide a useful starting point.

The F-parameter is defined as the ratio of the distance from the beginning to the point of maximum brightness to the full length of the light curve: an F-parameter smaller than 0.5 indicates the light curve peaks early, greater than 0.5 indicates that it peaks late, and 0.5 represents a symmetrical lightcurve. For consistency, the F-parameter is generally measured some fixed number of magnitudes below the peak rather than from the true beginning and ending of the curve; we used the F-parameter measured from 0.75 magnitudes below the peak. This value was chosen because it allowed the parameter to be calculated even for faint meteors. Murray and Beech (1999) reported values measured from three different magnitudes below the peak: 0.5, 0.75 and 1.0.

The grain mass indices of our meteors were found to range from 1.50 to 2.85 using this approach. The smallest grains were typically 10^{-12} kg, and the largest grains used were 10^{-9} kg.

Using the grain distribution above and the range of values for each free parameter previously described, we computed about a hundred thousand models for each meteor, and compared the model lightcurves and deceleration to the measured curves (Figure 5.4 and 5.3). We defined a good fit as one where the reduced chi-squared between the model values for the lightcurve and velocity as function of height as compared to the observations were less than or equal to unity. We accepted at this stage an overlap of at least two thirds of points between the modelled values and the observed ones. Figure 5.5 shows an example (meteor 20060503-091349) of the density distribution of all solutions with $\chi_c^2 < 1$; there are solutions around densities of 680 kg m^{-3} , 920 kg m^{-3} and 1220 kg m^{-3} .

If the best fits were closely grouped, we chose the one having the χ_c^2 closest to 1 for both the lightcurve and deceleration for inclusion in the second stage refined

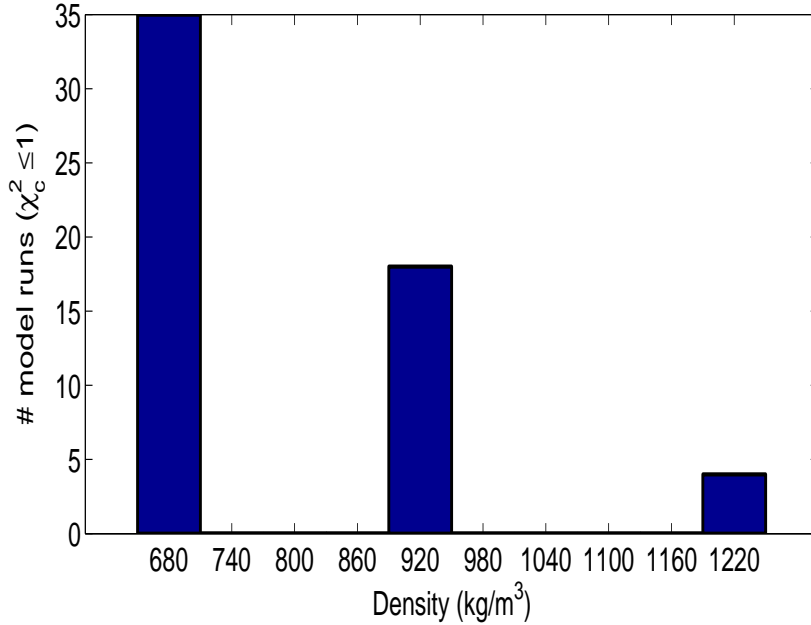


Figure 5.5: All model solutions with $\chi_c^2 \leq 1$ after the initial broad search for meteor 20060503-091349.

search, described below. In some cases ($\gg 10\%$), the best solutions formed isolated groups separated in density by more than 1000 kg m^{-3} . We then worked with the best solution from each group. In all of these cases, only one of the groups survived this stage; the others were eliminated because of unphysical parameters.

5.5.2 Refined search

Before beginning a second, more focused search for the best model fits, we adjusted the best solution found during the broad search to better fit the photometry and trajectory data. We forward modelled the grain distribution and slightly changed the other free parameters until the best possible agreement was obtained. This is similar to the procedure usually followed in meteor modelling: the advantage of our methodology is that we had starting values for each parameter and we were able to rule out other local minima as not producing good solutions based on χ_c^2 values.

For meteor 20060503-091349, the best model solution is shown in Figure 5.6 for the lightcurve and for the deceleration in Figure 5.7. The best fit grain distribution

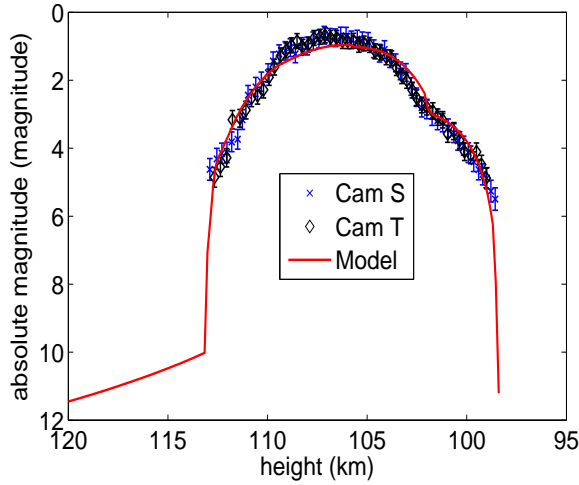


Figure 5.6: The best lightcurve fit for the meteor 20060503-091349. The corresponding density is 970 kg m^{-3} .

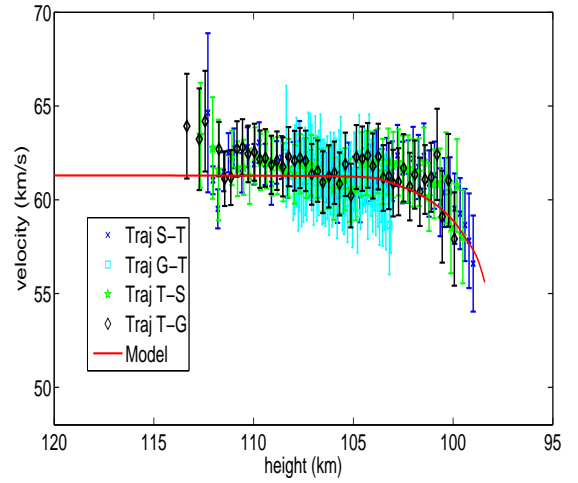


Figure 5.7: The best trajectory fit for the meteor 20060503-091349 (see Fig.??).

Table 5.4: Grain distribution found from modelling for meteor 20060503-091349 for the broad search and as determined through forward modelling for the refined search.

Broad search		Refined search	
# grains	mass of each grain	# grains	mass of each grain
39278	$6.60 \text{ } \pounds \text{ } 10^{-11}$	75767	$0.93 \text{ } \pounds \text{ } 10^{-11}$
15358	$1.11 \text{ } \pounds \text{ } 10^{-10}$	55130	$1.11 \text{ } \pounds \text{ } 10^{-10}$
10146	$1.40 \text{ } \pounds \text{ } 10^{-10}$	1198	$1.15 \text{ } \pounds \text{ } 10^{-09}$

for this event is given in Table 5.4. The corresponding density is 970 kg m^{-3} and the values of other free parameters are given in Table 5.5.

Using this approach we obtained the best fit density for each meteor, but we proceeded with another search of the parameter space to define the uncertainty range of this best fit density value. This time, we use a narrower range of densities, clustered around the best fit, and a higher search resolution (steps of 100 kg m^{-3}). All solutions from this final search with $\chi_c^2 \cdot 1$ for both the lightcurve and trajectory were considered possible solutions for the meteoroid and define our uncertainty range in density.

The density distribution of meteor 20060503-091349 (Figure 5.8) suggests that the lowest possible density is 570 kg m^{-3} , and the highest is 1170 kg^{-3} . Using

Table 5.5: The best fit values of the free parameters from the broad search and for the final best solution for meteor 20060503-091349 from the refined search

Free parameter	Broad search	Refined search
Heat of ablation (J/kg)	9.0×10^6	6.5×10^6
T_{lim} (K)	1000	930
T_{boil} (K)	1800	1900
Specific heat (J/kg K)	1000	1400
Molar mass (atomic unit)	36	36
Thermal Conduct (J/m s K or W/m K)	0.5	0.5

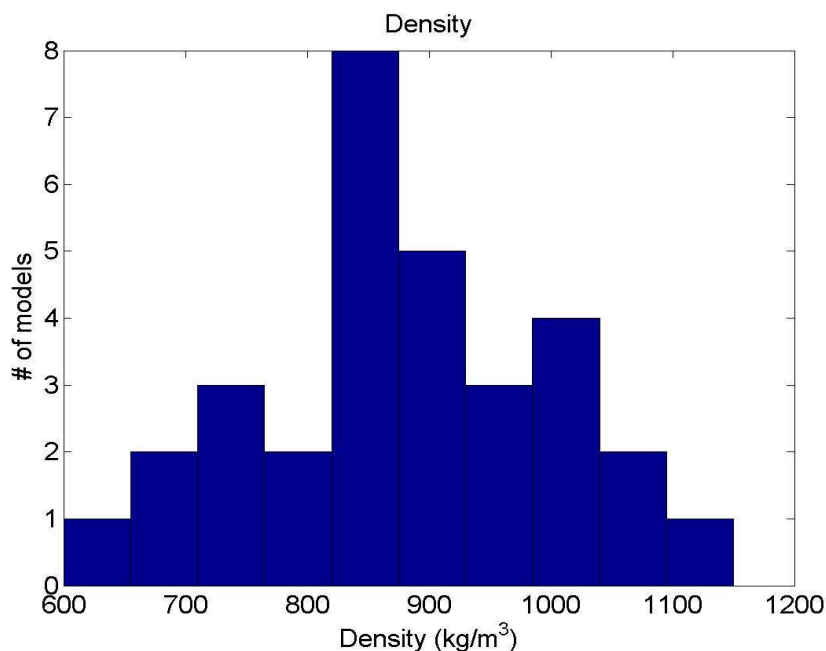


Figure 5.8: The distribution of density solutions with $\chi_c^2 \cdot 1$ for meteor 20060503-091349. The best solution is 970_{-400}^{+200} kg m⁻³.

our methodology we find that meteor 20060503-091349 had a density of 970_{-400}^{+200} kg m⁻³. This meteor was photometrically saturated, and when we ran the model on the uncorrected lightcurve, the density was 480_{-130}^{+170} kg m⁻³, demonstrating the importance of including saturation corrections fully in meteor photometry (Kikwaya et al., 2010).

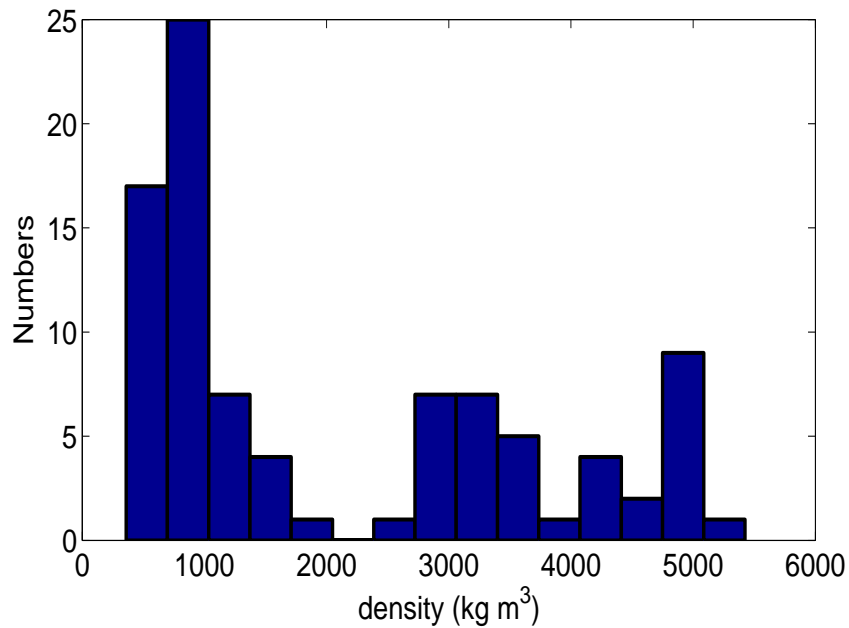


Figure 5.9: Histogram showing the distribution of the best fit value for our meteoroid densities from our model fit to data (92 meteoroids total).

5.6 Results and discussion

5.6.1 Origin of our meteoroids

Densities were computed for all 92 meteors. The densities ranged from 360_{-100}^{+400} kg m⁻³ to 5425_{-800}^{+500} kg m⁻³. The distribution of densities (Figure 6.1) shows three peaks (though the number statistics are low) : one around 1000 kg m⁻³, one around 3000 kg m⁻³ and one around 5000 kg m⁻³.

Fig 6.1 suggests a major population we interpret to be meteoroids rich in some form of Iron with densities ranging from 4150 kg m⁻³ to 5425 kg m⁻³. We make this interpretation following the study of Borovicka et al., (2005), who found a high percentage of meteoroids on Apollo-type orbits to have spectra indicating high Fe abundance; our bulk density measurements support this interpretation. A second population with average bulk density around 3000 kg m⁻³ we interpret to be similar in structure to chondrites based on similarity of these density values to the measured bulk density of recovered chondritic meteorites (see Consolmagno and Britt,

1998). This population has orbits which are like Jupiter-family comets (JFC) and also span Apollo-type orbits, suggestive of a main asteroid belt origin. By far our best represented population are meteoroids with relatively low density and Halley-type (HTC) or Nearly isotropic comets (NIC) - these represent 55% of our entire sample and range in density from 360 kg m^{-3} to 1510 kg m^{-3} . One of the most interesting results of our study is the apparent gap around 2000 kg m^{-3} - this suggests that our sample does not contain many meteoroids with bulk properties similar to carbonaceous chondrites. We caution that these relative population sizes should not be treated as representative of the true mass-limited population weightings as the HTC/NICs have higher impact velocities and hence we see “deeper” into the mass distribution for HTC/NIC meteoroid population relative to the JFC/asteroidal population.

To quantify the likely origin for our mm-sized particles, as a first step we can use the Tisserand parameter relative to Jupiter to discriminate between meteoroids of Jupiter-family comet / Halley-type / nearly isotropic comet origin or asteroidal origin (Levison, 1996, Weissman et al. 2002, Borovicka et al. 2005, Christou, 2009).

The Tisserand parameter is given by:

$$T_j = \left(\frac{a_j}{a}\right) + 2\sqrt{\left(\frac{a}{a_j}\right)(1 - e^2)\cos(i)} \quad (5.5)$$

where a_j is the semimajor axis of Jupiter, a is the semimajor axis of the meteoroid, and i and e are respectively the inclination and the eccentricity of the meteoroid’s orbit. In broad terms, a Tisserand parameter less than 2 is characteristic of Halley type comets (originating in the Oort cloud), $2 < T_j < 3$ is characteristic of Jupiter family comets (originating in the Kuiper belt) and Tisserand parameters greater than 3 are typical of asteroidal orbits. This classification works for bodies which are subject only to gravitational perturbations and whose orbits are dominated by Jupiter. Both are good approximations at our large particle sizes as the Poynting-Robertson lifetime for mm-sized particles is two orders of magnitude larger than

the expected collisional lifetime (Grun et al., 1985). Further evidence that our meteoroid sample is largely unaffected by Poynting-Robertson drag is the lack of low eccentricity orbits, despite the fact that such orbits have much higher collisional probabilities with the Earth.

Of our sample, 51 meteoroids (55%) had $T_j < 2$, 17 meteoroids (19%) had T_j between 2 and 3, and 24 meteoroids (26%) had a $T_j > 3$ (Figure 6.3). Two of our meteoroids (20070420-082356 and 20080911-075207) had nominally hyperbolic velocities based on our procedure for computing initial velocity, but we observe that the hyperbolic excess was less than the spread in initial velocity computed between all three cameras in both cases. As both had low ($<1000 \text{ kg m}^{-3}$) bulk density and were likely cometary we omit them from further analysis noting that their inclusion to the large HTC/NIC meteoroid sample would change none of the conclusions which follow.

It must be noted that the Tisserand parameter cannot unambiguously discriminate these categories. There is some overlap close to the boundaries; also, a few asteroids (sometimes called Damocloids) (see Borovicka et al. 2005) are on Halley-type orbits, and some comets (notably 2P/Encke) have asteroidal-like orbits.

In our data comparing density with orbit-type, the clearest division is between the HTC/NIC meteoroids and the objects on JFC or Asteroid-type orbits; meteoroids with $T_j < 2$ consistently have the lowest densities (smaller than 2000 kg m^{-3} in all cases), while those with $T_j > 2$ had densities greater than 2500 kg m^{-3} . The division between Jupiter family comets and asteroids is less clear; while all high-density objects (densities greater than 4500 kg m^{-3}) had $T_j > 3$, objects of intermediate density were found in both categories. This is similar to the distinct albedo distribution versus T_j found by Fernandez et al., 2001. They suggest that an old comet that loses all of its available volatiles or is covered by a mantle that prevents sublimation of subsurface ice will appear observationally as a near-Earth asteroid (NEA) or unusual asteroid (UA) (see Fig 5.10). The dynamical lifetime

of short-period comets being about 10-100 times longer than the devolatilization timescale (Levison and Duncan, 1994) allows one to observe extinct comets (as near-Earth asteroids or unusual asteroids) before they can disintegrate or collide with a planet. However, while Fernandez et al. (2006) finds that the albedo distribution of JFCs match HTC and NICs well, but are distinct from asteroidal objects, we find the opposite trend with density, i.e. JFC related meteoroids appear to have nearly chondritic bulk density and are not low density cometary objects which we find exclusively with HTC and NIC-type meteoroids.

The most complete study of compositional variations among meteoroids at our sizes was reported by Borovicka et al. (2005), who in studying the orbital distribution of meteors with different spectral characterizations, used three more parameters to classify meteoroid orbits: perihelion distance, q , aphelion distance, Q , and inclination, i . Asteroids have aphelia inside Jupiter's orbit, while most comets have aphelia outside (see, for example, Figure 12 in Borovicka et al., 2005), although there are exceptions. High inclination objects tend to be cometary, while low inclination objects may be asteroids or prograde comets.

Borovicka et al. (2005) divided meteoroid orbits into 5 classes based on a priori expected physical differences:

1. (SA) Sun-approaching orbits: $q < 0.2 \text{ AU}$.
2. (ES) Ecliptic shower orbits: Meteor showers having orbits on the boundary of the Jupiter family and asteroidal objects; some of these would be classified as asteroidal though there are some clearly cometary parent bodies.
3. (HT) Halley-type orbits: $T_j < 2$ or $2 < T_j < 3$ and $i > 45^\circ$.
4. (JF) Jupiter family orbits: $2 < T_j < 3$ and $i < 45^\circ$ and $Q > 4.5 \text{ AU}$.
5. (A-C) Asteroidal-chondritic orbits: $T_j > 3$ or $Q < 4.5 \text{ AU}$.

We use Borovicka et al. (2005) populations to examine our data and relate his

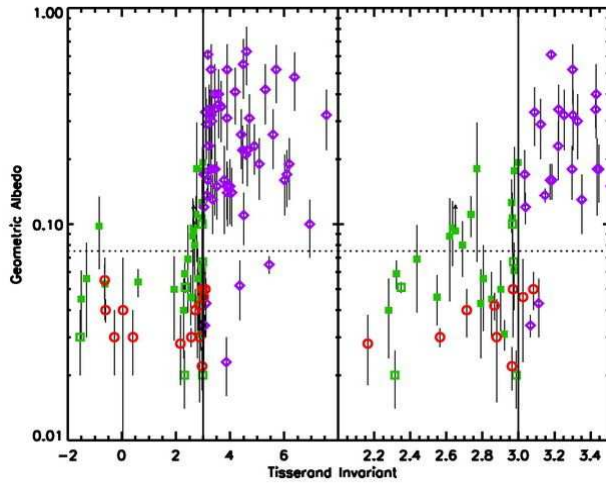


Figure 5.10: Plot of known geometric albedos vs. Tisserand invariant for $T_j < 3$ NEAs and UAs (green squares) and $T_j > 3$ NEAs and UAs (purple diamonds). Active cometary nuclei are represented by red circles. A vertical line marks the dynamical boundary $T_j=3$. There are 57 high-Tisserand albedos plotted, 56 of which are NEAs. The left panel shows the entire range of Tisserand values, and the right panel shows just the region near $T_j=3$. The fraction of objects with comet-like albedos differs greatly from one side of the dynamical boundary to the other. A large fraction of the objects with $T_j < 3$ or precisely with T_j between 2 and 3 have comet-like albedos (from Fernandez et al. 2001).

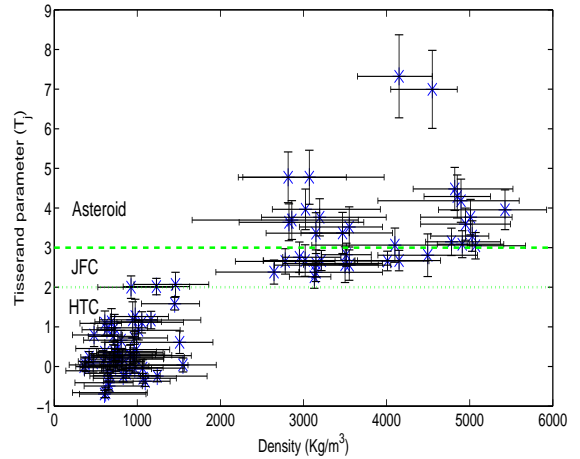


Figure 5.11: Tisserand parameter versus density for our sample of meteoroids. Two lines are drawn at $T_j = 2$ and $T_j = 3$ to mark clearly the boundaries of different dynamical classes following Levison (1996).

compositional findings with our bulk density measurements. We found 9 meteoroids (» 10% of the total sample) that belong to the class of Sun-approaching orbits (SA) (Figure 5.12). Borovicka et al. (2005) separated these meteoroids into a distinct class because they were, as a group, highly depleted in sodium compared to normal meteor spectra. The authors attribute this to thermal processing of the meteoroids when they are close to the sun. Although we cannot judge the sodium content of our meteors, it would be plausible to expect trends in density with perihelion distance, since thermal processing may include sintering of the meteoroid material, with meteoroids becoming more compact as volatiles are lost or altered. Of the 9 meteors in the SA group, 6 have Tisserand parameters between 2 and 3, and 3 have Tisserand parameters above 3; none of the meteoroids with Tisserand parameter less than 2 are found in the SA group. The density of meteoroids belonging to this group in our sample ranges from » 1000 kg m⁻³ to » 4000 kg m⁻³ (table 5.6), but most of the low- q meteoroids have higher (>2500 kg m⁻³) densities. Whether this is due to their parent bodies or to thermal effects is not clear. Our results are consistent with the notion that low q meteoroids are sintered, but small number statistics prevents us from stating this as a strong conclusion.

The inclinations of meteoroid orbits in the SA group are all close to the ecliptic, except for meteoroid 20090902-085534, with an inclination approaching 150°. From its aphelion $Q = 3.4$, the orbit of the meteoroid 20090902-085534 is inside Jupiter. It looks very much like a Halley type orbit (high inclination), possibly with a reduced a due to a high ejection velocity from the sun-approaching parent comet when near perihelion. Surprisingly, this meteoroid has one of the highest densities in our sample (4495§ 600 kg m⁻³), but is highly unlikely to be of asteroidal origin, since it is dynamically nearly impossible for asteroidal orbits to reach such high inclination. It may be an iron-rich inclusion from a Halley type comet, or a thermally processed meteoroid which has lost its volatiles and been sintered.

Our sample contained 24 meteoroids falling into Borovicka's Asteroid-chondritic

Table 5.6: All nine meteoroids of the Sun-approaching orbit class and values of their different parameters: photometric mass, perihelion, semi-major axis, eccentricity, inclination, pre-atmospheric velocity, Tisserand parameter, and bulk density.

code	phot mass (kg)	q (AU)	a (AU)	e	i (\pm)	v_{∞} (km s $^{-1}$)	T_j	density kg m $^{-3}$
20060504-093103	(7.9 \S 0.6) $\text{\textcircled{E}}$ 10 $^{-6}$	0.051 \S 0.002	1.599 \S 0.038	0.968 \S 0.001	15.160 \S 1.059	41.2 \S 0.6	3.5 \S 0.5	3550 $^{+400}_{-600}$
20070813-065828	(1.0 \S 0.1) $\text{\textcircled{E}}$ 10 $^{-5}$	0.137 \S 0.003	2.397 \S 0.073	0.943 \S 0.001	18.279 \S 0.684	38.8 \S 0.6	2.6 \S 0.3	3150 $^{+800}_{-400}$
20080910-052352	(1.5 \S 0.8) $\text{\textcircled{E}}$ 10 $^{-5}$	0.112 \S 0.015	2.348 \S 0.314	0.952 \S 0.004	30.495 \S 3.600	40.7 \S 0.7	2.6 \S 0.5	3500 $^{+400}_{-500}$
20080910-053428	(2.0 \S 0.2) $\text{\textcircled{E}}$ 10 $^{-6}$	0.132 \S 0.007	1.984 \S 0.116	0.933 \S 0.002	6.871 \S 1.694	37.6 \S 0.3	3.1 \S 0.4	4100 $^{+900}_{-1000}$
20080911-094844	(1.7 \S 0.2) $\text{\textcircled{E}}$ 10 $^{-6}$	0.104 \S 0.011	1.741 \S 0.140	0.940 \S 0.002	14.436 \S 3.198	38.0 \S 0.7	3.4 \S 0.5	3470 $^{+600}_{-500}$
20090825-053106	(1.9 \S 0.2) $\text{\textcircled{E}}$ 10 $^{-6}$	0.098 \S 0.007	2.255 \S 0.176	0.957 \S 0.003	17.181 \S 2.169	40.2 \S 0.9	2.7 \S 0.4	3020 $^{+500}_{-500}$
20090825-065903	(3.9 \S 0.4) $\text{\textcircled{E}}$ 10 $^{-6}$	0.162 \S 0.004	2.704 \S 0.097	0.940 \S 0.002	21.310 \S 0.641	38.6 \S 0.5	2.4 \S 0.3	2645 $^{+300}_{-700}$
20090825-061542	(1.7 \S 0.2) $\text{\textcircled{E}}$ 10 $^{-6}$	0.160 \S 0.006	3.422 \S 0.364	0.953 \S 0.005	10.242 \S 1.022	38.9 \S 0.4	2.0 \S 0.3	925 $^{+500}_{-400}$
20090902-085534	(1.6 \S 0.2) $\text{\textcircled{E}}$ 10 $^{-6}$	0.031 \S 0.007	1.734 \S 0.161	0.982 \S 0.005	152.186 \S 8.482	50.9 \S 0.8	2.8 \S 0.5	4495 $^{+600}_{-600}$

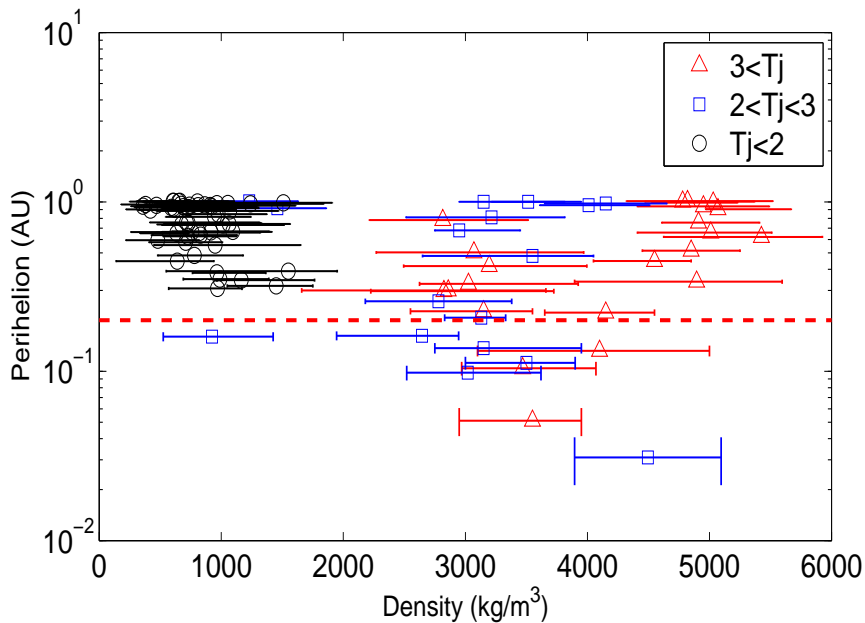


Figure 5.12: The perihelion distance versus bulk density for our observed sample. The dashed line marks the boundary of meteoroid orbits with perihelion (q) below 0.2 AU identified by Borovicka et al. (2005) as being in the class of Sun-approaching orbits.

class (table 5.7), five of which overlap with the SA group. The average density of meteoroids in this class is 4100 kg m^{-3} (see figure 5.13) with a wide spread from 3000 - 5000. Of the 24 meteors, 22 satisfy the criteria because of their Tisserand parameter ($T_j > 3$), and the other two because of their small ($Q < 4.5 \text{ AU}$) aphelia.

In our observations, 55% of meteoroids fall into the HT class of high-inclination, cometary orbits (figure 5.14). Most of these meteoroids have low densities, with a minimum density of $360_{-100}^{+400} \text{ kg m}^{-3}$ and maximum density of $1510_{-900}^{+400} \text{ kg m}^{-3}$. There is one exception: the previously mentioned meteoroid 20090902-085534, with an unambiguously cometary orbit but a very high density. Its perihelion is much smaller than the other HT meteoroids, which may explain its very different physical structure.

The fourth Borovicka class (Jupiter family orbits), are low-inclination cometary orbits. We have 13 of these in our sample, including a 4th which overlaps with the SA class. The average density of JF meteoroids in our sample is $3190_{-480}^{+490} \text{ kg m}^{-3}$,

Table 5.7: All 24 meteoroids with Asteroidal-chondritic orbits (AC) (including 5 which overlap with the SA class and 4 with the ES class) and values of their different parameters: photometric mass, aphelion, semi-major axis, eccentricity, inclination, pre-atmospheric velocity, Tisserand parameter, density, and class.

code	photo mass (kg)	Q (AU)	a (AU)	e	i (\pm)	v_{∞} (km s $^{-1}$)	T_j	density kg m $^{-3}$	class
20060504-093103	(7.9\$ 0.6)£ 10 $^{-6}$	3.147\$ 0.076	1.599\$ 0.038	0.968\$ 0.001	15.160\$ 1.059	41.20\$ 0.61	3.522\$ 0.507	3550 $^{+400}_{-600}$	AC/SA
20060505-102944	(2.0\$ 0.2)£ 10 $^{-5}$	1.187\$ 0.013	0.818\$ 0.013	0.452\$ 0.012	27.281\$ 0.812	20.60\$ 0.25	6.994\$ 0.984	4550 $^{+300}_{-500}$	AC
20080910-053428	(2.0\$ 0.1)£ 10 $^{-6}$	3.837\$ 0.226	1.984\$ 0.116	0.933\$ 0.002	6.871\$ 1.694	37.60\$ 0.33	3.063\$ 0.432	4100 $^{+900}_{-1000}$	AC/SA
20080911-071428	(1.1\$ 0.1)£ 10 $^{-5}$	1.312\$ 0.017	0.767\$ 0.011	0.711\$ 0.010	5.768\$ 1.091	22.80\$ 0.43	7.323\$ 1.048	4150 $^{+400}_{-500}$	AC
20080911-084529	(2.2\$ 0.2)£ 10 $^{-6}$	3.487\$ 0.355	1.856\$ 0.187	0.878\$ 0.004	10.217\$ 2.478	33.50\$ 0.43	3.366\$ 0.515	3150 $^{+600}_{-400}$	AC
20080911-094844	(1.7\$ 0.1)£ 10 $^{-6}$	3.378\$ 0.269	1.741\$ 0.140	0.940\$ 0.002	14.436\$ 3.198	38.00\$ 0.67	3.371\$ 0.519	3470 $^{+600}_{-500}$	AC/SA
20090825-033603	(1.2\$ 0.1)£ 10 $^{-6}$	3.178\$ 0.080	1.738\$ 0.042	0.829\$ 0.002	4.354\$ 0.540	30.90\$ 0.26	3.639\$ 0.466	2825 $^{+900}_{-600}$	AC/ES
20090825-035228	(2.9\$ 0.2)£ 10 $^{-6}$	2.828\$ 0.067	1.578\$ 0.034	0.792\$ 0.005	5.756\$ 0.398	29.20\$ 0.40	3.967\$ 0.512	3025 $^{+900}_{-400}$	AC/ES
20090825-053106	(2.0\$ 0.1)£ 10 $^{-6}$	4.412\$ 0.349	2.255\$ 0.176	0.957\$ 0.003	17.181\$ 2.169	40.20\$ 0.93	2.674\$ 0.398	3020 $^{+600}_{-500}$	AC/SA
20090825-070044	(6.3\$ 0.4)£ 10 $^{-7}$	2.630\$ 0.061	1.484\$ 0.029	0.772\$ 0.007	4.859\$ 0.125	28.10\$ 0.96	4.184\$ 0.544	4895 $^{+700}_{-1000}$	AC/ES
20090825-081927	(8.0\$ 0.4)£ 10 $^{-8}$	2.736\$ 0.154	1.679\$ 0.084	0.630\$ 0.011	14.171\$ 0.787	22.40\$ 0.41	3.955\$ 0.501	5425 $^{+500}_{-800}$	AC
20090825-091030	(8.7\$ 0.6)£ 10 $^{-7}$	1.854\$ 0.031	1.179\$ 0.017	0.573\$ 0.005	62.338\$ 0.429	36.10\$ 0.73	4.777\$ 0.682	3070 $^{+900}_{-800}$	AC
20090825-032616	(4.3\$ 0.2)£ 10 $^{-6}$	3.161\$ 0.176	2.050\$ 0.088	0.542\$ 0.020	0.901\$ 0.344	14.80\$ 0.20	3.593\$ 0.405	4950 $^{+540}_{-540}$	AC
20090825-035145	(1.4\$ 0.1)£ 10 $^{-6}$	1.742\$ 0.041	1.261\$ 0.023	0.381\$ 0.008	44.584\$ 0.399	27.70\$ 0.30	4.775\$ 0.639	2815 $^{+700}_{-600}$	AC
20090825-050631	(1.3\$ 0.1)£ 10 $^{-6}$	3.034\$ 0.080	1.726\$ 0.040	0.758\$ 0.006	3.881\$ 0.338	27.10\$ 0.70	3.765\$ 0.469	3195 $^{+800}_{-700}$	AC
20090825-050904	(5.1\$ 0.3)£ 10 $^{-6}$	1.969\$ 0.067	1.490\$ 0.033	0.322\$ 0.015	12.770\$ 0.510	13.80\$ 0.20	4.481\$ 0.542	4820 $^{+700}_{-500}$	AC
20090825-060500	(2.6\$ 0.2)£ 10 $^{-6}$	3.113\$ 0.149	1.706\$ 0.077	0.824\$ 0.007	4.966\$ 0.913	30.50\$ 0.30	3.696\$ 0.489	2860 $^{+800}_{-1200}$	AC/ES
20090826-020835	(1.1\$ 0.1)£ 10 $^{-6}$	3.887\$ 0.248	2.445\$ 0.124	0.590\$ 0.021	23.277\$ 0.434	19.20\$ 0.30	3.146\$ 0.345	4780 $^{+590}_{-310}$	AC
20090902-085534	(1.6\$ 0.2)£ 10 $^{-6}$	3.437\$ 0.328	1.734\$ 0.161	0.982\$ 0.005	152.186\$ 8.482	50.90\$ 0.80	2.808\$ 0.539	4910 $^{+500}_{-300}$	AC/SA
20090909-010643	(2.5\$ 0.2)£ 10 $^{-6}$	4.212\$ 0.264	2.483\$ 0.131	0.696\$ 0.017	3.134\$ 0.216	20.60\$ 0.30	3.086\$ 0.341	4910 $^{+500}_{-300}$	AC
20090909-012810	(2.2\$ 0.2)£ 10 $^{-6}$	2.979\$ 0.107	1.819\$ 0.054	0.638\$ 0.010	4.336\$ 0.362	21.40\$ 0.46	3.769\$ 0.448	5010 $^{+500}_{-600}$	AC
20090909-013647	(4.9\$ 0.4)£ 10 $^{-6}$	3.674\$ 0.366	2.332\$ 0.183	0.575\$ 0.034	14.262\$ 0.597	16.10\$ 0.40	3.293\$ 0.385	5030 $^{+200}_{-500}$	AC
20090911-021830	(1.5\$ 0.1)£ 10 $^{-6}$	4.184\$ 0.273	2.544\$ 0.136	0.644\$ 0.019	20.443\$ 0.392	20.15\$ 0.70	3.048\$ 0.333	5070 $^{+600}_{-100}$	AC
20090911-034442	(1.7\$ 0.1)£ 10 $^{-6}$	2.472\$ 0.072	1.494\$ 0.038	0.655\$ 0.007	4.452\$ 0.469	23.40\$ 0.63	4.291\$ 0.543	4850 $^{+400}_{-400}$	AC

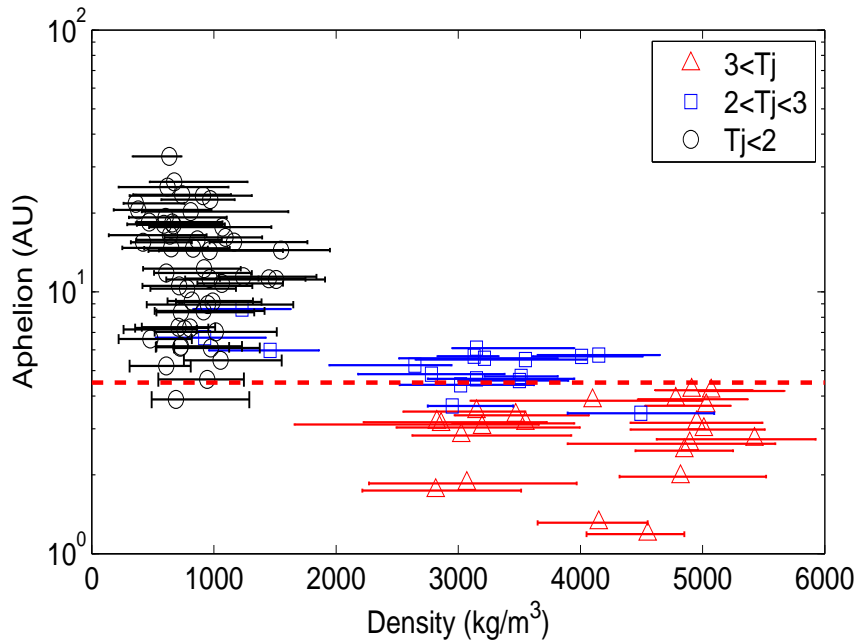


Figure 5.13: Aphelion versus density for our meteoroid sample. The horizontal line indicates an aphelion (Q) of 4.5 AU, below which meteoroids are expected to be of asteroidal origin following Borovicka et al., 2005.

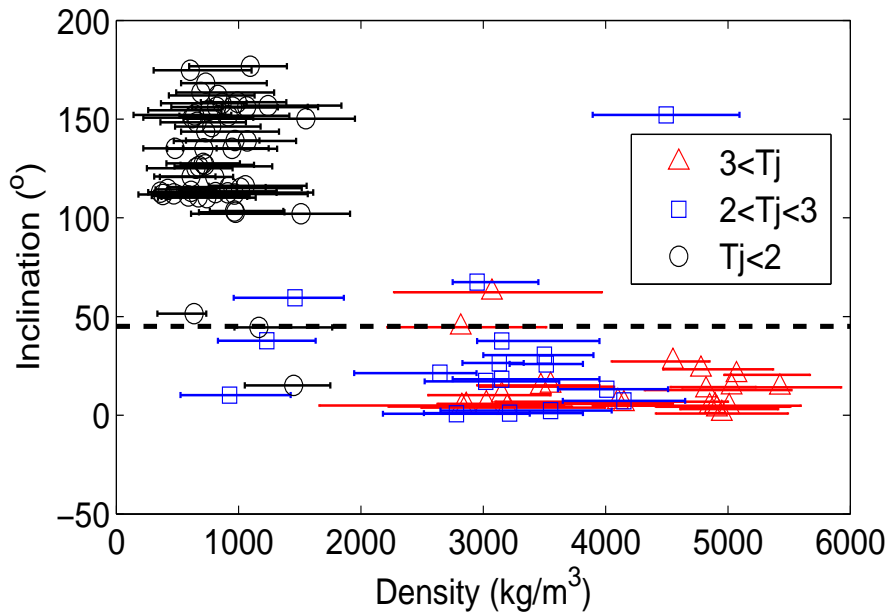


Figure 5.14: The orbital inclination versus bulk density for our meteoroid sample. The horizontal dashed line marks the boundary of meteoroid orbits with inclination (i) above 45° . Meteoroids with inclination $i > 45^\circ$ and $2 < T_j < 3$ or $T_j < 2$ form the class of meteoroids with Halley type orbits (HT) according to the scheme of Borovicka et al. (2005).

suggesting bulk properties akin to ordinary chondrites with low porosity. One of these, meteor 20090825-061442, has a bulk density (ρ) less than 1000 kg m^{-3} , but also a low T_j ; within error it can be placed in the HTC (Halley type comets) class.

This is perhaps our most significant result. We are sampling from a range of original JF bodies (as the JFC meteoroids were observed from a wide range of radiant over the course of the year). JFCs are believed to be derived from the Kuiper-Belt and then being perturbed inward to become active comets, retaining their flat inclination distribution (see Fernandez, 1980 and recent review by Morbidelli, 2008). In this scenario JFCs form in the outer part of the solar system and are not likely collisional fragments of larger bodies - ie. they are expected to be primitive. Prior to the sample return from 81P/Wild 2, expectations were that most material in JFCs would resemble chondritic porous (CP) IDPs in chemistry; instead analysis of the aerogel-captured particles from Wild 2 has shown that a large fraction of this JFCs material is chondrite-like with abundant refractory material indicative of formation of some of Wild 2 in the inner solar system (Ishii et al., 2008; Brownlee et al., 2006). This refractory material was found from primary particles impacting aerogel which originally had sizes estimated to be in the tens of micron range in most cases (Horz et al., 2006).

Our findings suggest that the trend found for 81P/Wild 2 applies to other JFCs and extends the existence of refractory-rich particles in JFCs up to mm-sized particles which in our model are comprised of micron - tens of micron-sized grains. The implication is that the process which implanted refractory material in the JFC population was ubiquitous (and not confined to 81P/Wild 2). Furthermore, we find a clear distinction in the bulk density properties of cometary meteoroids originating from JFCs versus those from HTC/NICs suggesting different formation locations and/or evolutionary pathways.

In Borovicka's final class, the ecliptic showers, we found four meteoroids, all members of the Northern Iota Aquariids. If it were not for this class, all of these

Table 5.8: All thirteen meteoroids with Jupiter Family orbits (JF) (including 4 which overlap with the SA class) and values of their different parameters: photometric mass, aphelion, semi-major axis, eccentricity, inclination, pre-atmospheric velocity, Tisserand parameter, density, and class.

code	photo mass (kg)	Q (AU)	a (AU)	e	i (\pm)	v_∞ (km s $^{-1}$)	T_j	density kg m $^{-3}$	class
20070813-065828	(1.0 \S 0.1) \pounds 10 $^{-5}$	4.656 \S 0.145	2.397 \S 0.073	0.943 \S 0.001	18.279 \S 0.684	38.8 \S 0.6	2.6 \S 0.3	3150 $^{+400}_{-800}$	JF/SA
20080910-052352	(1.5 \S 0.1) \pounds 10 $^{-5}$	4.583 \S 0.616	2.348 \S 0.314	0.952 \S 0.004	30.495 \S 3.600	40.7 \S 0.7	2.6 \S 0.5	3500 $^{+500}_{-400}$	JF/SA
20080910-064102	(5.2 \S 0.4) \pounds 10 $^{-6}$	5.516 \S 0.930	2.997 \S 0.474	0.840 \S 0.019	2.392 \S 1.539	28.2 \S 0.5	2.6 \S 0.4	3550 $^{+500}_{-900}$	JF
20090825-065903	(3.9 \S 0.4) \pounds 10 $^{-6}$	5.247 \S 0.192	2.704 \S 0.097	0.940 \S 0.002	21.310 \S 0.641	38.6 \S 0.5	2.4 \S 0.3	2645 $^{+700}_{-300}$	JF/SA
20090825-043435	(4.8 \S 0.5) \pounds 10 $^{-6}$	4.850 \S 0.149	2.555 \S 0.076	0.898 \S 0.002	0.767 \S 0.437	34.2 \S 0.3	2.7 \S 0.3	2780 $^{+600}_{-600}$	JF
20090820-014058	(5.0 \S 0.4) \pounds 10 $^{-6}$	6.097 \S 0.339	3.554 \S 0.169	0.716 \S 0.014	37.598 \S 0.248	26.2 \S 0.5	2.4 \S 0.2	3150 $^{+800}_{-200}$	JF
20090825-034528	(1.1 \S 0.7) \pounds 10 $^{-6}$	5.737 \S 0.439	3.357 \S 0.219	0.709 \S 0.019	7.325 \S 0.245	15.7 \S 0.3	2.7 \S 0.3	4150 $^{+500}_{-500}$	JF
20090825-061542	(1.7 \S 0.2) \pounds 10 $^{-6}$	6.684 \S 0.728	3.422 \S 0.364	0.953 \S 0.005	10.242 \S 1.022	38.9 \S 0.4	2.1 \S 0.3	925 $^{+400}_{-500}$	JF/SA
20090825-070933	(3.1 \S 0.2) \pounds 10 $^{-6}$	5.572 \S 0.157	3.191 \S 0.079	0.746 \S 0.006	1.064 \S 0.122	19.6 \S 0.4	2.7 \S 0.3	3215 $^{+600}_{-700}$	JF
20090902-084143	(6.3 \S 0.5) \pounds 10 $^{-6}$	8.595 \S 1.091	4.801 \S 0.545	0.790 \S 0.024	37.713 \S 0.513	26.7 \S 0.7	2.0 \S 0.2	1230 $^{+400}_{-400}$	JF
20090911-030523	(4.8 \S 0.6) \pounds 10 $^{-6}$	5.675 \S 0.357	2.941 \S 0.178	0.929 \S 0.005	26.498 \S 0.526	38.2 \S 0.3	2.3 \S 0.3	3130 $^{+200}_{-300}$	JF
20090911-035942	(1.4 \S 0.2) \pounds 10 $^{-6}$	4.756 \S 0.273	2.879 \S 0.137	0.652 \S 0.017	26.004 \S 0.319	20.6 \S 0.2	2.8 \S 0.3	3515 $^{+300}_{-300}$	JF
20090911-040433	(2.3 \S 0.2) \pounds 10 $^{-5}$	5.670 \S 0.203	3.313 \S 0.101	0.711 \S 0.009	13.201 \S 0.157	17.4 \S 0.3	2.7 \S 0.2	4010 $^{+500}_{-400}$	JF

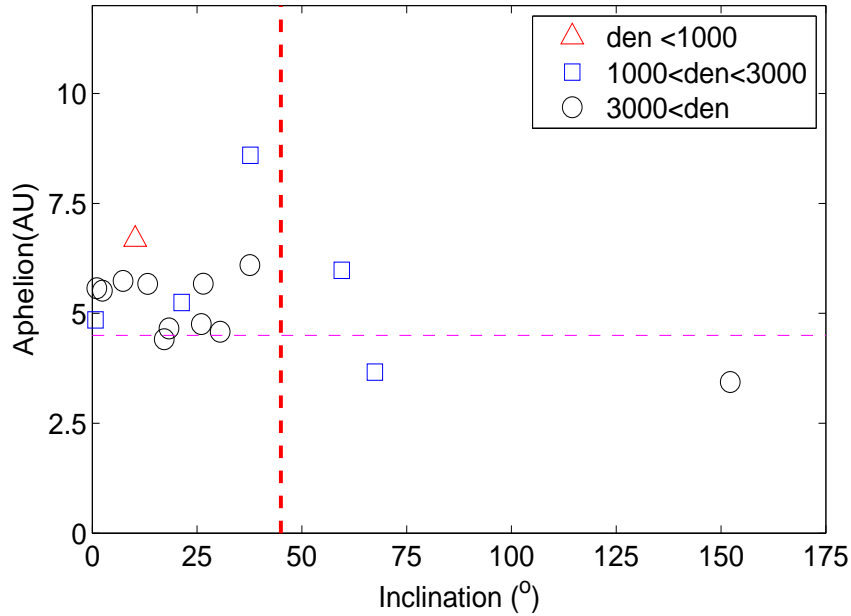


Figure 5.15: Inclination versus aphelion for meteoroid orbits with Tisserand parameter $2 < T_j < 3$ nominally in the JFC (Jupiter family comets) class. The vertical line denotes the boundary of meteoroid orbits with inclination $i < 45$, and the horizontal line the boundary for meteoroid orbits with aphelion $Q > 4.5$ AU. These meteoroids constitute the class of Jupiter family orbits (see Borovicka et al., 2005).

meteoroids would fall into the asteroidal class because of the large Tisserand parameter. The average density of these meteoroids is 3200 kg m^{-3} , so these objects appear to be chondritic, similar to our findings for the Jupiter family material. The fact that, if not for their shower association, these meteoroids would be classified as asteroidal, suggests that many of the meteoroids in the asteroidal-chondritic class may actually be from Jupiter family comets. Indeed the NIA shower is thought to be part of the Taurid complex, linked to 2P/Encke (Brown et al., 2008).

5.6.2 Meteoroid strength and density

Meteor beginning height has been used in past work as a measure of the strength of meteoroids in the millimeter size range (see Ceplecha, 1958, 1967, 1968, 1988, Borovicka et al., 2005). For two meteoroids having the same pre-atmospheric velocity, a stronger/denser meteoroid will start to ablate at a lower height than a

Table 5.9: All 4 meteoroids of the Ecliptic shower orbits class (ES) and values of their different parameters: photometric mass, perihelion, semi-major axis, eccentricity, inclination, pre-atmospheric velocity, Tisserand parameter, and density.

code	photom. mass (kg)	q (AU)	a (AU)	e	i (\pm)	v_{∞} (km s $^{-1}$)	T_j	density kg m $^{-3}$
20090825033603	(1.2 \S 0.1) \pounds 10 $^{-6}$	0.297 \S 0.005	1.738 \S 0.042	0.829 \S 0.002	4.354 \S 0.540	30.90 \S 0.26	3.639 \S 0.5	2825 $^{+600}_{-900}$
20090825035228	(2.9 \S 0.2) \pounds 10 $^{-6}$	0.328 \S 0.005	1.578 \S 0.034	0.792 \S 0.005	5.756 \S 0.398	29.20 \S 0.40	3.967 \S 0.5	3025 $^{+400}_{-900}$
20090825070044	(6.3 \S 0.4) \pounds 10 $^{-7}$	0.338 \S 0.004	1.484 \S 0.029	0.772 \S 0.007	4.859 \S 0.125	28.10 \S 0.96	4.184 \S 0.5	4895 $^{+1000}_{-700}$
20090825060500	(2.6 \S 0.2) \pounds 10 $^{-6}$	0.300 \S 0.009	1.706 \S 0.077	0.824 \S 0.007	4.966 \S 0.913	30.50 \S 0.30	3.696 \S 0.5	2860 $^{+1200}_{-800}$

weaker/low density meteoroid. Fig. 5.16 shows the beginning height versus density for the meteoroids in our sample, divided into five classes described in the previous section. The figure clearly shows that meteoroids from the AC class, which have the highest density, start at lower heights, while the HT meteoroids, with low densities, have high beginning heights, trends entirely as expected.

We found that the beginning heights of meteoroids in our sample seem to be mass-independent. This is in agreement with the work done by Koten et al. (2004) on several meteor showers (see their Figure 3 on beginning heights versus photometric mass of fainter Perseid meteors). For the size of meteoroids in our sample with an average mass around $\gg 10^{-6}$ kg, as predicted by dust-ball model (Hawkes and Jones, 1975), there is no clear dependence between beginning heights and photometric mass. There is a clear relationship between beginning heights and velocity, as expected (see Figure 5.19). HT meteoroids in our sample (low density material) have high velocity and start to ablate very high in the atmosphere, whereas AC meteoroids have lower beginning heights, but high densities, again as found in earlier works.

Figure 5.17 shows the plot of velocity versus density. The general trend of our plot is that high density meteoroids (AC) have small velocities, and low density meteoroids (HT) have high velocities as expected from their orbital properties and the conditions of encounter with the Earth. The only meteoroid with a large velocity and high density is meteor 20090902-085534, with a cometary, Sun-approaching orbit whose origin and probable history have already been discussed. We observe that the bulk density trends we see with velocity make clear that we are not biasing the measurements due to limitations of our measurements; in general one expects high velocity meteors to show the least deceleration and if we were not properly measuring deceleration (or it was below our measurement precision) our model would tend to show artificially high bulk densities (all else being the same) which is the opposite of the trend we see.

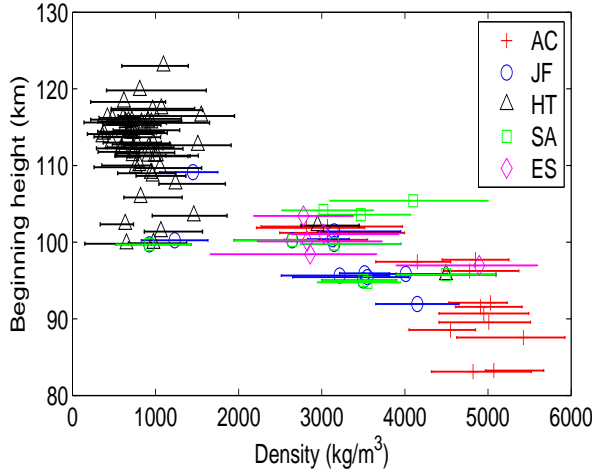


Figure 5.16: Beginning height versus density of meteoroids of our sample. The meteoroids are divided according to the orbital classes defined above.

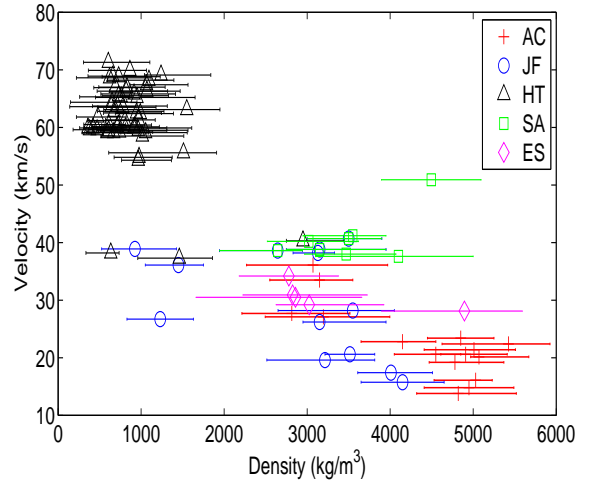


Figure 5.17: Velocity versus density of meteoroids of our sample. The meteoroids are divided according to the orbital classes defined above.

5.6.3 Comparison using the K_B parameter

Ceplecha introduced a parameter, K_B , which classifies meteoroids according to their beginning height, while simultaneously taking into account their pre-atmospheric velocity and the trajectory slope. The parameter is based on the assumption that all meteoroids begin to be luminous at the same surface temperature and hence beginning height will be a strong function of the meteoroid composition. Inclusion of velocity and entry angle helps to remove the dependence on geometry of the beginning height, and gives a parameter closely tied to the material strength of the meteoroid. K_B is defined as (Ceplecha, 1967):

$$K_B = \log \rho_B + 2.5 \log v_\infty + 0.5 \log \cos Z_R \quad (5.6)$$

where ρ_B is the air density at the beginning of the luminous trajectory, expressed in g cm^{-3} , v_∞ is the initial velocity (pre-atmospheric velocity) expressed in cm s^{-1} , and z_R is the zenithal angle of the radiant. Ceplecha (1988) used the K_B parameter to separate meteoroids in the mm to cm-size range into four populations:

1. group A: $7.30 \cdot K_B < 8.00$

2. group B: $7.10 \cdot K_B < 7.30$

3. group C: $6.60 \cdot K_B < 7.10$

4. group D: $K_B < 6.60$

He associated group A with ordinary chondrite material, group B with carbonaceous chondrites, group C with dense and regular cometary material, and D with weak cometary meteoroids (Ceplecha, 1988). Later, Ceplecha (1988) also added a fifth group, Asteroidal, to the four mentioned here, for meteoroids with $K_B \leq 8$. He also divided Group C into three subgroups based on orbital elements, but due to our small number statistics, we treat these as one.

Equation 5.6 was developed and first applied to meteors photographed by Super-Schmidt cameras (see Ceplecha, 1967, Ceplecha, 1988, Bellot Rubio et al., 2002). For the fainter meteors observed by intensified video systems, the parameter K_B is calculated in the same way, but an offset of 0.15 is added (see Ceplecha, 1988) because the K_B criterion is based on meteor beginning heights, which depend on the sensitivity of the camera. TV systems being more sensitive than Super-Schmidt cameras (see Sarma and Jones, 1985), the meteors will be observed higher up, and K_B will be systematically shifted to lower values.

Fig. 5.18 shows a histogram of the K_B values for our sample using a nominal shift for our observations of +0.18 relative to that used by Ceplecha (1988). Two clear peaks are evident: one around $K_B \approx 7.0$, likely corresponding to group C; one around $K_B \approx 7.8$, which we believe is actually the A group. We note that the general form of this distribution is similar to that found by Ceplecha (1967) for Super-Schmidt meteors, but our peaks are offset by 0.18 from the Ceplecha (1967) peaks. This is a larger shift than suggested for the TV data by Ceplecha (1988), but can be understood as the improvement in sensitivity of modern electro-optical system compared to the early ISIT systems used by Sarma and Jones (1985). The peak of group D is not clearly visible, because only a few meteoroids in our sample belong

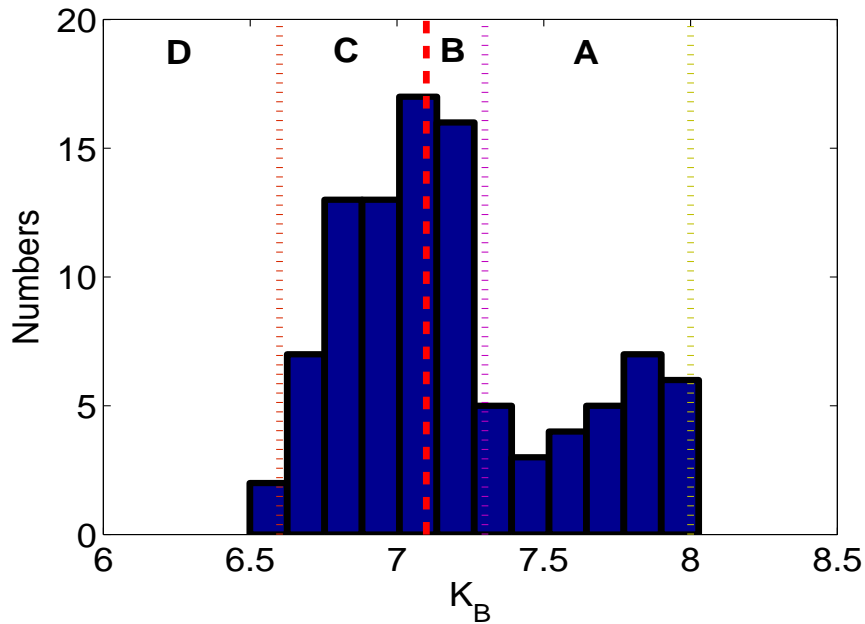


Figure 5.18: Histogram of K_B values of our sample. Two groups are clearly distinguishable: group A around $K_B \gg 7.8$ and group C around $K_B \gg 7.0$. The nominal population demarcations follow Ceplecha’s (1967) bin sizes for each group but shifted by +0.18.

to this group. There is no evidence for a distinct peak corresponding to group B in our data. Group C contains most of the meteoroids in our sample (44%). Although we have no meteoroids in Ceplecha’s asteroidal class ($K_B < 8$), we may still have asteroidal material in group A, which overlaps significantly with Borovicka’s A-C class. We do not find evidence for a distinct class B, but rather there seems to be a continuum from class A to C. We do find a very clear distinction between the various Ceplecha classes based on K_B and T_j and bulk density supporting the notion that physical differences are dominated by origin rather than evolution.

We can compare the average density of meteoroids in these groups found from our data to previous results. Table 5.10 summarizes the results from five studies, including ours. Three of the studies (Ceplecha 1966, 1967; and Bellot Rubio et al., 2002) used Super-Schmidt data, for meteoroids slightly larger than those in our data set. Ceplecha finds densities for these meteoroids which are nearly twice those found by Bellot Rubio. The density calculation of Ceplecha (1967) is based

on the Levin (1956) formula describing the meteoroid surface temperature $\tau(0, h)$ at height h . For the analysis by Ceplecha (1967), τ is calculated at the beginning height. Thus, Ceplecha's densities are averages, and not derived from individual fits to each meteor in his sample. Bellot Rubio et al. (2002) described the dynamical and photometric behavior of individual faint meteors observed with Super-Schmidt cameras by means of the single body theory to arrive at the densities values in Table ???. Our values are larger than these other studies for Groups A, and D which may reflect a physical change in meteoroid properties with mass or particular differences between our model approach and these works.

5.6.4 Comparison of bulk density and meteoroid spectra

Borovicka et al. (2005) has argued that the dependence of beginning height on speed is sufficient to recognize different material strength among different spectral classes of meteoroids. In their figure 15, they clearly show that the average beginning height of Na-free meteoroids and Iron meteoroids as being lower than other meteoroids. In contrast, the Fe-poor meteoroids tend to have higher beginning heights.

Fig. 5.19 based on our data, shows the same relationship between beginning height and speed using the 4 classes identified by Borovicka et al. (2005). Fig. 5.20 also shows the same relationship, but for the 4 groups according to Ceplecha's classification. Group A is clearly concentrated in the lower part of the thick line. There are 4 meteoroids of group A at high velocity. This might be smeared by the zenith angle of the radiant. Groups C and D are all concentrated in the upper part of the thick line, as expected. We found 5 meteoroids with beginning heights below » 90 km (Fig. 5.19). They all belong to the AC (Asteroid-chondritic) class and are likely iron-rich (following Borovicka et al.,2005), based on their density. The same meteoroids in Fig. 5.20 fall into the A-group, whose average density from our analysis is $3800 \pm 800 \text{ kg m}^{-3}$ (see Table 5.10).

The sun-approaching meteoroids (SA class) with perihelion $q < 0.22 \text{ AU}$ have

Table 5.10: Average density in Ceplecha's four meteor classes from different studies

Work	Instruments	group A density (kg m^{-3})	group B density (kg m^{-3})	group C density (kg m^{-3})	group D density (kg m^{-3})
Ceplecha, 1966	Photographic Super-Schmidt	4000	2200	1400	-
Ceplecha, 1967	Photographic Super-Schmidt	4000	2200	1400	-
Ceplecha, 1988 (table 6)	Photographic and TV	1400 - 2700	650 - 1700	550 - 910	180 - 380
Bellot Rubio et al. 2002	Photographic Super-Schmidt	2400	1400	400	-
This work	TV systems	3800	-	800	-

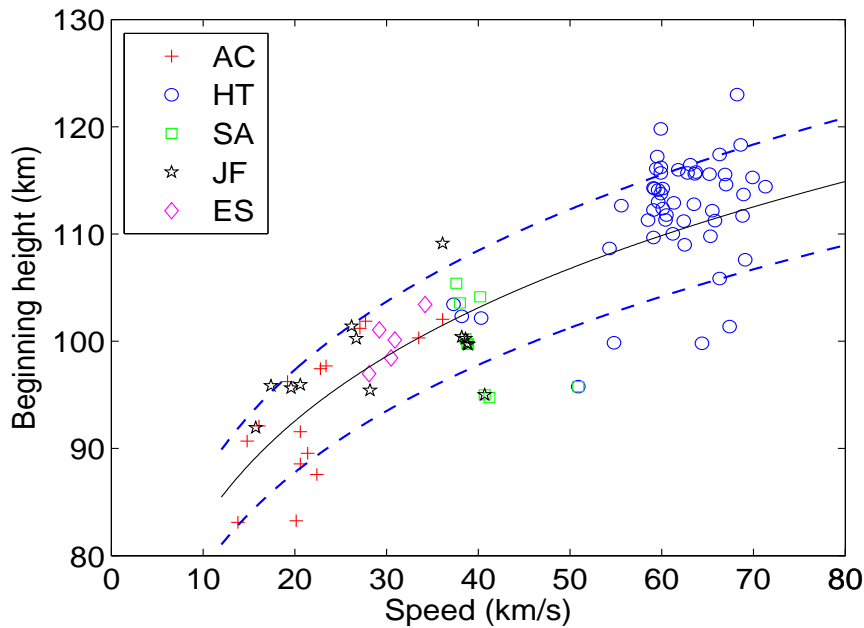


Figure 5.19: Meteor beginning height as a function of initial velocity for our sample. Different classes of meteoroids are shown using different symbols (AC, HT, SA, and JF following the classification of Borovicka et al., 2005). The solid line and two dashed lines mark the mean beginning of average strength meteoroids and their limits. The equation of the empirical mean line is $h_B = 58 \text{ km} v^{0.156}$ (see Borovicka et al. 2005).

no sodium in their spectra according to Borovicka et al. 2005. In Fig. 5.20, these meteoroids appeared to be spread over three different groups (A-group, C-group and D-group). We cannot then attach to them a unique average density. This is a consequence of the fact that SA meteoroids evolve from different dynamical populations and hence likely have very different starting compositions, and structures. They all have thermal heating in common, but the final products are still quite different. Indeed, while most SA densities are high, supporting the notion that evolution dominates over origin for this population, at least one has a low density and probable HT origin suggesting this is not the case. Our Fe-poor meteoroids with higher beginning heights all can be easily assigned to the HT class (Halley type orbits) (Fig. 5.19). They also belong to the C-group which has an average bulk density of 1000 kg m^{-3} . They are all likely cometary meteoroids.

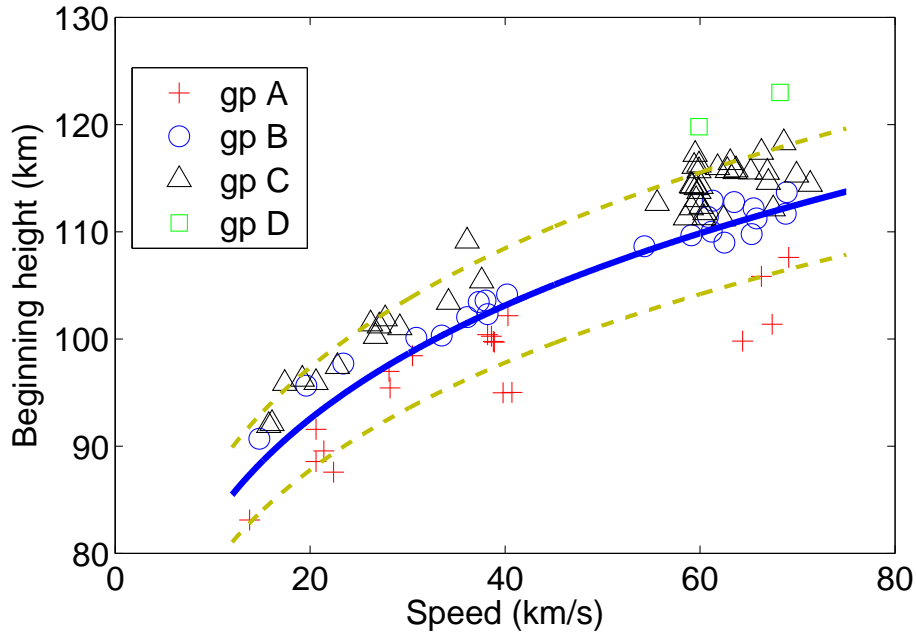


Figure 5.20: Meteor beginning height as a function of initial velocity. We have plotted Ceplecha’s classes of meteoroids in our sample (A-group, B-group, C-group, and D-group). The solid line and two dashed lines mark the mean beginning of average strength meteoroids and their limits, with the empirical mean line being $h_B = 58 \text{ km} v^{0.156}$ (see Borovicka et al. 2005).

5.6.5 Interpretation of meteoroid physical properties

In broad terms our meteoroid bulk density results can be broken down into a high density class (density $\geq 3000 \text{ kg m}^{-3}$) and low density (density $< 2000 \text{ kg m}^{-3}$) class. For the former particles, a high density is required for constituent grains. Indeed, most of these particles have bulk densities reminiscent of chondritic objects within our uncertainty. A few of the densest objects have significantly higher modelled bulk densities. As Iron is the most cosmochemically abundant element with a bulk density in this range, we presume this is a major component, though the mineralogy is quite unconstrained. These so called “iron” meteoroids have density values most closely matching stony-iron meteorites, which have grain densities around 4820 kg m^{-3} , and porosities of 6% (Consolmagno and Britt, 1998, Table 1, Britt and Consolmagno, 2003, Table 5). It is possible that these high density ($\rho > 4000 \text{ kg m}^{-3}$) meteoroids may be related to IDPs with sulfide inclusions, described by Love et al. (1994).

From our measurements, these make up a large fraction of the meteoroid population at mass (m) $\gg 10^{-6}$ kg, possibly even higher than at IDP masses (10^{-8} kg) (see figure 1 of Love et al., 1994).

Our A group contains mostly material with chondrite-like bulk densities, which for bulk meteoroid samples has a grain density of typically 3640 kg m^{-3} , and average porosity $\gg 10\%$ (Britt and Consolmagno, 2003). These meteoroids appear to most closely resemble chondritic - filled (CF) IDPs (Bradley et al., 2003). The density of HTC/NIC - related particles we find to be $(350-1500) \text{ kg m}^{-3}$. This is close to that of many IDPs which have an average density of 600 kg m^{-3} , indicating appreciable porosity (Love et al., 1994). The cometary meteoroid bulk density is consistent with the bulk density inferred for the several cometary nuclei (see Asphaug and Benz, 1996; Davidson and Gutierrez, 2004, 2005) suggesting microporosity could dominate cometary nucleus structure for HTC/NICs. However, we caution that most of these measurements are for Jupiter-family comets.

The aei plot of our samples (Fig. 5.21) compared to Figures 4 and 6 of Bottke et al. (2002) shows a concentration of meteoroids originating from the $\nu 6$ secular resonance, and the 3:1 mean motion resonance. This suggests that most of these objects are asteroidal. Their density is uniformly high, as expected of asteroidal material.

We have also examined the relationship between our estimated bulk densities and meteoroid orbits as a function of the various parameters which are fit in our model. This included examining trends in the heat of ablation, boiling point, temperature at which the grains are released, specific heat, average molar mass and thermal conductivity of the meteoroids as a function of bulk density and (separately) orbit-type. We found that most parameters showed no strong correlation, except thermal conductivity and bulk density.

When plotting thermal conductivity versus bulk density of our sample (Figure 5.22) (we took the average of thermal conductivity in density bins of 1000 kg m^{-3})

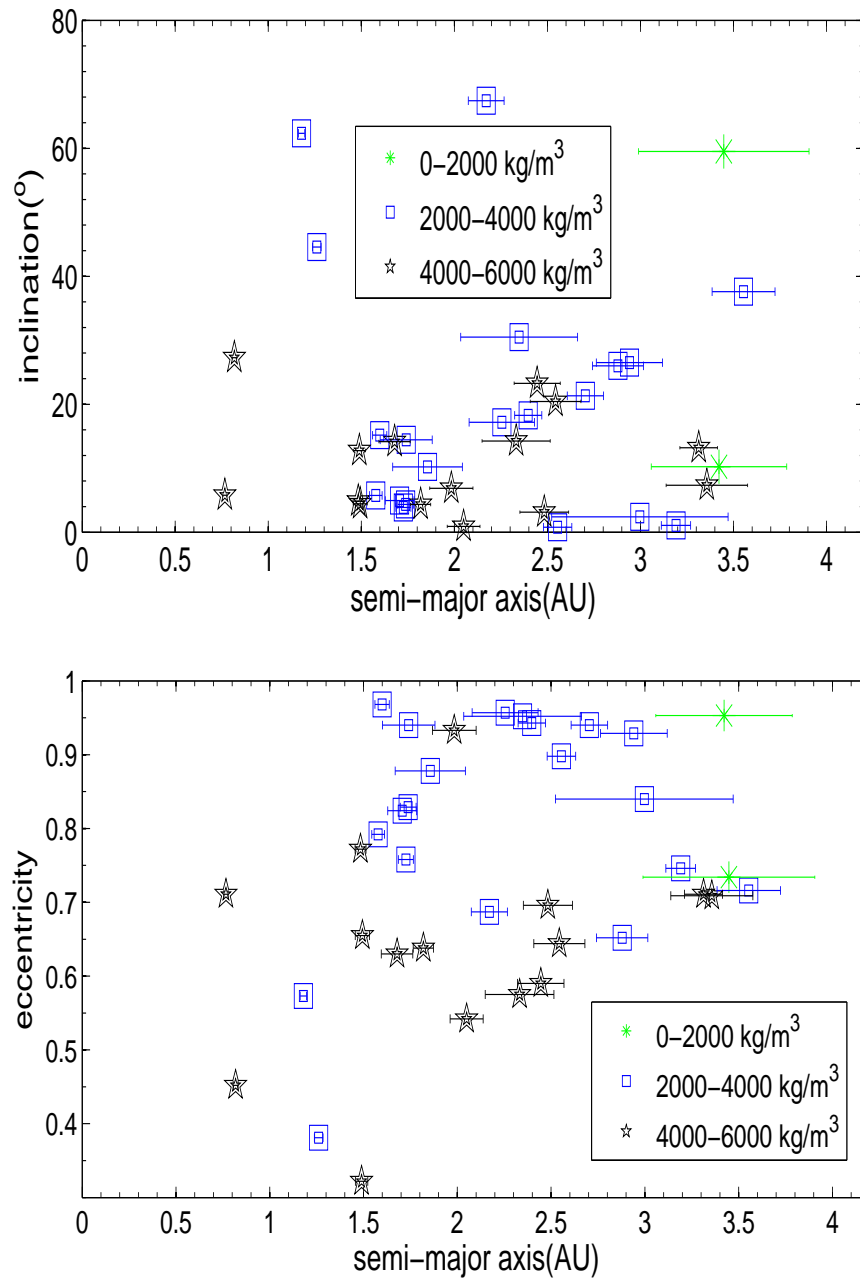


Figure 5.21: Plot of aei of our sample for meteoroids with semi-major axis $a \cdot 4.2$ AU, and inclination $i \cdot 80^\circ$.

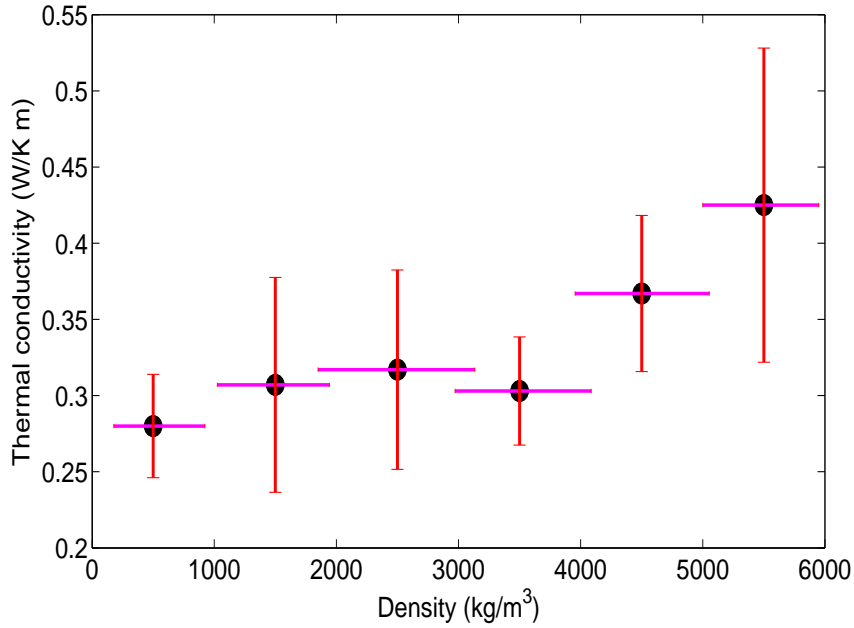


Figure 5.22: Plot of thermal conductivity versus bulk density of our sample. The data are binned in approximately 1000 kg m^{-3} steps (indicated by the extent of the horizontal error bars and the vertical error bars are the standard error of the mean in that bin).

m^{-3} sizes), we find that thermal conductivity has a correlation with bulk density, as expected. All our low density meteoroids have low thermal conductivity suggesting their porous property, consistent with the thermal conductivity value assumed by Vokrouhlicky and Farinella (2000) for porous and fragmented rocks in their work on efficient delivery of meteorites to the Earth.

5.6.6 Meteor showers

Our dataset has two noticeable shower populations: one around geocentric right ascension $\alpha_g \gg 50^\circ$ and geocentric declination $\delta_g \gg 60^\circ$, another around $\alpha_g \gg 350^\circ$ and $\delta_g \gg 2^\circ$. We used the catalog of meteor showers published by Brown et al. (2010) to identify the two concentrations of radiants: 10 meteoroids belong to the Perseids ($\alpha_g = 52.17^\circ$, $\delta_g = 58.07^\circ$, $v_g = 61.9 \text{ km s}^{-1}$), and another 4 meteoroids to the Northern Iota Aquarids ($\alpha_g = 352.25^\circ$, $\delta_g = 1.84^\circ$, $v_g = 28.7 \text{ km s}^{-1}$).

We find the average bulk density of Perseids in our sample to be $620 \pm 200 \text{ kg}$

m^{-3} . This average bulk density is close to the value of 600 kg m^{-3} found by Bellot Rubio et al. (2002) but somewhat smaller than the 1300 kg m^{-3} value reported by Babadzhanov, 2002 (see also Borovicka, 2005, Table 3). The 4 Northern Iota Aquarids found in our sample have an average bulk density of $\approx 3200 \pm 400 \text{ kg m}^{-3}$. Their K_B values put them in the A-group. Their Tisserand parameters are below 3, except for one (20090825-070044) whose $T_j = 4.184$. From this small sample it appears that the Northern Iota Aquarids have closer affinities to chondritic bodies than low density cometary objects. Their high density may reflect a small q in the past, and perhaps also a JF/(Encke) origin.

5.7 Conclusion

Our study combined very precise meteor observations with a complete model of meteor ablation to estimate the bulk density of very small (mean mass $\approx 10^{-6} \text{ kg}$) optical LLLTV meteoroids. Of 107 meteors captured with three different TV systems, 78% showed noticeable deceleration, an important constraint for the ablation model. While some meteors (9 in total) saturated our Gen III cameras, a technique for saturation correction was applied in order to get an accurate photometric mass; without this correction, there would be significant error in measured photometric mass and bulk density.

We were able to compute the bulk density of 92 meteoroids using a model of meteor ablation based on the work of Campbell-Brown and Koschny (2004), where we required that the complete observed lightcurve and deceleration be fitted simultaneously to the modeled lightcurve and deceleration. We found that our values of bulk density covered the entire range of possible meteoroid bulk density values: from very porous cometary bodies (low density) to very high values, consistent with asteroidal bodies made largely of iron in some form.

We were able to identify in our sample the 5 different classes used by Borovicka

et al. (2005): (AC): asteroidal and chondritic orbits, (SA): Sun-approaching orbits, (JF): Jupiter family orbits, and (HT): Halley type orbits. Meteoroids with orbits belonging to the Ecliptic shower class were all members of the Northern Iota Aquariid shower. The average density of meteoroids whose orbits belong to the (AC) class was found to be 4200 kg m^{-3} , suggesting that they are asteroidal bodies with substantial iron content.

Meteoroids with Jupiter family orbits (JF) have an average density of 3100 kg m^{-3} . This is also the average bulk density for the 4 meteoroids with orbits belonging to the Ecliptic shower orbits (ES), consistent with the notion that the NIA derive from 2P/Encke. Both categories (JF and ES) are physically chondritic-like. The high bulk density of JFC-type meteoroids is an unexpected result. Current models suggest JF meteoroids have undergone more thermal processing than HTC or NIC-related meteoroids, the high bulk densities we find for JFCs are most consistent with chondritic-like meteorite properties or porous bodies with highly refractory inclusions. The latter interpretation is supported by observations of high bulk density IDPs (Love et al., 1994), some of which approach 7000 kg m^{-3} , and the fact that our observed lightcurves cannot be reproduced by single body ablation of a solid chondritic stone. The existence of exclusively high density meteoroids within this class is perhaps also related to longer collisional lifetimes of such particles. Whether such high bulk densities for small meteoroids from the JFC population as a whole are consistent with the early results from the stardust analysis of 81P/Wild 2 remains an open question (see Ishii et al., 2008), but the clear requirement for a substantial refractory component to match our high bulk densities supports the notion that many JFCs have incorporated substantial amounts of material formed in the inner Solar System. A possible interpretation of this result is that the process of radial transport of refractory material outward at the time of solar system formation was a common process for materials up to tens - hundreds of microns in size, supporting models of nebular formation which suggest radial transport was an integral part of

protoplanetary disk dynamics (Ciesla, 2007). Alternatively, the JFCs as a population formed much closer to the sun than previously thought.

Meteoroids of the HT (Halley type) class have a minimum bulk density of 360_{-100}^{+400} kg m^{-3} and a maximum value of 1510_{-900}^{+400} kg m^{-3} . These bulk densities are consistent with that found for CP and cluster IDPs (Bradley, 2003). They are also consistent with our notion of cometary bodies. SA (Sun-approaching)-type meteoroids show a wide spread in their densities, ranging from 1000 kg m^{-3} to 4000 kg m^{-3} .

Our lack of significant numbers of meteoroids with densities of $\gg 2000\text{-}2500 \text{ kg m}^{-3}$, consistent with carbonaceous chondrites, is also puzzling. While it is possible number statistics are partially responsible, this seems unlikely for a dataset approaching 92 meteoroid density measurements. On the surface, it suggests few truly carbonaceous-type materials in pure form at our sizes, in contradiction to earlier work by Ceplecha (1988), who suggests $\gg 1/4$ of the total meteoroid population at these masses had density $\gg 2000 \text{ kg m}^{-3}$, but this was an inferred theoretical value, rather than directly measured.

We were also able to identify in our sample the 2 principal groups according to Ceplecha's classification (Ceplecha, 1988): A-group, C-group, with hints of the D-group. We find no evidence for a separate peak belonging to Ceplecha's (1967) B-class, which he associated with carbonaceous chondrites. The average bulk density was found to be 4700 kg m^{-3} for the A-group (asteroidal meteoroids), 1000 kg m^{-3} for C-group, and 600 kg m^{-3} for D-group. These values are close to those adopted by Ceplecha (1966, 1968), based on photographic Super-Schmidt meteors. They are quite different from the average bulk density values of Ceplecha (1988). Two possible reasons for these differences are that we use different assumptions and a different model of ablation; as well the luminous efficiency we use is different.

We detected two different meteor showers in our sample: Perseids (10 meteoroids, $\gg 11\%$ of our sample) and Northern Iota Aquariids (4 meteoroids). The average bulk density of Perseids was 620 kg m^{-3} , close to Bellot Rubio et al's bulk density

value. It is consistent with the HTC origin of Perseids, as expected.

Bibliography

- [Asphaug and Benz (1996)] Asphaug, E., & Benz, W. 1996, *Icarus*, 121, 225
- [Babadzhanov (2002)] Babadzhanov, P. B. 2002, *A&A*, 384, 317
- [Bellot Rubio et al. (2002)] Bellot Rubio, L. R., Martinez Gonzalez, M. J., Ruiz Herrera, L., et al. 2002, *A&A*, 389, 680
- [Bevington and Robinson (2003)] Bevington, P. R., & Robinson, D. K. 2003, *Data Reduction and Error Analysis for the Physical Science*, McGraw-Hill (New York)
- [Borovicka (1990)] Borovicka, J. 1990, *Bull. Astr. Inst. Czechosl.*, 41, 391
- [Borovicka et al. (2005)] Borovicka, J., Kotten, P., Spurny, P., et al. 2005, *Icarus*, 174, 15
- [Borovicka (2005)] Borovicka, J. 2005, *Proceedings of the International Astronomy Union* (Cambridge Univ. Press), 249
- [Borovicka et al. (2007)] Borovicka, J., Spurny, P., Kotten, P. 2007, *A&A*, 473, 661
- [Bottke et al. (2002)] Bottke, W. F., Morbidelli, A., Jedicke, R., et al. 2002, *Icarus*, 156, 399
- [Bradley (2003)] Bradley, J. P. 2003, *TrGeo*, 1, 689
- [Britt and Consolmagno (2003)] Britt, D. T., & Consolmagno, G. J. 2003, *M&PS*, 38, 1161

- [Bronshten (1983)] Bronshten, V. A. 1983, *The Physics of Meteoritic Phenomena* (Dordrecht:Reidel)
- [Brown et al. (2008)] Brown, P., Weryk, R. J., Wong, D. K., et al. 2008, *Icarus*, 195, 317
- [Brown et al. (2010)] Brown, P., Wong, D. K., Weryk, R. J., et al. 2010, *Icarus*, 207, 66
- [Brownlee et al. (2006)] Brownlee, D., Tsou, P., Alton, J., et al. 2006, *Science*, 314, 1711.
- [Campbell-Brown and Koschny (2004)] Campbell-Brown, M. D., & Koschny, D. 2004, *A&A*, 418, 751
- [Ceplecha, 1958] Ceplecha, Z. 1958, *BAICz*, 9, 154
- [Ceplecha (1966)] Ceplecha, Z. 1966, *BAICz*, 17, 96
- [Ceplecha (1967)] Ceplecha, Z. 1967, *SCoA*, 11, 35
- [Ceplecha (1968)] Ceplecha, Z. 1968, *SAO Special Report*, 279, 1
- [Ceplecha (1987)] Ceplecha, Z. 1987, *BAICz*, 38, 4, 222
- [Ceplecha (1988)] Ceplecha, Z. 1988, *BAICz*, 39, 4, 221
- [Ceplecha et al. (1998)] Ceplecha, Z., Borovicka, J., Elford, W. G., et al. 1998, *Space Science Rev.*, 84, 327
- [Ceplecha et al. (2000)] Ceplecha, Z., Borovicka, J., Spurny, P. 2000, *A&A*, 357, 1115
- [Christou (2010)] Christou, A. A. 2010, *MNRAS*, 402, 2759
- [Ciesla (2007)] Ciesla, F. J. 2007, *Science*, 318, 613

- [Consolmagno and Britt (1998)] Consolmagno, G. J., & Britt, D. T. 1998, *M&PS*, 33, 1231
- [davidson and Gutierrez (2004)] Davidson, B. J. R., & Gutierrez, P. J. 2004, *Icarus*, 168, 392
- [davidson and Gutierrez (2005)] Davidson, B. J. R. & Gutierrez, P. J. 2005, *Icarus*, 176, 453
- [Fernandez (1980)] Fernandez, J. A., 1980, *Icarus*, 42, 406
- [Fernandez et al. (2001)] Fernandez, Y. R., Jewitt, D. C., Sheppard, S. S. 2001, *ApJ*, 553, 197
- [Fisher et al.(2000)] Fisher, A. A., Hawkes, R. L., Murray, I. S., et al. 2000, *Planetary and Space Science*, 48, 911
- [Grun et al.(2002)] Grun, E., et al. 2002, *The Observatory*, 122, 128
- [Hawkes & Jones(1975)c] Hawkes, R. L., & Jones, J. 1975, *MNRAS*, 173, 339
- [Hawkes et al.(2001)] Hawkes,R.L., Bussey,J.E., Macphee,S.L., et al. 2001, *Proceedings of the Meteoroids 2001 Conference*, 281
- [Hawkes (2002)] Hawkes, R. L. 2002, *Meteors in the Earth's atmosphere* (ed. Edmond Murad and Iwan P. Williams), 97
- [Hedin(1991)] Hedin, A. 1991, *J. Geophys. Res.*, 96, 1154
- [Hill et al. (2005)] Hill, K. A., Rogers, L. A., Hawkes, R. L. 2005, *A&A*, 444, 615
- [Horz et al. (2006)] Horz, F.,Bastien, R., Borg, J., et al. 2006, *Science*, 314, 1716
- [Ishii et al. (2008)] Ishii, H. A., Bradley, J. P., Dai, Z. R., et al. 2008, *Science*, 319, 447
- [Jacchia (1955)] Jacchia, L. G. 1955, *ApJ*, 121, 521

- [1] Jones, J., & Kaiser, T. R. 1966, MNRAS, 133, 411
- [Kikwaya(2009)] Kikwaya, J. B., Campbell-Brown, M. D., Brown, P. G., et al. 2009, A&A, 497, 851
- [Kikwaya et al. (2010)] Kikwaya, J. B., Weryk, R. J., Campbell-Brown, M. D., et al. 2010, MNRAS, 404, 387
- [Koten et al. (2004)] Koten, P., Borovicka, J., Spurny, P., et al. 2004, A&A, 428, 683
- [Koten et al. (2006)] Koten, P., Spurny, P., Borovicka, J., et al. 2006, M&PS, 41, 1271
- [Levin (1956)] Levin, B. J. 1956, BAICz 7, 58
- [Levison and Duncan (1994)] Levison, H. F., & Duncan, M. J. 1994, Icarus, 108, 18
- [Levison (1996)] Levison, H. F. 1996, ASPC (Astronomical Society of the Pacific Conference), 107, 173
- [Love et al. (1994)] Love, S. G., Joswiak, D. J., Brownlee, D. E. 1994, Icarus, 111, 227
- [Morbidelli et al. (2008)] Morbidelli, A. 2008, Saas-Fee Advanced Course 35 (Jewitt, D., Morbidelli, A., Rauer, H.), 79
- [Murray and Beech (2000)] Murray, I. S., Beech, M., Taylor, M. J., et al. 2000, EM&P, 82/83, 351
- [2] Myers, J. R., Sande, C. B., Miller, A. C., et al. 2001, Sky 2000 Catalog v4 (Goddard Space Flight Center, Ycat 5109)
- [Popova (2005)] Popova, O. P. 2004, EM&P, 95, 303
- [Sarma and Jones, 1985] Sarma, T., & Jones, J. 1985, BAICz 36, 9

[Vokrouhlicky and Farinella (2000)] Vokrouhlicky, D., & Farinella, P. 2000, *Nature*, 407, 606

[Weissman et al. (2002)] Weissman, P. R., Bottke, Jr, W. F., Levison, H. F. 2002, *Asteroids III* (University of Arizona, Tucson), 669

Chapter 6

Conclusions and Future Work

6.1 Conclusion

In the preceding chapters, a new method and technique has been applied to meteor observations in an effort to estimate the bulk density of meteoroids in the mass range of 10^{-5} to 10^{-8} kg. We used both dynamic and photometric observations of meteoroids to determine their bulk density, using a complete model of meteoroid ablation, including fragmentation. Our method has two advantages over previous methods. First, it uses both dynamics and photometry, addressing Borovicka (2005)'s concern with the work of Bellot Rubio et al. (2002), for not taking into account the fragmentation process in their estimation of meteoroid densities; and with Babadzhanov (2002) who neglected meteoroid dynamics in his approach of determining the bulk density of meteoroids. Second, it searches the full parameter space to make sure that the density limits we determine from the model cover the entire possible range of density; previous studies of meteoroid density have confined their search around a single model solution which matches the observations (either dynamical or photometric, but not both simultaneously), neglecting the fact that other combinations of the free parameters might provide equally good fits. Meteoroid densities from our model are given as a region where possible solutions fall, taking into account every

different combination of free parameters.

One of our model assumptions is that the grain density is the same as the bulk density meaning zero porosity. Other authors (e.g. Babadzhanov and Kokhirova (2009)) have examined density and porosity of small meteoroids, but we don't try to determine the grain density. We recognize this is a limitation of our current model approach. We will try to address this in our future work.

The investigation of our 92 meteors shows that 53 % of them are seen before the grain release, 34 % during the grain release and only 13 % after the grain release. So the majority of the time grain release occurs after the meteor becomes visible.

This work was possible because of precise observations and a complete ablation model. We gathered our data using four different video systems (Gen II, Gen III, Gated camera, and Cooke camera), with image sizes ranging from 640 × 480 to 1360 × 1036 pixels, and image scales ranging from 0.01° per pixel to 0.05° per pixel. This resolution is capable of showing small decelerations, which is an important constraint in meteoroid ablation models. We also used a new photometric method based on quantum efficiency of the instruments. Gen III cameras, with 8-bit pixel depth images, are easily saturated by meteors of +2.3 magnitude and brighter. We applied a saturation correction on these meteors to estimate their true magnitude, in order to get an accurate photometric mass. In some cases, the correction was +1 magnitude or more (Kikwaya et al. 2010). When this effect is neglected, the photometric mass is underestimated and, with it, the bulk density. Our complete model of meteoroid ablation is based on the model described by Campbell-Brown and Koschny (2004). It is based on (a) thermal fragmentation (release of grains at a specified temperature), (b) conservation of momentum, giving an estimation of deceleration, (c) mass loss, which takes into account all different processes of ablation, notably spallation and evaporation, and (d) light production, used to simulate the meteoroid lightcurve.

Applying our method to six meteors between 10^{-7} and 10^{-8} kg, captured with Gen II camera systems (chapter 3 of this work), we noted that taking fragmentation

into account does not necessarily lead to higher bulk densities, as it appeared to do in Babadzhanov's work (Babadzhanov, 2002). The main reason may be the fact that many parameters which were fixed by Babadzhanov (2002) are kept free in our work, notably the heat of ablation. We also found that the proportion of small meteoroids with high densities is underestimated. These high density meteoroids may be the remains from collisional grinding of asteroids with ordinary chondrite compositions. Horz et al. (2005) demonstrated in the lab that the process of impact can lead to the production of nearly pure iron particles.

With a narrow field of view ($\gg 6^\circ$ with a scale of $\gg 30''$ per pixel, which is $\gg 10$ m per pixel, approaching photographic resolution) and very high sensitivity, the Gen II instrument is able to capture very faint meteoroids. The drawback is that only short trails ablating very low in the atmosphere and therefore having high density begin and end in the field of view, and are therefore selected for modelling. To enlarge our search, we used instruments with fields of view in the range of 15 to 30 degrees, able to record longer trails (Gen III, Gated Camera, and Cooke cameras). In high velocity meteoroids with long trails, the kinetic energy is used more in ablation processes than in producing deceleration, but we found that $\gg 80\%$ of our sample showed noticeable deceleration (chapter 5 of our work).

We estimated the bulk density of 92 meteors captured with video systems with large field of views (Gen III, Gated camera, and Cooke cameras), by simultaneously fitting the observed deceleration and lightcurve using the ablation model of Campbell-Brown and Koschny (2004). The results are shown in Fig. (6.1). The values of bulk density range from 380 kg m^{-3} to 5450 kg m^{-3} . Three distinct peaks are present: one around 950 kg m^{-3} corresponding to cometary meteoroids, one around 3000 kg m^{-3} associated with asteroidal-chondritic meteoroids, in good agreement with the bulk density of stony meteorites (see Consolmagno and Britt, 1998; Britt and Consolmagno, 2003), and one around 5000 kg m^{-3} which we believe corresponds to meteoroids with high iron content (Borovicka et al. 2005) and/or sulfide

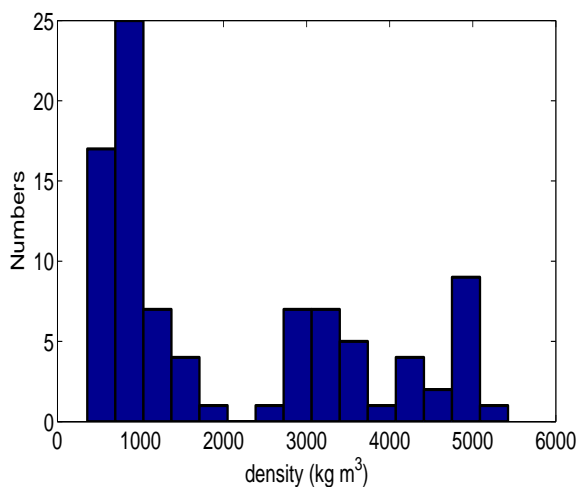


Figure 6.1: Bulk densities of meteoroids from our sample.

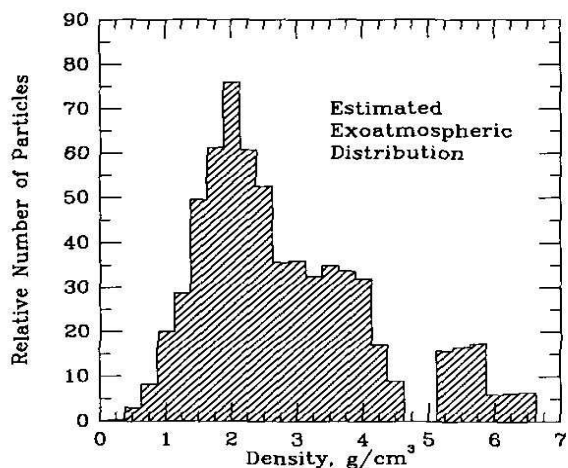


Figure 6.2: Estimated relative exoatmospheric density distribution (from Love et al. 1994).

content (Love et al. 1994). Direct measurements of the density of meteoroids closest to our size range have been done on IDPs (Interplanetary dust particles). Love et al. (1994) estimated the bulk density of these IDPs (particularly exoatmospheric IDPs) and found values ranging from $\approx 50 \text{ kg m}^{-3}$ to $\approx 7000 \text{ kg m}^{-3}$ (Fig. 6.2). They found that IDPs with very high bulk densities have high sulfide content. The high bulk densities we found for some meteoroids in our sample are also in agreement with the bulk density of some stony-iron meteorites, particularly pallasites, whose bulk density is reported by Consolmagno and Britt (1998), and Britt and Consolmagno (2003) to be $\approx 5000 \pm 200 \text{ kg m}^{-3}$, with a porosity reaching 6%.

To link each meteoroid to its origin, we calculated its orbital elements (Ceplecha, 1987) and computed the value of its Tisserand parameter (T_j). We put meteoroids from our sample in three different groups: $T_j < 2$ (cometary origin), $2 < T_j < 3$ (Jupiter family origin), and $T_j > 3$ (asteroidal origin) (Fig. 6.3). As we cannot unambiguously distinguish meteoroid origin using only the Tisserand parameter, we adopted the Borovicka et al. (2005) classes to group meteoroids from our sample.

We found that meteoroids belonging to the HT group had densities ranging from 380 to 1510 kg m^{-3} . They have a cometary origin, from their orbits. The average of

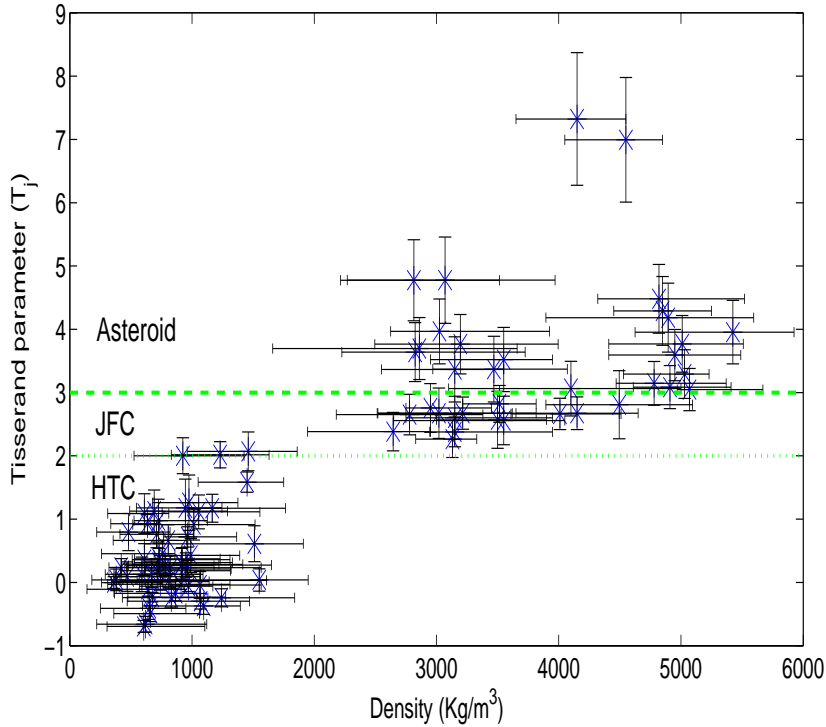


Figure 6.3: Tisserand parameter versus density of meteoroids from our sample.

A-C meteoroids is 4200 kg m^{-3} , consistent with an asteroidal origin. Some of them do have very high densities, suggesting that they have significant iron or sulfide content. We found four ES meteoroids, all belonging to the Northern Iota Aquariids; their average density is 3200 kg m^{-3} . This value is consistent with the fact that this shower is associated with 2P/Encke. SA meteoroids have a wide range of densities, suggesting that they have different origins. In addition to the NIA shower, we also found members of the Perseid stream. The average density of our 10 Perseids is $620 \pm 200 \text{ kg m}^{-3}$, consistent with its HT-type parent, comet 109P/Swift-Tuttle.

The most surprising result in our bulk density measurements is the very high value of JF meteoroid bulk density. We found 13 JF meteoroids in our sample, and their average density is approximately $3100 \pm 300 \text{ kg m}^{-3}$, suggesting that JF meteoroids contain an important fraction of refractory material, and have more chondritic than porous cometary composition. A similar result was reported from measurements of 81P/Wild 2 by the Stardust mission (Brownlee et al. 2006, Ishii

et al. 2008). Our results show that Wild 2 is not the only JF comet with refractory material, implying that this may be characteristic of this class of objects in general. If this is so, there is a need to revisit the present "Nice" model of solar system formation, where JFCs originate from the Kuiper belt, to a new scenario where JFCs are formed in the inner solar system.

6.2 Future work

Aside from the fact that we need to increase our sample size (we note that there is a project currently under way in the meteor physics group, which automatically collects data from meteors detected simultaneously at two different sites: Elginfield and Tavistock in Ontario, Canada), future work needs to focus on two directions: the first will be to improve the implementation of the ablation model, and the second will be to select useful targets for future observations.

In the present state of the model, we do two thorough searches to find the region where the distribution of the bulk density of the meteoroid may fall. The next goal should be to search just once, automatically, and produce the final results without human intervention. This project will require a method which automatically explores the parameter space to find the deepest minimum without running even hundreds of thousands of meteoroid solutions. We will need from the beginning to set very small steps of each free parameter.

For future observations, some of the most interesting targets are meteors from major meteor showers. In particular, we are interested in those which are associated with Jupiter family comets like 2P/Encke, for example the Taurids and North Iota Aquariids, to confirm our finding that JF meteoroids contain significant refractory material and have a bulk densities which place them closer in composition to asteroidal meteoroids than cometary meteoroids.

Bibliography

- [1] Babadzhanov, P. B. 2002, *A&A*, 384, 317
- [2] Babadzhanov, P. B., & Kokhirova, G. I. 2009, *A&A*, 495, 353
- [3] Bellot Rubio, L. R., Martinez Gonzalez, M. J., Ruiz Herrera, L., et al. 2002, *A&A*, 389, 680
- [4] Borovicka, J., Koten, P., Spurny, P., et al. 2005, *Icarus*, 174, 15
- [5] Borovicka, J. 2005, *Proceedings of the International Astronomy Union*, Cambridge University Press, 249
- [6] Britt, D. T., & Consolmagno, G. J. 2003, *M&PS*, 38, 1161
- [7] Brownlee, D. et al. 2006, *Science*, 314, 1711
- [8] Campbell-Brown, M. D., & Koschny, D. 2004, *A&A*, 418, 751
- [9] Ceplecha, Z. 1987, *Bull. Astron. Inst. Czech.*, 38, 4, 222
- [10] Consolmagno, G. J., & Britt, D.T. 1998, *M&PS*, 33, 1231
- [11] Horz, F. et al. 2006, *Science*, 314, 1716
- [12] Ishii, H. A., Bradley, J. P., Dai, Z. R., et al. 2008, *Science*, 319, 447
- [13] Kikwaya, J. B., Weryk, R. J., Campbell-Brown, M. D., et al. 2010, *MNRAS* 404, 387
- [14] Love, S. G., Joswiak, D. J., Brownlee, D. E. 1994, *Icarus*, 111, 227

Appendix A

Properties of meteoroids of our sample

We give here the properties of meteoroids of our sample (chapter 5), according to our ablation model. The values are those of the best model fit from the refining search. For each event, we give the observed and modelled values.

The observed values are:

² Date(UTC) (YYYYMMDD:HH:MM:SS)

² Observed photometric mass (kg)

² Observed peak magnitude (magnitude): the brightest point along the meteoroid trail.

² Perihelion (AU)

² Aphelion (AU)

² Semi-major axis (AU)

² Eccentricity

² Inclination (°)

- 2 Argument of periapsis ($^{\circ}$)
- 2 Longitude of the ascending node ($^{\circ}$)
- 2 Velocity (geocentric) (km s^{-1})
- 2 Velocity (helion) (km s^{-1})
- 2 Velocity (infinity) (km s^{-1})
- 2 Beginning height (km)
- 2 Maximum height (km)
- 2 Ending height (km)
- 2 Average Range (km)
- 2 Radiant Right asc (geocentric) ($^{\circ}$)
- 2 Radiant Declination (geocentric) ($^{\circ}$)
- 2 cos zenithal angle
- 2 Angle of intercept ($^{\circ}$)
- 2 Tisserand Parameter
- 2 Heat of ablation (Jkg^{-1})
- 2 Tlim (K)
- 2 Tboil (K)
- 2 Specific heat ($\text{Jkg}^{-1}\text{K}^{-1}$)
- 2 Molar mass (atomic unit)
- 2 Thermal conductivity ($\text{W m}^{-1} \text{K}^{-1}$)
- 2 Density (kg m^{-3})

Properties of meteoroids of our sample, according to our ablation model. Maximum height refers to the height of maximum brightness. Angular elements are J2000

Code		20060430084301	20060430103000	20060430104845	20060502100335
Date(UTC) (YYYYMMDD:HH:MM:SS)		20060430:08:43:01	20060430:10:30:00	20060430:10:48:45	20060502:10:03:35
Observed photometric mass (kg)		(7.10\$ 0.54)\$ £ 10 ⁻⁶	(6.15\$ 0.52)\$ £ 10 ⁻⁶	(6.85\$ 0.64)\$ £ 10 ⁻⁶	(6.75\$ 0.77)\$ £ 10 ⁻⁶
Observed peak magnitude (magnitude)		3.05\$ 0.23	2.75\$ 0.23	2.34\$ 0.22	2.27\$ 0.26
Perihelion (AU)	q	0.319\$ 0.003	0.556\$ 0.005	0.937\$ 0.003	0.483\$ 0.004
Aphelion (AU)	Q	11.213\$ 1.033	8.937\$ 0.794	3.885\$ 0.103	10.283\$ 0.575
Semi-major axis (AU)	a	5.766\$ 0.516	4.747\$ 0.399	2.411\$ 0.052	5.383\$ 0.288
Eccentricity	e	0.945\$ 0.005	0.883\$ 0.009	0.612\$ 0.008	0.910\$ 0.005
Inclination (°)	i	15.151\$ 0.323	156.087\$ 0.285	163.450\$ 0.338	146.282\$ 0.301
Argument of periapsis (°)	ω	293.940\$ 0.478	87.393\$ 0.834	35.406\$ 0.846	95.347\$ 0.487
Longitude of the ascending node (°)	Ω	39.794\$ 0.000	219.865\$ 0.000	219.879\$ 0.000	221.789\$ 0.000
Velocity (geocentric) (km s ⁻¹)	V_g	34.358\$ 0.210	64.096\$ 0.203	65.844\$ 0.101	62.361\$ 0.102
Velocity (helion) (km s ⁻¹)	V_h	40.094\$ 0.172	39.679\$ 0.198	37.328\$ 0.106	39.946\$ 0.110
Velocity (infinity) (km s ⁻¹)	V_∞	36.10\$ 0.91	65.20\$ 0.62	67.00\$ 0.72	63.50\$ 0.93
Beginning height (km)	H_{beg}	109.13\$ 0.12	115.58\$ 0.17	114.60\$ 0.16	112.77\$ 0.10
Maximum height (km)	H_{max}	92.55\$ 0.45	107.61\$ 0.41	106.73\$ 0.38	106.13\$ 0.31
Ending height (km)	H_{end}	86.52\$ 0.19	100.36\$ 0.17	101.17\$ 0.32	102.66\$ 0.21
Average Range (km)	Range _{avg}	120.08\$ 0.12	122.80\$ 0.27	125.06\$ 0.24	120.40\$ 0.34
Radiant Right asc (geocentric) (°)	α_{geo}	232.117\$ 0.206	288.163\$ 0.157	306.441\$ 0.212	286.574\$ 0.175
Radiant Declination (geocentric) (°)	δ_{geo}	-8.355\$ 0.206	-33.511\$ 0.132	-28.535\$ 0.187	-37.296\$ 0.140
cos zenithal angle	COSZR	0.775	0.366	0.350	0.298
Angle of intercept (°)	Q	57.2	21.9	12.4	22.7
Tisserand Parameter	T_j	1.585\$ 0.161	0.275\$ 0.192	1.126\$ 0.335	0.266\$ 0.157
K'b value		6.653	6.955	7.060	7.208
Heat of ablation (Jkg ⁻¹)		3.80E+06	7.00E+06	7.30E+06	7.00E+06
Tlim (K)		1350	1370	1100	1200
Tboil (K)		1500	2100	1800	2100
Specific heat (Jkg ⁻¹ Kj 1)		1800	1500	1200	1400
Molar mass (atomic unit)		36	36	36	30
Thermal conductivity (W m ⁻¹ K ⁻¹)		0.1	0.2	0.2	0.2
Density (kg m ⁻³)		1450 ⁺³⁰⁰ ₋₄₀₀	950 ⁺⁷⁰⁰ ₋₅₀₀	690 ⁺⁶⁰⁰ ₋₂₀₀	780 ⁺⁴⁰⁰ ₋₃₀₀

Properties of meteoroids of our sample, according to our ablation model. Maximum height refers to the height of maximum brightness. Angular elements are J2000. (nc: lightcurve and deceleration not computed).

Code		20060503091349	20060504093103	20060504094650	20060505102944
Date(UTC) (YYYYMMDD:HH:MM:SS)		20060503:09:13:49	20060504:09:31:03	20060504:09:46:50	20060505:10:29:44
Observed photometric mass (kg)		(7.65\$ 0.23)\$ $\times 10^{-6}$	(7.95\$ 0.64)\$ $\times 10^{-6}$	(1.60\$ 0.14)\$ $\times 10^{-5}$	(1.95\$ 0.15)\$ $\times 10^{-5}$
Observed peak magnitude (magnitude)		0.86\$ 0.26	2.87\$ 0.23	3.12\$ 0.27	3.05\$ 0.24
Perihelion (AU)	q	0.308\$ 0.002	0.051\$ 0.002	0.565\$ 0.003	0.448\$ 0.015
Aphelion (AU)	Q	22.492\$ 2.383	3.147\$ 0.076	2.842\$ 0.043	1.187\$ 0.013
Semi-major axis (AU)	a	11.400\$ 1.192	1.599\$ 0.038	1.703\$ 0.022	0.818\$ 0.013
Eccentricity	e	0.973\$ 0.003	0.968\$ 0.001	0.668\$ 0.004	0.452\$ 0.012
Inclination ($^{\circ}$)	i	139.160\$ 0.222	15.160\$ 1.059	5.139\$ 0.186	27.281\$ 0.812
Argument of periaapsis ($^{\circ}$)	ω	114.127\$ 0.366	338.447\$ 0.448	95.634\$ 0.525	38.246\$ 1.926
Longitude of the ascending node ($^{\circ}$)	Ω	222.725\$ 0.000	43.708\$ 0.000	223.709\$ 0.000	44.716\$ 0.000
Velocity (geocentric) (km s $^{-1}$)	V_g	60.111\$ 0.102	39.645\$ 0.208	21.008\$ 0.113	16.955\$ 0.300
Velocity (helion) (km s $^{-1}$)	V_h	41.015\$ 0.099	34.712\$ 0.190	35.196\$ 0.097	25.964\$ 0.318
Velocity (infinity) (km s $^{-1}$)	V_{∞}	61.30\$ 0.99	41.20\$ 0.61	23.60\$ 0.71	20.60\$ 0.25
Beginning height (km)	H_{beg}	112.90\$ 0.11	94.75\$ 0.09	88.37\$ 0.06	88.56\$ 0.07
Maximum height (km)	H_{max}	104.95\$ 0.29	90.85\$ 0.48	87.29\$ 0.22	86.14\$ 0.22
Ending height (km)	H_{end}	98.57\$ 0.20	82.62\$ 0.16	77.21\$ 0.09	80.54\$ 0.14
Average Range (km)	$Range_{avg}$	122.77\$ 0.53	111.37\$ 0.08	105.04\$ 0.06	105.08\$ 0.13
Radiant Right asc (geocentric) ($^{\circ}$)	α_{geo}	278.005\$ 0.105	254.048\$ 0.258	221.755\$ 0.274	345.319\$ 1.443
Radiant Declination (geocentric) ($^{\circ}$)	δ_{geo}	-37.762\$ 0.083	-19.067\$ 0.246	-23.458\$ 0.257	37.968\$ 1.084
cos zenithal angle	COSZR	0.277	0.644	0.493	0.559
Angle of intercept ($^{\circ}$)	Q	20.6	38.5	55.0	35.4
Tisserand Parameter	T_j	-0.059\$ 0.085	3.522\$ 0.507	3.903\$ 0.472	6.994\$ 0.984
K'b value		7.190	8.013	7.982	7.789
Heat of ablation (Jkg $^{-1}$)		6.50E+06	5.00E+06	nc	5.00E+06
Tlim (K)		930	1250	nc	1200
Tboil (K)		1900	1900	nc	1800
Specific heat (Jkg $^{-1}$ Kj 1)		1400	1600	nc	1200
Molar mass (atomic unit)		36	30	nc	36
Thermal conductivity (W m $^{-1}$ K $^{-1}$)		0.5	0.2	nc	0.5
Density (kg m $^{-3}$)		970 $^{+200}_{-400}$	3550 $^{+400}_{-600}$	nc	4550 $^{+300}_{-500}$

Properties of meteoroids of our sample, according to our ablation model. Maximum height refers to the height of maximum brightness. Angular elements are J2000

Code		20070420082356	200704222061849	20070519040843	20070519075753
Date(UTC) (YYYYMMDD:HH:MM:SS)		20070420:08:23:56	20070422:06:18:49	20070519:04:08:43	20070519:07:57:53
Observed photometric mass (kg)		(4.05\$ 0.34)\$ 10 ⁻⁶	(2.20\$ 0.17)\$ 10 ⁻⁶	(6.15\$ 0.68)\$ 10 ⁻⁶	(2.80\$ 0.73)\$ 10 ⁻⁵
Observed peak magnitude (magnitude)		2.64\$ 0.22	3.47\$ 0.26	1.98\$ 0.22	-0.76\$ 0.20
Perihelion (AU)	q	0.813\$ 0.006	0.750\$ 0.005	0.846\$ 0.031	0.975\$ 0.004
Aphelion (AU)	Q	-10.766\$ 0.966	8.352\$ 1.087	6.109\$ 1.724	11.428\$ 0.903
Semi-major axis (AU)	a	-4.976\$ 0.483	4.551\$ 0.546	3.478\$ 0.865	6.202\$ 0.451
Eccentricity	e	1.163\$ 0.016	0.835\$ 0.019	0.757\$ 0.059	0.843\$ 0.012
Inclination (°)	i	108.324\$ 0.471	143.705\$ 0.283	102.779\$ 2.019	156.894\$ 0.636
Argument of periaapsis (°)	ω	130.225\$ 0.918	243.706\$ 1.134	231.657\$ 5.388	156.998\$ 1.343
Longitude of the ascending node (°)	Ω	29.791\$ 0.000	31.658\$ 0.000	57.732\$ 0.000	57.883\$ 0.000
Velocity (geocentric) (km s ⁻¹)	V_g	59.487\$ 0.102	64.245\$ 0.304	53.329\$ 0.102	67.903\$ 0.101
Velocity (helion) (km s ⁻¹)	V_h	44.095\$ 0.196	39.627\$ 0.295	38.714\$ 0.819	40.134\$ 0.130
Velocity (infinity) (km s ⁻¹)	V_∞	60.80\$ 0.83	65.50\$ 0.63	54.80\$ 0.75	69.10\$ 1.21
Beginning height (km)	H_{beg}	111.38\$ 0.40	112.18\$ 1.21	99.85\$ 0.10	107.60\$ 0.20
Maximum height (km)	H_{max}	102.49\$ 0.57	105.98\$ 0.35	92.86\$ 0.35	95.24\$ 0.49
Ending height (km)	H_{end}	96.93\$ 0.66	101.15\$ 2.39	87.31\$ 0.81	90.37\$ 0.33
Average Range (km)	Range _{avg}	111.26\$ 0.21	112.93\$ 0.09	112.21\$ 0.18	115.47\$ 0.07
Radiant Right asc (geocentric) (°)	α_{geo}	313.778\$ 0.382	282.343\$ 0.142	298.432\$ 1.723	331.083\$ 0.374
Radiant Declination (geocentric) (°)	δ_{geo}	23.369\$ 0.350	-4.197\$ 0.142	21.086\$ 1.605	2.240\$ 0.374
cos zenithal angle	COSZR	0.608	0.334	0.357	0.433
Angle of intercept (°)	Q	11.5	15.0	13.5	13.4
Tisserand Parameter	T_j	hyp	0.314\$ 0.223	1.260\$ 0.437	-0.242\$ 0.143
K'b value		7.111	7.271	8.029	7.638
Heat of ablation (Jkg ⁻¹)		7.30E+06	7.00E+06	6.00E+06	8.00E+06
Tlim (K)		1250	1250	1100	1070
Tboil (K)		2100	2100	2000	2100
Specific heat (Jkg ⁻¹ Kj 1)		1200	1000	1200	1400
Molar mass (atomic unit)		20	36	36	36
Thermal conductivity (W m ⁻¹ K ⁻¹)		0.2	0.2	0.8	0.9
Density (kg m ⁻³)		630 ⁺⁶⁰⁰ ₋₃₀₀	730 ⁺⁶⁰⁰ ₋₄₀₀	975 ⁺³⁰⁰ ₋₄₀₀	1240 ⁺⁶⁰⁰ ₋₂₀₀

Properties of meteoroids of our sample, according to our ablation model. Maximum height refers to the height of maximum brightness. Angular elements are J2000

Code		20070519082713	20070812062117	20070812083450	20070813044452
Date(UTC) (YYYYMMDD:HH:MM:SS)		20070519:08:27:13	20070812:06:21:17	20070812:08:34:50	20070813:04:44:52
Observed photometric mass (kg)		(6.45\$ 0.76)\$ $\times 10^{-6}$	(2.10\$ 0.16)\$ $\times 10^{-6}$	(2.85\$ 0.24)\$ $\times 10^{-6}$	(4.35\$ 0.37)\$ $\times 10^{-6}$
Observed peak magnitude (magnitude)		1.96\$ 0.23	3.22\$ 0.24	2.74\$ 0.23	2.68\$ 0.23
Perihelion (AU)	q	0.636\$ 0.009	0.578\$ 0.006	0.936\$ 0.015	0.895\$ 0.007
Aphelion (AU)	Q	14.668\$ 2.372	7.332\$ 0.407	12.263\$ 3.881	15.467\$ 2.550
Semi-major axis (AU)	a	7.652\$ 1.186	3.955\$ 0.204	6.600\$ 1.941	8.181\$ 1.275
Eccentricity	e	0.917\$ 0.013	0.854\$ 0.008	0.858\$ 0.042	0.891\$ 0.017
Inclination ($^{\circ}$)	i	161.965\$ 0.650	127.536\$ 0.455	115.611\$ 1.399	114.354\$ 0.541
Argument of periaapsis ($^{\circ}$)	ω	102.981\$ 1.065	266.147\$ 0.791	146.556\$ 3.288	138.745\$ 1.238
Longitude of the ascending node ($^{\circ}$)	Ω	57.902\$ 0.000	139.086\$ 0.000	139.175\$ 0.000	139.022\$ 0.000
Velocity (geocentric) (km s^{-1})	V_g	65.649\$ 0.203	58.876\$ 0.102	58.923\$ 0.102	58.662\$ 0.102
Velocity (helion) (km s^{-1})	V_h	40.471\$ 0.222	39.069\$ 0.148	40.203\$ 0.491	40.525\$ 0.208
Velocity (infinity) (km s^{-1})	V_{∞}	66.90\$ 1.05	60.10\$ 0.94	60.10\$ 1.01	59.90\$ 1.05
Beginning height (km)	H_{beg}	115.55\$ 0.14	114.23\$ 0.26	112.37\$ 0.35	116.22\$ 0.36
Maximum height (km)	H_{max}	109.68\$ 0.40	105.50\$ 0.81	104.74\$ 0.85	110.84\$ 0.52
Ending height (km)	H_{end}	101.66\$ 0.26	99.03\$ 0.46	97.99\$ 0.62	100.39\$ 0.51
Average Range (km)	$Range_{avg}$	128.07\$ 0.12	116.73\$ 0.25	117.19\$ 0.08	119.52\$ 0.38
Radiant Right asc (geocentric) ($^{\circ}$)	α_{geo}	346.780\$ 0.325	10.359\$ 0.295	48.505\$ 1.842	53.167\$ 0.722
Radiant Declination (geocentric) ($^{\circ}$)	δ_{geo}	3.912\$ 0.324	30.992\$ 0.250	55.934\$ 1.031	56.822\$ 0.394
cos zenithal angle	COSZR	0.354	0.866	0.876	0.501
Angle of intercept ($^{\circ}$)	Q	10.2	16.6	21.4	17.1
Tisserand Parameter	T_j	-0.241\$ 0.148	0.762\$ 0.213	0.289\$ 0.262	0.237\$ 0.139
K'b value		7.008	6.781	6.922	6.761
Heat of ablation (Jkg^{-1})		6.90E+06	7.00E+06	6.00E+06	8.80E+06
Tlim (K)		1100	1200	1000	1200
Tboil (K)		1900	2000	2100	2100
Specific heat ($\text{Jkg}^{-1}\text{K}^{-1}$)		1600	1300	1300	1300
Molar mass (atomic unit)		30	36	20	20
Thermal conductivity ($\text{W m}^{-1}\text{K}^{-1}$)		0.8	0.5	0.2	0.2
Density (kg m^{-3})		830 ⁺³⁰⁰ ₋₄₀₀	710 ⁺³⁰⁰ ₋₃₀₀	920 ⁺³⁰⁰ ₋₅₀₀	420 ⁺⁴⁰⁰ ₋₁₀₀

Properties of meteoroids of our sample, according to our ablation model. Maximum height refers to the height of maximum brightness. Angular elements are J2000

Code	20070813045726	20070813055649	20070813055909	20070813064415
Date(UTC) (YYYYMMDD:HH:MM:SS)	20070813:04:57:26	20070813:05:56:49	20070813:05:59:09	20070813:06:44:15
Observed photometric mass (kg)	(1.70\$ 0.63)\$ $\times 10^{-5}$	(1.55\$ 1.06)\$ $\times 10^{-5}$	(4.20\$ 0.36)\$ $\times 10^{-6}$	(1.20\$ 0.31)\$ $\times 10^{-5}$
Observed peak magnitude (magnitude)	-0.56\$ 0.21	0.31\$ 0.21	2.67\$ 0.23	-0.08\$ 0.21
Perihelion (AU)	0.949\$ 0.004	0.594\$ 0.014	0.957\$ 0.006	0.919\$ 0.012
Aphelion (AU)	20.241\$ 3.374	6.606\$ 0.950	23.498\$ 6.862	11.812\$ 3.401
Semi-major axis (AU)	10.595\$ 1.687	3.600\$ 0.478	12.226\$ 3.431	6.366\$ 1.701
Eccentricity	0.910\$ 0.014	0.835\$ 0.021	0.922\$ 0.022	0.856\$ 0.038
Inclination ($^{\circ}$)	112.838\$ 0.377	135.230\$ 0.897	110.239\$ 0.610	113.484\$ 1.077
Argument of periaapsis ($^{\circ}$)	150.199\$ 0.875	95.160\$ 2.035	152.167\$ 1.426	142.953\$ 2.573
Longitude of the ascending node ($^{\circ}$)	139.990\$ 0.000	140.030\$ 0.000	140.031\$ 0.000	140.061\$ 0.000
Velocity (geocentric) (km s^{-1})	58.663\$ 0.102	60.533\$ 0.407	57.963\$ 0.102	58.162\$ 0.305
Velocity (helion) (km s^{-1})	40.832\$ 0.163	38.789\$ 0.422	40.969\$ 0.248	40.145\$ 0.464
Velocity (infinity) (km s^{-1})	59.90\$ 0.73	61.80\$ 0.97	59.20\$ 0.99	59.40\$ 0.89
Beginning height (km)	119.80\$ 0.40	115.98\$ 0.34	114.24\$ 0.22	116.09\$ 0.84
Maximum height (km)	106.42\$ 0.60	108.13\$ 0.39	105.99\$ 0.70	103.33\$ 0.67
Ending height (km)	100.39\$ 0.31	99.02\$ 0.41	99.30\$ 0.27	95.97\$ 0.14
Average Range (km)	124.76\$ 0.65	122.74\$ 0.56	117.23\$ 0.33	121.05\$ 0.65
Radiant Right asc (geocentric) ($^{\circ}$)	47.787\$ 0.535	70.814\$ 0.641	46.335\$ 0.941	51.602\$ 1.468
Radiant Declination (geocentric) ($^{\circ}$)	57.997\$ 0.283	43.369\$ 0.466	59.563\$ 0.475	40.145\$ 0.464
cos zenithal angle	0.559	0.369	0.680	0.713
Angle of intercept ($^{\circ}$)	18.4	12.9	17.9	21.1
Tisserand Parameter	0.033\$ 0.109	0.796\$ 0.294	0.014\$ 0.136	0.361\$ 0.252
K'b value	6.499	6.873	6.816	6.682
Heat of ablation (Jkg^{-1})	8.80E+06	9.00E+06	6.00E+06	8.80E+06
Tlim (K)	1300	1000	1000	1300
Tboil (K)	1750	1800	1800	1750
Specific heat ($\text{Jkg}^{-1}\text{K}^{-1}$)	1400	1600	1200	1500
Molar mass (atomic unit)	20	20	20	20
Thermal conductivity ($\text{W m}^{-1}\text{K}^{-1}$)	0.8	0.1	0.2	0.8
Density (kg m^{-3})	810 ⁺⁸⁰⁰ ₋₄₀₀	480 ⁺³⁴⁰ ₋₂₆₀	740 ⁺⁴⁰⁰ ₋₄₀₀	610 ⁺⁷⁰⁰ ₋₁₀₀

Properties of meteoroids of our sample, according to our ablation model. Maximum height refers to the height of maximum brightness. Angular elements are J2000

Code		20070813065047	20070813065828	20070813073054	20070813075355
Date(UTC) (YYYYMMDD:HH:MM:SS)		20070813:06:50:47	20070813:06:58:28	20070813:07:30:54	20070813:07:53:55
Observed photometric mass (kg)		(4.10\$ 0.39)\$ 10^{-6}	(1.00\$ 0.07)\$ 10^{-5}	(2.15\$ 0.16)\$ 10^{-6}	(5.20\$ 0.56)\$ 10^{-6}
Observed peak magnitude (magnitude)		2.34\$ 0.22	3.21\$ 0.23	3.09\$ 0.23	2.03\$ 0.22
Perihelion (AU)	q	0.953\$ 0.011	0.137\$ 0.003	0.966\$ 0.007	0.968\$ 0.008
Aphelion (AU)	Q	18.463\$ 7.887	4.656\$ 0.145	20.558\$ 6.821	18.026\$ 6.554
Semi-major axis (AU)	a	9.708\$ 3.944	2.397\$ 0.073	10.761\$ 3.410	9.497\$ 3.277
Eccentricity	e	0.902\$ 0.040	0.943\$ 0.001	0.910\$ 0.028	0.898\$ 0.035
Inclination ($^{\circ}$)	i	112.160\$ 1.139	18.279\$ 0.684	111.800\$ 0.824	110.635\$ 0.939
Argument of periaapsis ($^{\circ}$)	ω	151.033\$ 2.671	141.456\$ 0.602	154.324\$ 1.932	154.760\$ 2.225
Longitude of the ascending node ($^{\circ}$)	Ω	140.066\$ 0.000	320.069\$ 0.000	140.093\$ 0.000	140.108\$ 0.000
Velocity (geocentric) (km s^{-1})	V_g	58.377\$ 0.204	37.128\$ 0.104	58.397\$ 0.102	57.904\$ 0.204
Velocity (helion) (km s^{-1})	V_h	40.738\$ 0.455	37.160\$ 0.153	40.848\$ 0.320	40.714\$ 0.396
Velocity (infinity) (km s^{-1})	V_{∞}	59.60\$ 0.82	38.80\$ 0.61	59.60\$ 0.95	59.10\$ 0.99
Beginning height (km)	H_{beg}	113.00\$ 0.30	99.77\$ 0.25	114.11\$ 0.26	114.30\$ 0.19
Maximum height (km)	H_{max}	106.19\$ 0.76	92.84\$ 0.36	102.62\$ 0.84	107.54\$ 0.88
Ending height (km)	H_{end}	99.18\$ 0.34	83.74\$ 0.16	98.37\$ 0.38	98.87\$ 0.33
Average Range (km)	Range_{avg}	114.80\$ 0.41	107.17\$ 0.44	116.54\$ 0.39	117.09\$ 0.43
Radiant Right asc (geocentric) ($^{\circ}$)	α_{geo}	47.192\$ 1.660	348.273\$ 0.292	45.188\$ 1.220	44.604\$ 1.419
Radiant Declination (geocentric) ($^{\circ}$)	δ_{geo}	58.347\$ 0.869	-13.030\$ 0.003	58.491\$ 0.637	59.098\$ 0.728
cos zenithal angle	COSZR	0.752	0.577	0.816	0.844
Angle of intercept ($^{\circ}$)	Q	17.4	37.0	21.6	25.7
Tisserand Parameter	T_j	0.091\$ 0.233	2.601\$ 0.340	0.041\$ 0.170	0.129\$ 0.207
K'b value		6.903	7.474	6.796	6.762
Heat of ablation (Jkg^{-1})		9.00E+06	8.50E+06	2.00E+06	3.50E+06
Tlim (K)		1100	1300	1400	1300
Tboil (K)		2100	2100	1800	2100
Specific heat ($\text{Jkg}^{-1}\text{K}^{-1}$)		1600	1200	1600	1600
Molar mass (atomic unit)		36	36	36	36
Thermal conductivity ($\text{W m}^{-1} \text{K}^{-1}$)		0.2	0.2	0.1	0.5
Density (kg m^{-3})		470 ⁺⁶⁰⁰ ₋₁₀₀	3150 ⁺⁸⁰⁰ ₋₄₀₀	380 ⁺⁶⁰⁰ ₋₂₀₀	670 ⁺⁴⁰⁰ ₋₃₀₀

Properties of meteoroids of our sample, according to our ablation model. Maximum height refers to the height of maximum brightness. Angular elements are J2000

Code	20070813081229	20070813084353	20070813084901	20070813085448
Date(UTC) (YYYYMMDD:HH:MM:SS)	20070813:08:12:29	20070813:08:43:53	20070813:08:49:01	20070813:08:54:48
Observed photometric mass (kg)	(1.90\$ 0.87)\$ 10 ⁻⁵	(1.40\$ 0.09)\$ 10 ⁻⁶	(3.55\$ 0.35)\$ 10 ⁻⁶	(2.40\$ 0.20)\$ 10 ⁻⁶
Observed peak magnitude (magnitude)	0.46\$ 0.21	3.46\$ 0.24	2.25\$ 0.22	2.59\$ 0.22
Perihelion (AU)	0.390\$ 0.012	0.987\$ 0.007	0.942\$ 0.002	0.928\$ 0.016
Aphelion (AU)	14.434\$ 2.950	11.154\$ 3.573	21.789\$ 2.934	18.107\$ 9.069
Semi-major axis (AU)	7.412\$ 1.473	6.071\$ 1.787	11.365\$ 1.467	9.518\$ 4.535
Eccentricity	0.947\$ 0.011	0.837\$ 0.048	0.917\$ 0.011	0.902\$ 0.046
Inclination (°)	150.187\$ 1.259	102.032\$ 1.108	112.955\$ 0.241	111.070\$ 1.451
Argument of periaapsis (°)	74.710\$ 1.324	160.735\$ 2.828	148.487\$ 0.556	145.421\$ 3.384
Longitude of the ascending node (°)	140.119\$ 0.000	140.142\$ 0.000	140.145\$ 0.000	140.149\$ 0.000
Velocity (geocentric) (km s ⁻¹)	61.825\$ 0.203	54.393\$ 0.306	58.736\$ 0.102	57.925\$ 0.102
Velocity (helion) (km s ⁻¹)	40.390\$ 0.294	40.061\$ 0.537	40.902\$ 0.123	40.716\$ 0.545
Velocity (infinity) (km s ⁻¹)	63.10\$ 0.68	55.60\$ 0.95	59.90\$ 0.91	59.10\$ 0.79
Beginning height (km)	116.46\$ 0.32	112.64\$ 0.17	113.76\$ 0.19	112.24\$ 0.20
Maximum height (km)	102.43\$ 0.60	107.62\$ 0.88	107.61\$ 0.87	106.53\$ 0.83
Ending height (km)	97.20\$ 0.21	97.94\$ 0.29	98.45\$ 0.26	99.12\$ 0.24
Average Range (km)	121.45\$ 0.67	114.61\$ 0.81	118.45\$ 0.68	115.99\$ 0.62
Radiant Right asc (geocentric) (°)	79.847\$ 0.656	37.770\$ 2.083	49.161\$ 0.338	50.776\$ 2.168
Radiant Declination (geocentric) (°)	35.033\$ 0.536	63.456\$ 0.931	58.047\$ 0.176	59.123\$ 1.112
cos zenithal angle	0.532	0.895	0.891	0.886
Angle of intercept (°)	27.0	34.7	26.4	29.2
Tisserand Parameter	0.039\$ 0.176	0.611\$ 0.285	-0.002\$ 0.092	0.128\$ 0.274
Kb value	6.792	6.815	6.812	6.907
Heat of ablation (Jkg ⁻¹)	7.00E+06	5.00E+06	7.00E+06	7.00E+06
Tlim (K)	1100	1150	1300	1200
Tboil (K)	2100	1900	1900	1900
Specific heat (Jkg ⁻¹ Kj 1)	1400	1000	1400	1200
Molar mass (atomic unit)	36	36	36	30
Thermal conductivity (W m ⁻¹ K ⁻¹)	0.1	0.5	0.5	0.5
Density (kg m ⁻³)	1550 ⁺⁴⁰⁰ ₋₁₀₀₀	1510 ⁺⁴⁰⁰ ₋₉₀₀	360 ⁺⁴⁰⁰ ₋₁₀₀	590 ⁺⁵⁰⁰ ₋₃₀₀

Properties of meteoroids of our sample, according to our ablation model. Maximum height refers to the height of maximum brightness. Angular elements are J2000

Code	200708130855457	20070813085548	20080910052352	20080910053428
Date(UTC) (YYYYMMDD:HH:MM:SS)	20070813:08:54:57	20070813:08:55:48	20080910:05:23:52	20080910:05:34:28
Observed photometric mass (kg)	(5.80\$ 0.63)\$ $\times 10^{-6}$	(2.30\$ 0.20)\$ $\times 10^{-6}$	(1.45\$ 0.86)\$ $\times 10^{-5}$	(1.95\$ 0.13)\$ $\times 10^{-6}$
Observed peak magnitude (magnitude)	2.03\$ 0.22	2.56\$ 0.22	-0.32\$ 0.19	3.58\$ 0.24
Perihelion (AU)	0.951\$ 0.001	0.447\$ 0.004	0.112\$ 0.015	0.132\$ 0.007
Aphelion (AU)	23.308\$ 2.842	16.450\$ 1.450	4.583\$ 0.616	3.837\$ 0.226
Semi-major axis (AU)	12.130\$ 1.421	8.448\$ 0.725	2.348\$ 0.314	1.984\$ 0.116
Eccentricity	0.922\$ 0.009	0.947\$ 0.004	0.952\$ 0.004	0.933\$ 0.002
Inclination ($^{\circ}$)	112.713\$ 0.161	152.151\$ 0.317	30.495\$ 3.600	6.871\$ 1.694
Argument of periaapsis ($^{\circ}$)	150.693\$ 0.367	278.534\$ 0.468	325.282\$ 2.916	323.054\$ 1.398
Longitude of the ascending node ($^{\circ}$)	140.149\$ 0.000	140.149\$ 0.000	167.760\$ 0.000	167.768\$ 0.000
Velocity (geocentric) (km s^{-1})	58.744\$ 0.102	62.602\$ 0.102	39.014\$ 0.104	35.789\$ 0.210
Velocity (helion) (km s^{-1})	40.962\$ 0.105	40.571\$ 0.111	37.206\$ 0.679	36.264\$ 0.360
Velocity (infinity) (km s^{-1})	59.90\$ 0.72	63.60\$ 0.79	40.70\$ 0.71	37.60\$ 0.33
Beginning height (km)	115.69\$ 0.49	115.61\$ 0.23	95.01\$ 0.19	105.41\$ 0.14
Maximum height (km)	103.61\$ 0.89	107.45\$ 0.96	90.04\$ 0.54	100.36\$ 0.55
Ending height (km)	94.64\$ 0.81	94.30\$ 0.38	82.09\$ 0.27	95.04\$ 0.25
Average Range (km)	118.81\$ 0.62	118.79\$ 0.78	119.89\$ 0.19	138.42\$ 0.88
Radiant Right asc (geocentric) ($^{\circ}$)	47.805\$ 0.211	15.000\$ 0.149	9.806\$ 1.431	9.980\$ 0.713
Radiant Declination (geocentric) ($^{\circ}$)	58.163\$ 0.111	19.212\$ 0.141	15.503\$ 1.382	7.412\$ 0.710
cos zenithal angle	0.903	0.915	0.838	0.713
Angle of intercept ($^{\circ}$)	26.0	66.8	22.5	18.6
Tisserand Parameter	-0.029\$ 0.083	-0.107\$ 0.108	2.570\$ 0.452	3.063\$ 0.432
K'b value	6.657	6.723	7.834	6.980
Heat of ablation (Jkg^{-1})	7.50E+06	7.00E+06	4.00E+06	7.00E+06
Tlim (K)	1200	1250	1200	1000
Tboil (K)	1900	1800	1900	1800
Specific heat ($\text{Jkg}^{-1}\text{K}^{-1}$)	1400	1400	1200	1200
Molar mass (atomic unit)	36	36	36	36
Thermal conductivity ($\text{W m}^{-1} \text{K}^{-1}$)	0.1	0.2	0.3	0.5
Density (kg m^{-3})	910 ⁺⁴⁰⁰ ₋₆₀₀	640 ⁺³⁰⁰ ₋₅₀₀	3500 ⁺⁴⁰⁰ ₋₅₀₀	4100 ⁺⁹⁰⁰ ₋₁₀₀₀

Properties of meteoroids of our sample, according to our ablation model. Maximum height refers to the height of maximum brightness. Angular elements are J2000. (nc: lightcurve and deceleration not computed)

Code	20080910064008	20080910064102	20080910075255	20080910075454
Date(UTC) (YYYYMMDD:HH:MM:SS)	20080910:06:40:08	20080910:06:41:02	20080910:07:52:55	20080910:07:54:54
Observed photometric mass (kg)	(2.35\$ 0.26)\$ $\times 10^{-6}$	(5.20\$ 0.35)\$ $\times 10^{-6}$	(3.75\$ 0.43)\$ $\times 10^{-6}$	(3.40\$ 0.39)\$ $\times 10^{-6}$
Observed peak magnitude (magnitude)	1.92\$ 0.21	3.27\$ 0.22	1.64\$ 0.19	1.67\$ 0.19
Perihelion (AU)	0.719\$ 0.020	0.479\$ 0.021	0.350\$ 0.016	0.926\$ 0.016
Aphelion (AU)	12.287\$ 2.668	5.516\$ 0.930	9.147\$ 1.801	6.196\$ 0.412
Semi-major axis (AU)	6.503\$ 1.330	2.997\$ 0.474	4.748\$ 0.898	3.561\$ 0.201
Eccentricity	0.889\$ 0.024	0.840\$ 0.019	0.926\$ 0.015	0.740\$ 0.018
Inclination ($^{\circ}$)	142.689\$ 1.531	2.392\$ 1.539	158.565\$ 1.985	168.173\$ 1.687
Argument of periaapsis ($^{\circ}$)	246.891\$ 2.396	278.508\$ 3.391	290.902\$ 1.791	324.139\$ 3.506
Longitude of the ascending node ($^{\circ}$)	167.811\$ 0.000	167.815\$ 0.002	167.860\$ 0.000	347.863\$ 0.000
Velocity (geocentric) (km s^{-1})	64.054\$ 0.102	25.987\$ 0.327	61.304\$ 0.305	67.604\$ 0.101
Velocity (helion) (km s^{-1})	40.320\$ 0.346	38.291\$ 0.611	39.691\$ 0.445	38.898\$ 0.181
Velocity (infinity) (km s^{-1})	65.20\$ 0.67	28.20\$ 0.47	62.40\$ 0.90	68.80\$ 0.89
Beginning height (km)	112.47\$ 0.24	95.43\$ 0.14	111.20\$ 0.24	111.68\$ 0.25
Maximum height (km)	98.48\$ 0.80	87.98\$ 0.28	103.09\$ 0.93	103.87\$ 0.65
Ending height (km)	94.32\$ 0.41	84.84\$ 0.24	95.19\$ 0.15	100.87\$ 1.57
Average Range (km)	139.53\$ 0.45	124.81\$ 0.09	139.69\$ 0.36	142.13\$ 0.39
Radiant Right asc (geocentric) ($^{\circ}$)	50.496\$ 1.093	351.488\$ 1.631	42.150\$ 0.879	86.856\$ 0.983
Radiant Declination (geocentric) ($^{\circ}$)	38.204\$ 0.859	-0.892\$ 1.652	24.937\$ 0.798	16.870\$ 0.940
cos zenithal angle	0.845	0.706	0.927	0.5510
Angle of intercept ($^{\circ}$)	17.5	19.9	21.1	10.7
Tisserand Parameter	-0.013\$ 0.205	2.559\$ 0.383	0.426\$ 0.267	0.373\$ 0.239
K'b value	7.068	7.466	7.066	7.257
Heat of ablation (Jkg^{-1})	nc	6.00E+06	6.00E+06	7.00E+06
Tlim (K)	nc	1200	1300	1200
Tboil (K)	nc	1900	2000	2000
Specific heat ($\text{Jkg}^{-1}\text{K}^{-1}$)	nc	1200	1200	1300
Molar mass (atomic unit)	nc	36	36	36
Thermal conductivity ($\text{W m}^{-1}\text{K}^{-1}$)	nc	0.1	0.1	0.1
Density (kg m^{-3})	nc	3550 ⁺⁵⁰⁰ ₋₉₀₀	990 ⁺⁴⁰⁰ ₋₃₀₀	730 ⁺⁵⁰⁰ ₋₂₀₀

Properties of meteoroids of our sample, according to our ablation model. Maximum height refers to the height of maximum brightness. Angular elements are J2000

Code		20080910091403	20080911060638	20080911065211	20080911071428
Date(UTC) (YYYYMMDD:HH:MM:SS)		20080910:09:14:03	20080911:06:06:38	20080911:06:52:11	20080911:07:14:28
Observed photometric mass (kg)		(4.15\$ 0.56)\$ 10^{-6}	(7.40\$ 1.40)\$ 10^{-6}	(5.10\$ 0.44)\$ 10^{-7}	(1.10\$ 0.08)\$ 10^{-5}
Observed peak magnitude (magnitude)		1.48\$ 0.20	-1.11\$ 0.21	2.80\$ 0.24	3.34\$ 0.24
Perihelion (AU)	q	0.658\$ 0.018	0.669\$ 0.012	0.815\$ 0.015	0.222\$ 0.010
Aphelion (AU)	Q	9.232\$ 1.193	16.148\$ 2.405	4.632\$ 0.976	1.312\$ 0.017
Semi-major axis (AU)	a	4.945\$ 0.591	8.409\$ 1.198	2.724\$ 0.493	0.767\$ 0.011
Eccentricity	e	0.867\$ 0.018	0.920\$ 0.012	0.701\$ 0.050	0.711\$ 0.010
Inclination (°)	i	155.978\$ 1.483	176.784\$ 1.030	135.206\$ 0.846	5.768\$ 1.091
Argument of periaapsis (°)	ω	284.723\$ 1.984	252.561\$ 1.270	237.450\$ 3.470	151.234\$ 1.135
Longitude of the ascending node (°)	Ω	347.916\$ 0.000	168.759\$ 0.001	168.791\$ 0.000	348.805\$ 0.000
Velocity (geocentric) (km s ⁻¹)	V_g	65.189\$ 0.102	67.016\$ 0.101	61.322\$ 0.813	19.820\$ 0.345
Velocity (helion) (km s ⁻¹)	V_h	39.784\$ 0.270	40.708\$ 0.185	37.907\$ 0.778	24.403\$ 0.345
Velocity (infinity) (km s ⁻¹)	V_∞	66.30\$ 0.89	68.20\$ 1.01	62.50\$ 0.82	22.80\$ 0.43
Beginning height (km)	H_{beg}	105.84\$ 0.13	122.99\$ 0.45	108.99\$ 0.20	97.43\$ 0.32
Maximum height (km)	H_{max}	103.12\$ 0.61	104.14\$ 0.72	103.82\$ 0.92	87.60\$ 0.29
Ending height (km)	H_{end}	91.98\$ 0.36	97.26\$ 0.77	100.61\$ 0.39	82.56\$ 0.05
Average Range (km)	Range _{avg}	141.01\$ 0.30	148.45\$ 0.41	144.90\$ 0.72	124.29\$ 0.11
Radiant Right asc (geocentric) (°)	α_{geo}	99.018\$ 0.774	56.431\$ 0.554	55.865\$ 0.605	24.403\$ 1.002
Radiant Declination (geocentric) (°)	δ_{geo}	11.340\$ 0.759	21.511\$ 0.515	43.984\$ 0.434	4.463\$ 1.017
cos zenithal angle	COSZR	0.5787	0.6373	0.8546	0.7942
Angle of intercept (°)	Q	13.4	10.9	18.2	22.1
Tisserand Parameter	T_j	0.213\$ 0.205	-0.373\$ 0.130	1.178\$ 0.454	7.323\$ 1.048
K'b value		7.605	6.519	7.269	7.097
Heat of ablation (Jkg ⁻¹)		7.00E+06	4.90E+06	6.60E+06	4.30E+06
Tlim (K)		1400	1300	1400	1350
Tboil (K)		2100	1600	2000	1380
Specific heat (Jkg ⁻¹ Kj 1)		1100	1700	1200	1800
Molar mass (atomic unit)		36	36	36	36
Thermal conductivity (W m ⁻¹ K ⁻¹)		0.1	0.5	0.1	0.3
Density (kg m ⁻³)		820 ⁺⁵⁰⁰ ₋₂₀₀	1095 ⁺³⁰⁰ ₋₅₀₀	945 ⁺³⁰⁰ ₋₄₀₀	4150 ⁺⁴⁰⁰ ₋₅₀₀

Properties of meteoroids of our sample, according to our ablation model. Maximum height refers to the height of maximum brightness. Angular elements are J2000

Code	20080911075207	20080911075323	20080911075846	20080911081630
Date(UTC) (YYYYMMDD:HH:MM:SS)	20080911:07:52:07	20080911:07:53:23	20080911:07:58:46	20080911:08:16:30
Observed photometric mass (kg)	(7.20\$ 0.46)£ 10 ⁻⁷	(2.60\$ 0.27)£ 10 ⁻⁶	(3.20\$ 0.37)£ 10 ⁻⁶	(3.15\$ 0.36)£ 10 ⁻⁶
Observed peak magnitude (magnitude)	3.29\$ 0.21	1.81\$ 0.19	1.89\$ 0.22	1.91\$ 0.22
Perihelion (AU)	0.746\$ 0.013	1.000\$ 0.002	0.885\$ 0.007	0.961\$ 0.006
Aphelion (AU)	-11.793\$ 1.644	7.275\$ 1.027	17.661\$ 2.853	15.810\$ 1.865
Semi-major axis (AU)	-5.523\$ 0.820	4.138\$ 0.514	9.273\$ 1.426	8.386\$ 0.932
Eccentricity	1.135\$ 0.019	0.758\$ 0.030	0.905\$ 0.015	0.885\$ 0.013
Inclination (°)	138.006\$ 1.059	120.693\$ 0.630	138.940\$ 0.673	157.993\$ 0.844
Argument of periaapsis (°)	239.152\$ 1.611	189.773\$ 1.546	41.782\$ 1.307	334.706\$ 1.724
Longitude of the ascending node (°)	168.832\$ 0.000	168.833\$ 0.000	348.837\$ 0.000	348.849\$ 0.000
Velocity (geocentric) (km s ⁻¹)	66.472\$ 0.102	60.045\$ 0.305	65.136\$ 0.102	68.733\$ 0.101
Velocity (helion) (km s ⁻¹)	43.855\$ 0.272	39.348\$ 0.338	40.829\$ 0.180	40.705\$ 0.144
Velocity (infinity) (km s ⁻¹)	67.50\$ 0.65	61.20\$ 0.98	66.30\$ 0.75	69.90\$ 0.44
Beginning height (km)	112.14\$ 0.17	110.01\$ 0.32	117.41\$ 0.17	115.28\$ 0.14
Maximum height (km)	106.53\$ 1.04	102.70\$ 0.94	110.66\$ 0.66	104.58\$ 0.68
Ending height (km)	99.23\$ 0.30	96.82\$ 0.55	100.46\$ 0.26	100.65\$ 0.25
Average Range (km)	143.66\$ 0.55	151.39\$ 0.53	164.43\$ 0.11	136.74\$ 0.71
Radiant Right asc (geocentric) (°)	48.588\$ 0.825	68.728\$ 0.790	67.951\$ 0.414	86.435\$ 0.504
Radiant Declination (geocentric) (°)	40.938\$ 0.623	56.605\$ 0.434	-1.174\$ 0.415	10.852\$ 0.495
cos zenithal angle	0.9580	0.8781	0.5508	0.5607
Angle of intercept (°)	22.6	17.3	13.5	13.0
Tisserand Parameter	hyp	0.664\$ 0.249	-0.297\$ 0.122	-0.173\$ 0.118
K'b value	7.090	7.123	6.821	6.987
Heat of ablation (Jkg ⁻¹)	6.00E+06	6.00E+06	6.00E+06	7.00E+06
Tlim (K)	1300	1200	1300	1250
Tboil (K)	2000	2000	2000	2000
Specific heat (Jkg ⁻¹ Kj 1)	1200	1100	1200	1200
Molar mass (atomic unit)	36	36	36	36
Thermal conductivity (W m ⁻¹ K ⁻¹)	0.1	0.1	0.1	0.1
Density (kg m ⁻³)	980 ⁺²⁰⁰ ₋₅₀₀	1070 ⁺¹⁵⁰ ₋₄₅₀	1070 ⁺⁴⁰⁰ ₋₆₀₀	865 ⁺²⁰⁰ ₋₅₀₀

Properties of meteoroids of our sample, according to our ablation model. Maximum height refers to the height of maximum brightness. Angular elements are J2000

Code	20080911084108	20080911084529	20080911084739	20080911085605
Date(UTC) (YYYYMMDD:HH:MM:SS)	20080911:08:41:08	20080911:08:45:29	20080911:08:47:39	20080911:08:56:05
Observed photometric mass (kg)	(3.80\$ 0.25)\$ 10 ⁻⁷	(2.15\$ 0.15)\$ 10 ⁻⁶	(1.17\$ 0.09)\$ 10 ⁻⁶	(8.35\$ 0.50)\$ 10 ⁻⁷
Observed peak magnitude (magnitude)	3.89\$ 0.26	3.46\$ 0.24	2.92\$ 0.23	3.65\$ 0.22
Perihelion (AU)	1.003\$ 0.002	0.226\$ 0.019	1.006\$ 0.001	0.740\$ 0.025
Aphelion (AU)	14.715\$ 3.337	3.487\$ 0.355	5.209\$ 0.656	10.770\$ 2.031
Semi-major axis (AU)	7.859\$ 1.668	1.856\$ 0.187	3.107\$ 0.328	5.755\$ 1.008
Eccentricity	0.872\$ 0.027	0.878\$ 0.004	0.676\$ 0.034	0.871\$ 0.025
Inclination (°)	125.146\$ 0.932	10.217\$ 2.478	120.965\$ 0.895	156.236\$ 1.964
Argument of periaapsis (°)	187.308\$ 2.162	311.176\$ 3.156	175.968\$ 2.403	115.583\$ 2.971
Longitude of the ascending node (°)	168.865\$ 0.000	168.869\$ 0.000	168.870\$ 0.000	168.875\$ 0.000
Velocity (geocentric) (km s ⁻¹)	62.476\$ 0.102	31.772\$ 0.106	59.350\$ 0.305	66.237\$ 0.102
Velocity (helion) (km s ⁻¹)	40.617\$ 0.295	35.844\$ 0.670	38.434\$ 0.392	40.106\$ 0.337
Velocity (infinity) (km s ⁻¹)	64.37\$ 0.88	33.50\$ 0.43	60.50\$ 1.08	67.40\$ 0.90
Beginning height (km)	99.80\$ 0.19	100.31\$ 0.15	111.77\$ 0.28	101.37\$ 0.27
Maximum height (km)	93.81\$ 1.01	94.14\$ 0.36	103.24\$ 0.93	98.22\$ 0.76
Ending height (km)	89.17\$ 0.32	90.84\$ 0.28	98.30\$ 0.48	92.13\$ 0.62
Average Range (km)	128.79\$ 0.96	141.46\$ 0.97	131.58\$ 0.79	125.03\$ 0.83
Radiant Right asc (geocentric) (°)	70.416\$ 1.133	5.328\$ 1.541	75.787\$ 1.141	98.646\$ 1.291
Radiant Declination (geocentric) (°)	54.592\$ 0.656	9.036\$ 1.527	56.694\$ 0.626	35.456\$ 1.050
cos zenithal angle	0.9230	0.7089	0.9072	0.7370
Angle of intercept (°)	21.7	14.8	22.0	13.3
Tisserand Parameter	-0.410\$ 0.173	3.366\$ 0.515	1.089\$ 0.312	-0.040\$ 0.211
K'b value	7.971	7.277	7.005	7.967
Heat of ablation (Jkg ⁻¹)	5.80E+06	7.20E+06	6.80E+06	7.20E+06
Tlim (K)	1000	1000	1250	1400
Tboil (K)	2000	2000	2000	2100
Specific heat (Jkg ⁻¹ Kj 1)	1300	1200	1400	1100
Molar mass (atomic unit)	36	30	30	36
Thermal conductivity (W m ⁻¹ K ⁻¹)	0.2	0.3	0.4	0.3
Density (kg m ⁻³)	650 ⁺³⁰⁰ ₋₄₀₀	3150 ⁺⁴⁰⁰ ₋₆₀₀	610 ⁺²⁰⁰ ₋₃₀₀	1065 ⁺⁵⁰⁰ ₋₂₀₀

Properties of meteoroids of our sample, according to our ablation model. Maximum height refers to the height of maximum brightness. Angular elements are J2000

Code		20080911090242	20080911090512	20080911093436	20080911094752
Date(UTC) (YYYYMMDD:HH:MM:SS)		20080911:09:02:42	20080911:09:05:12	20080911:09:34:36	20080911:09:47:52
Observed photometric mass (kg)		(1.85\$ 0.16)\$ 10 ⁻⁶	(2.05\$ 0.22)\$ 10 ⁻⁶	(4.90\$ 0.48)\$ 10 ⁻⁶	(9.95\$ 0.75)\$ 10 ⁻⁷
Observed peak magnitude (magnitude)		2.16\$ 0.19	2.04\$ 0.22	1.95\$ 0.19	3.32\$ 0.25
Perihelion (AU)	q	0.664\$ 0.004	0.665\$ 0.027	0.978\$ 0.003	0.730\$ 0.011
Aphelion (AU)	Q	7.187\$ 0.300	8.459\$ 1.476	5.473\$ 0.402	7.035\$ 0.747
Semi-major axis (AU)	a	3.926\$ 0.150	4.562\$ 0.731	3.225\$ 0.201	3.883\$ 0.375
Eccentricity	e	0.831\$ 0.006	0.854\$ 0.027	0.697\$ 0.019	0.812\$ 0.018
Inclination (°)	i	154.459\$ 0.294	151.694\$ 2.112	116.203\$ 0.410	115.039\$ 0.696
Argument of periaapsis (°)	ω	255.489\$ 0.555	105.313\$ 2.952	21.339\$ 1.071	112.775\$ 1.607
Longitude of the ascending node (°)	Ω	168.880\$ 0.000	168.881\$ 0.000	348.902\$ 0.000	168.910\$ 0.000
Velocity (geocentric) (km s ⁻¹)	V_g	64.290\$ 0.102	64.616\$ 0.102	57.905\$ 0.204	57.264\$ 0.204
Velocity (helion) (km s ⁻¹)	V_h	39.200\$ 0.110	39.6\$ 0.393	38.57\$ 0.223	39.169\$ 0.281
Velocity (infinity) (km s ⁻¹)	V_∞	65.30\$ 0.69	65.80\$ 0.97	59.10\$ 0.52	58.50\$ 1.17
Beginning height (km)	H_{beg}	109.78\$ 0.05	111.24\$ 0.30	109.67\$ 0.09	111.29\$ 0.26
Maximum height (km)	H_{max}	101.31\$ 1.00	103.65\$ 0.77	101.71\$ 0.48	104.92\$ 0.75
Ending height (km)	H_{end}	94.17\$ 0.08	97.94\$ 0.54	96.81\$ 0.16	96.38\$ 0.45
Average Range (km)	$Range_{avg}$	132.76\$ 0.95	143.58\$ 0.94	127.37\$ 0.51	142.06\$ 0.63
Radiant Right asc (geocentric) (°)	α_{geo}	53.624\$ 0.179	102.13\$ 1.380	75.349\$ 0.291	109.662\$ 0.797
Radiant Declination (geocentric) (°)	δ_{geo}	32.257\$ 0.151	36.977\$ 1.101	-13.665\$ 0.284	55.122\$ 0.455
cos zenithal angle	COSZR	0.9712	0.7354	0.4918	0.8195
Angle of intercept (°)	Q	23.2	13.2	19.8	16.8
Tisserand Parameter	T_j	0.453\$ 0.210	0.284\$ 0.253	1.115\$ 0.268	0.914\$ 0.243
K'b value		7.197	7.173	7.249	7.019
Heat of ablation (Jkg ⁻¹)		6.60E+06	7.50E+06	7.30E+06	6.70E+06
Tlim (K)		1300	1230	1050	1000
Tboil (K)		2050	2000	2100	1950
Specific heat (Jkg ⁻¹ Kj 1)		1100	1200	1300	1100
Molar mass (atomic unit)		30	36	30	30
Thermal conductivity (W m ⁻¹ K ⁻¹)		0.4	0.2	0.5	0.3
Density (kg m ⁻³)		760 ⁺¹⁰⁰ ₋₅₀₀	915 ⁺⁵⁰⁰ ₋₄₀₀	1055 ⁺⁵⁰⁰ ₋₃₀₀	1015 ⁺⁵⁰⁰ ₋₅₀₀

Properties of meteoroids of our sample, according to our ablation model. Maximum height refers to the height of maximum brightness. Angular elements are J2000. (nf: partial lightcurve).

Code		20080911094844	20090624054307	20090819072950	20090825033603
Date(UTC) (YYYYMMDD:HH:MM:SS)		20080911:09:48:44	20090624:05:43:07	20090819:07:29:50	20090825:03:36:03
Observed photometric mass (kg)		(1.70\$ 0.12)\$ 10 ⁻⁶	(2.75\$ 0.20)\$ 10 ⁻⁶	nf	(1.19\$ 0.07)\$ 10 ⁻⁶
Observed peak magnitude (magnitude)		3.34\$ 0.23	2.88\$ 0.21	nf	4.21\$ 0.24
Perihelion (AU)	q	0.104\$ 0.011	0.381\$ 0.003	0.633\$ 0.010	0.297\$ 0.005
Aphelion (AU)	Q	3.378\$ 0.269	11.242\$ 1.063	8.003\$ 0.964	3.178\$ 0.080
Semi-major axis (AU)	a	1.741\$ 0.140	5.811\$ 0.533	4.318\$ 0.485	1.738\$ 0.042
Eccentricity	e	0.940\$ 0.002	0.934\$ 0.005	0.853\$ 0.015	0.829\$ 0.002
Inclination (°)	i	14.436\$ 3.198	103.488\$ 0.267	47.628\$ 0.561	4.354\$ 0.540
Argument of periaapsis (°)	ω	328.216\$ 2.240	287.065\$ 0.594	100.792\$ 1.537	303.939\$ 0.837
Longitude of the ascending node (°)	Ω	168.911\$ 0.000	92.730\$ 0.000	146.328\$ 0.000	151.960\$ 0.001
Velocity (geocentric) (km s ⁻¹)	V_g	36.547\$ 0.105	53.928\$ 0.204	34.130\$ 0.210	28.569\$ 0.107
Velocity (helion) (km s ⁻¹)	V_h	35.400\$ 0.577	39.911\$ 0.175	39.342\$ 0.293	35.281\$ 0.175
Velocity (infinity) (km s ⁻¹)	V_∞	38.00\$ 0.67	54.30\$ 0.52	36.00\$ 0.41	30.90\$ 0.26
Beginning height (km)	H_{beg}	103.58\$ 0.23	108.65\$ 0.02	107.26\$ 0.11	100.11\$ 0.06
Maximum height (km)	H_{max}	99.56\$ 0.46	96.89\$ 1.88	\$	95.91\$ 0.84
Ending height (km)	H_{end}	94.34\$ 0.53	88.11\$ 0.04	99.97\$ 0.16	89.93\$ 0.09
Average Range (km)	Range _{avg}	143.34\$ 0.98	114.41\$ 0.61	113.05\$ 0.87	112.43\$ 0.68
Radiant Right asc (geocentric) (°)	α_{geo}	12.898\$ 1.211	314.970\$ 0.062	150.269\$ 1.162	347.558\$ 0.406
Radiant Declination (geocentric) (°)	δ_{geo}	11.177\$ 1.190	11.754\$ 0.061	59.478\$ 0.603	-1.748\$ 0.408
cos zenithal angle	COSZR	0.6624	0.7014	0.3067	0.5487
Angle of intercept (°)	Q	13.0	55.5	23.4	18.0
Tisserand Parameter	T_j	3.371\$ 0.519	0.720\$ 0.160	1.845\$ 0.229	3.639\$ 0.466
K _b value		7.203	7.130	6.864	7.165
Heat of ablation (Jkg ⁻¹)		7.80E+06	7.40E+06	nf	7.70E+06
T _{lim} (K)		1300	800	nf	1200
T _{boil} (K)		2100	2100	nf	2100
Specific heat (Jkg ⁻¹ Kj 1)		1600	1300	nf	1400
Molar mass (atomic unit)		36	30	nf	36
Thermal conductivity (W m ⁻¹ K ⁻¹)		0.3	0.2	nf	0.3
Density (kg m ⁻³)		3470 ⁺⁶⁰⁰ ₋₅₀₀	965 ⁺⁴⁰⁰ ₋₂₀₀	nf	2825 ⁺⁹⁰⁰ ₋₆₀₀

Properties of meteoroids of our sample, according to our ablation model. Maximum height refers to the height of maximum brightness. Angular elements are J2000

Code		20090825035228	20090825040835	20090825043435	20090825053106
Date(UTC) (YYYYMMDD:HH:MM:SS)		20090825:03:52:28	20090825040835	20090825:04:34:35	20090825:05:31:06
Observed photometric mass (kg)		(2.89\$ 0.21)\$ $\times 10^{-6}$	(3.75\$ 0.41)\$ $\times 10^{-6}$	(4.80\$ 0.45)\$ $\times 10^{-6}$	(1.95\$ 0.14)\$ $\times 10^{-6}$
Observed peak magnitude (magnitude)		3.09\$ 0.22	1.91\$ 0.21	2.81\$ 0.26	2.88\$ 0.21
Perihelion (AU)	q	0.328\$ 0.005	0.736\$ 0.002	0.259\$ 0.004	0.098\$ 0.007
Aphelion (AU)	Q	2.828\$ 0.067	26.295\$ 3.204	4.850\$ 0.149	4.412\$ 0.349
Semi-major axis (AU)	a	1.578\$ 0.034	13.515\$ 1.603	2.555\$ 0.076	2.255\$ 0.176
Eccentricity	e	0.792\$ 0.005	0.946\$ 0.006	0.898\$ 0.002	0.957\$ 0.003
Inclination ($^{\circ}$)	i	5.756\$ 0.398	126.068\$ 0.089	0.767\$ 0.437	17.181\$ 2.169
Argument of periaapsis ($^{\circ}$)	ω	301.843\$ 0.663	116.117\$ 0.315	304.764\$ 0.600	147.985\$ 1.478
Longitude of the ascending node ($^{\circ}$)	Ω	151.969\$ 0.000	151.975\$ 0.000	152.029\$ 0.021	332.029\$ 0.000
Velocity (geocentric) (km s^{-1})	V_g	26.761\$ 0.217	61.627\$ 0.102	32.154\$ 0.106	38.459\$ 0.312
Velocity (helion) (km s^{-1})	V_h	34.542\$ 0.176	41.106\$ 0.095	37.524\$ 0.138	36.904\$ 0.417
Velocity (infinity) (km s^{-1})	V_{∞}	29.20\$ 0.40	62.80\$ 0.12	34.20\$ 0.32	40.20\$ 0.93
Beginning height (km)	H_{beg}	101.05\$ 0.06	115.70\$ 0.05	103.42\$ 0.05	104.14\$ 0.22
Maximum height (km)	H_{max}	93.10\$ 0.84	106.53\$ 0.82	90.84\$ 1.00	101.38\$ 1.18
Ending height (km)	H_{end}	89.14\$ 0.09	102.54\$ 0.06	87.75\$ 0.09	89.99\$ 0.29
Average Range (km)	$Range_{avg}$	111.74\$ 0.24	124.07\$ 0.29	109.75\$ 0.96	113.51\$ 0.69
Radiant Right asc (geocentric) ($^{\circ}$)	α_{geo}	346.279\$ 0.324	83.205\$ 0.064	348.645\$ 0.279	1.064\$ 0.739
Radiant Declination (geocentric) ($^{\circ}$)	δ_{geo}	-0.603\$ 0.327	50.868\$ 0.041	-4.344\$ 0.280	-5.725\$ 0.740
cos zenithal angle	COSZR	0.6052	0.2633	0.6059	0.5925
Angle of intercept ($^{\circ}$)	Q	19.2	14.7	21.0	20.9
Tisserand Parameter	T_j	3.967\$ 0.512	-0.232\$ 0.075	2.652\$ 0.319	2.674\$ 0.398
K'b value		7.036	7.014	7.060	7.196
Heat of ablation (Jkg^{-1})		9.20E+06	6.20E+06	4.20E+06	7.50E+06
Tlim (K)		1400	800	900	1400
Tboil (K)		2150	2200	2180	2200
Specific heat ($\text{Jkg}^{-1}\text{K}^{-1}$)		1600	1200	1600	1500
Molar mass (atomic unit)		36	30	36	36
Thermal conductivity ($\text{W m}^{-1} \text{K}^{-1}$)		0.2	0.1	0.2	0.3
Density (kg m^{-3})		3025 $^{+900}_{-400}$	675 $^{+600}_{-200}$	2780 $^{+600}_{-600}$	3020 $^{+600}_{+500}$

Properties of meteoroids of our sample, according to our ablation model. Maximum height refers to the height of maximum brightness. Angular elements are J2000

Code		20090825063604	20090825063641	20090825064646	20090825065903
Date(UTC) (YYYYMMDD:HH:MM:SS)		20090825:06:36:04	20090825:06:36:41	20090825:06:46:46	20090825:06:59:03
Observed photometric mass (kg)		(2.35\$ 0.32)\$ $\times 10^{-6}$	(1.25\$ 0.10)\$ $\times 10^{-6}$	(1.80\$ 0.22)\$ $\times 10^{-6}$	(3.90\$ 0.37)\$ $\times 10^{-6}$
Observed peak magnitude (magnitude)		1.46\$ 0.20	2.57\$ 0.21	2.15\$ 0.26	2.10\$ 0.20
Perihelion (AU)	q	0.757\$ 0.011	0.976\$ 0.001	1.009\$ 0.000	0.162\$ 0.004
Aphelion (AU)	Q	10.533\$ 1.528	14.363\$ 1.075	18.312\$ 3.437	5.247\$ 0.192
Semi-major axis (AU)	a	5.645\$ 0.764	7.670\$ 0.538	9.660\$ 1.718	2.704\$ 0.097
Eccentricity	e	0.866\$ 0.018	0.873\$ 0.009	0.895\$ 0.019	0.940\$ 0.002
Inclination ($^{\circ}$)	i	134.968\$ 0.772	112.089\$ 0.136	148.358\$ 0.240	21.310\$ 0.641
Argument of periaapsis ($^{\circ}$)	ω	242.7\$ 1.487	157.972\$ 0.308	355.282\$ 0.500	137.196\$ 0.647
Longitude of the ascending node ($^{\circ}$)	Ω	152.074\$ 0.000	152.075\$ 0.000	332.082\$ 0.000	332.088\$ 0.000
Velocity (geocentric) (km s $^{-1}$)	V_g	62.534\$ 0.203	60.18\$ 0.187	67.664\$ 0.203	36.929\$ 0.104
Velocity (helion) (km s $^{-1}$)	V_h	39.977\$ 0.266	40.493\$ 0.100	40.786\$ 0.200	37.780\$ 0.156
Velocity (infinity) (km s $^{-1}$)	V_{∞}	63.70\$ 0.55	59.50\$ 0.93	68.90\$ 0.72	38.60\$ 0.47
Beginning height (km)	H_{beg}	115.77\$ 0.07	117.22\$ 0.04	113.69\$ 0.04	100.25\$ 0.07
Maximum height (km)	H_{max}	101.41\$ 1.62	107.79\$ 1.20	108.91\$ 0.93	95.40\$ 1.13
Ending height (km)	H_{end}	93.88\$ 0.09	95.97\$ 0.04	103.51\$ 0.07	86.64\$ 0.09
Average Range (km)	$Range_{avg}$	118.49\$ 0.32	119.72\$ 0.70	126.01\$ 0.43	109.98\$ 0.68
Radiant Right asc (geocentric) ($^{\circ}$)	α_{geo}	31.679\$ 0.558	60.18\$ 0.187	65.243\$ 0.142	359.030\$ 0.300
Radiant Declination (geocentric) ($^{\circ}$)	δ_{geo}	37.727\$ 0.455	60.872\$ 0.091	2.799\$ 0.142	-10.614\$ 0.298
cos zenithal angle	COSZR	0.8576	0.7348	0.2752	0.6010
Angle of intercept ($^{\circ}$)	Q	31.8	45.3	20.0	13.4
Tisserand Parameter	T_j	0.186\$ 0.189	0.233\$ 0.115	-0.494\$ 0.127	2.382\$ 0.304
K'b value		6.779	6.660	7.271	7.441
Heat of ablation (Jkg $^{-1}$)		7.80E+06	8.20E+06	8.20E+06	6.20E+06
Tlim (K)		1050	1300	1390	1440
Tboil (K)		2200	2100	2200	2200
Specific heat (Jkg $^{-1}$ Kj 1)		1300	1500	1300	1500
Molar mass (atomic unit)		30	30	30	36
Thermal conductivity (W m $^{-1}$ K $^{-1}$)		0.1	0.2	0.1	0.4
Density (kg m $^{-3}$)		715 $^{+600}_{-300}$	965 $^{+600}_{-500}$	660 $^{+400}_{-300}$	2645 $^{+300}_{-700}$

Properties of meteoroids of our sample, according to our ablation model. Maximum height refers to the height of maximum brightness. Angular elements are J2000. (nf: partial lightcurve).

Code		20090825070044	20090825081927	20090825082615	20090825091030
Date(UTC) (YYYYMMDD:HH:MM:SS)		20090825:07:00:44	20090825:08:19:27	20090825:08:26:15	20090825:09:10:30
Observed photometric mass (kg)		(6.25\$ 0.38)\$ 10 ⁻⁷	(7.95\$ 0.39)\$ 10 ⁻⁸	nf	(8.70\$ 0.59)\$ 10 ⁻⁷
Observed peak magnitude (magnitude)		4.75\$ 0.29	4.52\$ 0.22	nf	3.69\$ 0.25
Perihelion (AU)	q	0.338\$ 0.004	0.621\$ 0.015	0.934\$ 0.002	0.503\$ 0.007
Aphelion (AU)	Q	2.630\$ 0.061	2.736\$ 0.154	6.845\$ 0.279	1.854\$ 0.031
Semi-major axis (AU)	a	1.484\$ 0.029	1.679\$ 0.084	3.890\$ 0.140	1.179\$ 0.017
Eccentricity	e	0.772\$ 0.007	0.630\$ 0.011	0.760\$ 0.009	0.573\$ 0.005
Inclination (°)	i	4.859\$ 0.125	14.171\$ 0.787	146.307\$ 0.205	62.338\$ 0.429
Argument of periaapsis (°)	ω	301.870\$ 0.095	269.893\$ 2.676	214.377\$ 0.499	67.799\$ 1.084
Longitude of the ascending node (°)	Ω	152.096\$ 0.000	152.145\$ 0.000	152.147\$ 0.000	152.178\$ 0.000
Velocity (geocentric) (km s ⁻¹)	V_g	25.841\$ 0.327	19.676\$ 0.115	65.126\$ 0.102	34.170\$ 0.210
Velocity (helion) (km s ⁻¹)	V_h	34.021\$ 0.169	35.027\$ 0.376	39.081\$ 0.105	31.668\$ 0.176
Velocity (infinity) (km s ⁻¹)	V_∞	28.10\$ 0.96	22.40\$ 0.41	66.20\$ 0.50	36.10\$ 0.73
Beginning height (km)	H_{beg}	96.97\$ 0.49	87.57\$ 0.06	104.62\$ 0.09	102.04\$ 0.06
Maximum height (km)	H_{max}	93.01\$ 1.02	86.16\$ 0.66	\$	97.48\$ 1.10
Ending height (km)	H_{end}	88.84\$ 1.34	83.07\$ 0.12	91.33\$ 0.07	91.53\$ 0.15
Average Range (km)	Range _{avg}	108.48\$ 0.59	102.03\$ 0.77	109.49\$ 0.71	114.94\$ 0.91
Radiant Right asc (geocentric) (°)	α_{geo}	346.639\$ 0.016	328.450\$ 1.287	45.032\$ 0.151	122.391\$ 0.618
Radiant Declination (geocentric) (°)	δ_{geo}	-1.074\$ 0.046	10.298\$ 1.270	36.650\$ 0.121	64.191\$ 0.267
cos zenithal angle	COSZR	0.7229	0.6512	0.9321	0.6269
Angle of intercept (°)	Q	22.8	30.5	36.8	38.0
Tisserand Parameter	T_j	4.184\$ 0.544	3.955\$ 0.501	0.403\$ 0.211	4.777\$ 0.682
Kb value		7.353	7.900	7.639	7.247
Heat of ablation (Jkg ⁻¹)		5.50E+06	5.70E+06	nf	7.80E+06
Tlim (K)		1300	1300	nf	1300
Tboil (K)		2300	2300	nf	2100
Specific heat (Jkg ⁻¹ Kj 1)		1800	1900	nf	1500
Molar mass (atomic unit)		36	36	nf	36
Thermal conductivity (W m ⁻¹ K ⁻¹)		0.6	0.7	nf	0.4
Density (kg m ⁻³)		4895 ⁺⁷⁰⁰ ₋₁₀₀₀	5425 ⁺⁵⁰⁰ ₋₈₀₀	nf	3070 ⁺⁹⁰⁰ ₋₈₀₀

Properties of meteoroids of our sample, according to our ablation model. Maximum height refers to the height of maximum brightness. Angular elements are J2000. (nc: lightcurve and deceleration not computed).

Code		20090625053313	20090820014058	20090822034136	20090825032616
Date(UTC) (YYYYMMDD:HH:MM:SS)		20090625:05:33:13	20090820:01:40:58	20090822:03:41:36	20090825:03:26:16
Observed photometric mass (kg)		(3.05\$ 0.25)\$ $\times 10^{-6}$	(4.99\$ 0.39)\$ $\times 10^{-6}$	(3.93\$ 0.24)\$ $\times 10^{-6}$	(4.30\$ 0.22)\$ $\times 10^{-6}$
Observed peak magnitude (magnitude)		2.83\$ 0.23	2.43\$ 0.19	3.49\$ 0.21	4.47\$ 0.23
Perihelion (AU)	q	0.679\$ 0.006	1.001\$ 0.000	0.984\$ 0.001	0.940\$ 0.004
Aphelion (AU)	Q	3.663\$ 0.189	6.097\$ 0.339	5.086\$ 0.154	3.161\$ 0.176
Semi-major axis (AU)	a	2.171\$ 0.096	3.554\$ 0.169	3.035\$ 0.077	2.050\$ 0.088
Eccentricity	e	0.687\$ 0.012	0.716\$ 0.014	0.676\$ 0.008	0.542\$ 0.020
Inclination ($^{\circ}$)	i	67.428\$ 0.450	37.598\$ 0.248	19.729\$ 0.160	0.901\$ 0.344
Argument of periaapsis ($^{\circ}$)	ω	100.697\$ 1.176	184.024\$ 0.186	158.967\$ 0.289	36.851\$ 1.019
Longitude of the ascending node ($^{\circ}$)	Ω	93.678\$ 0.000	147.058\$ 0.000	149.066\$ 0.000	331.916\$ 0.012
Velocity (geocentric) (km s^{-1})	V_g	38.566\$ 0.312	23.696\$ 0.221	15.380\$ 0.124	9.733\$ 0.306
Velocity (helion) (km s^{-1})	V_h	36.563\$ 0.248	38.779\$ 0.153	38.235\$ 0.097	36.368\$ 0.254
Velocity (infinity) (km s^{-1})	V_{∞}	40.30\$ 0.30	26.20\$ 0.54	18.80\$ 0.20	14.80\$ 0.20
Beginning height (km)	H_{beg}	102.16\$ 0.13	101.40\$ 0.11	93.56\$ 0.17	90.69\$ 0.05
Maximum height (km)	H_{max}	95.65\$ 1.08	89.71\$ 1.17	84.05\$ 0.49	86.24\$ 0.40
Ending height (km)	H_{end}	91.59\$ 0.23	84.12\$ 0.14	79.77\$ 0.28	84.14\$ 0.10
Average Range (km)	Range_{avg}	113.72\$ 0.16	105.24\$ 1.02	102.89\$ 0.42	109.90\$ 0.61
Radiant Right asc (geocentric) ($^{\circ}$)	α_{geo}	22.455\$ 0.526	269.866\$ 0.277	220.524\$ 0.384	296.341\$ 1.172
Radiant Declination (geocentric) ($^{\circ}$)	δ_{geo}	63.268\$ 0.235	62.947\$ 0.127	44.819\$ 0.261	-24.572\$ 1.300
cos zenithal angle	COSZR	0.5398	0.9489	0.6318	0.5597
Angle of intercept ($^{\circ}$)	Q	15.9	63.3	19.7	22.6
Tisserand Parameter	T_j	2.757\$ 0.384	2.379\$ 0.236	2.774\$ 0.267	3.593\$ 0.405
K'b value		7.318	6.733	7.174	7.170
Heat of ablation (Jkg^{-1})		7.40E+06	7.50E+06	nc	9.30E+06
Tlim (K)		1200	900	nc	1400
Tboil (K)		2000	1900	nc	2100
Specific heat ($\text{Jkg}^{-1}\text{K}^{-1}$)		1600	1400	nc	1300
Molar mass (atomic unit)		36	30	nc	36
Thermal conductivity ($\text{W m}^{-1}\text{K}^{-1}$)		0.6	0.6	nc	0.1
Density (kg m^{-3})		2950 ⁺⁵⁰⁰ ₋₂₀₀	3150 ⁺⁸⁰⁰ ₋₂₀₀	nc	4950 ⁺⁵⁴⁰ ₋₅₄₀

Properties of meteoroids of our sample, according to our ablation model. Maximum height refers to the height of maximum brightness. Angular elements are J2000

Code		20090825034528	20090825035145	20090825040603	20090825050631
Date(UTC) (YYYYMMDD:HH:MM:SS)		20090825:03:45:28	20090825:03:51:45	20090825:04:06:03	20090825:05:06:31
Observed photometric mass (kg)		(1.02\$ 0.07)£ 10 ⁻⁶	(1.35\$ 0.07)£ 10 ⁻⁶	(8.85\$ 0.64)£ 10 ⁻⁷	(1.25\$ 0.08)£ 10 ⁻⁶
Observed peak magnitude (magnitude)		3.22\$ 0.21	4.38\$ 0.23	3.19\$ 0.23	3.83\$ 0.24
Perihelion (AU)	q	0.978\$ 0.001	0.781\$ 0.008	0.653\$ 0.010	0.418\$ 0.005
Aphelion (AU)	Q	5.737\$ 0.439	1.742\$ 0.041	32.911\$ 14.090	3.034\$ 0.080
Semi-major axis (AU)	a	3.357\$ 0.219	1.261\$ 0.023	16.782\$ 7.458	1.726\$ 0.040
Eccentricity	e	0.709\$ 0.019	0.381\$ 0.008	0.961\$ 0.017	0.758\$ 0.006
Inclination (°)	i	7.325\$ 0.245	44.584\$ 0.399	51.477\$ 0.530	3.881\$ 0.338
Argument of periaapsis (°)	ω	202.690\$ 0.370	100.130\$ 2.020	253.835\$ 1.481	291.075\$ 0.699
Longitude of the ascending node (°)	Ω	151.963\$ 0.000	151.965\$ 0.000	151.974\$ 0.000	152.022\$ 0.001
Velocity (geocentric) (km s ⁻¹)	V_g	11.302\$ 0.281	25.382\$ 0.219	36.441\$ 0.105	24.601\$ 0.220
Velocity (helion) (km s ⁻¹)	V_h	38.615\$ 0.224	32.434\$ 0.201	41.261\$ 0.284	35.233\$ 0.170
Velocity (infinity) (km s ⁻¹)	V_∞	15.75\$ 0.30	27.70\$ 0.30	38.20\$ 0.41	27.10\$ 0.70
Beginning height (km)	H_{beg}	91.93\$ 0.05	101.87\$ 0.03	102.32\$ 0.10	101.21\$ 0.06
Maximum height (km)	H_{max}	86.05\$ 0.56	98.25\$ 0.77	96.59\$ 1.83	96.51\$ 0.89
Ending height (km)	H_{end}	82.51\$ 0.09	93.06\$ 0.09	91.86\$ 0.13	90.65\$ 0.09
Average Range (km)	Range _{avg}	98.13\$ 0.96	117.90\$ 0.93	117.09\$ 0.54	115.69\$ 0.62
Radiant Right asc (geocentric) (°)	α_{geo}	276.657\$ 0.484	158.326\$ 1.647	331.558\$ 0.782	341.887\$ 0.334
Radiant Declination (geocentric) (°)	δ_{geo}	2.180\$ 0.530	74.711\$ 0.443	38.182\$ 0.653	-3.371\$ 0.340
cos zenithal angle	COSZR	0.7442	0.5422	0.9678	0.6904
Angle of intercept (°)	Q	26.0	49.8	33.2	22.8
Tisserand Parameter	T_j	2.674\$ 0.259	4.775\$ 0.639	0.928\$ 0.146	3.765\$ 0.469
K'b value		7.097	6.953	7.151	6.945
Heat of ablation (Jkg ⁻¹)		7.50E+06	7.30E+06	6.20E+06	7.20E+06
Tlim (K)		1150	1300	1200	1100
Tboil (K)		2000	2000	2000	2000
Specific heat (Jkg ⁻¹ Kj 1)		1300	1400	1300	1400
Molar mass (atomic unit)		36	36	30	36
Thermal conductivity (W m ⁻¹ K ⁻¹)		0.1	0.2	0.4	0.4
Density (kg m ⁻³)		4150 ⁺⁵⁰⁰ ₋₅₀₀	2815 ⁺⁷⁰⁰ ₋₆₀₀	635 ⁺¹⁰⁰ ₋₃₀₀	3195 ⁺⁸⁰⁰ ₋₇₀₀

Properties of meteoroids of our sample, according to our ablation model. Maximum height refers to the height of maximum brightness. Angular elements are J2000

Code		20090825050904	20090825060500	20090825061542	20090825070933
Date(UTC) (YYYYMMDD:HH:MM:SS)		20090825:05:09:04	20090825:06:05:00	20090825:06:15:42	20090825:07:09:33
Observed photometric mass (kg)		(5.05\$ 0.27)\$ $\times 10^{-6}$	(2.55\$ 0.19)\$ $\times 10^{-6}$	(1.70\$ 0.12)\$ $\times 10^{-6}$	(3.10\$ 0.16)\$ $\times 10^{-6}$
Observed peak magnitude (magnitude)		4.56\$ 0.24	2.82\$ 0.21	3.17\$ 0.22	4.52\$ 0.23
Perihelion (AU)	q	1.011\$ 0.000	0.300\$ 0.009	0.160\$ 0.006	0.811\$ 0.002
Aphelion (AU)	Q	1.969\$ 0.067	3.113\$ 0.149	6.684\$ 0.728	5.572\$ 0.157
Semi-major axis (AU)	a	1.490\$ 0.033	1.706\$ 0.077	3.422\$ 0.364	3.191\$ 0.079
Eccentricity	e	0.322\$ 0.015	0.824\$ 0.007	0.953\$ 0.005	0.746\$ 0.006
Inclination (°)	i	12.770\$ 0.510	4.966\$ 0.913	10.242\$ 1.022	1.064\$ 0.122
Argument of periaapsis (°)	ω	179.274\$ 0.907	303.846\$ 1.434	136.524\$ 0.996	57.485\$ 0.364
Longitude of the ascending node (°)	Ω	152.018\$ 0.000	152.059\$ 0.001	332.058\$ 0.000	332.071\$ 0.003
Velocity (geocentric) (km s ⁻¹)	V_g	8.422\$ 0.333	28.346\$ 0.323	37.200\$ 0.418	16.350\$ 0.121
Velocity (helion) (km s ⁻¹)	V_h	34.058\$ 0.196	35.148\$ 0.335	38.679\$ 0.357	38.437\$ 0.089
Velocity (infinity) (km s ⁻¹)	V_∞	13.80\$ 0.20	30.50\$ 0.30	38.90\$ 0.40	19.60\$ 0.40
Beginning height (km)	H_{beg}	83.11\$ 0.35	98.44\$ 0.07	99.70\$ 0.10	95.64\$ 0.07
Maximum height (km)	H_{max}	79.34\$ 0.50	90.47\$ 1.09	94.76\$ 0.22	89.94\$ 0.40
Ending height (km)	H_{end}	72.75\$ 0.70	86.81\$ 0.13	86.74\$ 0.17	85.86\$ 0.15
Average Range (km)	$Range_{avg}$	97.58\$ 0.28	111.94\$ 0.42	109.17\$ 0.26	107.93\$ 0.91
Radiant Right asc (geocentric) (°)	α_{geo}	249.373\$ 1.323	347.466\$ 0.691	355.415\$ 0.451	315.216\$ 0.274
Radiant Declination (geocentric) (°)	δ_{geo}	42.426\$ 0.866	-1.235\$ 0.700	-6.898\$ 0.453	-19.364\$ 0.275
cos zenithal angle	COSZR	0.7250	30.5000	0.6415	0.3854
Angle of intercept (°)	Q	27.4	23.2	23.7	16.7
Tisserand Parameter	T_j	4.481\$ 0.543	3.696\$ 0.489	2.002\$ 0.284	2.674\$ 0.254
K'b value		7.675	7.396	7.478	7.173
Heat of ablation (Jkg ⁻¹)		7.20E+06	5.30E+06	8.40E+06	9.20E+06
Tlim (K)		1400	1570	1200	800
Tboil (K)		2000	1590	2100	2100
Specific heat (Jkg ⁻¹ Kj 1)		1400	2200	1300	1400
Molar mass (atomic unit)		56	20	36	36
Thermal conductivity (W m ⁻¹ K ⁻¹)		0.6	0.2	0.2	0.3
Density (kg m ⁻³)		4820 ⁺⁷⁰⁰ ₋₅₀₀	2860 ⁺⁸⁰⁰ ₋₁₂₀₀	925 ⁺⁵⁰⁰ ₋₄₀₀	3215 ⁺⁶⁰⁰ ₋₇₀₀

Properties of meteoroids of our sample, according to our ablation model. Maximum height refers to the height of maximum brightness. Angular elements are J2000. (sp: small number of points).

Code		20090825085804	20090825090312	20090826020835	20090902084143
Date(UTC) (YYYYMMDD:HH:MM:SS)		20090825:08:58:04	20090825:09:03:12	20090826:02:08:35	20090902:08:41:43
Observed photometric mass (kg)		(1.80\$ 0.21)\$ $\times 10^{-6}$	(5.90\$ 0.61)\$ $\times 10^{-7}$	(1.10\$ 0.05)\$ $\times 10^{-6}$	(6.25\$ 0.48)\$ $\times 10^{-6}$
Observed peak magnitude (magnitude)		1.73\$ 0.20	1.95\$ 0.20	4.75\$ 0.23	2.87\$ 0.22
Perihelion (AU)	q	0.903\$ 0.012	0.739\$ 0.035	1.003\$ 0.000	1.008\$ 0.000
Aphelion (AU)	Q	25.132\$ 7.055	10.364\$ 4.517	3.887\$ 0.248	8.595\$ 1.091
Semi-major axis (AU)	a	13.018\$ 3.525	5.552\$ 2.260	2.445\$ 0.124	4.801\$ 0.545
Eccentricity	e	0.931\$ 0.019	0.867\$ 0.054	0.590\$ 0.021	0.790\$ 0.024
Inclination ($^{\circ}$)	i	150.777\$ 1.164	116.854\$ 2.294	23.277\$ 0.434	37.713\$ 0.513
Argument of periaapsis ($^{\circ}$)	ω	38.840\$ 2.144	245.123\$ 4.762	168.411\$ 0.318	177.363\$ 0.081
Longitude of the ascending node ($^{\circ}$)	Ω	332.170\$ 0.000	152.172\$ 0.000	152.861\$ 0.000	159.889\$ 0.000
Velocity (geocentric) (km s^{-1})	V_g	67.433\$ 0.101	58.054\$ 0.407	15.768\$ 0.368	24.365\$ 0.440
Velocity (helion) (km s^{-1})	V_h	41.076\$ 0.225	39.945\$ 0.814	37.321\$ 0.246	39.672\$ 0.265
Velocity (infinity) (km s^{-1})	V_{∞}	68.60\$ 0.40	59.10\$ 0.40	19.20\$ 0.30	26.70\$ 0.71
Beginning height (km)	H_{beg}	118.30\$ 0.29	97.43\$ 0.23	96.24\$ 0.07	100.24\$ 0.03
Maximum height (km)	H_{max}	105.76\$ 0.32	93.71\$ 0.95	91.09\$ 0.81	92.54\$ 0.55
Ending height (km)	H_{end}	97.08\$ 0.40	88.44\$ 0.36	86.01\$ 0.13	86.13\$ 0.05
Average Range (km)	Range_{avg}	127.80\$ 1.28	117.25\$ 0.12	112.01\$ 0.02	111.27\$ 0.16
Radiant Right asc (geocentric) ($^{\circ}$)	α_{geo}	52.617\$ 0.686	22.565\$ 2.129	239.211\$ 0.432	260.630\$ 0.174
Radiant Declination (geocentric) ($^{\circ}$)	δ_{geo}	2.133\$ 0.687	44.324\$ 1.523	51.861\$ 0.239	63.101\$ 0.098
cos zenithal angle	COSZR	0.6820	0.9979	0.8861	0.4618
Angle of intercept ($^{\circ}$)	Q	19.9	37.5	50.5	41.3
Tisserand Parameter	T_j	-0.660\$ 0.124	0.472\$ 0.408	3.146\$ 0.345	2.016\$ 0.207
K'b value		6.765	8.049	6.934	7.091
Heat of ablation (Jkg^{-1})		7.50E+06	sp	6.30E+06	6.90E+06
Tlim (K)		1200	sp	1300	1050
Tboil (K)		2200	sp	2100	2100
Specific heat ($\text{Jkg}^{-1}\text{K}^{-1}$)		1300	sp	1700	1200
Molar mass (atomic unit)		36	sp	36	36
Thermal conductivity ($\text{W m}^{-1}\text{K}^{-1}$)		0.3	sp	0.3	0.2
Density (kg m^{-3})		620 ⁺⁵⁰⁰ ₋₄₀₀	sp	4780 ⁺⁵⁹⁰ ₋₃₁₀	1230 ⁺⁴⁰⁰ ₋₄₀₀

Properties of meteoroids of our sample, according to our ablation model. Maximum height refers to the height of maximum brightness. Angular elements are J2000. (sp: small number of points).

Code	20090902085534	20090902085832	20090902091711	20090902092028
Date(UTC) (YYYYMMDD:HH:MM:SS)	20090902:08:55:34	20090902:08:58:32	20090902:09:17:11	20090902:09:20:28
Observed photometric mass (kg)	(1.55\$ 0.18)\$ 10^{-6}	(1.55\$ 0.10)\$ 10^{-6}	(1.20\$ 0.13)\$ 10^{-6}	(6.40\$ 0.51)\$ 10^{-7}
Observed peak magnitude (magnitude)	2.01\$ 0.23	3.16\$ 0.21	1.86\$ 0.20	2.62\$ 0.21
Perihelion (AU)	0.031\$ 0.007	0.345\$ 0.015	0.940\$ 0.014	0.626\$ 0.023
Aphelion (AU)	3.437\$ 0.328	15.482\$ 4.689	17.934\$ 5.366	6.149\$ 1.072
Semi-major axis (AU)	1.734\$ 0.161	7.913\$ 2.350	9.437\$ 2.682	3.388\$ 0.538
Eccentricity	0.982\$ 0.005	0.956\$ 0.012	0.900\$ 0.029	0.815\$ 0.029
Inclination (°)	152.186\$ 8.482	44.463\$ 1.141	141.680\$ 1.575	126.842\$ 1.543
Argument of periaapsis (°)	342.930\$ 1.763	110.242\$ 2.236	148.862\$ 3.228	98.973\$ 3.026
Longitude of the ascending node (°)	159.898\$ 0.000	339.900\$ 0.000	159.912\$ 0.000	159.914\$ 0.000
Velocity (geocentric) (km s ⁻¹)	49.718\$ 0.103	38.320\$ 0.104	66.115\$ 0.011	59.165\$ 0.407
Velocity (helion) (km s ⁻¹)	35.314\$ 0.673	40.578\$ 0.410	40.800\$ 0.327	38.688\$ 0.537
Velocity (infinity) (km s ⁻¹)	50.90\$ 0.80	39.80\$ 0.30	67.20\$ 0.40	60.40\$ 0.45
Beginning height (km)	95.77\$ 0.08	94.98\$ 0.10	114.30\$ 0.11	111.31\$ 0.28
Maximum height (km)	89.42\$ 0.97	92.96\$ 0.70	105.36\$ 0.93	102.41\$ 0.36
Ending height (km)	83.46\$ 0.12	87.45\$ 0.21	99.30\$ 0.34	93.41\$ 0.47
Average Range (km)	108.33\$ 0.39	112.14\$ 1.14	124.91\$ 1.47	124.10\$ 0.66
Radiant Right asc (geocentric) (°)	23.043\$ 1.343	11.747\$ 0.937	76.927\$ 1.378	97.178\$ 1.330
Radiant Declination (geocentric) (°)	13.875\$ 1.305	-23.733\$ 0.872	44.707\$ 0.979	48.511\$ 0.880
cos zenithal angle	0.8594	0.3581	0.8938	0.7821
Angle of intercept (°)	26.4	20.6	21.1	13.1
Tisserand Parameter	2.808\$ 0.539	1.172\$ 0.220	-0.368\$ 0.178	0.976\$ 0.339
K'b value	7.928	7.996	6.937	7.064
Heat of ablation (Jkg ⁻¹)	8.80E+06	7.50E+06	sp	7.50E+06
Tlim (K)	750	1150	sp	1200
Tboil (K)	2100	2100	sp	2100
Specific heat (Jkg ⁻¹ Kj 1)	1300	1200	sp	1300
Molar mass (atomic unit)	36	30	sp	36
Thermal conductivity (W m ⁻¹ K ⁻¹)	0.3	0.1	sp	0.2
Density (kg m ⁻³)	4495 ⁺⁶⁰⁰ ₋₆₀₀	1165 ⁺⁶⁰⁰ ₋₂₀₀	sp	725 ⁺⁴⁰⁰ ₋₂₀₀

Properties of meteoroids of our sample, according to our ablation model. Maximum height refers to the height of maximum brightness. Angular elements are J2000

Code		20090902093338	20090909010643	20090909012810	20090909013647
Date(UTC) (YYYYMMDD:HH:MM:SS)		20090902:09:33:38	20090909:01:06:43	20090909:01:28:10	20090909:01:36:47
Observed photometric mass (kg)		(2.25\$ 0.42)\$ 10 ⁻⁶	(2.50\$ 0.17)\$ 10 ⁻⁶	(2.15\$ 0.16)\$ 10 ⁻⁶	(4.85\$ 0.39)\$ 10 ⁻⁶
Observed peak magnitude (magnitude)		1.03\$ 0.19	4.36\$ 0.29	3.82\$ 0.29	3.52\$ 0.28
Perihelion (AU)	q	1.007\$ 0.001	0.754\$ 0.004	0.658\$ 0.006	0.990\$ 0.001
Aphelion (AU)	Q	19.248\$ 1.990	4.212\$ 0.264	2.979\$ 0.107	3.674\$ 0.366
Semi-major axis (AU)	a	10.128\$ 0.995	2.483\$ 0.131	1.819\$ 0.054	2.332\$ 0.183
Eccentricity	e	0.901\$ 0.010	0.696\$ 0.017	0.638\$ 0.010	0.575\$ 0.034
Inclination (°)	i	174.707\$ 0.867	3.134\$ 0.216	4.336\$ 0.362	14.262\$ 0.597
Argument of periaapsis (°)	ω	5.277\$ 1.823	247.177\$ 0.454	263.670\$ 1.079	197.444\$ 0.593
Longitude of the ascending node (°)	Ω	339.927\$ 0.001	166.371\$ 0.000	166.385\$ 0.000	166.389\$ 0.000
Velocity (geocentric) (km s ⁻¹)	V_g	70.287\$ 0.101	17.006\$ 0.359	17.941\$ 0.236	11.629\$ 0.555
Velocity (helion) (km s ⁻¹)	V_h	40.879\$ 0.105	37.474\$ 0.251	35.689\$ 0.206	37.163\$ 0.401
Velocity (infinity) (km s ⁻¹)	V_∞	71.30\$ 0.35	20.60\$ 0.30	21.40\$ 0.46	16.10\$ 0.40
Beginning height (km)	H_{beg}	114.42\$ 0.14	91.56\$ 0.06	89.55\$ 0.10	92.10\$ 0.06
Maximum height (km)	H_{max}	102.81\$ 0.95	86.38\$ 0.48	86.80\$ 0.55	85.78\$ 0.72
Ending height (km)	H_{end}	94.75\$ 0.19	80.84\$ 0.12	81.95\$ 0.19	81.84\$ 0.10
Average Range (km)	$Range_{avg}$	126.64\$ 0.75	104.62\$ 1.24	100.11\$ 0.76	104.15\$ 0.97
Radiant Right asc (geocentric) (°)	α_{geo}	67.598\$ 0.532	332.953\$ 0.312	341.470\$ 0.583	281.927\$ 0.743
Radiant Declination (geocentric) (°)	δ_{geo}	18.733\$ 0.504	-4.552\$ 0.332	0.184\$ 0.589	28.742\$ 0.666
cos zenithal angle	COSZR	0.8483	0.5002	0.5173	0.9713
Angle of intercept (°)	Q	22.5	19.0	18.8	35.1
Tisserand Parameter	T_j	-0.694\$ 0.094	3.086\$ 0.341	3.769\$ 0.448	3.293\$ 0.385
K'b value		7.001	7.525	7.706	7.076
Heat of ablation (Jkg ⁻¹)		7.20E+06	5.20E+06	7.80E+06	7.20E+06
Tlim (K)		1400	700	1450	900
Tboil (K)		2300	2000	2100	2100
Specific heat (Jkg ⁻¹ Kj 1)		1100	1300	1800	1600
Molar mass (atomic unit)		36	36	36	36
Thermal conductivity (W m ⁻¹ K ⁻¹)		0.1	0.2	0.2	0.4
Density (kg m ⁻³)		605 ⁺⁵⁰⁰ ₋₃₀₀	4910 ⁺⁵⁰⁰ ₋₃₀₀	5010 ⁺⁵⁰⁰ ₋₆₀₀	5030 ⁺²⁰⁰ ₋₅₀₀

Properties of meteoroids of our sample, according to our ablation model. Maximum height refers to the height of maximum brightness. Angular elements are J2000

Code		20090911021830	20090911030523	20090911034442	20090911035942
Date(UTC) (YYYYMMDD:HH:MM:SS)		20090911:02:18:30	20090911:03:05:23	20090911:03:44:42	20090911:03:59:42
Observed photometric mass (kg)		(1.45\$ 0.09)\$ 10 ⁻⁶	(4.80\$ 0.55)\$ 10 ⁻⁶	(1.65\$ 0.09)\$ 10 ⁻⁶	(1.35\$ 0.08)\$ 10 ⁻⁶
Observed peak magnitude (magnitude)		4.31\$ 0.28	1.91\$ 0.22	4.31\$ 0.24	4.05\$ 0.24
Perihelion (AU)	q	0.904\$ 0.002	0.207\$ 0.003	0.515\$ 0.008	1.002\$ 0.001
Aphelion (AU)	Q	4.184\$ 0.273	5.675\$ 0.357	2.472\$ 0.072	4.756\$ 0.273
Semi-major axis (AU)	a	2.544\$ 0.136	2.941\$ 0.178	1.494\$ 0.038	2.879\$ 0.137
Eccentricity	e	0.644\$ 0.019	0.929\$ 0.005	0.655\$ 0.007	0.652\$ 0.017
Inclination (°)	i	20.443\$ 0.392	26.498\$ 0.526	4.452\$ 0.469	26.004\$ 0.319
Argument of periaapsis (°)	ω	222.235\$ 0.573	310.413\$ 0.472	103.504\$ 1.256	171.652\$ 0.621
Longitude of the ascending node (°)	Ω	168.361\$ 0.000	168.392\$ 0.000	348.416\$ 0.000	168.429\$ 0.000
Velocity (geocentric) (km s ⁻¹)	V_g	16.719\$ 0.361	36.275\$ 0.314	20.353\$ 0.228	17.523\$ 0.237
Velocity (helion) (km s ⁻¹)	V_h	37.599\$ 0.248	38.221\$ 0.239	34.184\$ 0.222	38.136\$ 0.192
Velocity (infinity) (km s ⁻¹)	V_∞	20.15\$ 0.70	38.20\$ 0.30	23.40\$ 0.63	20.60\$ 0.20
Beginning height (km)	H_{beg}	83.25\$ 0.03	100.40\$ 0.09	97.70\$ 0.07	95.94\$ 0.14
Maximum height (km)	H_{max}	79.90\$ 0.97	93.68\$ 1.26	93.61\$ 0.67	911.49\$ 0.72
Ending height (km)	H_{end}	72.47\$ 0.06	83.00\$ 0.10	89.75\$ 0.14	87.30\$ 0.12
Average Range (km)	$Range_{avg}$	96.16\$ 1.13	107.23\$ 0.08	106.65\$ 1.03	107.29\$ 1.27
Radiant Right asc (geocentric) (°)	α_{geo}	310.347\$ 0.457	3.518\$ 0.215	357.855\$ 0.623	251.238\$ 0.848
Radiant Declination (geocentric) (°)	δ_{geo}	32.976\$ 0.385	16.047\$ 0.206	-7.452\$ 0.633	51.516\$ 0.511
cos zenithal angle	COSZR	0.9803	0.6664	0.569	0.698
Angle of intercept (°)	Q	38.4	18.6	22.2	19.5
Tisserand Parameter	T_j	3.048\$ 0.333	2.266\$ 0.292	4.291\$ 0.543	2.822\$ 0.291
K'b value		7.814	7.392	7.145	7.081
Heat of ablation (Jkg ⁻¹)		8.20E+06	6.70E+06	7.50E+06	6.30E+06
Tlim (K)		1400	1150	1200	1150
Tboil (K)		2200	2300	2100	2100
Specific heat (Jkg ⁻¹ Kj 1)		1600	1200	1600	1400
Molar mass (atomic unit)		46	30	36	36
Thermal conductivity (W m ⁻¹ K ⁻¹)		0.4	0.1	0.4	0.4
Density (kg m ⁻³)		5070 ⁺⁶⁰⁰ ₋₁₀₀	3130 ⁺²⁰⁰ ₋₃₀₀	4850 ⁺⁴⁰⁰ ₋₄₀₀	3515 ⁺³⁰⁰ ₋₃₀₀

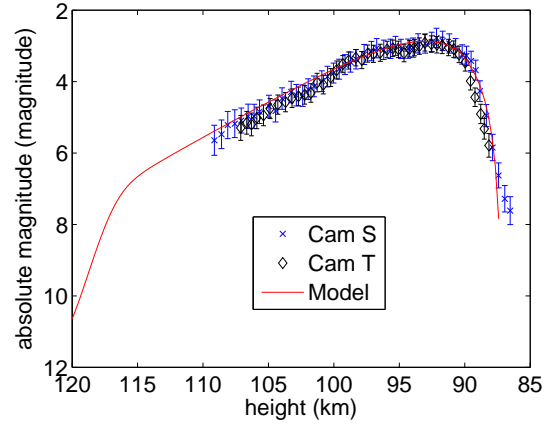
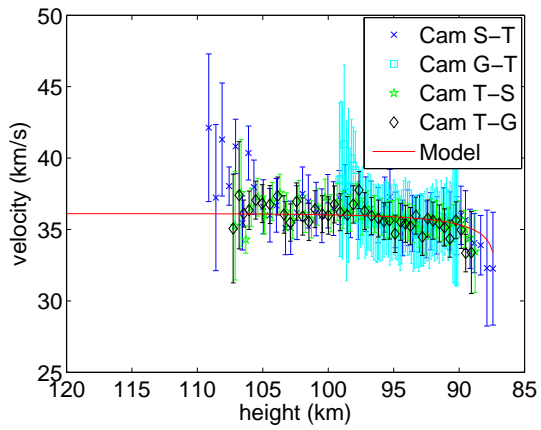
Properties of meteoroids of our sample, according to our ablation model. Maximum height refers to the height of maximum brightness. Angular elements are J2000

Code		20090911040233	20090911040433
Date(UTC) (YYYYMMDD:HH:MM:SS)		20090911:04:02:33	20090911:04:04:33
Observed photometric mass (kg)		(6.75\$ 0.41)£ 10 ⁻⁷	(2.25\$ 0.22)£ 10 ⁻⁵
Observed peak magnitude (magnitude)		4.16\$ 0.25	2.25\$ 0.22
Perihelion (AU)	q	0.917\$ 0.006	0.956\$ 0.001
Aphelion (AU)	Q	5.979\$ 0.913	5.670\$ 0.203
Semi-major axis (AU)	a	3.448\$ 0.458	3.313\$ 0.101
Eccentricity	e	0.734\$ 0.035	0.711\$ 0.009
Inclination (°)	i	59.512\$ 0.683	13.201\$ 0.157
Argument of periapsis (°)	ω	142.168\$ 1.579	208.402\$ 0.342
Longitude of the ascending node (°)	Ω	168.430\$ 0.000	168.432\$ 0.000
Velocity (geocentric) (km s ⁻¹)	V _g	35.634\$ 0.524	13.523\$ 0.130
Velocity (helion) (km s ⁻¹)	V _h	38.797\$ 0.440	38.661\$ 0.106
Velocity (infinity) (km s ⁻¹)	V _∞	37.30\$ 0.50	17.40\$ 0.30
Beginning height (km)	H _{beg}	103.45\$ 0.17	95.85\$ 0.05
Maximum height (km)	H _{max}	98.30\$ 1.05	82.65\$ 0.70
Ending height (km)	H _{end}	95.18\$ 0.30	78.14\$ 0.04
Average Range (km)	Range _{avg}	114.23\$ 0.69	107.50\$ 0.47
Radiant Right asc (geocentric) (°)	α_{geo}	187.706\$ 2.232	297.202\$ 0.381
Radiant Declination (geocentric) (°)	δ_{geo}	75.717\$ 0.913	19.451\$ 0.361
cos zenithal angle	COSZR	0.551	0.854
Angle of intercept (°)	Q	42.0	26.5
Tisserand Parameter	T _j	2.070\$ 0.307	2.663\$ 0.246
Kb value		7.205	6.859
Heat of ablation (Jkg ⁻¹)		7.40E+06	8.50E+06
Tlim (K)		1350	900
Tboil (K)		2100	2300
Specific heat (Jkg ⁻¹ K ⁻¹)		1600	800
Molar mass (atomic unit)		30	36
Thermal conductivity (W m ⁻¹ K ⁻¹)		0.2	0.5
Density (kg m ⁻³)		1460 ⁺⁴⁰⁰ ₋₅₀₀	4010 ⁺⁵⁰⁰ ₋₄₀₀

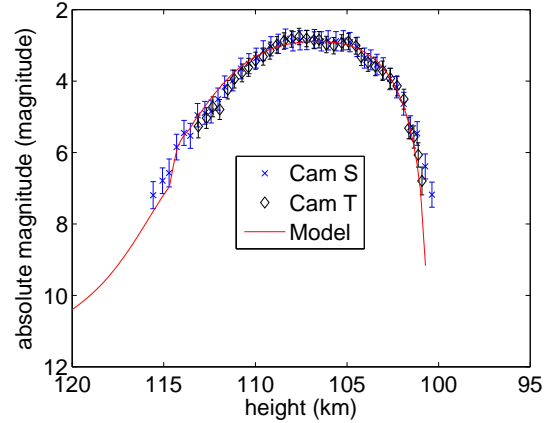
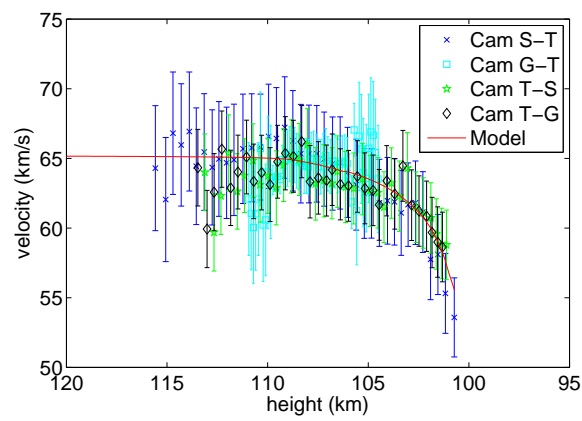
Appendix B

Decelerations and lightcurves of meteoroids of our sample

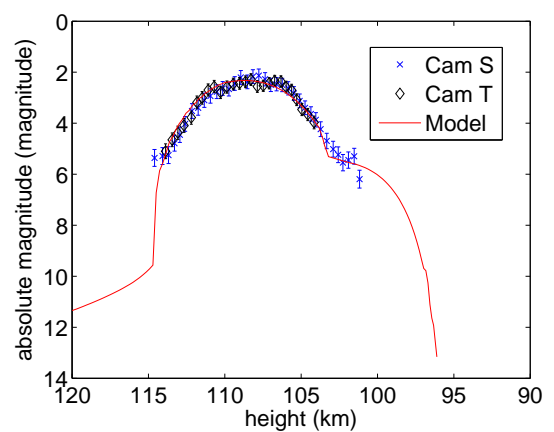
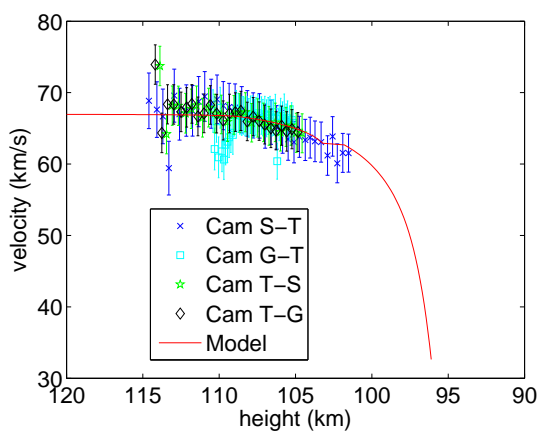
We give here the curves (decelerations and lightcurves) of meteoroids of our sample (chapter 5), according to our ablation model. The model fit is actually the best model fit from the refining search.



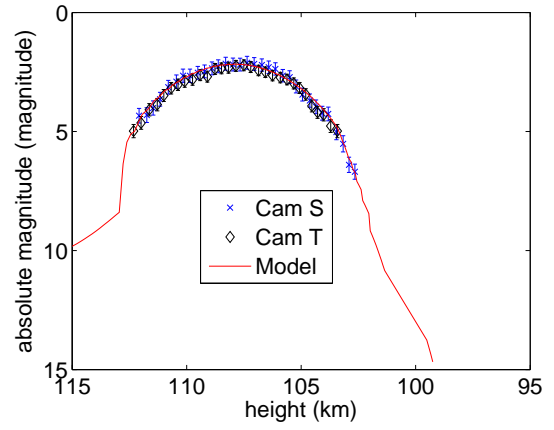
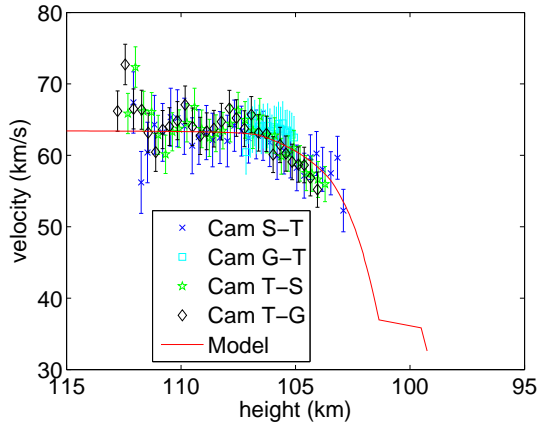
20060430-084301



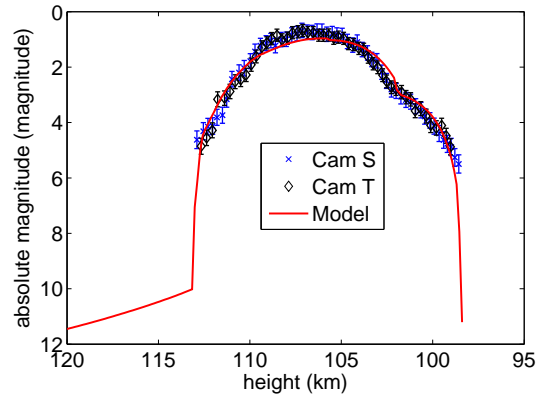
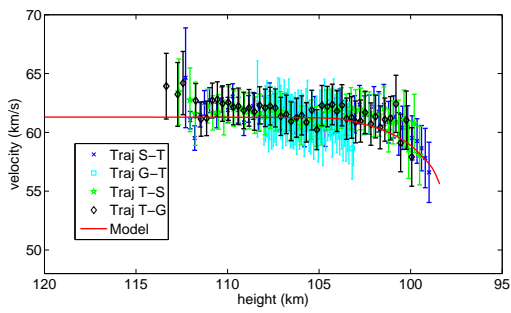
20060430-103000



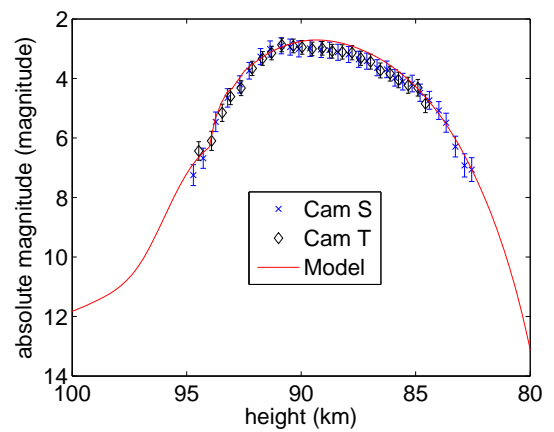
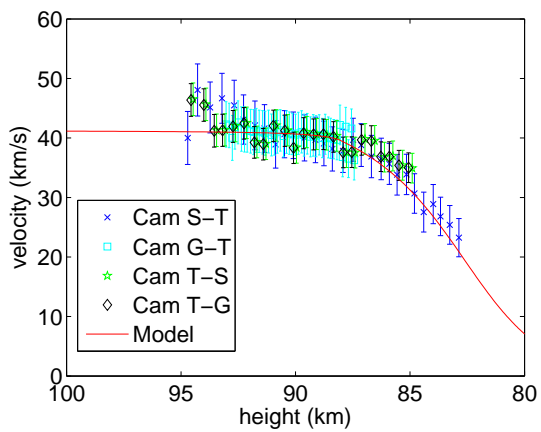
20060430-104845



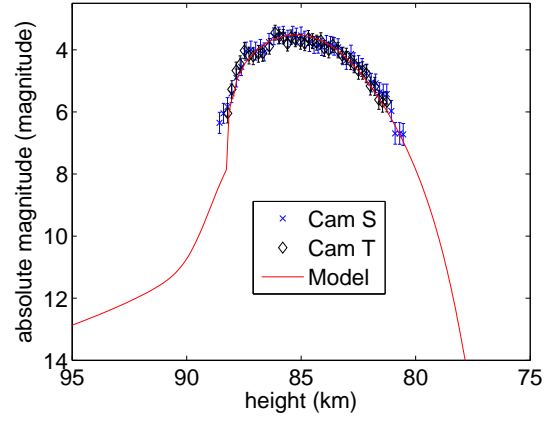
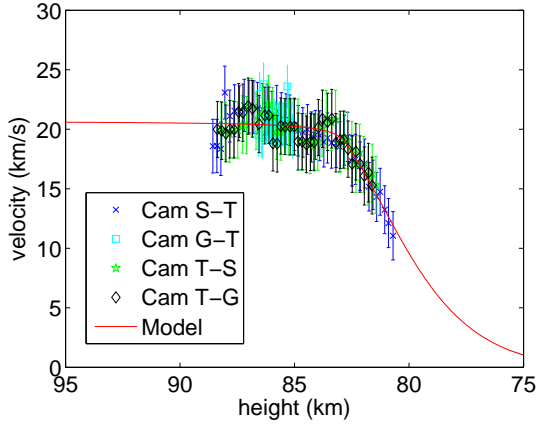
20060502-100335



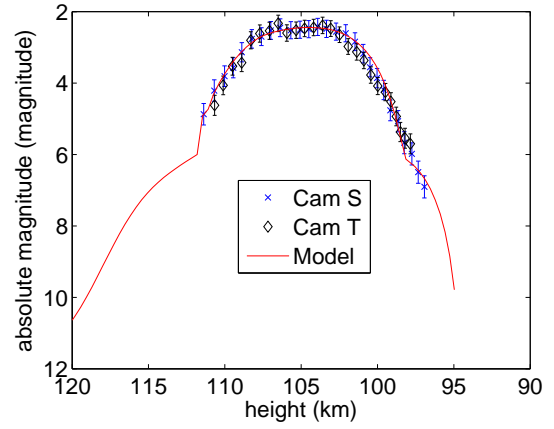
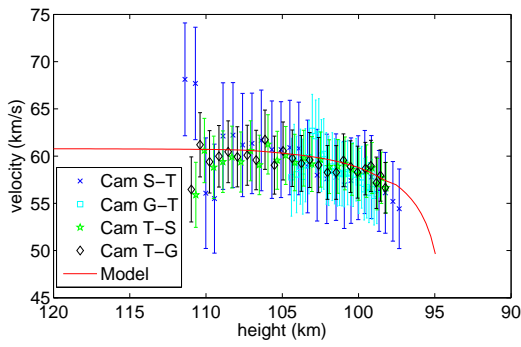
20060503-091349



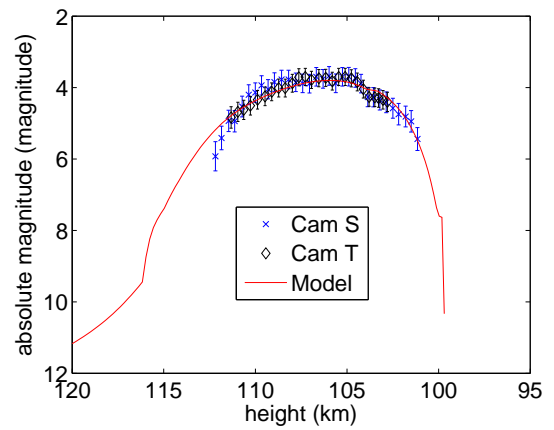
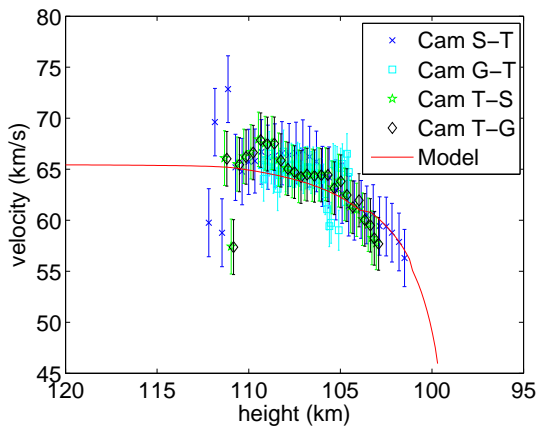
20060504-093103



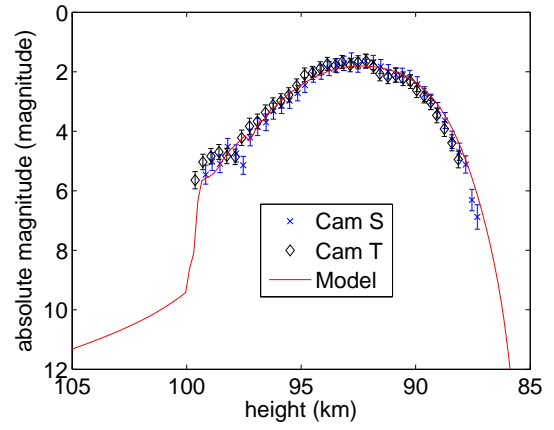
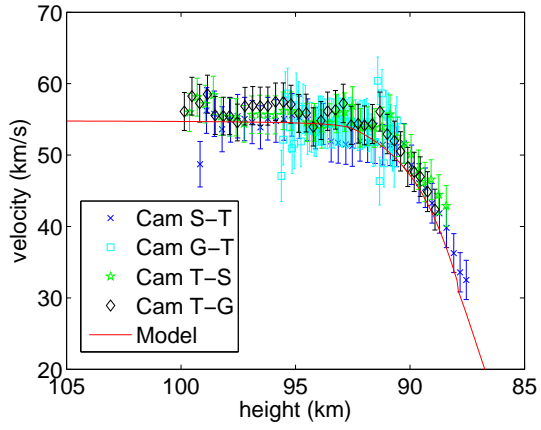
20060505-102944



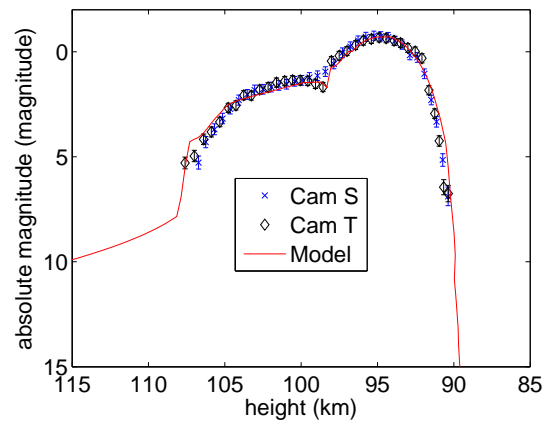
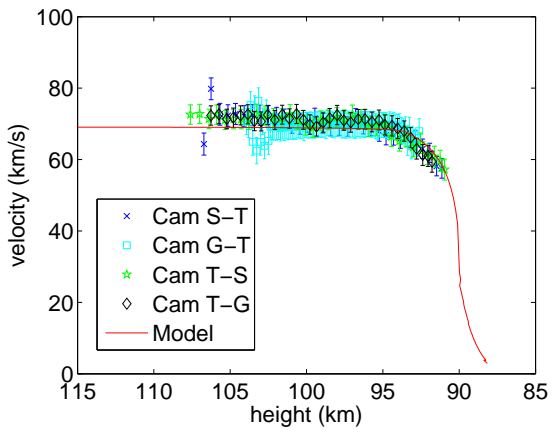
20070420-082356



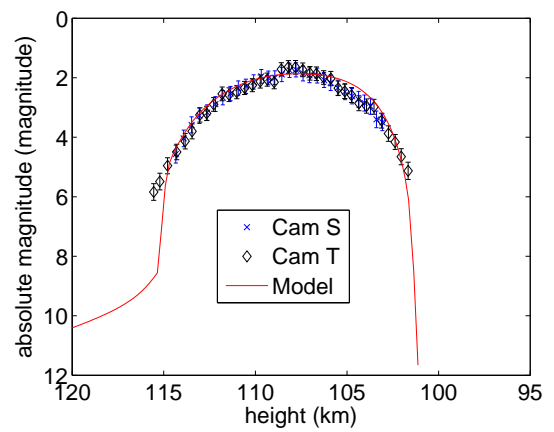
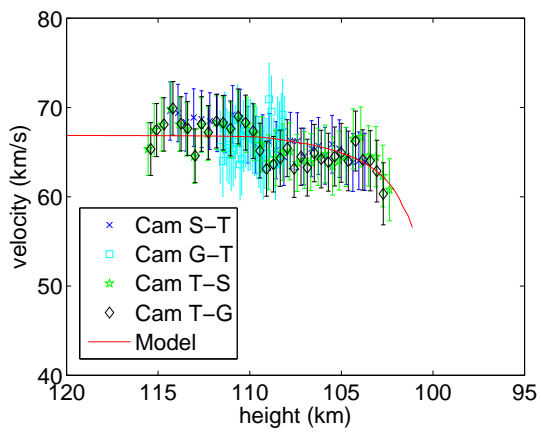
20070422-061849



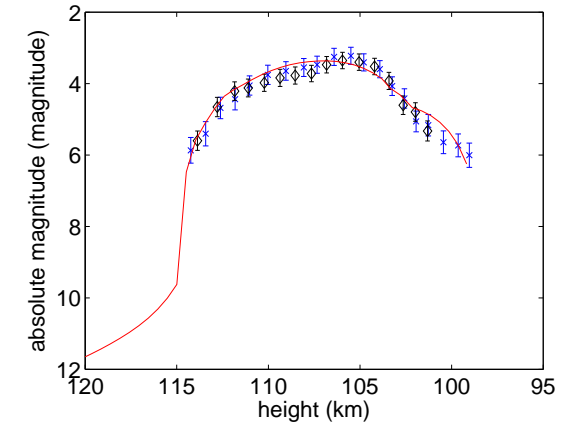
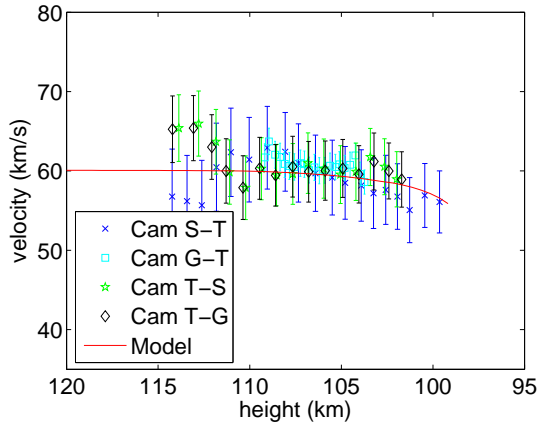
20070519-040843



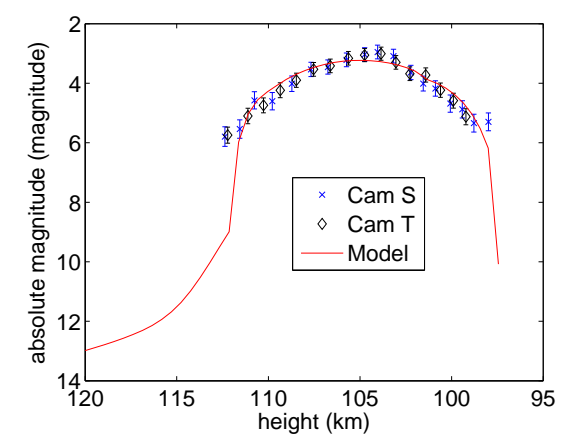
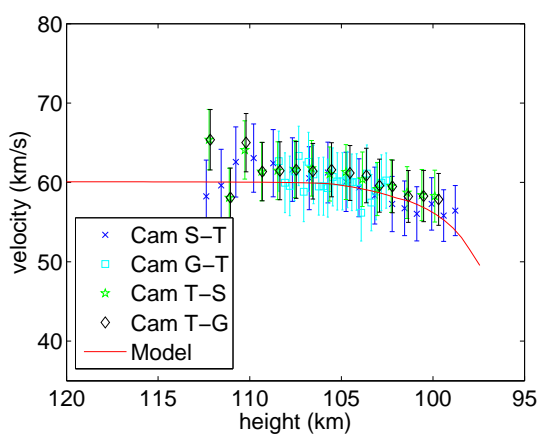
20070519-075753



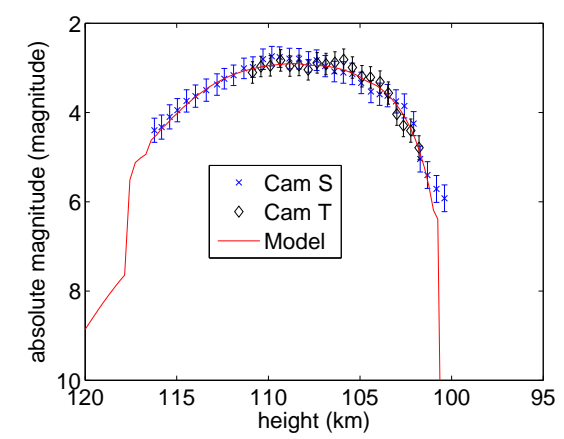
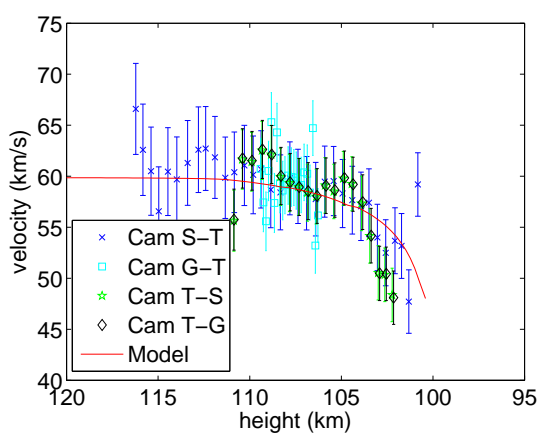
20070519-082713



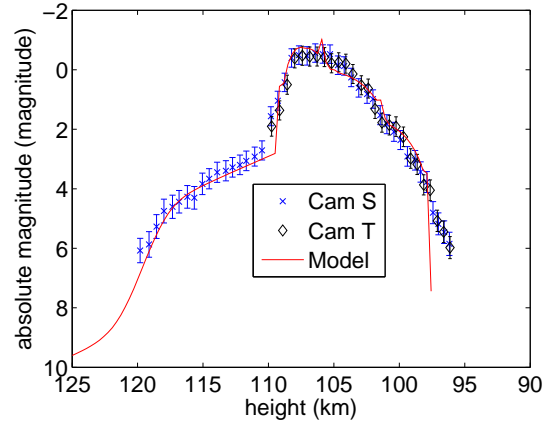
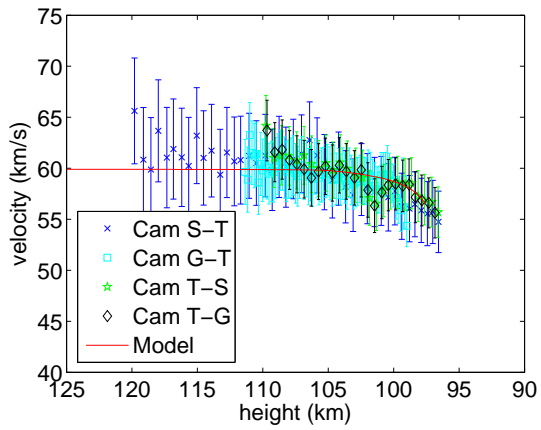
20070812-062117



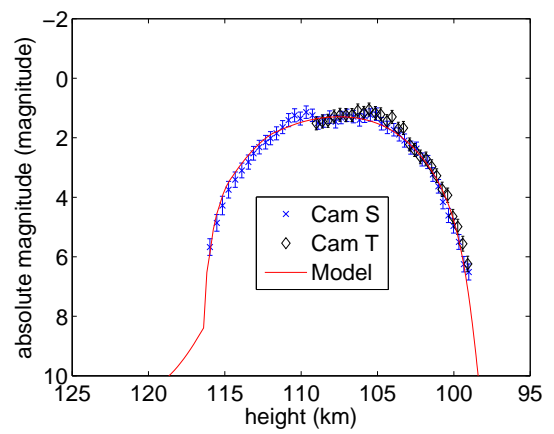
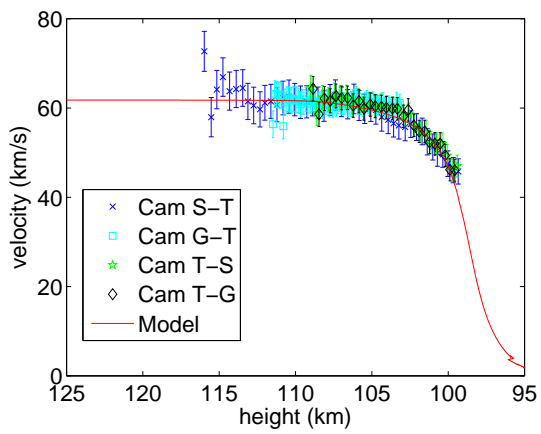
20070812-083450



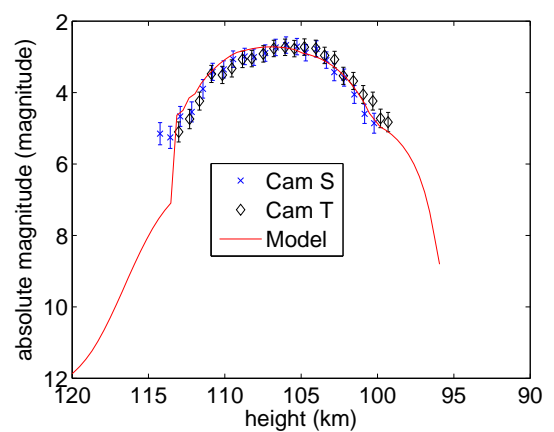
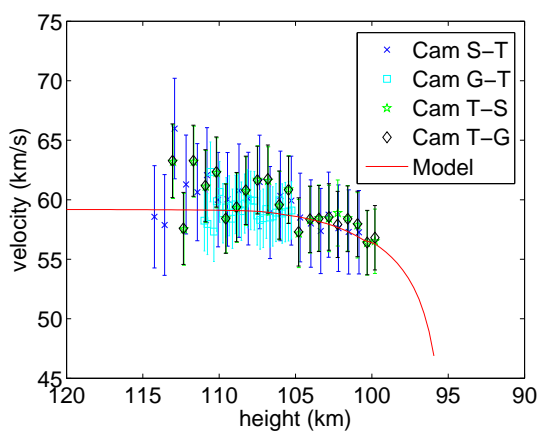
20070813-044452



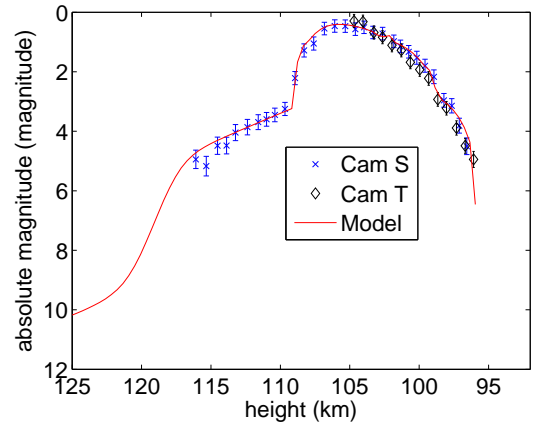
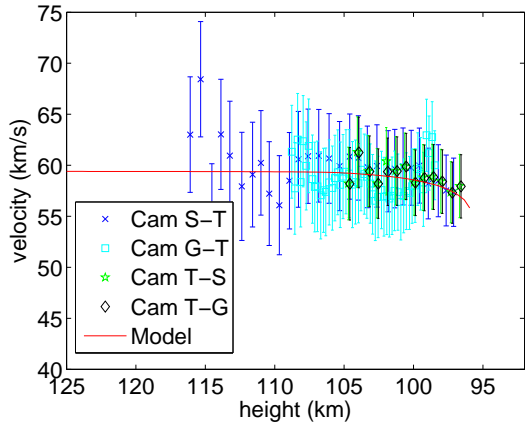
20070813-045726



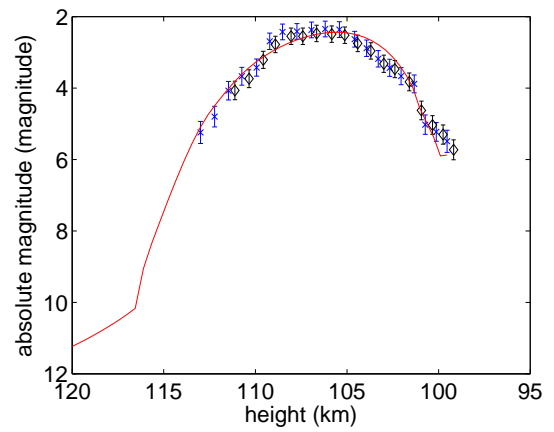
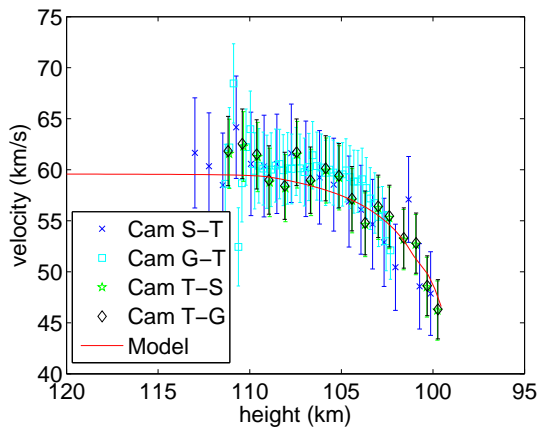
20070813-055649



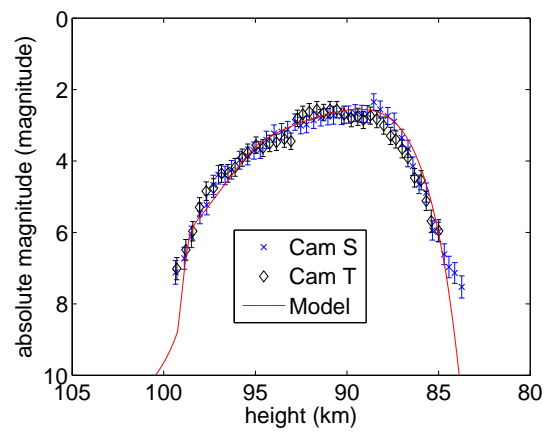
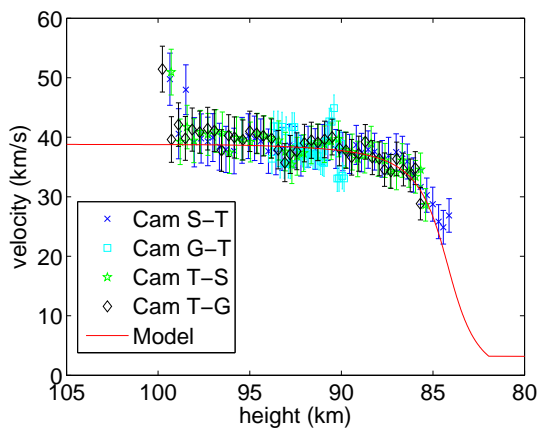
20070813-055909



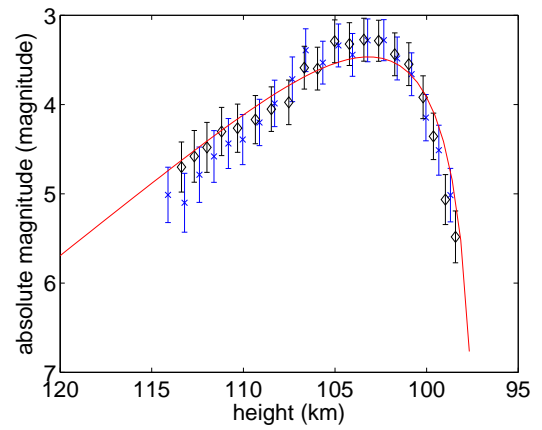
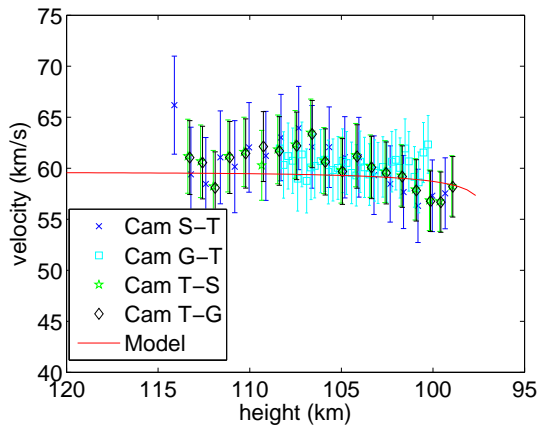
20070813-064415



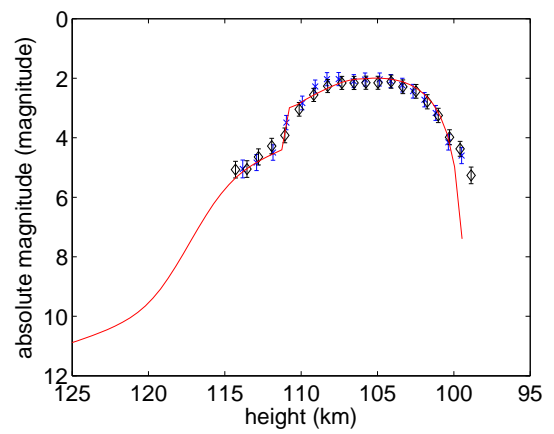
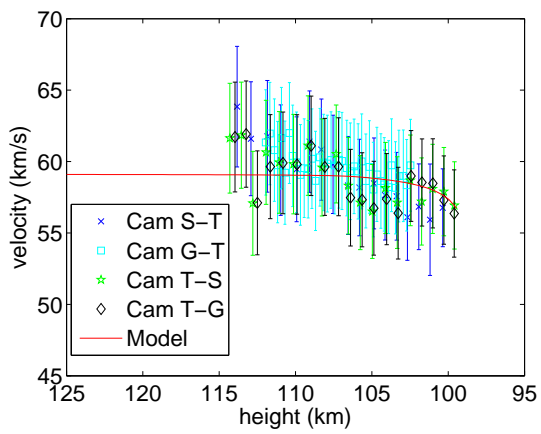
20070813-065047



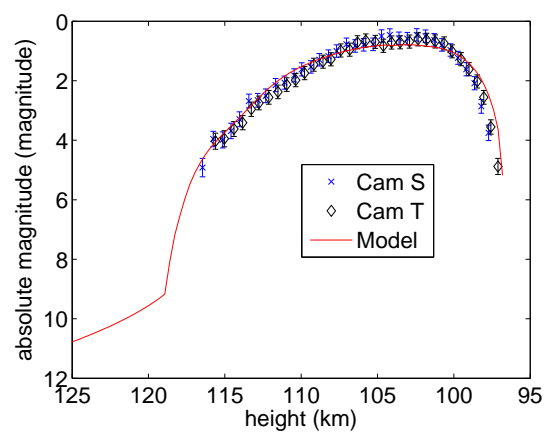
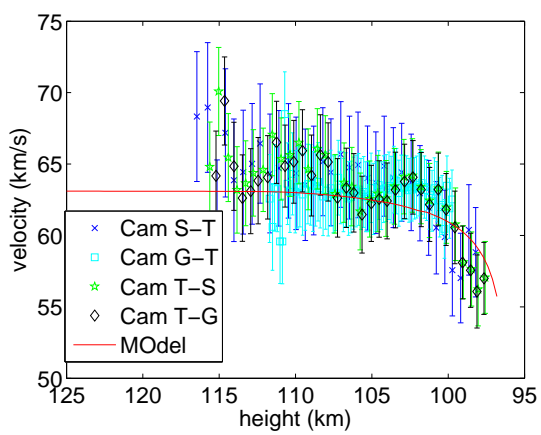
20070813-065828



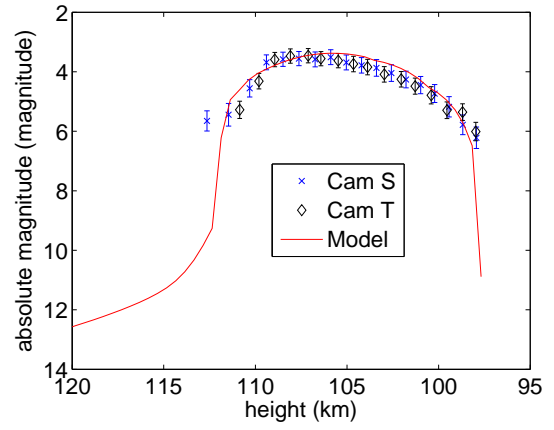
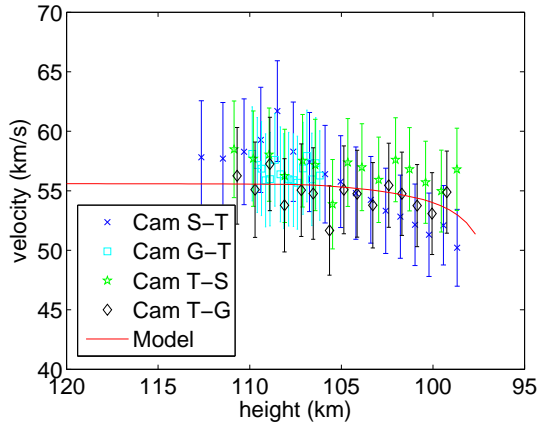
20070813-073054



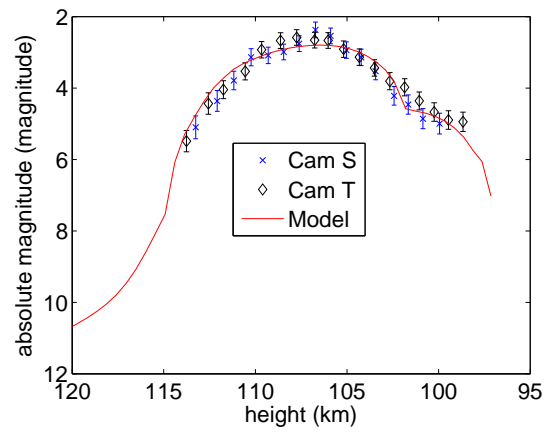
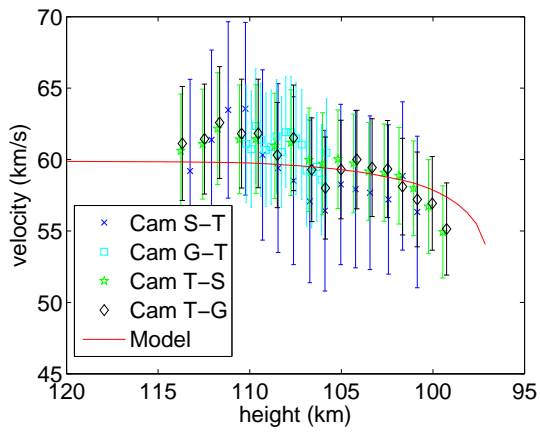
20070813-075355



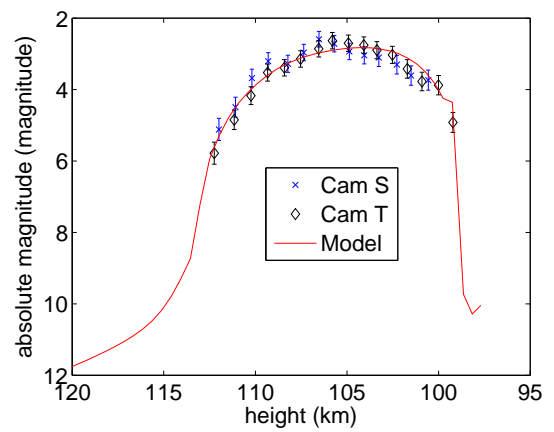
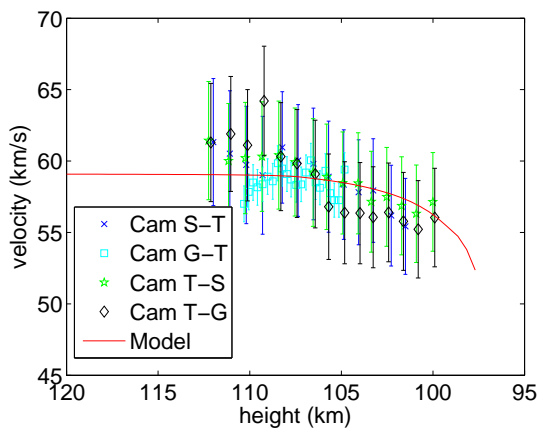
20070813-081229



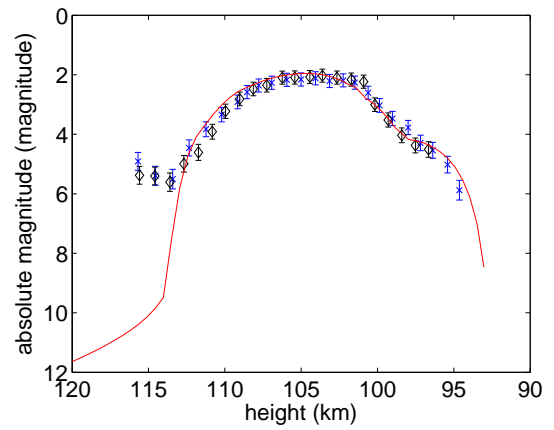
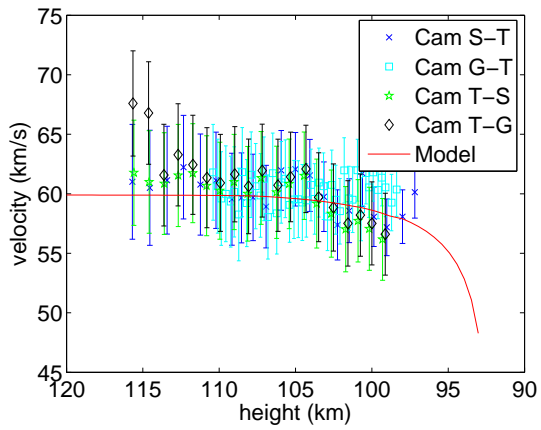
20070813-084353



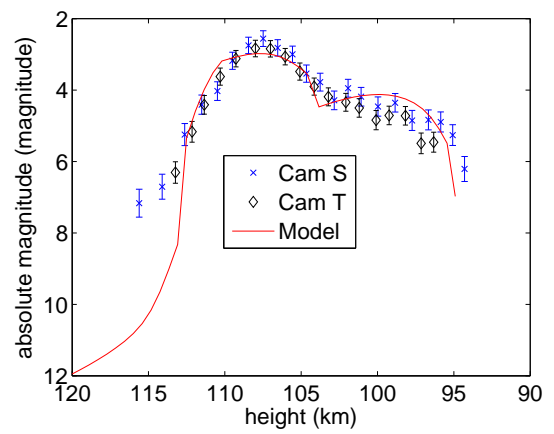
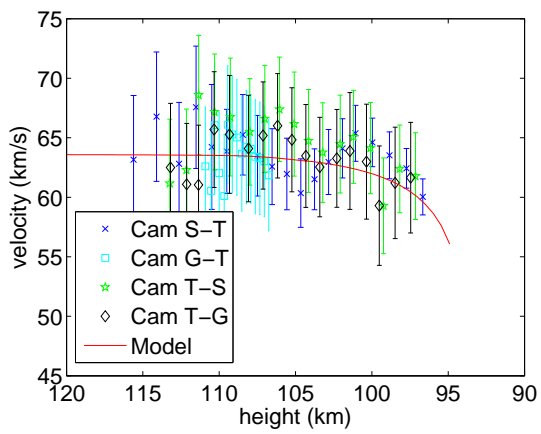
20070813-084901



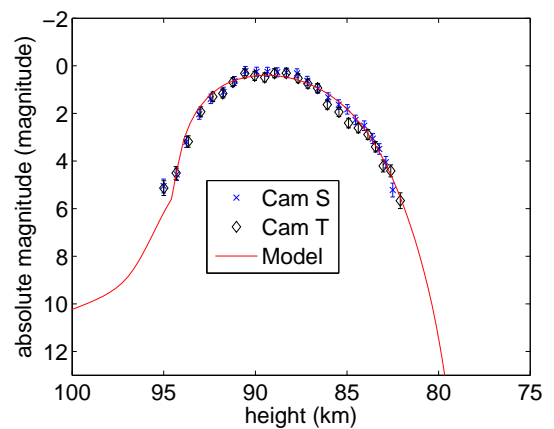
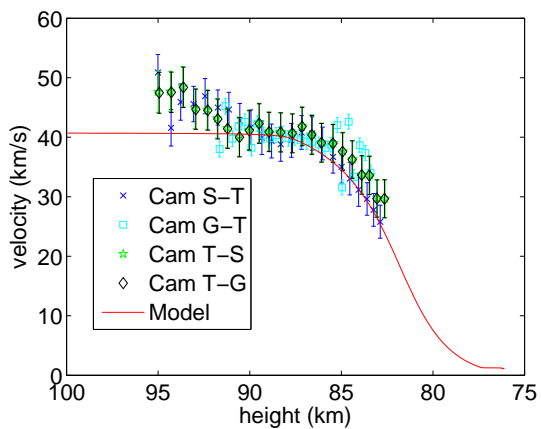
20070813-085448



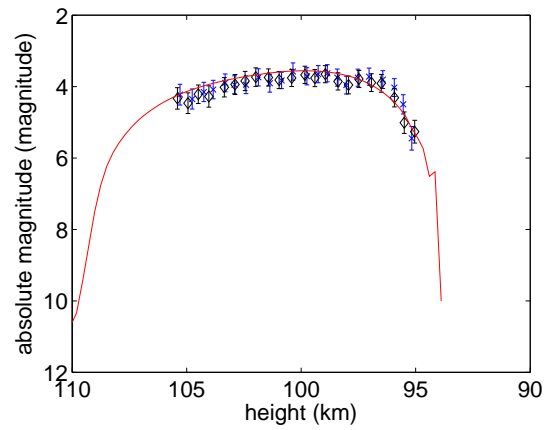
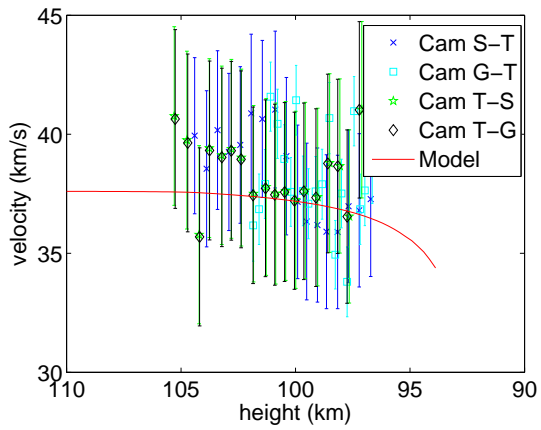
20070813-085457



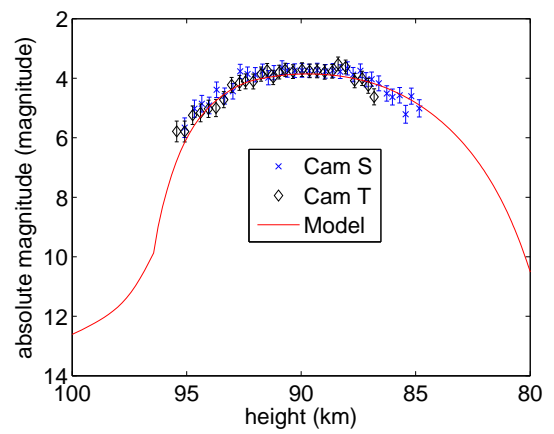
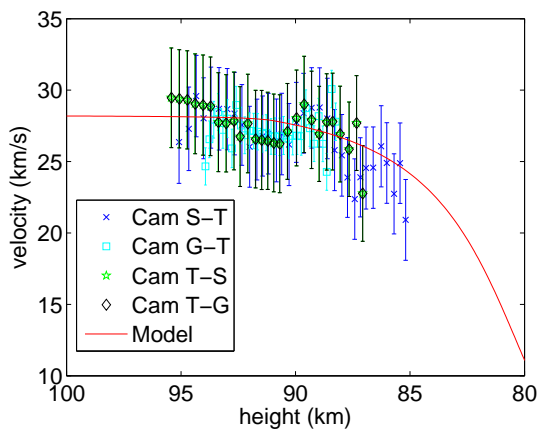
20070813-085548



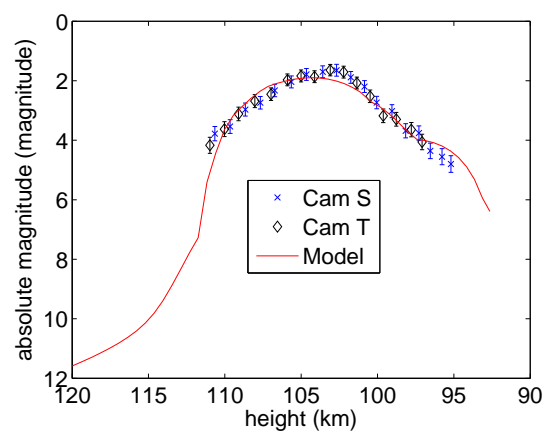
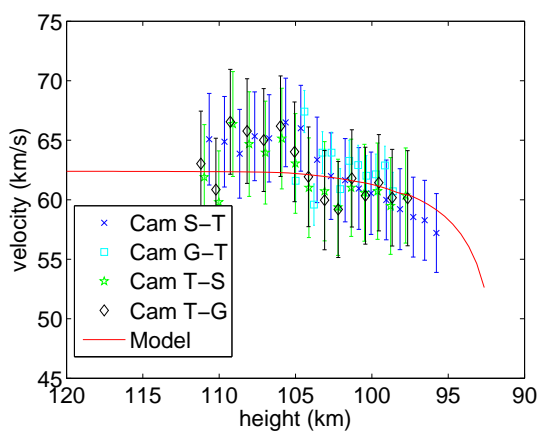
20080910-052352



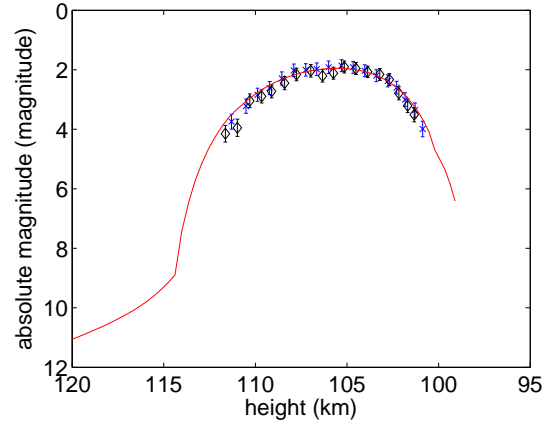
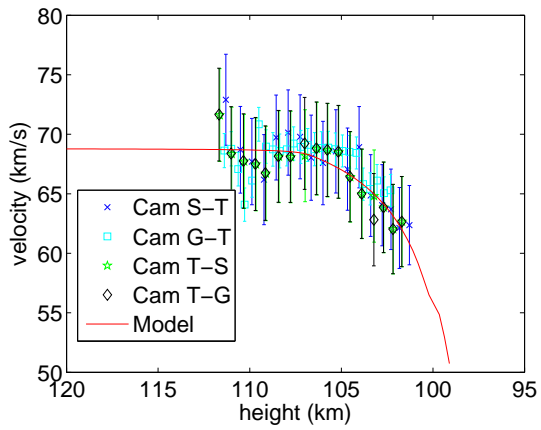
20080910-053428



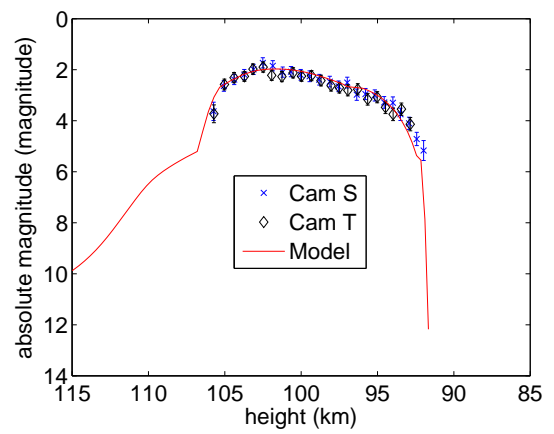
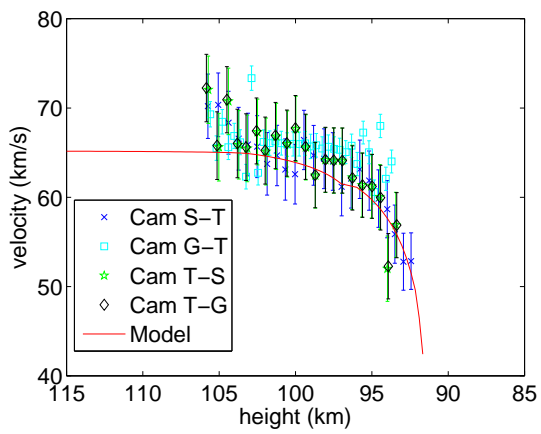
20080910-064102



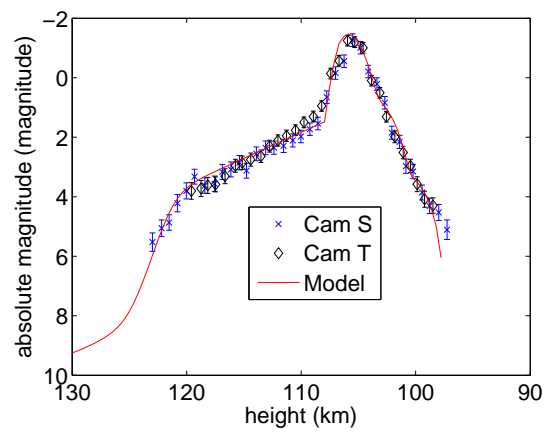
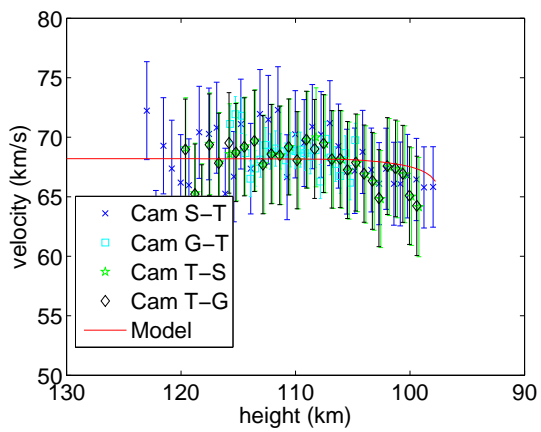
20080910-075255



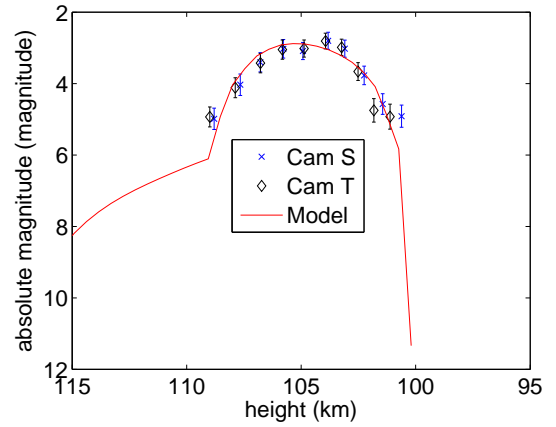
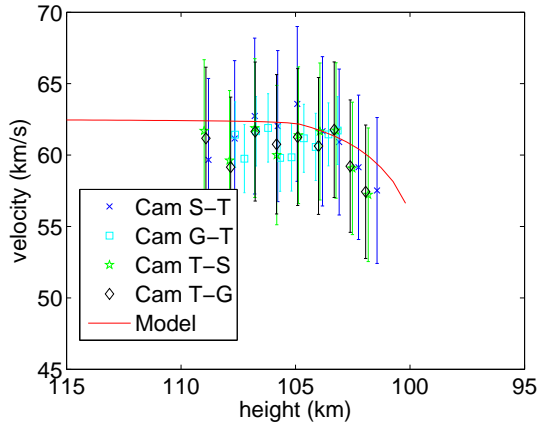
20080910-075454



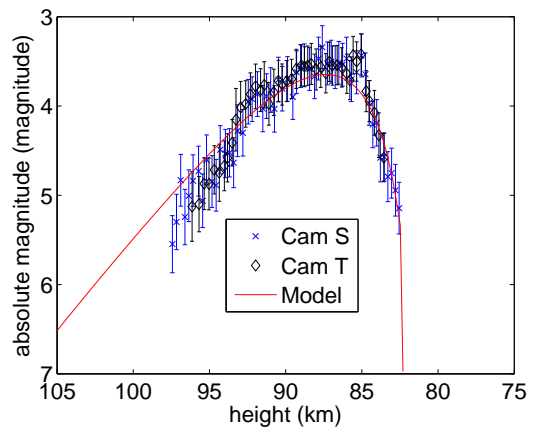
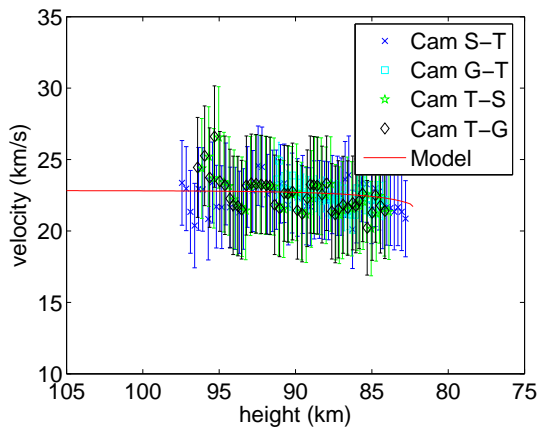
20080910-091403



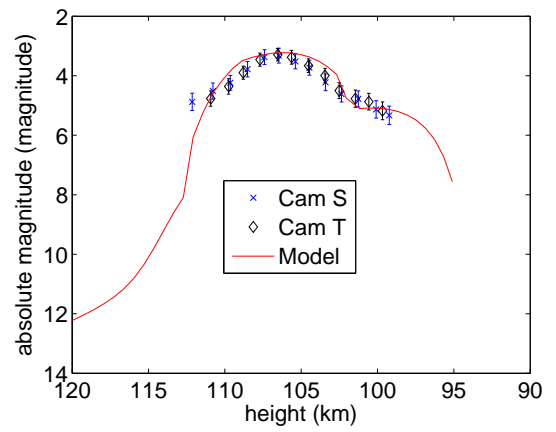
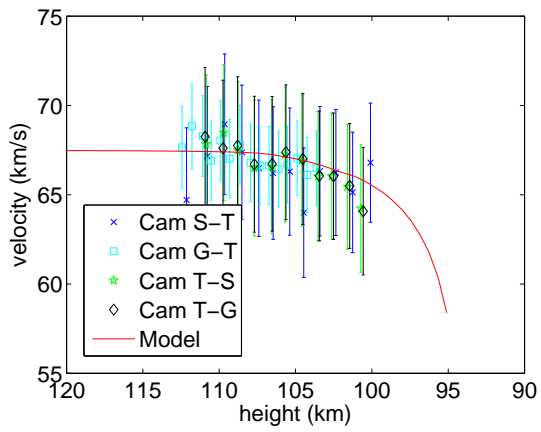
20080911-060638



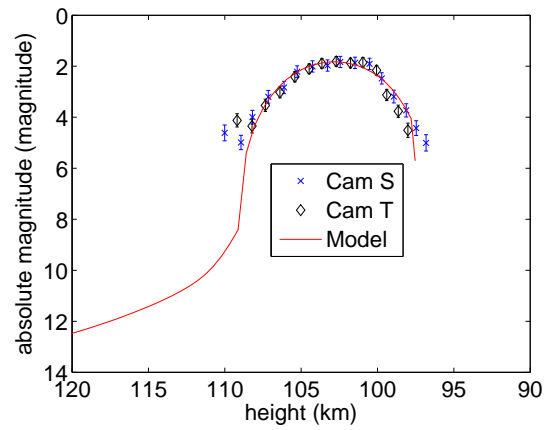
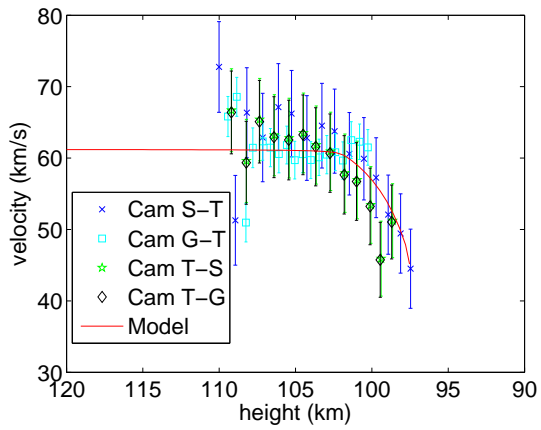
20080911-065211



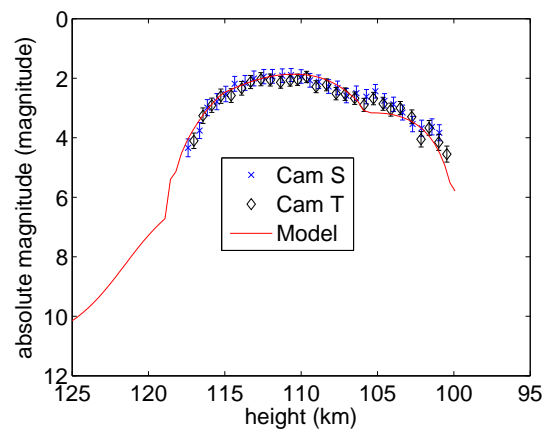
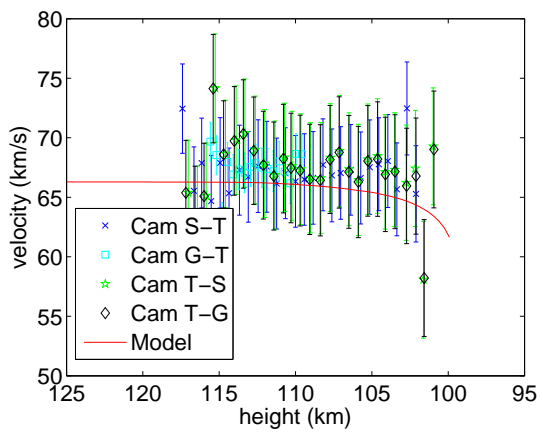
20080911-071428



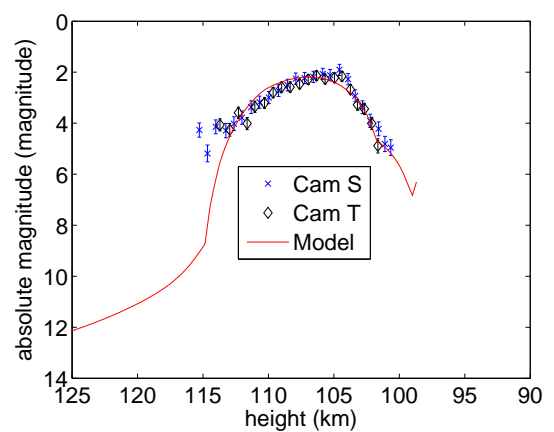
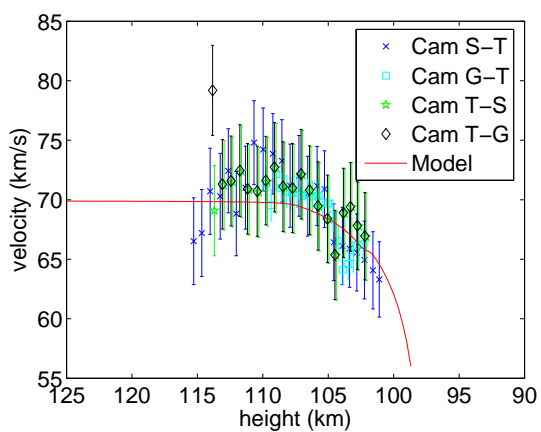
20080911-075207



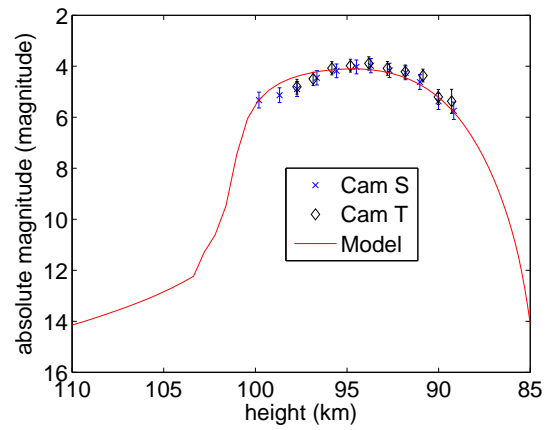
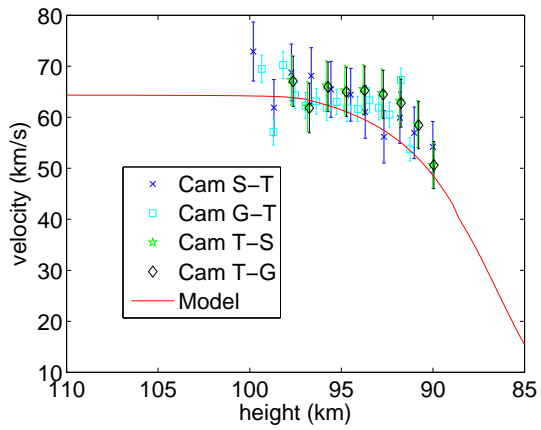
20080911-075323



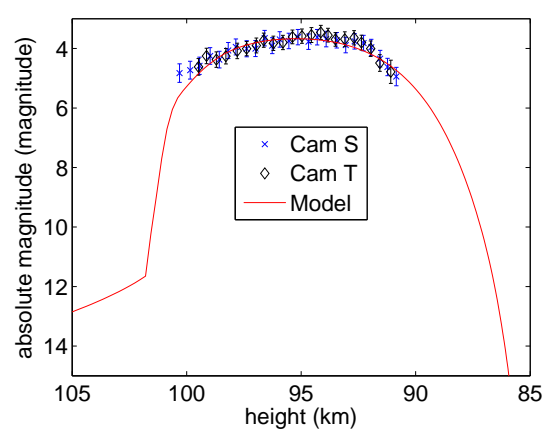
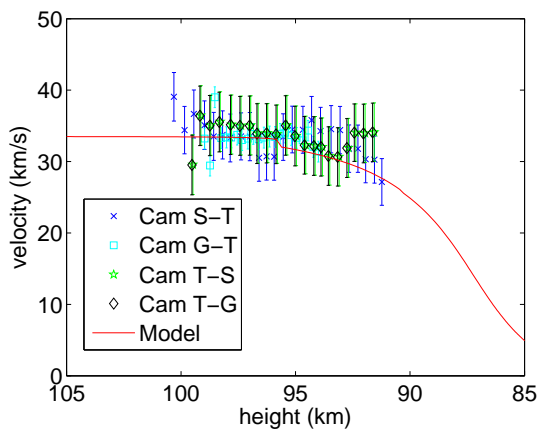
20080911-075846



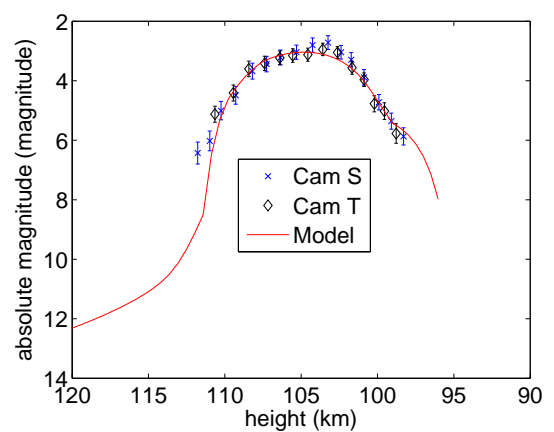
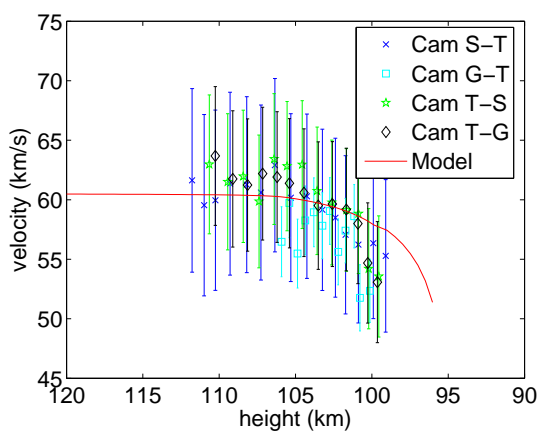
20080911-081630



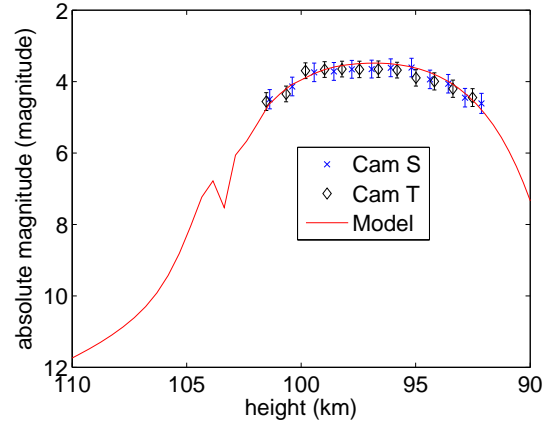
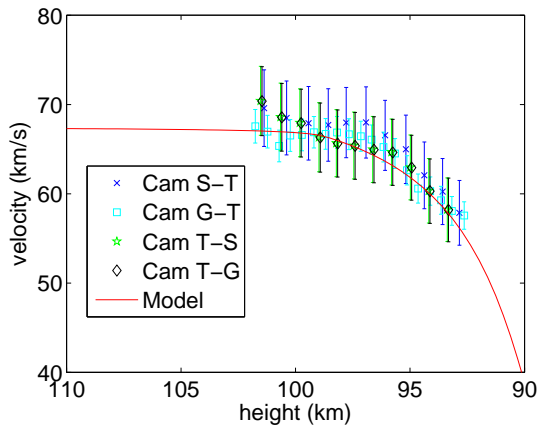
20080911-084108



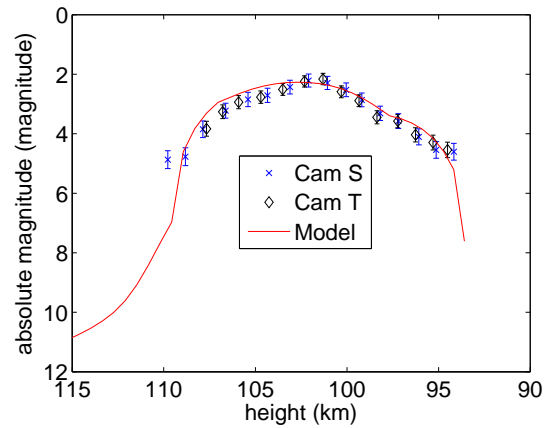
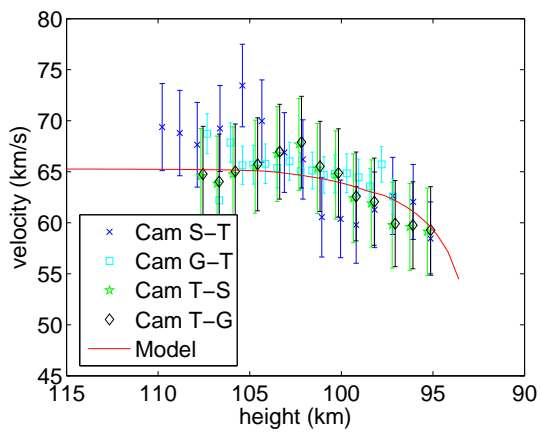
20080911-084529



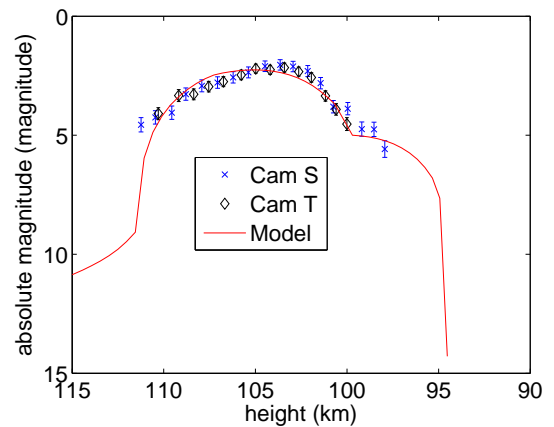
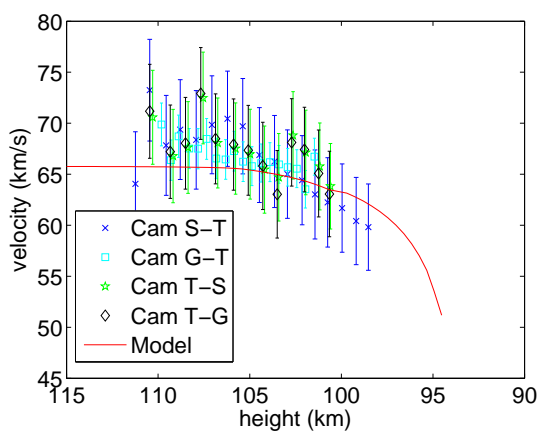
20080911-084739



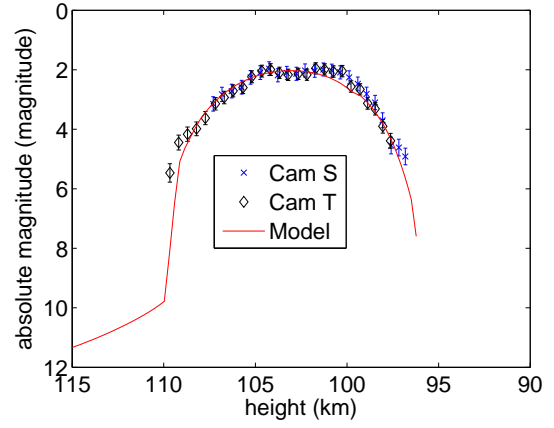
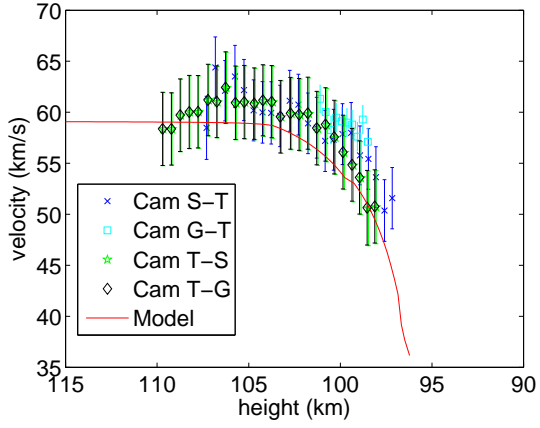
20080911-085605



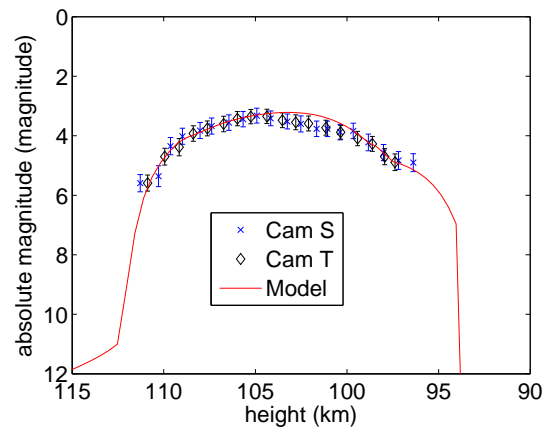
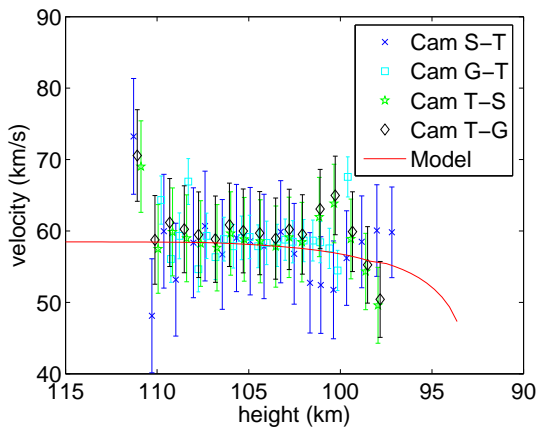
20080911-090242



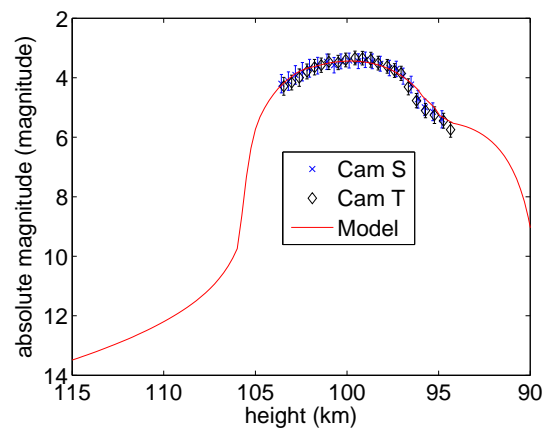
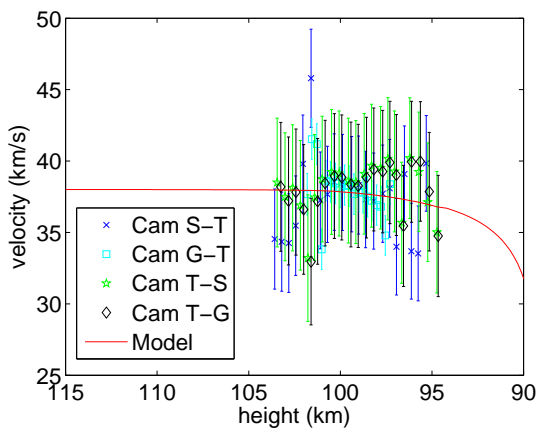
20080911-090512



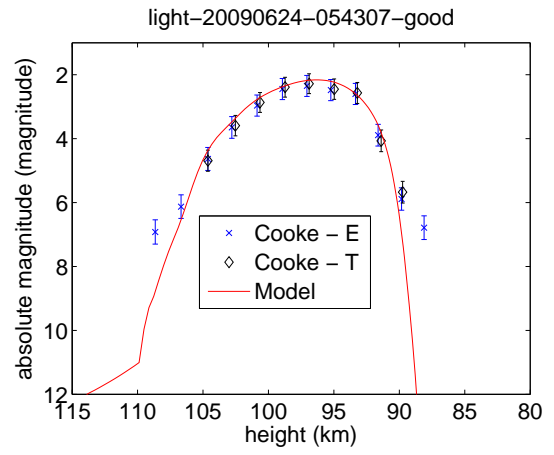
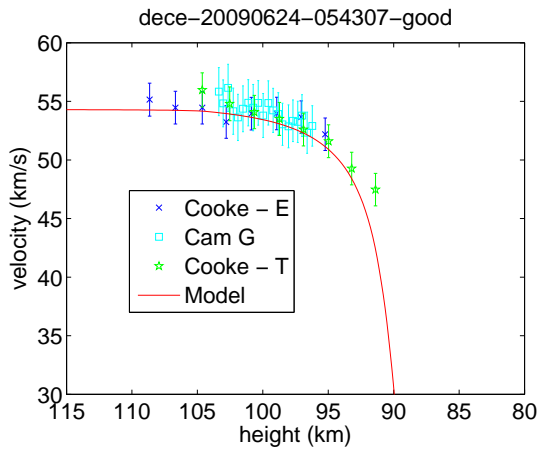
20080911-093436



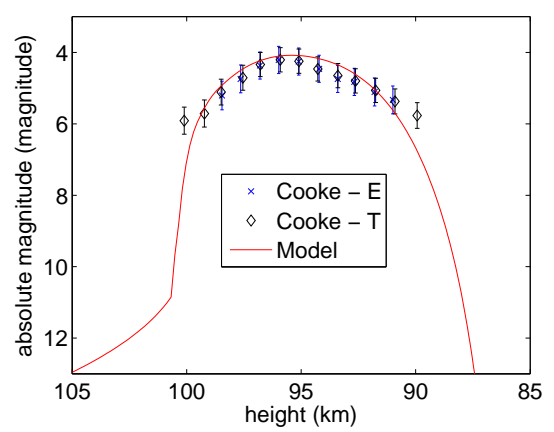
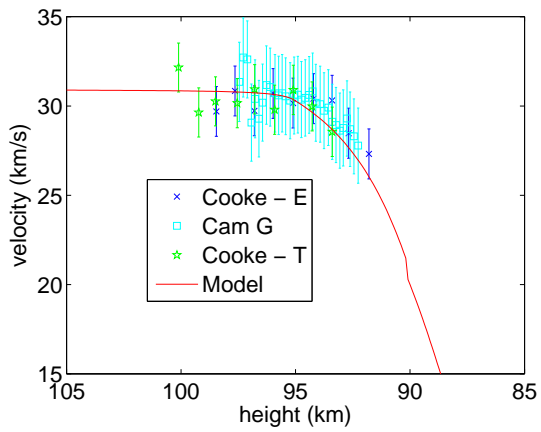
20080911-094752



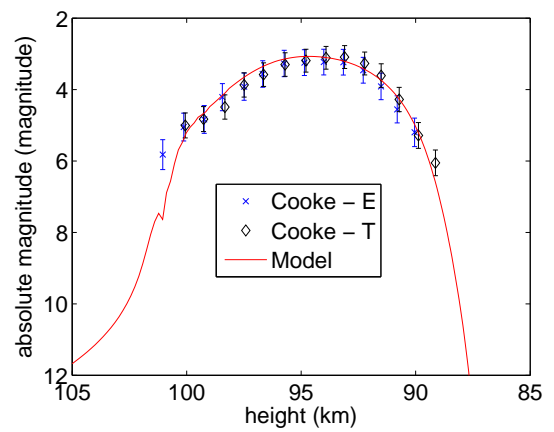
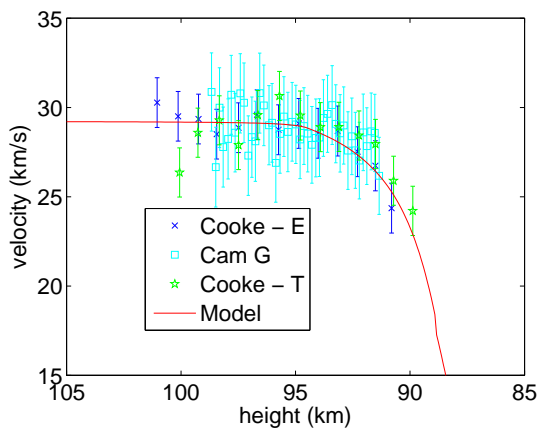
20080911-094844



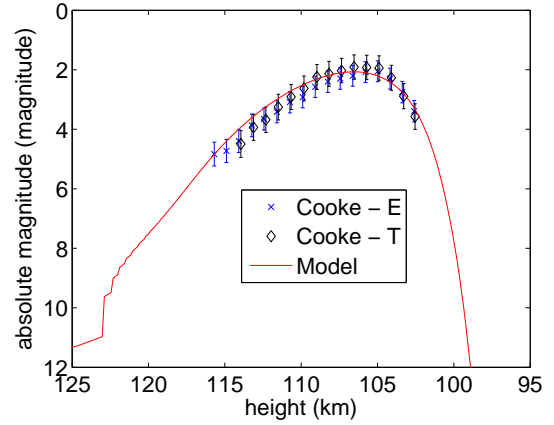
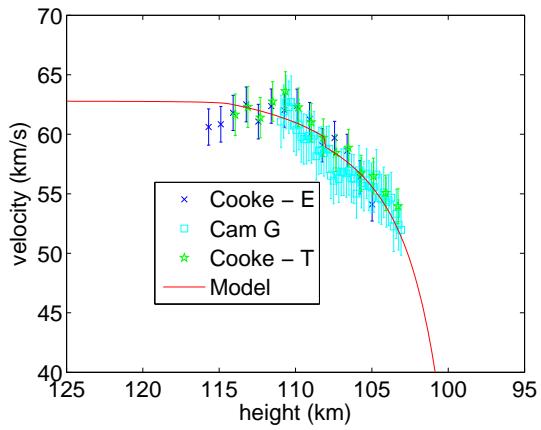
20090624-054307



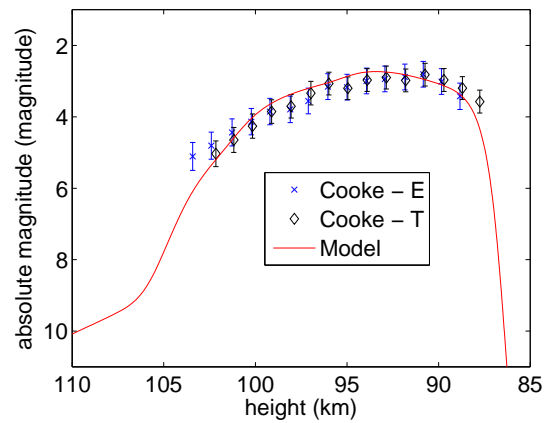
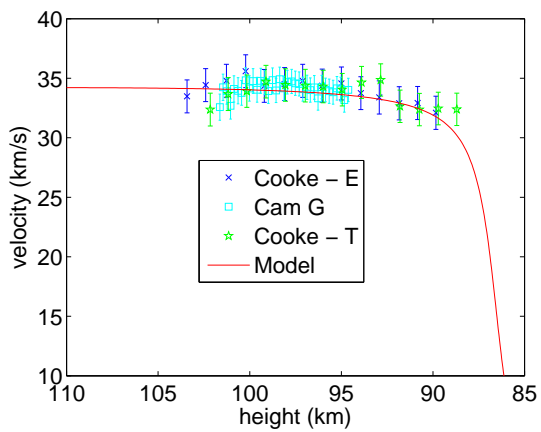
20090825-033603



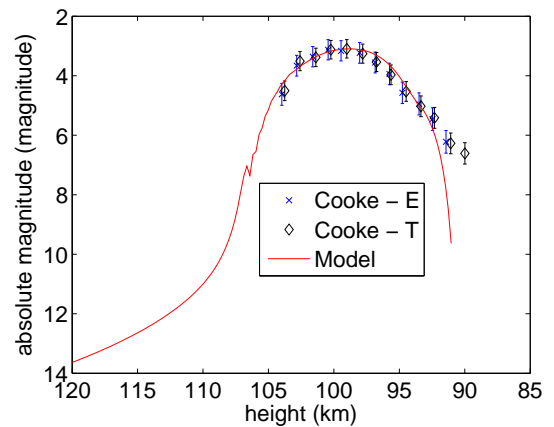
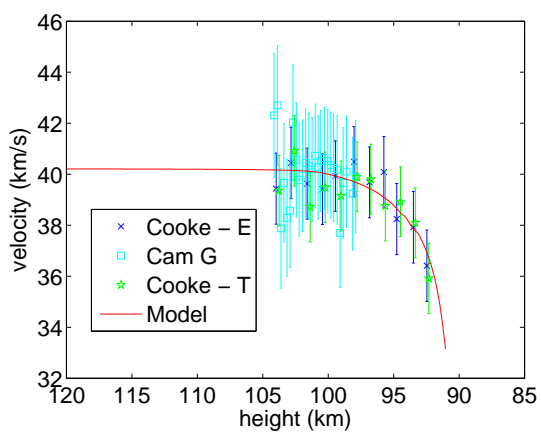
20090825-035228



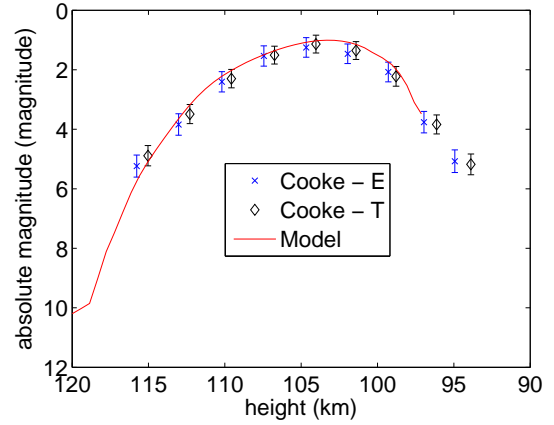
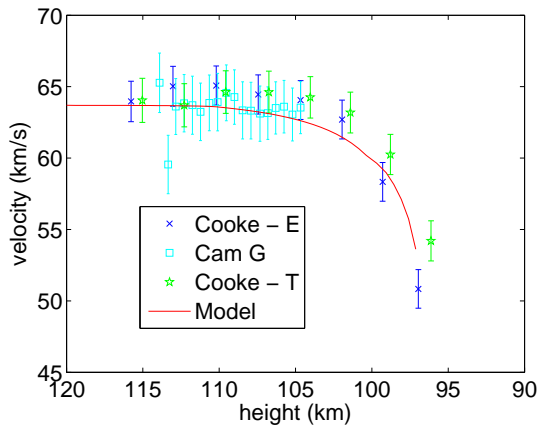
20090825-040835



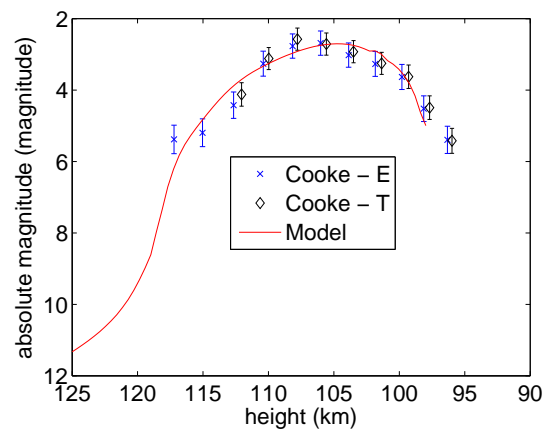
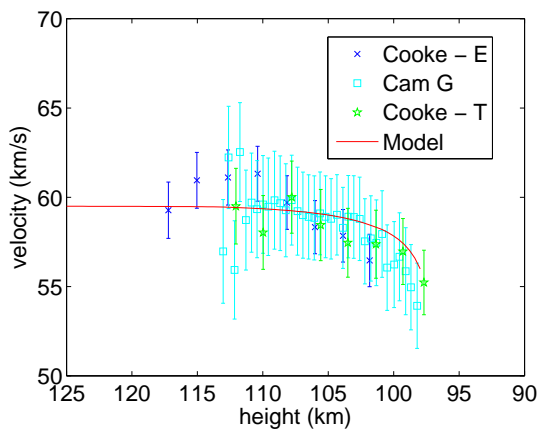
20090825-043435



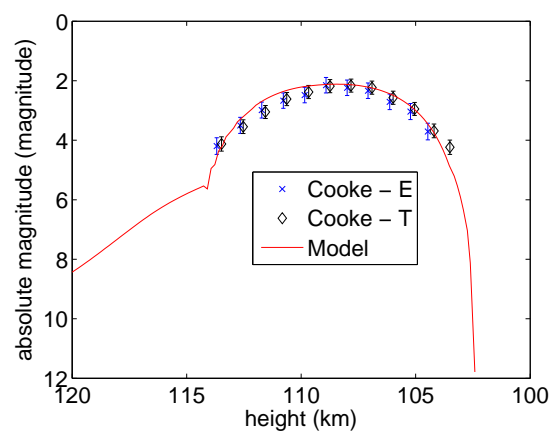
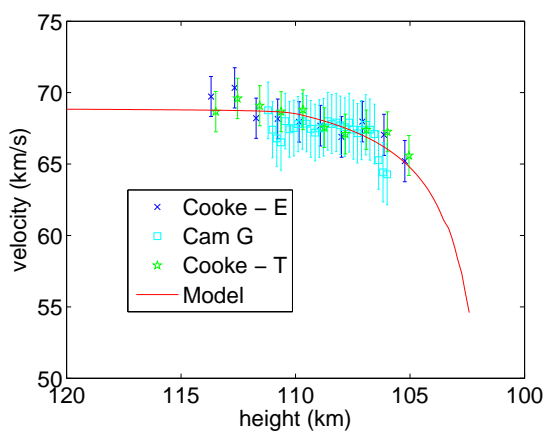
20090825-053106



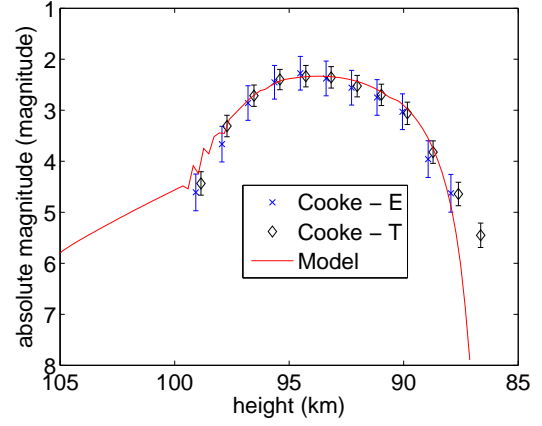
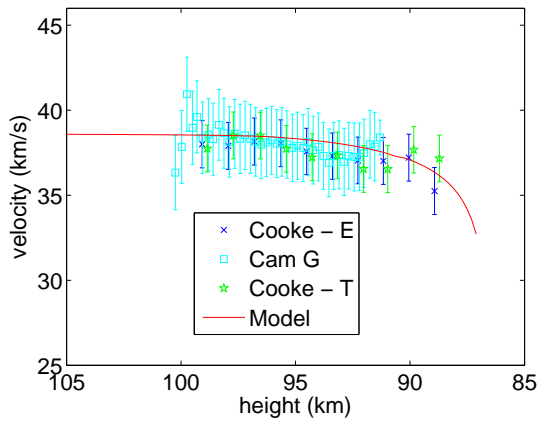
20090825-063604



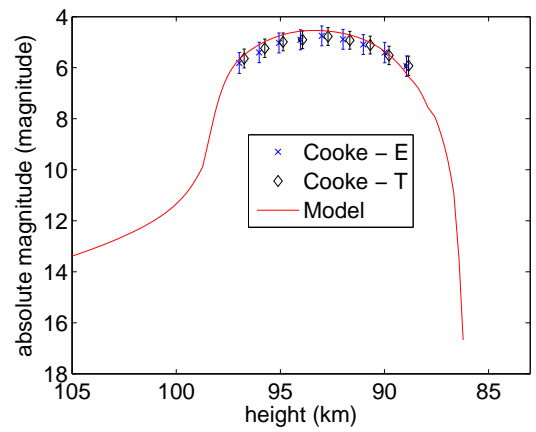
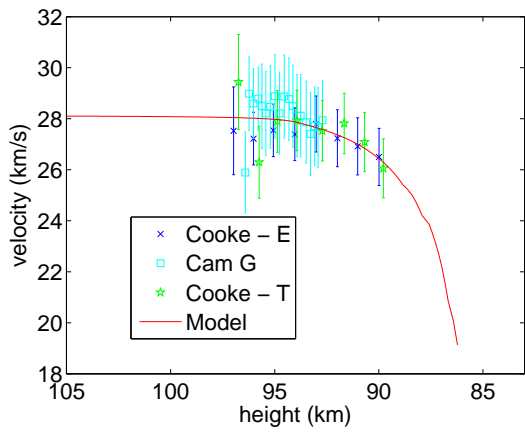
20090825-063641



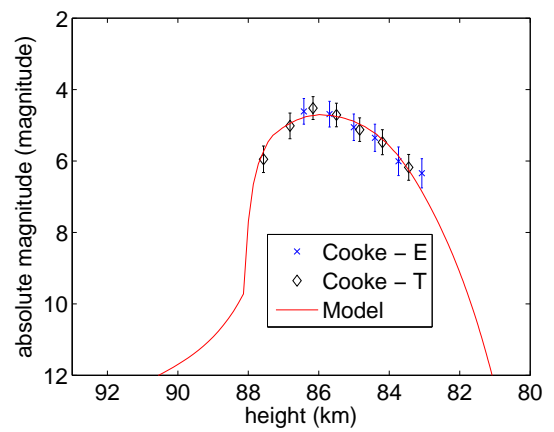
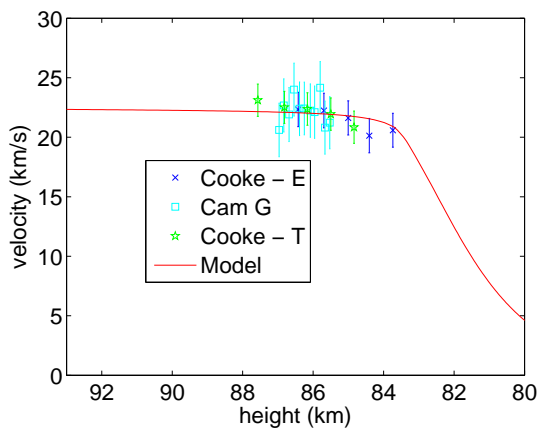
20090825-064646



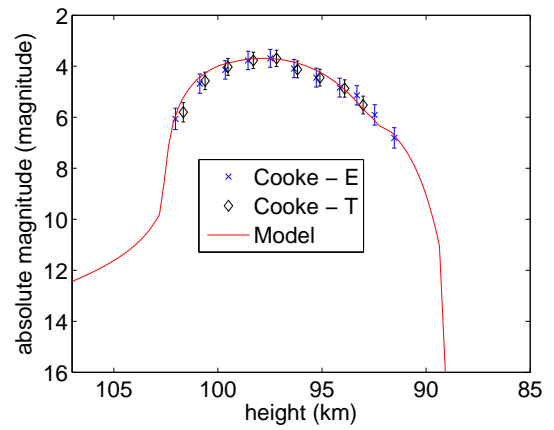
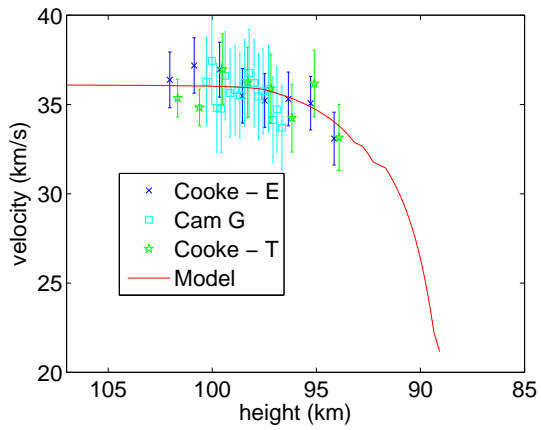
20090825-065903



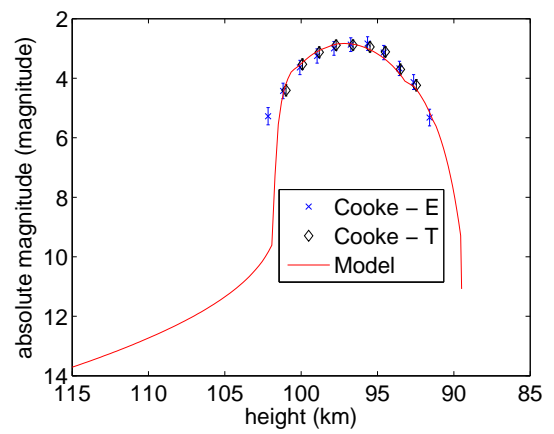
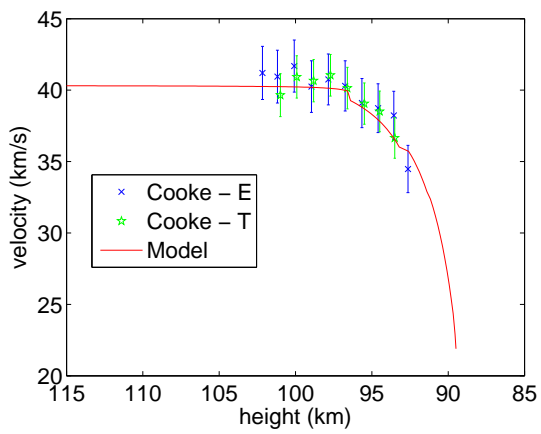
20090825-070044



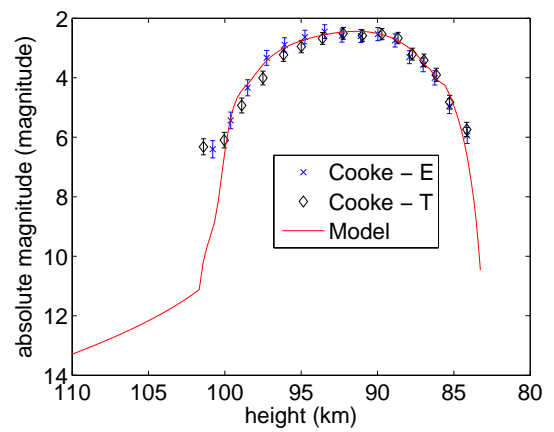
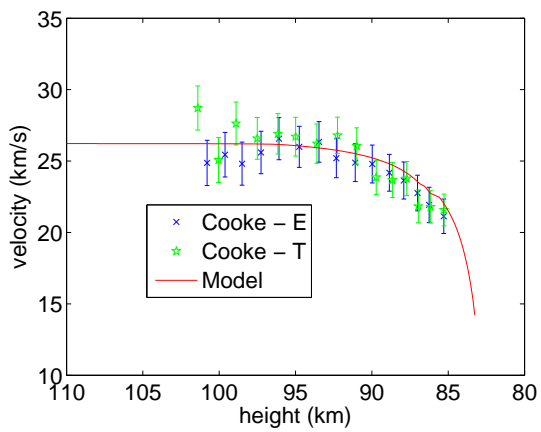
20090825-081927



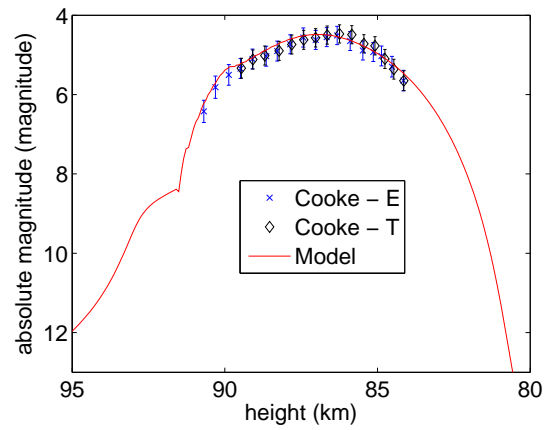
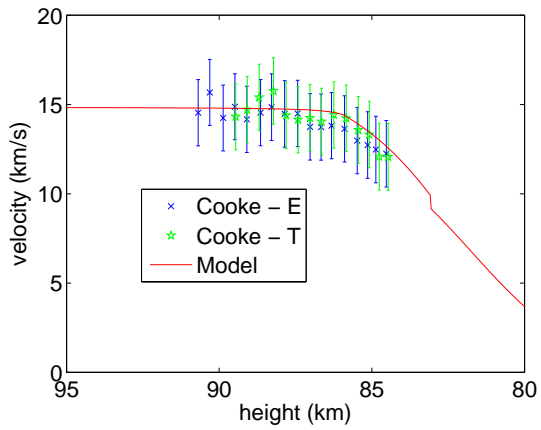
20090825-091030



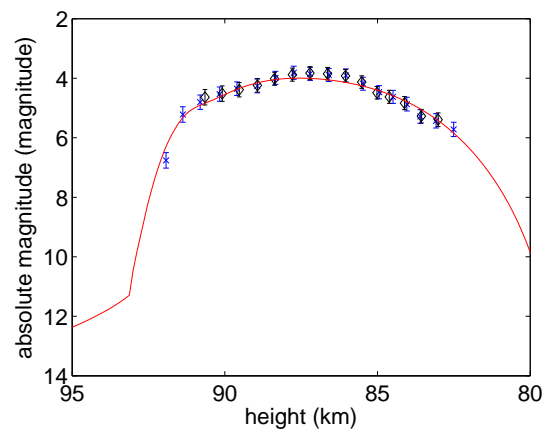
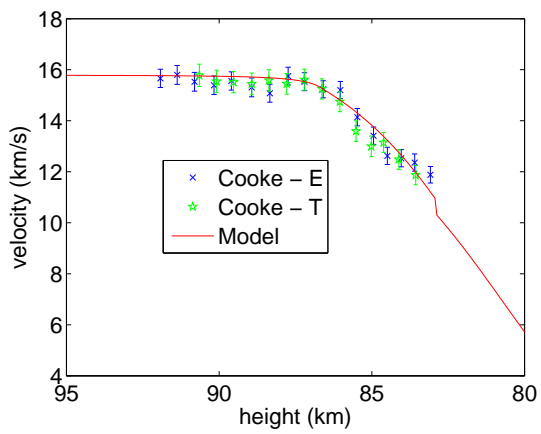
20090625-053313



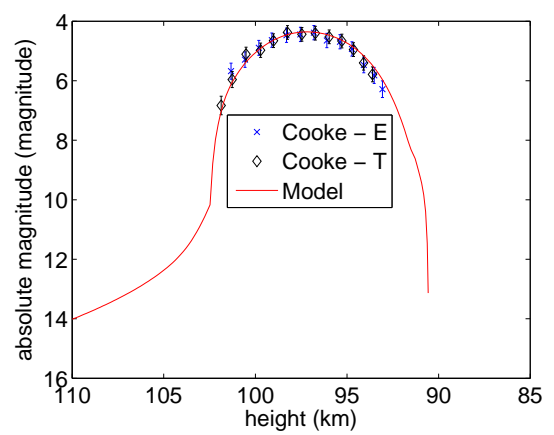
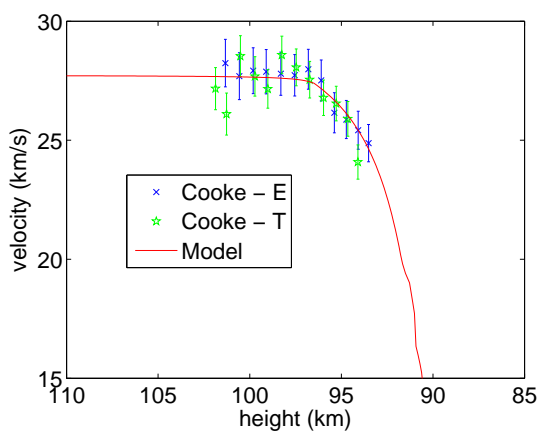
20090820-014058



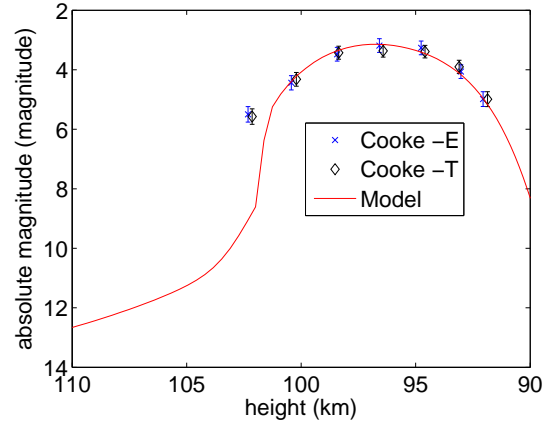
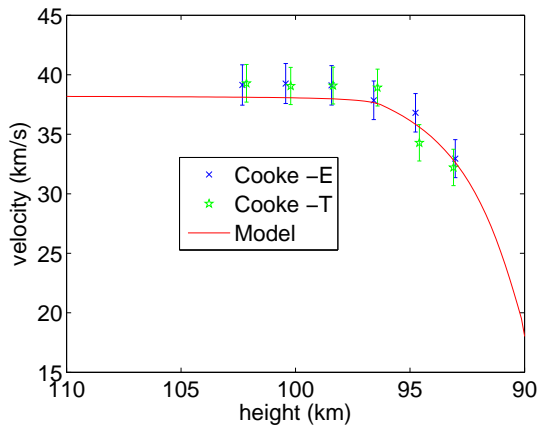
20090825-032616



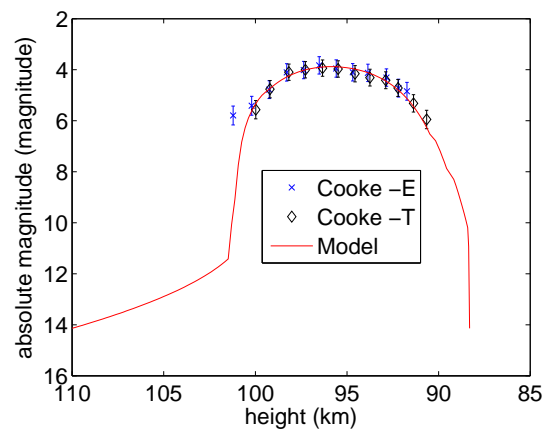
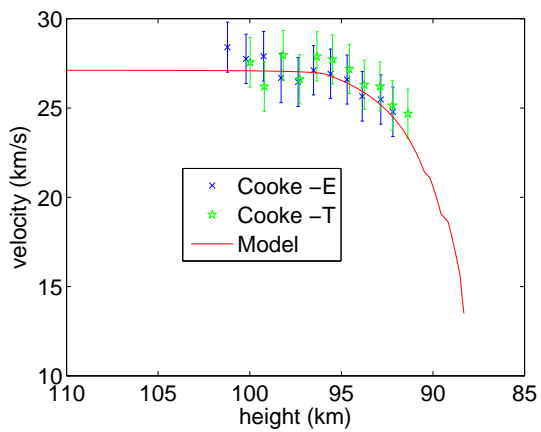
20090825-034528



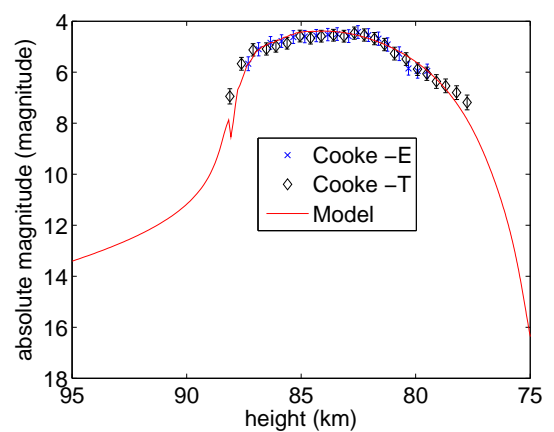
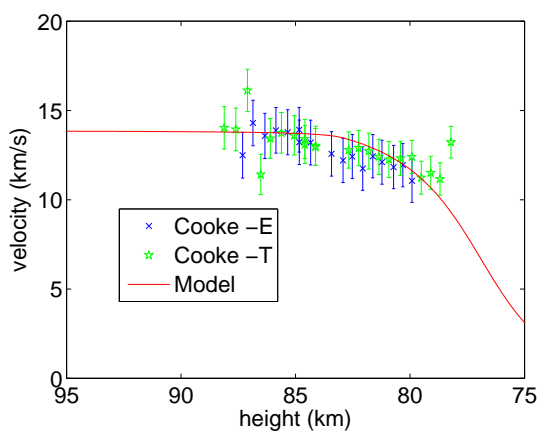
20090825-035145



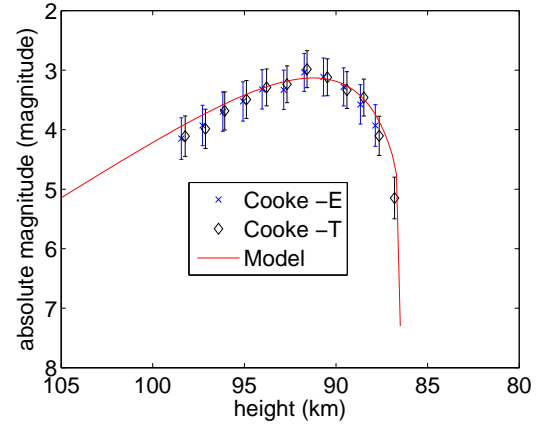
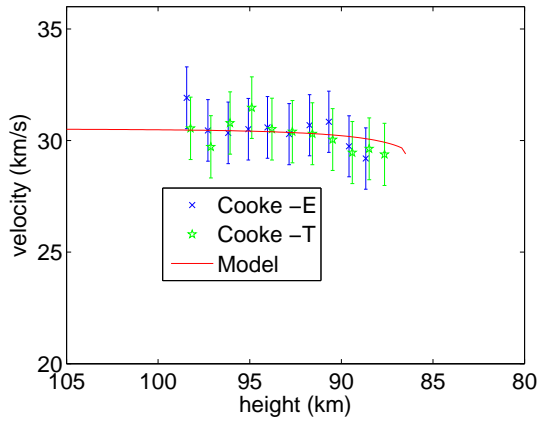
20090825-040603



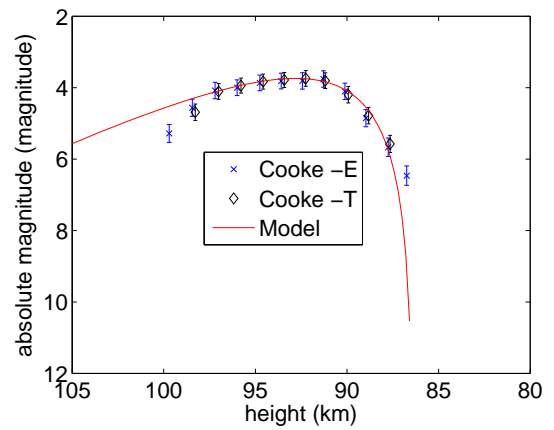
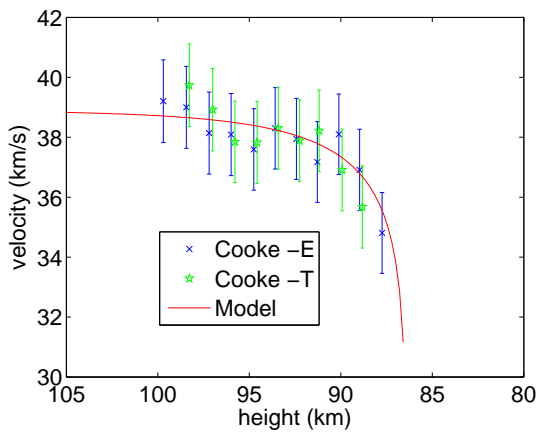
20090825-050631



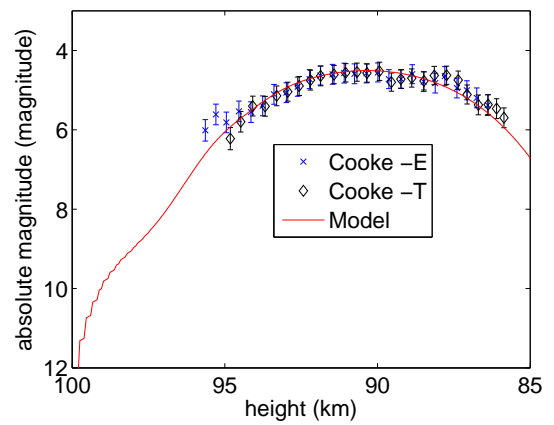
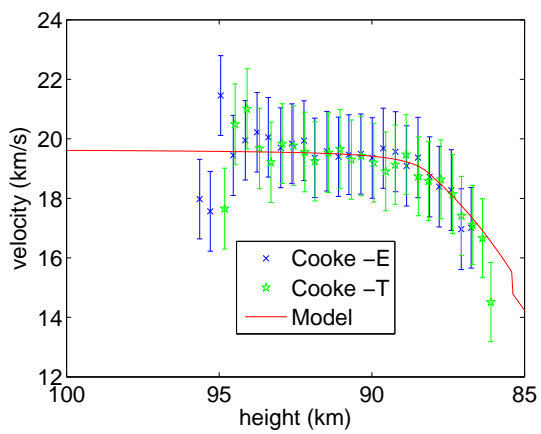
20090825-050904



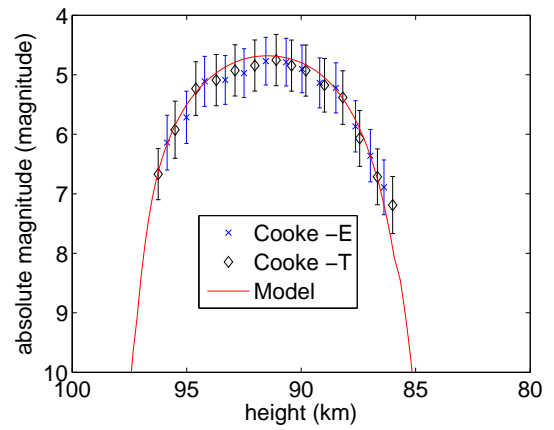
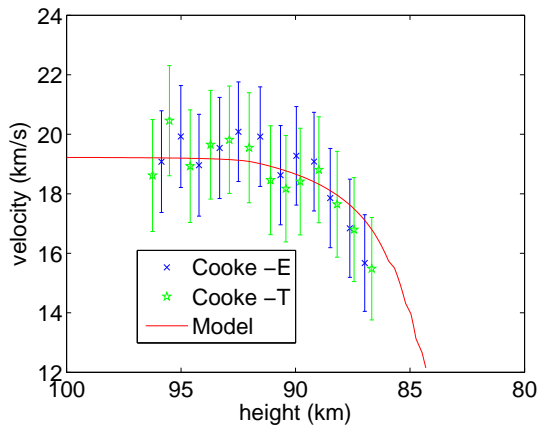
20090825-060500



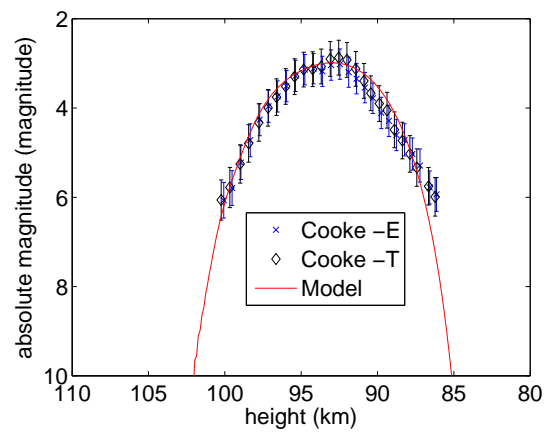
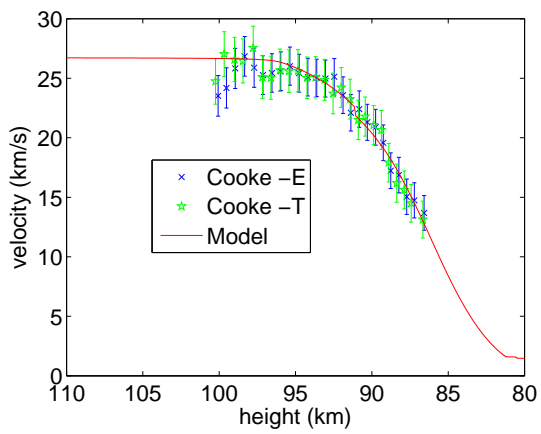
20090825-061542



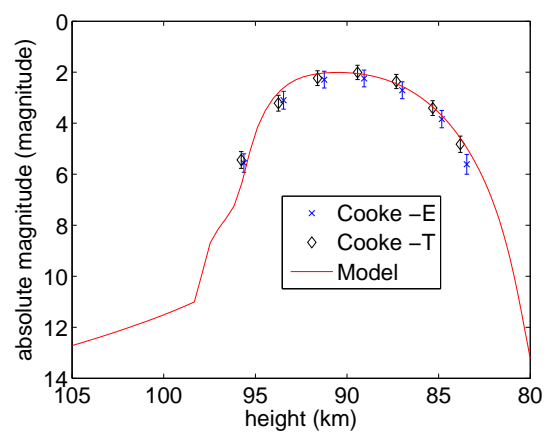
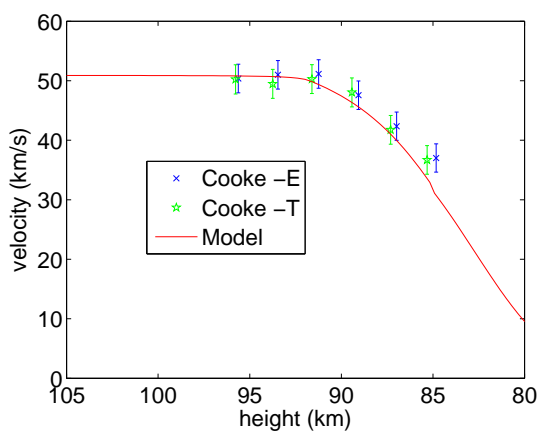
20090825-070933



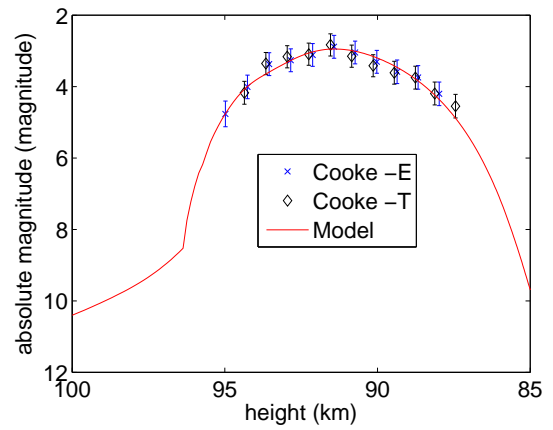
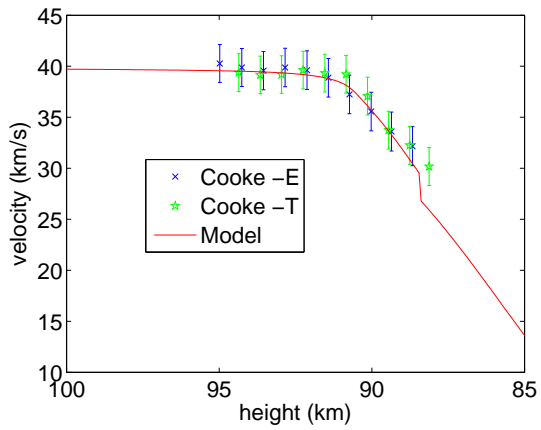
20090826-020835



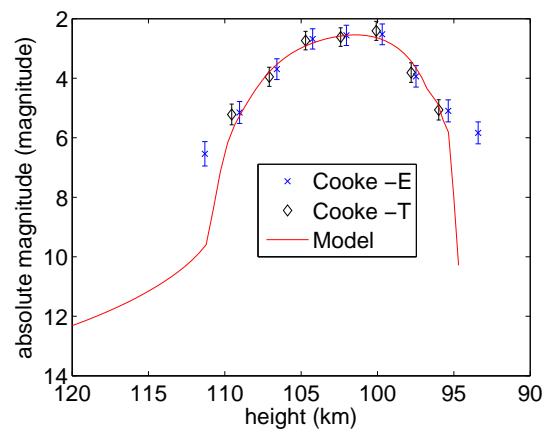
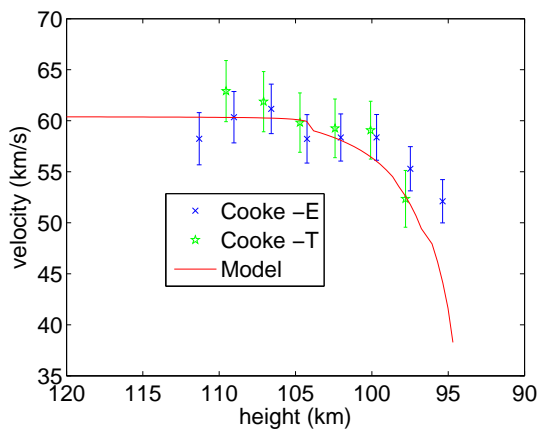
20090902-084143



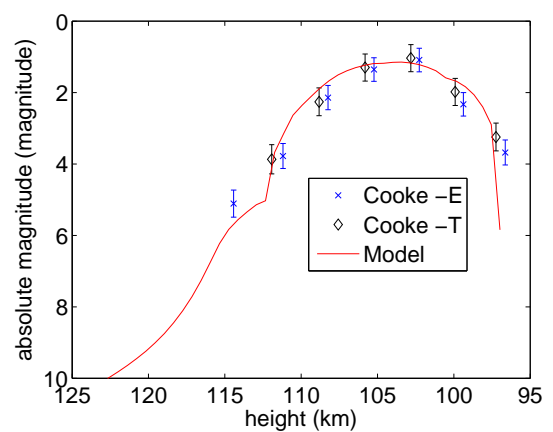
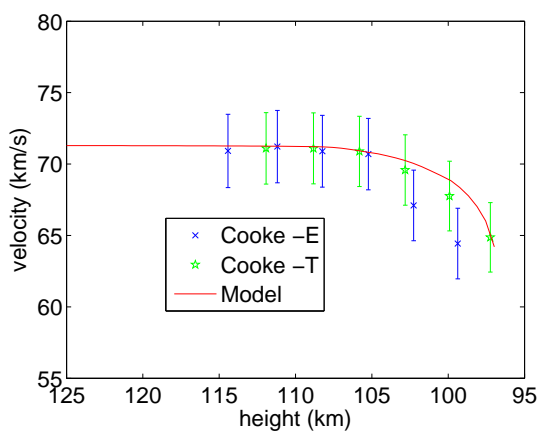
20090902-085534



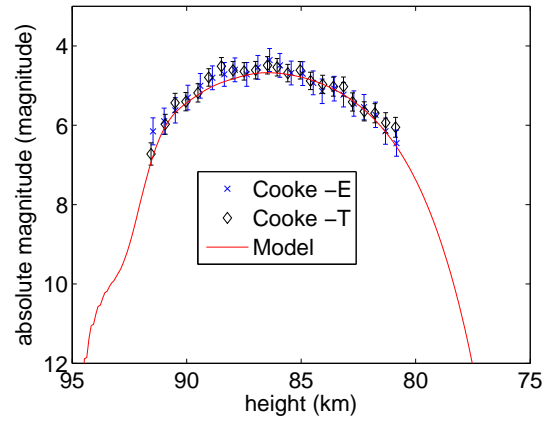
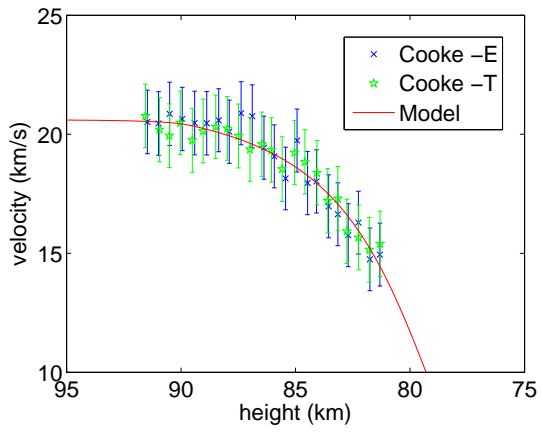
20090902-085832



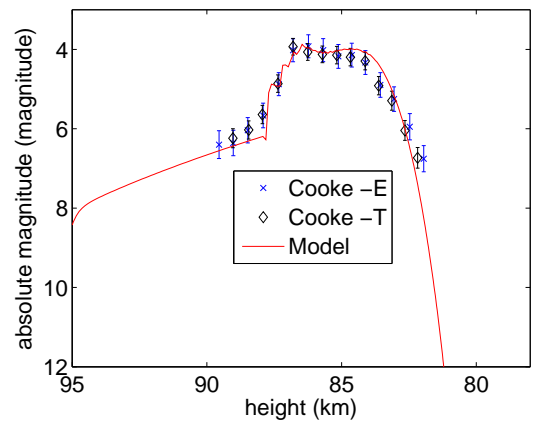
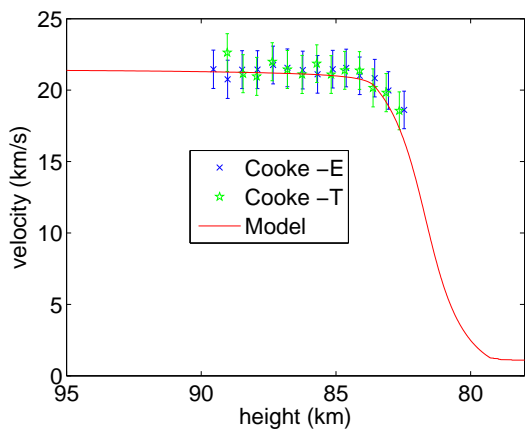
20090902-092028



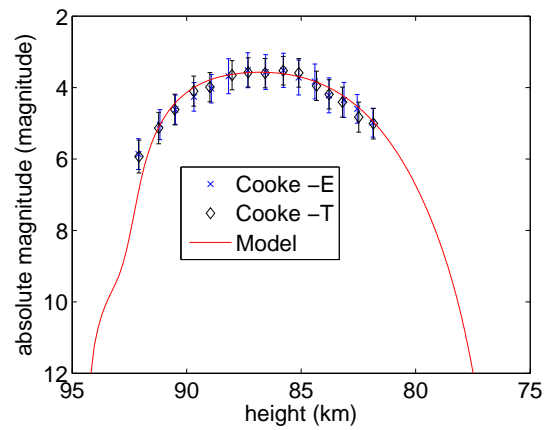
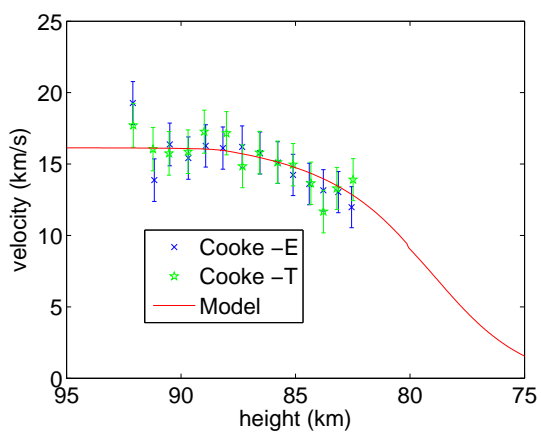
20090902-093338



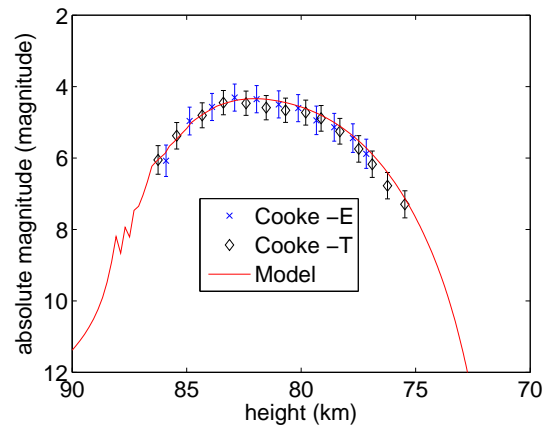
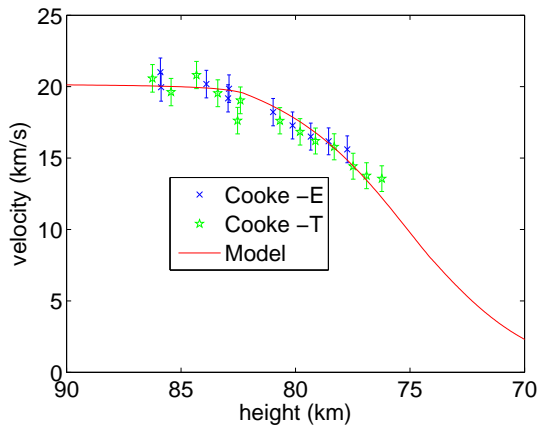
20090909-010643



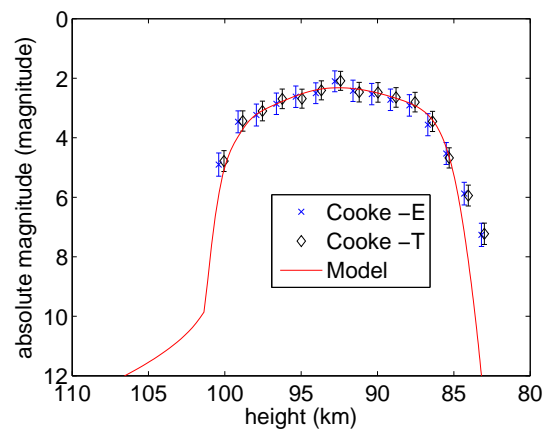
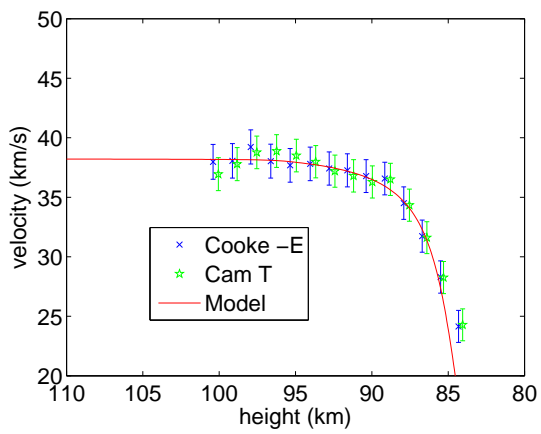
20090909-012810



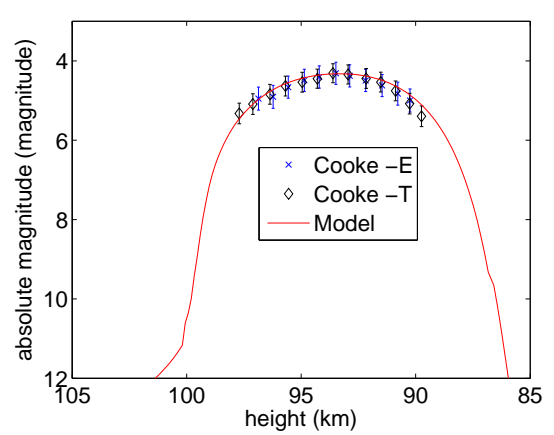
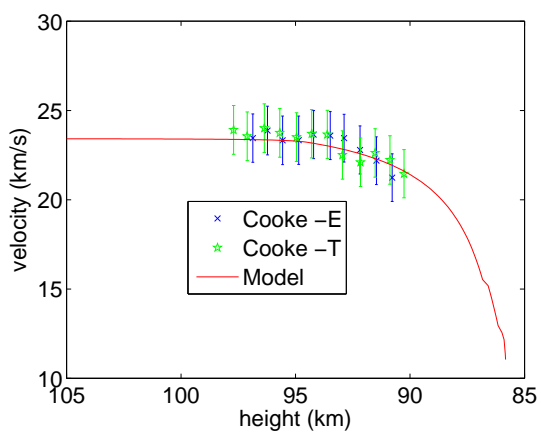
20090909-013647



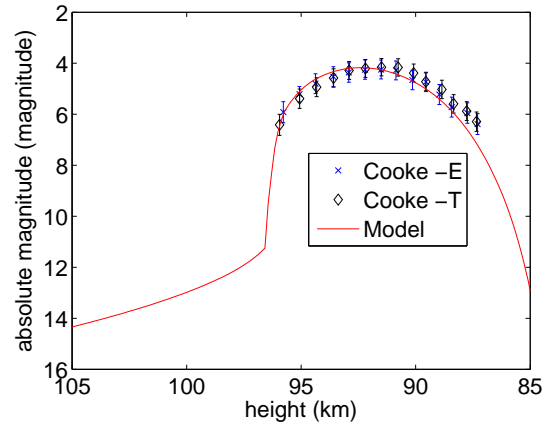
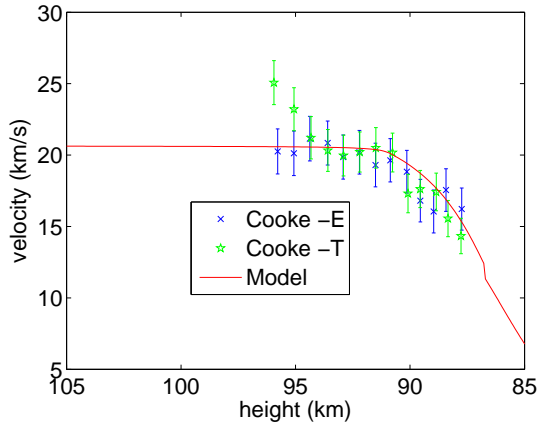
20090911-021830



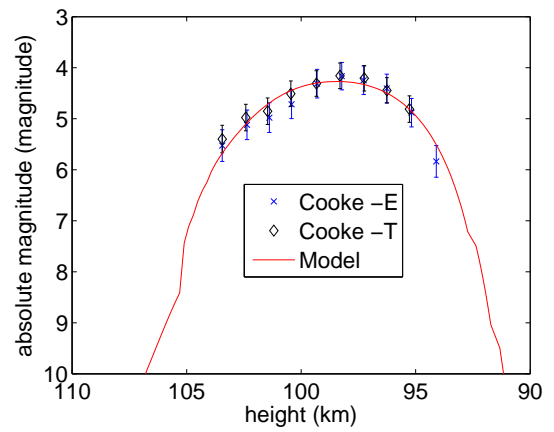
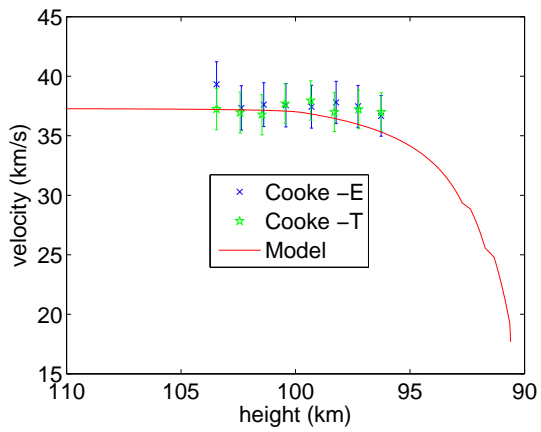
20090911-030523



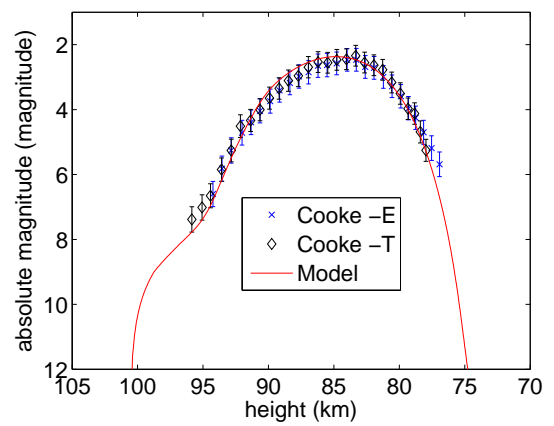
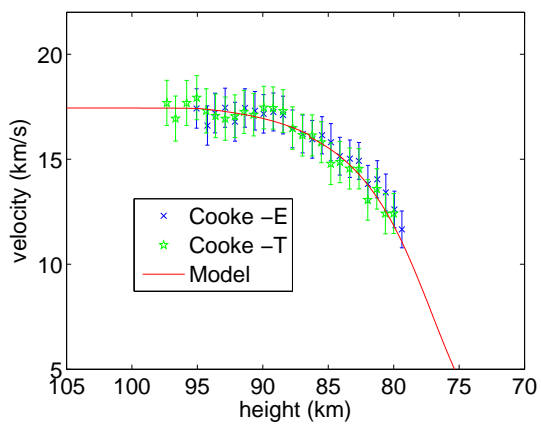
20090911-034442



20090911-035942



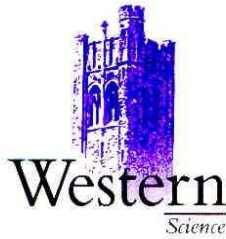
20090911-040233



20090911-040433

Appendix C

Copyright Waivers & Permissions for Published Thesis Chapters



Tuesday, October 05, 2010

To Whom It May Concern:

Re: Copyright waiver for A&A manuscript for the purpose of thesis inclusion

I am currently a Ph.D. candidate in the Department of Physics and Astronomy at the University of Western Ontario and I am currently preparing the written portion of my dissertation prior to defense of my thesis. As part of this dissertation I would like to include the material I have previously published in the *Astronomy and Astrophysics* (A&A), specially the article:

- **Jean-Baptiste Kikwaya**, Campbell-Brown, Brown, P.G., Hawkes, R.L., Weryk R.J., 2009. Physical characteristics of very small meteoroids, doi: 10.1051/0004-6361/200810839.

If you could send to me an official copyright waiver for the preceding article it would be greatly appreciated.

Thank you for your time and understanding in this matter in advance.

Sincerely,

Jean-Baptiste Kikwaya

The University of Western Ontario
Department of Physics and Astronomy
Physics & Astronomy Building • London, Ontario • CANADA - N6A 3K7
PH: 519-661-3283 • F: 519-661-2033 • www.physics.uwo.ca

Astronomy and Astrophysics

Editor in Chief: C. Bertout

C. Bertout

merging
Annales d'Astrophysique
Arkiv for Astronomi
Bulletin of the Astronomical Institutes
of the Netherlands
Bulletin Astronomique
Journal des Observateurs
Zeitschrift für Astrophysik
Bulletin of the Astronomical Institutes
of Czechoslovakia

Paris, October 11, 2010

Reprint Permission

Material:

Article by Kikwaya et al. 2009, A&A, 497, 851

To be used in:

Ph.D. thesis of the Department of Physics and Astronomy at the University of Western Ontario

Permission granted to:

Jean-Baptiste Kikwaya

I hold copyright on the material referred to above, and hereby grant permission for its use as requested herewith. The credit should be given as follows:

Credit: Author, A&A, vol, page, year, reproduced with permission © ESO.

Claude Bertout
A&A Editor-in-Chief

Sponsored by Argentina, Austria, Belgium, Brazil, Chile, Czech Republic, Denmark, Estonia, Finland, France, Germany, Greece, Hungary, Italy, Netherlands, Poland, Portugal, Slovak Republic, Spain, Sweden, and Switzerland.
Produced and distributed by EDP Sciences for ESO.

Subject: **Permission**

Date: 10/13/10 11:59 AM

Hi,

You are co-author of the following article published in the Astronomy and Astrophysics (A&A):

- **Jean-Baptiste Kikwaya**, Campbell-Brown, Brown, P.G., Hawkes, R.L., Weryk R.J., 2009. Physical characteristics of very small meteoroids, doi: 10.1051/0004-6361/200810839.

I would like to include the article as part of my thesis. If you could send me an official permission it would be greatly appreciated. Mostly, you would have to mention in detail your participation to the article.

Thanks,
Jean-Baptiste

Subject: **Re: Permission**

Date: 10/13/10 12:24 PM

I give my permission for you to use this paper in your thesis. I advised on the research, and gave feedback on the writing of the paper.

Margaret Campbell-Brown

On 13/10/2010 11:59 AM, Jean-Baptiste Kikwaya Eluo wrote:

Hi,

You are co-author of the following article published in the Astronomy and Astrophysics (A&A):

- **Jean-Baptiste Kikwaya**, Campbell-Brown, Brown, P.G., Hawkes, R.L., Weryk R.J., 2009. Physical characteristics of very small meteoroids, doi: 10.1051/0004-6361/200810839.

I would like to include the article as part of my thesis. If you could send me an official permission it would be greatly appreciated. Mostly, you would have to mention in detail your participation to the article.

Thanks,
Jean-Baptiste

--

Subject: **permission**

Date: 01/06/11 07:35 PM

I give my permission for you to use this paper in your thesis. I advised on the research, and gave feedback on the writing of the paper.

Peter Brown

2011 01 07

Subject: **Re: Permission**

Date: 10/13/10 12:16 PM

Hi Jean-Baptiste,

You certainly have my permission to include it in your thesis.

My main contribution to the work was with respect to development of the system to collect the data, and being part of the team that collected the data.

I did not have any significant role in the data analysis or the model aspects of the paper, nor in the actual writing.

I hope that all is well with you.

Bob

On 2010-10-13, at 12:59 PM, Jean-Baptiste Kikwaya Eluo wrote:

Hi,

You are co-author of the following article published in the Astronomy and Astrophysics (A&A):

- **Jean-Baptiste Kikwaya**, Campbell-Brown, Brown, P.G., Hawkes, R.L., Weryk R.J., 2009. Physical characteristics of very small meteoroids, doi: 10.1051/0004-6361/200810839.

I would like to include the article as part of my thesis. If you could send me an official permission it would be greatly appreciated. Mostly, you would have to mention in detail your participation to the article.

Thanks,
Jean-Baptiste

December 9th, 2010

To whom it may concern,

With regards to the article "Physical characteristics of very small meteoroids" by Kikwaya et al., my main involvement was to collect the data from the Finland observing station, and for the development of the analysis software used to measure both astrometric and photometric quantities.

I was involved in a very small role in the writing, mostly as a consultant to Mr. Kikwaya to explain the operating of the program code.

Rob Weryk



Tuesday, October 05, 2010

To Whom It May Concern:

Re: Copyright waiver for MNRAS manuscript for the purpose of thesis inclusion

I am currently a Ph.D. candidate in the Department of Physics and Astronomy at the University of Western Ontario and I am currently preparing the written portion of my dissertation prior to defense of my thesis. As part of this dissertation I would like to include the material I have previously published in the Monthly Notices of the Royal Astronomical Society (MNRAS), specially the article:

- **Jean-Baptiste Kikwaya**, Weryk R.J., Campbell-Brown, Brown, P.G., 2010. A model for saturation correction in meteor photometry, MNRAS, doi: 10.1111/j.1365-2966.2010.16294.x

If you could send to me an official copyright waiver for the preceding article it would be greatly appreciated.

Thank you for your time and understanding in this matter in advance.

Sincerely,

Jean-Baptiste Kikwaya

The University of Western Ontario
Department of Physics and Astronomy
Physics & Astronomy Building • London, Ontario • CANADA - N6A 3K7
PH: 519-661-3283 • F: 519-661-2033 • www.physics.uwo.ca

Bella Lock
Envoyé: Jeudi 7 Octobre 2010 10h26:39 GMT -05:00 US A/Canada - États de l'Est
Objet: RE: Copyright waiver for MNRAS manuscript for the purpose of thesis inclusion

Dear Jean-Baptiste,

Thank you for your email. As you are using material from your own paper you do not need permission. Also, permission does not need to be sought to reproduce figures in dissertations or reports which form part of the requirements for university qualifications, provided that suitable acknowledgement to the source of the material is made (see the section near the top of this page - <http://www.wiley.com/bw/submit.asp?ref=0035-8711&site=1> - titled Exclusive Licence Form).

Best wishes,

Bella

-----Original Message-----

Sent: 07 October 2010 12:03

To: Bella Lock

Subject: Copyright waiver for MNRAS manuscript for the purpose of thesis inclusion

Hi,

I am currently a Ph.D. candidate in the Department of Physics and Astronomy at the University of Western Ontario and I am currently preparing the written portion of my dissertation prior to defense of my thesis. As part of this dissertation I would like to include the material I have previously published in the Monthly Notices of the Royal Astronomical Society (MNRAS), specially the article:

- Jean-Baptiste Kikwaya, Weryk R.J., Campbell-Brown, Brown, P.G., 2010. A model for saturation correction in meteor photometry, MNRAS, doi: 10.1111/j.1365-2966.2010.16294.x

If you could send to me an official copyright waiver for the preceding article it would be greatly appreciated.

Thank you for your time and understanding in this matter in advance.

Sincerely,

Jean-Baptiste Kikwaya

Subject: **Permission**

Date: 10/13/10 12:05 PM

Hi,

You are co-author of the following article published in the Monthly Notices of the Royal Astronomical Society (MNRAS):

- **Jean-Baptiste Kikwaya**, Weryk R.J., Campbell-Brown, Brown, P.G., 2010. A model for saturation correction in meteor photometry, MNRAS, doi: 10.1111/j.1365-2966.2010.16294.x

I would like to include the article as part of my thesis. If you could send me an official permission it would be greatly appreciated. Mostly, you would have to mention in detail your participation to the article.

Thanks,
Jean-Baptiste

December 9th, 2010

To whom it may concern,

With regards to the article "A model for saturation correction in meteor photometry" by Kikwaya et al., my main involvement was to devise the experimental procedure and to develop the software to perform the numerical modeling. I did not gather the data or perform the analysis.

I was involved in a very small role in the writing, mostly as a consultant to Mr. Kikwaya to explain the operating of the program code.

Rob Weryk

Subject: **Re: Permission**

Date: 10/13/10 12:24 PM

I give my permission for you to use this paper in your thesis. I had input in the research, and gave feedback on the writing of the paper.

Margaret Campbell-Brown

On 13/10/2010 12:05 PM, Jean-Baptiste Kikwaya Eluo wrote:

Hi,

You are co-author of the following article published in the Monthly Notices of the Royal Astronomical Society (MNRAS):

- **Jean-Baptiste Kikwaya**, Weryk R.J., Campbell-Brown, Brown, P.G., 2010. A model for saturation correction in meteor photometry, MNRAS, doi: 10.1111/j.1365-2966.2010.16294.x

I would like to include the article as part of my thesis. If you could send me an official permission it would be greatly appreciated. Mostly, you would have to mention in detail your participation to the article.

Thanks,
Jean-Baptiste

--

Subject: **permission**

Date: 01/06/11 07:35 PM

I give my permission for you to use this paper in your thesis. I advised on the research, and gave feedback on the writing of the paper.

Peter Brown

2011 01 07

Appendix D

Curriculum Vitae

Name:	Jean-Baptiste Kikwaya Eluo
Date of Birth:	April 3, 1965
Citizenship	Congolese (DRC)

**Post-Secondary Education
and Degrees :**

Noviciate (Jesuit Education) 1983-1986

Institut Supérieur Philosophique de Kimwenza (Philosophy) Kinshasa, DRC (Democratic Republic of Congo) 1986-1989.

Université de Namur, Belgium, Master in Mathematics (Celestial Mechanics). 1989-1994.

Faculté de Théologie (Centre Sevres), Paris, France 1994-1997. Honours Bachelor of Theology.

Institut de Mécanique Céleste (IMCEE), Observatoire de Paris, France. 1999-2001. (DEA: Diplôme d'Études Approfondies in Celestial Mechanics - Binary system of asteroids)

Faculté de Théologie (Centre Sevres), Paris, France 2001-2003. Master of Theology

The University of Western Ontario, London, Ontario, Canada 2004-2010. Doctor of Philosophy (Ph.D)

Related Work Experience:

Institut Lisanga (high school), Bandundu, DRC. Teaching 1983-1984

Institut Supérieur d'Agro Vétérinaire (College), Kinshasa, DRC. Teaching 1997-1999

Teaching Assistant. The University of Western Ontario 2004-2005

Pastoral counsellor (Priest). Roman Catholic Diocese of Etampes (France) 1999-2001. Roman Catholic Diocese of Tucson, Arizona (USA) 2002-2003. Roman Catholic Diocese of London, Ontario (Canada) 2004-2010 (Saint Thomas Aquinas, Saint Marguerite d'Yvonne, Saint Michael, Saint Peter Basilica (Cathedral).

Publications: Peer Reviewed Journal Articles

1. Kikwaya, J.B., Campbell-Brown, M., Brown, P.G., Hawkes, R.L., Weryk, R.J., 2009, Physical characteristics of very small meteoroids, *Astronomy and Astrophysics*, **497**, 851-867.
2. Kikwaya, J.B., Weryk, R.J., Campbell-Brown, M., Brown, P.G., 2010, A model for saturation correction in meteor photometry, *Monthly Notices of the Royal Astronomical Society*, **404**, 387-398.

Article in Submission

1. Kikwaya, J.B., Campbell-Brown, M., Brown, P.G., 2011, Bulk density of small meteoroids, *Astronomy and Astrophysics*, Submitted December 2010.

Abstracts/International Conferences

1. Kikwaya, J.B., Thuillot, W., Rocher, P., Vieira Martins, R., Arlot, J.E., Angeli, Cl., 2002, Astrometric Research of Asteroidal Satellites, *American Astronomical Society, DPS Meeting #34*. Bulletin of the American Astronomical Society, Vol 34, p.861.
2. Kikwaya, J.B., Thuillot, W., Rocher, P., Viera Martins, R., Arlot, J.E., Angeli, Cl, 2003, Does 146 Lucina Have a Satellite? An Astrometric Approach, *34th Annual Lunar and Planetary Science Conference*, March 17-21, 2003, League City, Texas, abstract no.1214.
3. Kikwaya, J.B., Thuillot, W., Berthier, J., 2003, Pluto-Charon: a test of the astrometric approach for finding asteroidal satellites, *American Astronomical Society, DPS meeting #35*; Bulletin of the American Astronomical Society, Vol. 35, p.981.

4. Kikwaya, J.B., Brown, P., Hawkes, R.L., 2004, The Bulk Density of Meteoroids from Electro-Optical Measurements, *American Astronomical Society, DPS meeting #36*, Bulletin of the American Astronomical Society, Vol. 36, p. 1147.
5. Kikwaya, J.B., Brown, P., Campbell-Brown, M., Nudds, S., 2006, The Bulk Density of Meteoroids from Electro-Optical Measurements, *Pre-Solar Grains as Astrophysical Tools, 26th meeting of the IAU*, Joint Discussion 11, 21 August 2006, Prague, Czech Republic, JD11,#22.
6. Kikwaya, J.B., Brown, P., Campbell-Brown, M., 2006, Bulk Density of Meteoroids based on Single Body Theory, 2006, *American Astronomical Society, DPS meeting #38*, Bulletin of the American Astronomical Society, Vol. 38, p. 562.
7. Kikwaya, J.B., Brown, P.G., Campbell-Brown, M., Hawkes, R., Weryk, R.J., 2007, Physical Characteristics of Very Small Meteoroids, 2007, *American Astronomical Society, DPS meeting #39*, Bulletin of the American Astronomical Society, Vol. 39, p.523.